

# **Ignition of high-pressure hydrogen releases**

**Experimental study of impinging and non-impinging releases through a fast-acting valve, with and without a burst disc downstream of the valve**

**By**

**Jørgen Skivenesvåg**



**Master of Science  
Energy – Safety in energy production**

**Geophysical Institute  
University of Bergen  
August 2021**



# Abstract

A wide consensus of climate research indicate that anthropogenic greenhouse gas emissions affect the climate and causes the global mean temperature to rise compared to preindustrial levels. International treaties such as the *Paris Agreement* intend to mitigate these expected changes by commitments to greenhouse gas reductions from the voluntary attending nations. The reductions must be effectuated as continuous reductions during the coming decades.

Significant changes to the global energy systems are necessary to facilitate for emission reductions. As much as possible of the current fossil-based energy consumption must be substituted with carbon free alternatives. Hydrogen is a viable substitution for carbon-based energy carriers in many applications as it does not emit carbon during combustion and has a very high mass-energy density. However, there are some additional hazards associated with utilisation of hydrogen. It very reactive and has very low minimum ignition energy (MIE). As a consequence of this, it has a high propensity to give spontaneous ignition during unintended releases. Although hydrogen has been in use for industrial applications for more than a century, the mechanisms that lead to spontaneous ignition are not fully understood.

This thesis aimed to investigate the most important ignition sources that could contribute to spontaneous ignitions, and in particular the mechanism known as *diffusion ignition*. Based on the findings from previous work, an experimental setup was constructed, and relevant experiments conducted. The experiments investigated the propensity for spontaneous ignition to occur when hydrogen was released through a nozzle. Some experiments investigated conditions where the released hydrogen was impinged on objects of different size and shape located at various distances from the nozzle exit. Other experiments investigated non impinging jets. Two different setups were used. One setup used a fast-acting valve to control the hydrogen release and allowed investigation of release scenarios that developed in a time scale of 30-60 ms. Another setup used rupture discs. These discs enabled investigation of releases that developed in a timescale of a few microseconds.

Tests with pressures up to 165 bar were conducted with the release valve setup. Neither impinging, nor non-impinging releases were able to cause ignition. Tests with the rupture disc setup gave ignitions in impinging conditions, but never in non-impinging conditions. The impinging object also had to be close enough if ignition should occur. The ignition source was not identified, and both spontaneous ignition and ignition caused by impact of debris from the rupture disc on the obstruction object was possible. Diffusion ignition appeared to be the most probable ignition of these two.

The preliminary conclusions are that ignition repeatably occurs when hydrogen at sufficiently high pressure is released in a rapidly developed pattern and impinges on an object with satisfactory proximity. Further investigations are necessary to quantify the critical conditions.

# Acknowledgements

I would like to thank my supervisor, associate professor Trygve Skjold for giving me the opportunity to undertake this project. It has provided me a lot of valuable knowledge and experience, and despite the occasionally frustrating nature of experimental work – it has also been exciting. I am in particular grateful for the substantial amount of work you have put into this project. The contributions to the construction of the experimental setup have been crucial. Proofreading during the final stage of this thesis work, which unfortunately coincided with the summer holiday, is also deeply appreciated.

The contributions from PhD candidate Mattheus van Wingerden in the initial setup and testing of the instruments was of great importance.

I would also like to thank Knut Vågsæther, Andre Gaathaug and Joachim Lundberg from the University of South-Eastern Norway for providing me with a MATLAB script for video analysis. I am also grateful for the useful insights and encouraging feedback you gave during the picture analysis.

My friend Dennis O. Lien made the work with data processing and plotting a lot easier. Your guidance in programming during development of the scripts used in this thesis has probably saved me a week of “Googling”...

Finally, I would like to thank my fiancé Lise Margrethe for your useful insights in thesis writing. But most importantly, your great patience during these years. Combining a full-time job with this master’s degree study almost got the best of me.

# Nomenclature

This section explains the abbreviations and symbols used in this thesis, including the appendices.

## Abbreviations

<b>AI</b>	Analogue input
<b>AIT</b>	Auto-ignition temperature
<b>bara</b>	Bar absolute (pressure)
<b>barg</b>	Bar gauge (pressure)
<b>BEV</b>	Battery-electric vehicle
<b>CCUS</b>	Carbon capture, utilisation and storage
<b>CO<sub>2</sub>e</b>	CO <sub>2</sub> equivalents
<b>C<sub>v</sub></b>	Valve flow coefficient
<b>DAQ</b>	Data acquisition (module)
<b>DN</b>	Nominal diameter
<b>DI</b>	Digital input
<b>DO</b>	Digital output
<b>DoE</b>	U.S. Department of Energy
<b>EU</b>	European Union
<b>FCEV</b>	Fuel cell electric vehicle
<b>GHG</b>	Greenhouse gases
<b>GMST</b>	Global mean surface temperature
<b>GWP</b>	Global warming potential
<b>HDR</b>	High dynamic range
<b>HHV</b>	Higher heating value
<b>HP</b>	High-pressure
<b>ICE</b>	Internal combustion engine
<b>ID</b>	Internal diameter
<b>IEA</b>	International energy agency
<b>IFT</b>	Department of Physics and Technology at UiB
<b>IMO</b>	International Maritime Organisation
<b>IPCC</b>	Intergovernmental Panel on Climate Change

<b>IRPA</b>	Individual risk per annum
<b>LFL</b>	Lower flammability limit
<b>LH2</b>	Liquified hydrogen
<b>LHV</b>	Lower heating value
<b>LNG</b>	Liquified natural gas
<b>MESG</b>	Maximum experimental safe gap
<b>MIC</b>	Minimum ignition current
<b>MIE</b>	Minimum ignition energy
<b>NDC</b>	Nationally determined contributions
<b>NO<sub>x</sub></b>	Nitrogen oxides, primarily NO and NO <sub>2</sub>
<b>NPT</b>	National pipe thread
<b>OD</b>	Outer diameter
<b>OO</b>	Obstruction object
<b>P&amp;ID</b>	Piping and instrumentation diagram
<b>PN</b>	Nominal pressure
<b>PPP</b>	Purchasing power parity
<b>Sm<sup>3</sup></b>	Standard cubic metre
<b>SMR</b>	Steam methane reforming
<b>SDG</b>	Sustainable development goal
<b>UFL</b>	Upper flammability limit
<b>UiB</b>	University of Bergen
<b>UN</b>	United Nations
<b>WGS</b>	Water gas-shift

# Symbols

<b>"</b>	length/distance [inches]
<b><math>\gamma</math></b>	Ratio of specific heat of gases
<b><math>\delta</math></b>	Diaphragm thickness
<b><math>a</math></b>	Speed of sound for a gas at specified conditions
<b><math>C</math></b>	Electrical capacitance
<b><math>c_0</math></b>	Speed of light in vacuum
<b><math>D</math></b>	Diameter for various objects and applications
<b><math>D_0</math></b>	Initial diameter
<b><math>F_K</math></b>	Ratio of specific heats factor
<b><math>F_P</math></b>	Piping geometry factor
<b><math>Ma</math></b>	Mach number
<b><math>M_w</math></b>	Molar mass
<b><math>n</math></b>	Refractive index
<b><math>\rho</math></b>	Fluid density
<b><math>R</math></b>	Molar universal gas constant
<b><math>u</math></b>	Fluid velocity
<b><math>\mu</math></b>	Adiabatic Joule-Thomson coefficient
<b><math>v</math></b>	Actual light speed
<b><math>v</math></b>	Particle velocity
<b><math>V</math></b>	Voltage
<b><math>\chi</math></b>	Opening ratio for rupture disc
<b><math>X</math></b>	Pressure drop ratio
<b><math>X_T</math></b>	Rated pressure drop ratio
<b><math>Y</math></b>	Gas expansion factor
<b><math>Z</math></b>	Compressibility factor

# Contents

Abstract .....	i
Acknowledgements .....	ii
Nomenclature .....	iii
Abbreviations .....	iii
Symbols .....	v
1 Introduction .....	1
1.1 The global energy demand .....	1
1.2 Hydrogen as an energy carrier in industry and society .....	2
1.3 Safety concerns related to hydrogen as an energy carrier .....	4
1.3.1 Selected case histories with spontaneous ignition of hydrogen releases .....	4
1.3.2 Accidents involving hydrogen refuelling stations .....	5
1.4 Objectives and limitations .....	6
1.4.1 Objectives .....	6
1.4.2 Limitations .....	7
2 Theory .....	8
2.1 Physical and chemical properties of hydrogen .....	8
2.2 Flow rate calculations .....	9
2.2.1 Subsonic and choked flow conditions .....	9
2.2.2 Supersonic jet behaviour .....	10
2.2.3 Valve flow rate calculations based on empirical equations .....	12
2.2.4 Additional restriction in downstream tubing and nozzle .....	15
2.2.5 Discontinuous flow and shock waves .....	18
2.2.6 Volume rate estimations based on pressure change .....	18
2.3 Measuring principles .....	18
2.3.1 Shadowgraph visualisation technique .....	18
2.3.2 Piezoelectric pressure transducers .....	21
2.4 Potential ignition sources for spontaneous ignition of hydrogen-air mixtures .....	21
2.4.1 The diffusion ignition phenomena .....	21
2.4.2 Reverse Joule-Thomson effect .....	22
2.4.3 Electrostatic discharges .....	23
2.4.4 Sudden adiabatic compression .....	24
2.4.5 Ignition by hot surface .....	24
2.4.6 Ignition by mechanical impacts .....	24
3 Literature review .....	26
3.1 Relevant literature and results .....	26
3.1.1 Experiments by Wolański and co-workers .....	26



3.1.2	Experiments by Dryer and co-workers .....	29
3.1.3	Experiments by Jiang, Pan, Wang and co-workers .....	29
3.1.4	Experiments by Golub and co-workers .....	31
3.1.5	Experiments by Mogi and co-workers.....	32
3.1.6	Numerical simulations by Liu and co-workers.....	34
3.2	The effect of rupturing behaviour on ignition .....	35
3.2.1	Experiments by Golovastov and Bocharnikov .....	35
3.2.2	Experiments by Kaneko and Ishii.....	37
3.2.3	Experiments by Gong and co-workers .....	37
3.2.4	Numerical simulations by Wen, Xu and co-workers.....	39
3.3	The effect of obstacles and angles in the tube .....	40
3.3.1	Experiments by Pan and co-workers .....	40
3.3.2	Experiments by Gong, Duan, Sun and co-workers .....	41
3.4	The effect of modified atmosphere.....	43
3.5	Main characteristics from the literature review .....	44
4	Experimental work .....	46
4.1	Purpose of experiments .....	46
4.2	Experimental equipment.....	47
4.2.1	Mechanical equipment.....	47
4.2.2	Instrumentation.....	51
4.3	Safety considerations in design and experimental work .....	53
4.3.1	Inherent safety features in the design .....	53
4.3.2	Procedural safety features.....	54
4.4	Commissioning activities .....	54
4.4.1	Leakage tests .....	54
4.4.2	Initial setup and verification of instrumentation.....	57
4.5	Reference tests with nitrogen through the release valve .....	57
4.6	Testing with hydrogen through the release valve.....	58
4.7	Experiments with hydrogen release through rupture discs.....	59
4.8	Data recording and interpretation.....	60
4.8.1	Camera and transducer settings .....	60
4.8.2	Measurements and interpretation on the high-speed images.....	61
4.8.3	Calculations and plotting based on data from piezo electric sensors .....	62
5	Results and discussion.....	64
5.1	Visibility of gases and flames.....	64
5.2	Flow rates and jet properties.....	65
5.2.1	Calculated flow rates compared to empirical flow values.....	65

5.2.2	Jet structures and jet development.....	69
5.2.3	Jet development in experiments with rupture disc .....	73
5.2.4	Comparison of nitrogen and hydrogen .....	75
5.2.5	Time delay for valve opening and asynchronous time stamps .....	77
5.3	Results from experiments with release valve alone.....	78
5.4	Results from experiments with rupture discs .....	80
5.4.1	Rupture discs – 50 bars.....	82
5.4.2	Rupture discs – 80 bars.....	83
5.4.3	Rupture discs – 100 bars.....	84
5.5	Evaluation of different obstruction objects and distances .....	86
5.6	The “outlier” Test 73 .....	87
5.6.1	Pressure behaviour.....	87
5.6.2	Observations from high-speed footage.....	88
5.7	Possible ignition sources .....	89
5.7.1	Diffusion ignition mechanism .....	89
5.7.2	Ignition by impact of debris from the rupture discs .....	89
5.8	Repeatability and uncertainty .....	91
6	Conclusions .....	93
7	Suggestions for further work.....	94
	References .....	95
	Appendices .....	A
A	Technical and functional description.....	B
A.1	Explosion chamber and blowdown pipe.....	B
A.2	High-pressure hydrogen system .....	F
A.3	Instrumentation and logging systems .....	O
A.4	Structural supports.....	Y
A.5	Material selection .....	DD
B	Other aspects related to the design and construction work .....	EE
B.1	Background and early work.....	EE
B.2	Leakage testing.....	FF
B.3	Further improvements on the experimental setup .....	GG
C	Checklists and procedures .....	JJ
C.1	Daily safety check list .....	JJ
C.2	Procedures before first experiment each day.....	JJ
C.3	Procedure for each experiment.....	KK
C.4	Checklist after last experiment each day .....	LL
D	Documents and drawings .....	MM

D.1	MECH-01-01 .....	NN
D.2	MECH-01-02 .....	PP
D.3	MECH-02-01 .....	QQ
D.4	MECH-02-02 .....	RR
D.5	MECH-02-03 .....	SS
D.6	MECH-03-01 .....	UU
D.7	MECH-03-02 .....	VV
D.8	MECH-04-01 .....	WW
D.9	MECH-04-02 .....	XX
D.10	MECH-04-03 .....	YY
D.11	MECH-04-04 .....	ZZ
D.12	P&ID-01-01 .....	AAA
D.13	P&ID-01-02 .....	BBB
D.14	IFD-01-01 .....	CCC
E	Complete list of experiments .....	DDD

# 1 Introduction

This thesis addresses critical aspects concerning the safe use of hydrogen as an energy carrier in industry and society. Hydrogen has unique physical and chemical properties that must be properly accounted for in design, operation and maintenance of equipment and installations for production, storage, distribution and utilisation of hydrogen. In particular, hydrogen-air mixtures are highly reactive and can be ignited by ignition sources that often are not relevant to consider for conventional fuels such as natural gas, petrol or diesel.

## 1.1 The global energy demand

The global primary energy consumption increased from 12 000 TWh (43 EJ) in 1900 to almost 160 000 TWh (576 EJ) in 2019, i.e. an increase by more than 13 times [1]. During the last decade, the annual increase has been around 1.6 % [2]. Various energy forecasts suggest a continued increase up to around 2030, when the consumption is expected to stabilise and eventually decline {[3]–[5]}. Figure 1-1 shows the development in the primary energy demand and energy sources during the last four decades, as well as the forecasted development up to 2050. The forecast from 2019 onwards is strongly affected by the Covid-19 pandemic, with a decrease of 8.3 % compared to pre-pandemic values [4]. However, the long-term impact of the pandemic is uncertain.

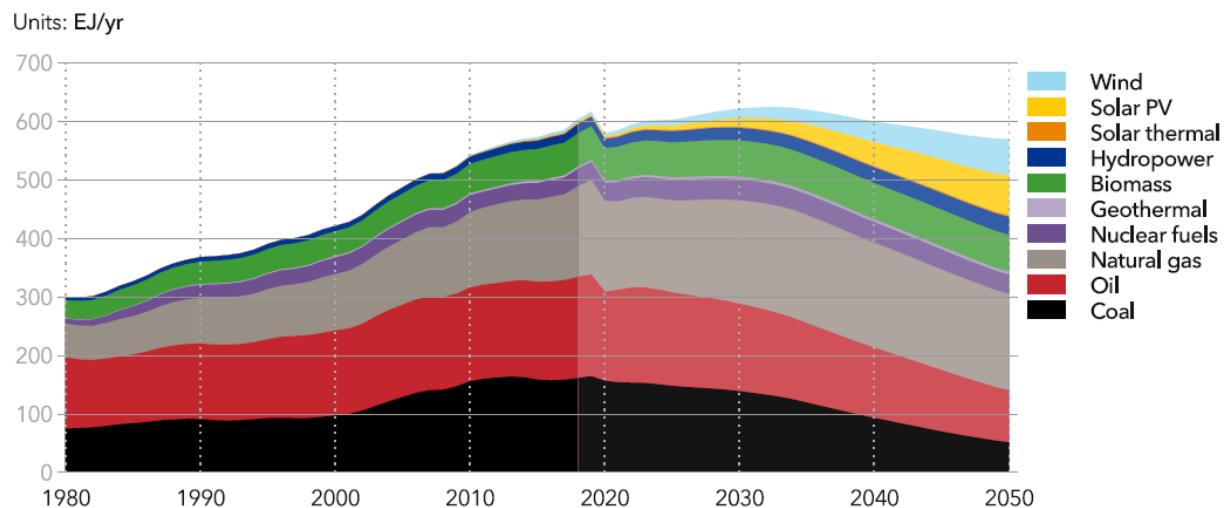


Figure 1-1: The development in primary energy consumption and estimated demand from 1980 to 2050, from [4].

The key drivers for the development in primary energy demand are population growth and a gradual increase in the average standard of living. The global population is expected to grow, but in a decreasing rate compared to the current situation. It is expected to reach 9.7 billion in 2050, and eventually converge to about 11 billion around 2100 [6]. The people with a standard of living defined as middle class<sup>1</sup> or higher accounted for more than half the global population in 2018 [7]. This share is expected to grow to 67 % in 2030. One billion people is expected to climb into the middle class between 2015 and 2022 [8].

---

<sup>1</sup> Homi Kharas from the Center for Sustainable Development at Brookings defines ‘middle class’ as households with per capita incomes in the range \$11 to \$110 per day in 2011 purchasing power parity-value. Purchasing power parity (PPP) is a method of normalizing the values from different countries based on how much it is possible to buy with the money in the respective country [8].

Energy consumption is closely correlated with greenhouse gas (GHG) emissions. The global GHG emissions were estimated to nearly 50 giga tonnes CO<sub>2</sub> equivalents (GtCO<sub>2</sub>e) in 2016, including about 36 GtCO<sub>2</sub>e in energy-related emissions {[9], [10]}. During the last centuries, the global mean temperature has increased significantly. However, the rate of increase accelerated in the beginning of the 20<sup>th</sup> century, coinciding with the escalation in anthropogenic CO<sub>2</sub> emissions due to the utilisation of fossil fuels. The temperature has increased more rapidly during the last 4-5 decades [11]. Although the global mean temperature is affected by several natural factors, most researchers, including the Intergovernmental Panel on Climate Change (IPCC), conclude that it is extremely likely that anthropogenic warming contributes to more than half the total warming [12, Ch. 10.3]. Quantitative estimates indicate that the sum of natural factors contributed with close to net zero warming during the last decades.

Several global initiatives aim at reducing the GHG emissions, and hence the anthropogenic impact on the temperature development. This is reflected in several of the Sustainable Development Goals (SDGs) from the United Nations (UN). The Paris agreement is a legally binding international treaty on climate change that came into force in 2016 [13], where the parties commit to reducing emissions according to their own *Nationally determined contributions* (NDC) [14]. The aim is to limit the maximum temperature increase to 1.5 °C compared to preindustrial levels. To achieve this, reports indicate that the emissions should approach net-zero in 2050 [15], or at least be significantly reduced compared to the current levels {[3], [4]}.

The energy forecasts depend on many technologies that are currently not mature at a commercial scale, including carbon capture, utilisation and storage (CCUS) [16], as well as widespread use of hydrogen or hydrogen-based fuels as energy carriers in industry and society.

## 1.2 Hydrogen as an energy carrier in industry and society

Hydrogen has been used as feedstock in the industry for more than a century. Estimates of the current annual production vary from 55 to 70 million tonnes (Mt) {[17]}, of which 55 Mt is currently used for industrial purposes [18]. A vast majority of the current hydrogen production originates from fossil feedstocks, mostly natural gas, without CCUS. This is referred to as ‘grey hydrogen’. Hydrogen can also be produced via electrolysis from renewable energy sources, so-called ‘green hydrogen’, or from fossil sources with CCUS (i.e. ‘blue hydrogen’). Only 2 % of the current hydrogen production is done with electrolysis [17, p. 38]. Although some hydrogen production plants with CCUS are in operation {[18, p. 10], [19]}, this method is not commonly used due to both cost and efficiency penalties compared to grey hydrogen, or direct use of fossil fuels when applicable.

Combustion of hydrogen produces water as the primary combustion product. In addition, combustion of hydrogen in air will also produce nitrogen oxides (NO<sub>x</sub>) [20]. Hydrogen has the highest specific energy density among all combustible fuels. On the contrary, its volumetric energy density is among the lowest (depending on storage conditions) for all energy carriers [21]. Nevertheless, hydrogen, whether it is ‘green’ and ‘blue’, can become one of the main energy carriers in an emission-free energy system. Several ongoing and planned projects entail the use hydrogen as the primary energy carrier, in various areas:

- *Transportation* – the International Energy Agency (IEA) estimated that the global transport sector, i.e. road, rail, marine and aviation combined, used 32 500 TWh of the total energy consumed by end users in 2015 – this corresponded to 26 % of the global energy-related GHG emissions [4, Ch. 1.1, 7.1].

- *Road*: Fuel cell electric vehicles (FCEV) could, together with battery electric vehicles (BEV), replace a major share of the conventional vehicles powered by internal combustion engines (ICE) using petrol or diesel. FCEV is especially interesting for larger vehicles, and DNV GL estimates that more than 50 % of all buses and 30-50 % of all medium and heavy-duty trucks will be powered by hydrogen fuel cells by 2050 [18, p. 22].
- *Rail*: Several ongoing initiatives explore the use of on-board hydrogen fuel as a source of energy to power the traction motors and/or auxiliaries on trains (hydrail) [22].
- *Marine*: Although most merchant ships today use bunker oils that originate from the distillation of crude oil, the International Maritime Organisation (IMO) has adopted an initial strategy for the reduction of GHG emissions from ships by at least 50% by 2050, relative to a 2008 baseline [23]. The measures for cutting emissions include increased use of zero-carbon fuels or energy sources, such as batteries, biofuels, hydrogen, and hydrogen-based fuels. Relevant ongoing initiatives in Norway include two ferries in Rogaland [24]–[26] and various other ships that will be powered by hydrogen [27].
- *Aviation*: A joint report from the Clean Sky 2 Joint Undertaking and Fuel Cells and Hydrogen 2 Joint Undertaking (FCH 2 JU) suggests that aircrafts powered by hydrogen have the potential to significantly reduce the global GHG emissions [28].
- *Industrial applications* – a transition from conventional energy carrier to hydrogen is highly relevant for various industries, such as:
  - Replacing coal or natural gas for high temperature heating in industrial processes [29].
  - Replacing solid state carbon as reduction agent in electrochemical processes where a redox reaction is used to refine an oxide or similar to a more valuable product. Relevant examples include Tizir Titanium in Odde [30] and iron production [31].
  - Production of chemical compounds, and alternative low-emission energy carriers, such as methanol and ammonia.
- *Peak shaving in the energy system* – existing technologies can convert renewable or non-renewable energy sources to hydrogen, hydrogen can be stored and transported in compressed, liquid or chemical form, and fuel cells or turbines can convert hydrogen or hydrogen-based fuels to electrical energy on demand. As such, hydrogen can compensate for the inherently intermittent nature of renewable energy sources such as wind and solar. However, energy conversion entails significant conversion losses, and DNV GL estimates a “round trip” efficiency of only 40% [18].
- *Domestic heating* – hydrogen can replace or complement hydrocarbon fuels as energy source for domestic heating and cooking. Existing distribution grids might be utilised to some extent. The H21 project in UK is a pilot-scale project with several subprojects involving substitution of fossil fuels with hydrogen in the domestic gas grid [32].

The forecasts of future energy demands vary significantly. In scenarios developed for 2050, DNV GL estimates the total annual demand to 108-275 Mt [18, p. 47], while the so-called *Sustainable Development Scenario* from IEA predicts 300 Mt [33, p. 141].

Both regulatory and technological steps are necessary before hydrogen can become competitive as an energy carrier in industry and society. Carbon fees or other forms of emission taxes can be implemented to minimise the cost difference between hydrogen and conventional fuels, as well as between grey and blue hydrogen. It is also necessary to scale up production and develop large-scale infrastructure for transportation and storage of hydrogen and carbon dioxide (to reduce the unit cost of CCUS, and thus blue hydrogen).

## 1.3 Safety concerns related to hydrogen as an energy carrier

Hydrogen-air mixtures are highly reactive and can be ignited by ignition sources that would not be able to ignite conventional fuels such as natural gas, petrol and diesel. This, in combination with hazards related to the high-pressure or cryogenic storage methods used to increase the volumetric energy density of hydrogen, imply significant challenges for the technical and operational safety in all parts of the hydrogen value chain. Although hydrogen has been used in industrial applications for more than a century, the legacy from past accidents demonstrates the damage potential and the implications severe accidents can have for the technological development<sup>2</sup>. Although the risks apparently have been mitigated sufficiently to make conventional applications of hydrogen in industrial settings acceptable from a health, safety and environment (HSE) perspective, there are still significant challenges concerning the widespread use of hydrogen as an energy carrier in society:

- The number of systems and facilities where hydrogen is handled will increase dramatically if hydrogen becomes a widespread fuel in the transport sector. The number of hydrogen-fuelled vehicles, trains, passenger ships and planes is expected to increase by several orders of magnitude, and this development must be supported by an appropriate infrastructure for production, storage and distribution. A heavy increase in the number of potential leakage points and potentially dangerous operations is likely to increase the incident frequency compared to the current level.
- At industrial sites, only people with experience and knowledge about hydrogen and the associated hazards will normally be allowed to operate the systems, and hence be exposed to the risks. In the public domain, such as hydrogen refuelling stations there are limited requirements for mandatory safety training or formal knowledge about hydrogen or technical knowledge in general. While industrial sites are located at remote areas and have restricted access, public infrastructure, such as hydrogen fuelling stations, will necessarily be located in densely populated areas. Such installations are also more accessible for people with harmful intentions, compared to fenced-in industrial facilities.
- The acceptance criteria for individual risk are often one or two orders of magnitude lower for members of the public, compared to on-site personnel in industrial sites {[34, p. 71], [35]}. Common values for unacceptable individual risk per annum for a certain activity (IRPA<sub>a</sub>) are  $10^{-3}$ - $10^{-4}$  for onsite personnel, and  $10^{-5}$ - $10^{-6}$  for third-parties people not involved in the work or operation that inflict risk [35]. Hydrogen systems in the public domain will expose everyone in their surroundings for the hazards, regardless of their involvement in any hydrogen related activities. Thus, many people will be exposed as third party to hydrogen systems in urban areas.

### 1.3.1 Selected case histories with spontaneous ignition of hydrogen releases

More than 86% of all major incidents reported to the Major Hazards Incident Data Service (MHIDAS) database involving ignited hydrogen-air mixtures did not have an identified ignition source [36]. The equivalent number for non-hydrogen incidents were 65.5%. However, since the database only contained 81 hydrogen-related accidents, compared to 1437 accidents with other fuels, the statistical significance of this difference can be questioned. Nevertheless, the fact that hydrogen-air mixtures are easily ignitable implies that it often is not straightforward to identify the ignition source that triggered an accidental fire or explosion. This section reviews selected examples of such incidents.

---

<sup>2</sup> Relevant accidents in this context include the hydrogen fire at airship LZ 129 *Hindenburg* on 6 May 1937 (36 fatalities), the hydrogen explosion at the ammonia production plant of Norsk Hydro on *Herøya* on 6 July 1985 (two fatalities), the hydrogen explosion at the *Fukushima Daiichi* nuclear disaster on 11 March 2011 (one confirmed cancer death, and severe implications for the global nuclear industry), and the explosion at the hydrogen refuelling station at *Kjørbo* on 10 June 2019 (no fatalities, but significant impact on the implementation of hydrogen as an energy carrier in Norway).

Astbury and Hawksworth mentioned an incident that occurred in 1922 [36], where hydrogen stored at 2.1 MPa ignited when released to the atmosphere. The results from the accident investigation were ambiguous, but it was suggested that the ignition source may have been a corona discharge. It is however unlikely that a single corona discharge would be able to ignite the hydrogen-air mixture, but multiple corona discharges can be incendiary [37].

Reider *et al.* describe an incident that occurred during acoustic testing in 1964 [38]. The intention was to perform two tests that involved discharges of a large volume of hydrogen stored at high pressure, and compare the level of noise generated by an unignited and an ignited release. However, ignition occurred in the first test, where ignition was not supposed to occur. Ignition occurred 3 second closing of the 150 mm ball valve started. The ignition source was not identified with absolute certainty, but one theory pointed to a possible impact by a metal rod that was welded across the nozzle. After the test, it was discovered that the rod was torn loose in one end.

Bond mentions two incidents [39]. The first happened when hydrogen at an initial pressure of 11.1 MPa was leaking through a flange. The leakage did not ignite in the first place, but when an impact wrench was used to tighten the bolts in the flange, in an attempt to stop the leak, ignition occurred. Although the time of ignition coincided with the second impact of the hammer on the wrench, it is not certain whether the ignition source was heat or mechanical sparks generated by the impact, or diffusional ignition. The second incident occurred when a laboratory technician opened a standard high-pressure bottle containing hydrogen to remove debris in the connected laboratory equipment and connections. The hydrogen ignited immediately after the bottle was opened, and Bond concluded that diffusion ignition was the source. However, results from experiments conducted over the last decades suggest that regular opening of a valve is not likely to result in ignition by the diffusion mechanism (this will be discussed further in the next chapter).

Wolański and Wojcicki published the paper that is generally acknowledged as the first scientific contribution to the study of the diffusion mechanism, often referred to as spontaneous ignition, for hydrogen-air mixtures [40]. This work was motivated by an accident that occurred few years earlier at an ammonia (NH<sub>3</sub>) plant in Poland [41]. The explosion occurred in a system containing synthesis gas, and the temperatures and pressures of process where the explosion occurred were 300 °C and 300 bars, respectively. The accident killed four people. The investigation excluded all conventional ignition sources, but Wolański & Wojcicki presented a consistent theory for ignition by the so-called diffusion mechanism and demonstrated this phenomenon experimentally.

### 1.3.2 Accidents involving hydrogen refuelling stations

Some 553 hydrogen fuelling stations were in operation by the end of 2020, of which 107 stations were put in operation during that year [42]. Even though the global number of hydrogen stations is still low, some statistics on relevant accidents are available. In Japan, 21 incidents involving hydrogen refuelling stations were registered between 2005 and 2014. Records for USA show 22 accidents from 2004 to 2012 [43]. One of the most common causes for loss of containment is inadequate torque on threaded joints and bolted flanges, including the filling hose.

Inadequate torque on the bolts on a flange has also been mentioned as a likely cause of the leakage that led to the strong explosion on the hydrogen refuelling station at Kjørbo, near Sandvika (near Oslo) on 10 June 2019. A preliminary accident investigation traced the origin of the release to a flange on a high-pressure unit, operating at a working pressure of about 900 bar [44]. Figure 1-2 illustrates the two-part plug where insufficient torque on the outer flange (blue bolts) may have initiated a release through the seals for the inner part of the plug (through the gasket marked red). The leak rate increased until it exceeded the rate the leak bore could mitigate. This led to pressure build up within the cavity confined by the other gaskets (blue and green). At some point, the inner bolts, which were inadequately tightened, allowed hydrogen to pass the outer gasket (marked blue on the drawing), eventually resulting in a failure



of this gasket with a subsequent large release rate [44]. The ignition source for the explosion at Kjørbo remains unknown.

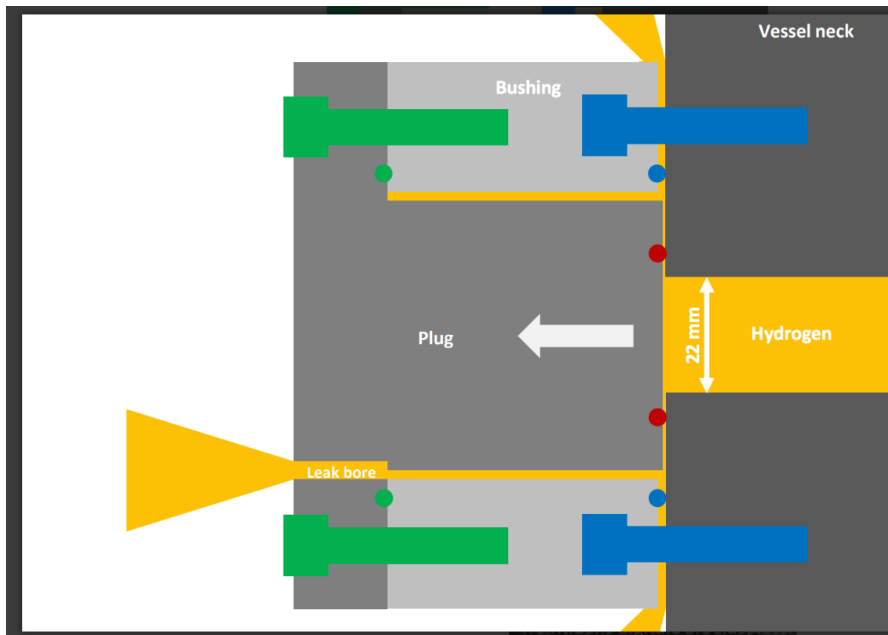


Figure 1-2: Sketch of the leaking plug that caused the Kjørbo incident, from [44].

A large release of hydrogen occurred at the AC Transit facility in Emeryville, California in 2012 [45]. This refuelling station serviced hydrogen-powered buses. Breakage of a nozzle within a safety valve resulted in the release of some 300 kg hydrogen over 2.5 hours, where 30 kg were released during the first minute. Ignition occurred shortly after the onset of the release, resulting in an explosion followed by a jet fire. The root cause of this accident was material failure in a part of the nozzle resulting from the use of a material not compatible for hydrogen (440-C stainless steel). The other parts of the safety valve were made from 316 SS, which is well suited for hydrogen service. The ignition source was not identified.

## 1.4 Objectives and limitations

This thesis is motivated by the prospects of future widespread use of hydrogen as an energy carrier in industry and society, as well as the implications severe accidents can have for people, property, and the development of the emerging hydrogen technologies. Hydrogen is often mentioned as an enabler for renewable energy sources ('green' hydrogen), as well as a sustainable solution for continued use of fossil fuels ('blue' hydrogen). However, the safety-related properties of hydrogen and hydrogen systems imply that it is not straightforward to achieve and document the same level of safety as for conventional fuels [46]. There are also significant knowledge gaps associated with both combustion and ignition phenomena, including the mechanisms involved in ignition of transient hydrogen releases from high pressure. The need for more knowledge and increased awareness of such hazards is also evident from incidents, including the explosion at the hydrogen refuelling station at Kjørbo on 10 June 2019.

### 1.4.1 Objectives

The *primary objective* of this thesis was to conduct an experimental investigation of mechanisms that may result in spontaneous ignition of releases from high-pressure storage of hydrogen.

Secondary objectives include:

- To establish a laboratory facility that facilitates safe storage, handling and testing of hydrogen.
- To complete a literature study on the possible mechanisms for ignition of abrupt hydrogen releases, including a basic study on miscellaneous mechanisms and a more detailed study on diffusion ignition.
- To conduct an experimental study based on the preliminary findings from the literature study.
- To discuss the practical implications of the results from the literature study and the experiments.

#### 1.4.2 Limitations

The experimental work was conducted during the first phase of the development of the new experimental facility called *Hydrogen Safety Laboratory* (HySALA) at the Department of Physics and Technology (IFT) at University of Bergen (UiB). This implied several limitations to the type and number of experiments that could be performed:

- Significant efforts went into the construction and assembly of the experimental apparatus, and this work was significantly delayed due to limited access to the premises during the Covid-19 pandemic.
- The laboratory was not fully operational until seven weeks before the extended deadline for submitting the thesis. Thus, all the experiments, as well as the interpretation of data and associated writing, had to be completed during this limited time window.
- It was only possible to perform tests with the pressures available in the 50-litre hydrogen bottles, i.e. pressured up to about 200 bar.
- Material cost and significant preparation time for each experiment limited the number of experiments that could be performed with rupture discs.

## 2 Theory

### 2.1 Physical and chemical properties of hydrogen

Table 2-1 summarises some of the safety-related properties for hydrogen and methane. The comparison to methane is included because methane is the main component of natural gas, including liquified natural gas (LNG), and hence a commonly used fuel in the industrial context. As storage and transport of liquified hydrogen (LH2) is expected to become more widespread in the coming years, it will in many cases be natural to compare LNG and LH2, and hence hydrogen and methane.

Table 2-1: Safety-related properties for hydrogen and methane.

Property	Hydrogen	Methane	Unit
Lower flammability limit (LFL) {[47], [48]}	4	5.4	vol.%
Upper flammability limit (UFL) {[47], [48]}	75	15.9	vol.%
Minimum ignition energy (MIE) [49]	0.017	0.28	mJ
Heat of combustion, HHV [50]	141.9	55.5	MJ/kg
Heat of combustion, LHV [50]	120.0	50.0	MJ/kg
Minimum ignition current (MIC) [51]	75	640	mA
Maximum experimental safe gap (MESG) [51],	0.23-0.29	1.12-1.14	mm
Auto-ignition temperature (AIT) [51, pp. 520, 640]	500-585	600-610	°C
Boiling point at atmospheric pressure {[47], [52]}	-252.9 (20.25)	-161.5 (111.65)	°C (K)
Molar mass ( $M_w$ )	2.016	16.04	g/mol
Adiabatic flame temperature [53]	2318	2158	K
Laminar burning velocity for stoichiometric mixture [54]	2.21	0.389	m/s
Maximum laminar burning velocity [54]	2.89	0.393	m/s
Lower detonation limit [53]	11-18	6.3	vol.%
Upper detonation limit [53]	59	13.5	vol.%
Gas group	IIC	I	–
Temperature class	1	1	–

The classification of flammable vapours and gases in Gas groups is based on the parameters maximum experimental safe gap (MESG) and *minimum ignition current* (MIC) [55]. Both hydrogen and methane are used as reference gases for their respective gas groups. A mixture of  $21 \pm 2$  % vol hydrogen in air is used as a reference for gas group IIC, while  $8.3 \pm 0.3$  % vol methane in air is used as reference for Gas group I [56, Ch. 10.2]. The gas groups are used to select the proper level of explosion proofing on electrical equipment in areas where flammable mixtures of different gases could occur. Gas group IIC is the group with the lowest values for MIC (MIC ratio<sup>3</sup> < 0.45) and MESG ( $\leq 0.5$  mm), and this will in general correspond to the lowest values of the minimum ignition energy (MIE). In addition to hydrogen, gas group II C includes acetylene and carbon disulphide [57].

The classification of flammable vapours and gases in Temperature classes is based on AIT [55]. Both hydrogen and methane belong to Temperature class T1, i.e., AIT > 450°C. The temperature classes are used to define the maximum allowable surface temperature on equipment located in areas where explosive atmospheres could occur {[56, Ch. 10.2], [58]}.

The values for laminar burning velocities for hydrogen given in Table 2-1 show that there is significantly larger difference between the maximum value and the value at stoichiometric conditions for hydrogen,

<sup>3</sup> The MIC ratio is calculated by dividing the MIC of the tested gas by the MIC for 8.3 vol.% methane in air.

compared to methane. The maximum value for hydrogen corresponds to an equivalence ratio of about 1.8, compared to 1.1 for methane [54].

## 2.2 Flow rate calculations

The system used in this thesis is neither ideal, nor steady state. However, some of the basic theory for such idealised systems is nevertheless relevant to the understanding of the phenomena involved.

### 2.2.1 Subsonic and choked flow conditions

When a differential pressure is applied across an opening, or nozzle, separating two gas reservoirs (e.g. a pressurised tank and the atmosphere), the gas will flow in the direction from higher to lower pressure. The pressure at the exit of the nozzle is referred to as the *back-pressure*, and the pressure at the entry is the *stagnation pressure* [59]. The ratio between these pressures controls the flow through the nozzle. For moderate pressure ratios, the flow velocity will increase for increasing stagnation pressures or lower back-pressures. The law of continuity implies that the highest velocity will occur at the smallest cross section of the flow. Bernoulli's law for a compressible, adiabatic ideal fluid can be expressed as:

$$\frac{1}{2}u^2 + \frac{\partial p}{\rho_0} + gz = \text{constant} \quad (1)$$

where  $u$  is the fluid velocity,  $p$  is the local static pressure at a point in the system,  $\rho_0$  is the initial density of the gas,  $g$  is the universal gravity constant and  $z$  is the elevation for a point in the system. In the present context, the gravity term can be neglected. *Vena contracta* is the point in a fluid stream where the diameter of the stream is the least and the fluid velocity is at its maximum [60, p. 18]. Eq. (1) implies that the static pressure will be lowest in this point. The narrowest section of a nozzle is called the throat. Due to separated flow near sharp corners, the *vena contracta* and the throat will not necessarily be located in the same position [60, p. 18].

At *critical conditions*, the flow velocity at the *vena contracta* becomes sonic, and a further increase in the differential pressure caused by decreased back pressure will not increase the velocity further. All conditions with differential pressures above this critical value are referred to as choked flow conditions. The speed of sound in an ideal gas is given by the relationship:

$$a = \sqrt{\frac{\gamma RT}{M_w}} \quad (2)$$

where  $\gamma$  is the ratio of specific heats (adiabatic constant),  $M_w$  is the molar mass of the gas,  $T$  is absolute temperature, and  $R$  is the universal gas constant ( $8.314 \text{ J mol}^{-1}\text{K}^{-1}$ ). From Eq. (2) the speed of sound for hydrogen at  $20^\circ\text{C}$  is about  $1300 \text{ m/s}$ . For flow velocities near or above sonic conditions it is convenient to introduce the Mach number  $\text{Ma}$ :

$$\text{Ma} = \frac{u}{a} \quad (3)$$

For isentropic conditions, the relation between the initial pressure  $p_0$  and the pressure  $p$  at a given point in a nozzle is given by [59, Ch. 3.5]:

$$\frac{p}{p_0} = \left(1 + \frac{\gamma - 1}{2} \text{Ma}^2\right)^{-\frac{\gamma}{\gamma - 1}} \quad (4)$$

The critical pressure corresponds to critical conditions, i.e. a Mach number of unity ( $Ma = 1$ ), for a given gas. For hydrogen and other diatomic gases ( $\gamma=1.4$ ) the critical pressure is  $p_{critical} = 0.528 p_0$ .

There are two ways to increase the mass flow rate through a system with choked flow:

1. Increasing the cross section of the restricting section, for the same velocity and pressure conditions.
2. Increasing the upstream pressure, for the same limiting cross section. This will increase the static pressure at the *vena contracta*, and hence the density of the fluid passing through the throat at choked flow conditions.

## 2.2.2 Supersonic jet behaviour

This section outlines the basic theory for ideal steady-state jet flow in a convergent-divergent nozzle, such as a Laval nozzle {[59, p. 9], [59], [61]}. Increased differential pressure caused by reduced back pressure, beyond critical conditions, will affect the behaviour of the flow downstream of the orifice, even though the mass flow rate will remain unchanged.

Figure 2-1 and Figure 2-2 illustrate pressure profiles and jet behaviours for selected pressure ratios in a convergent-divergent nozzle configuration:

- a) *Subsonic flow* (described above).
- b) *Choked flow* ( $M = 1$ ), at critical conditions (described above).
- c) When the flow has become choked, a further reduction in the back-pressure will cause an increased velocity at the section downstream the *vena contracta*, despite the increased cross-sectional area. The expansion of the gas due to the lower pressure more than outweighs for the increased cross-sectional area, resulting in supersonic velocities. At some point, the flow will meet a shock wave downstream of the throat, which brings the pressure up to the exit pressure. The pressure immediate downstream of the throat could be temporarily lower than the exit pressure.
- d) As the exit pressure is lowered further, the shock wave will move further away from the *vena contracta*, and at some point it will be positioned at the nozzle exit.
- e) A slight further reduction of the downstream pressure will force the shock wave to move to the outside of the nozzle. Under these conditions, the jet will exit the nozzle at a lower pressure than the ambient pressure. The jet will therefore be compressed by the ambient pressure, and this will cause the shock wave to become oblique in a way that the peripherals sections of the jet is directed inwards (centred). This is referred to as an *overexpanded jet*.
- f) At some point, the ambient pressure is equal to the static pressure in the jet upon its exit from the nozzle. In these situations, the jet will retain its shape for a significant distance behind the nozzle exit. The velocity will also remain supersonic for a relatively long distance behind the nozzle exit.

For a nozzle intended to generate thrust or deliver a high velocity jet for other purposes, this is the desired situation, and it is therefore referred to as '*design conditions*'.

- g) Expansion waves that reduce the pressure to ambient conditions will appear when the back-pressure becomes lower than the static pressure in the jet at the nozzle exit. The jet will also expand radially to equalise its pressure relative to its environment. This is known as an *underexpanded jet*.

An underexpanded jet will form a Mach disc at the location where the velocity in the free jet stream drops below Mach 1 [62]. At the same time, the boundaries of the jet will remain supersonic past the Mach disc in the centre of the jet. Figure 2-3 illustrates the structure of an underexpanded jet, which can be observed for jets emitted from nozzles with insufficient divergence to support supersonic velocities within the nozzle itself. Hence, most of the expansion and velocity increase take place outside the nozzle.

Due to the large differential pressures and low back pressure (ambient atmosphere pressure) used in the experiments in this thesis, underexpanded jets were likely to occur. The following sections elaborate on the application of ideal jet theory under non-ideal experimental conditions.

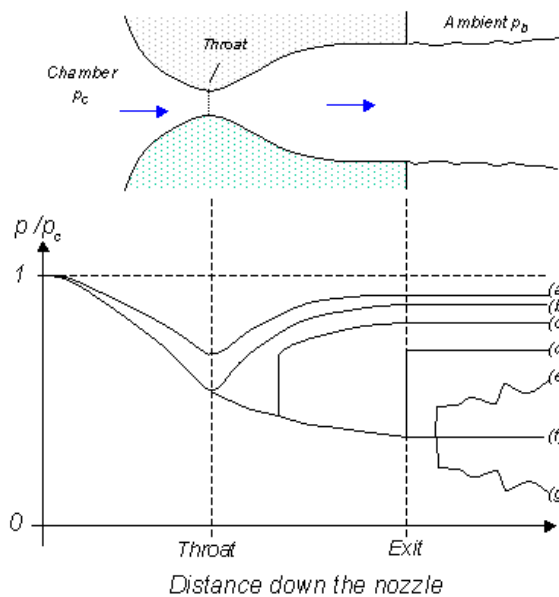


Figure 2-1: Illustrates the pressure profiles for jets under different back pressure conditions, from [61].

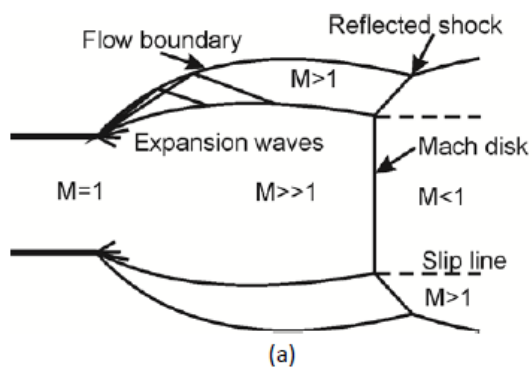


Figure 2-3: Jet structure of an underexpanded jet, from [63, p. 68].

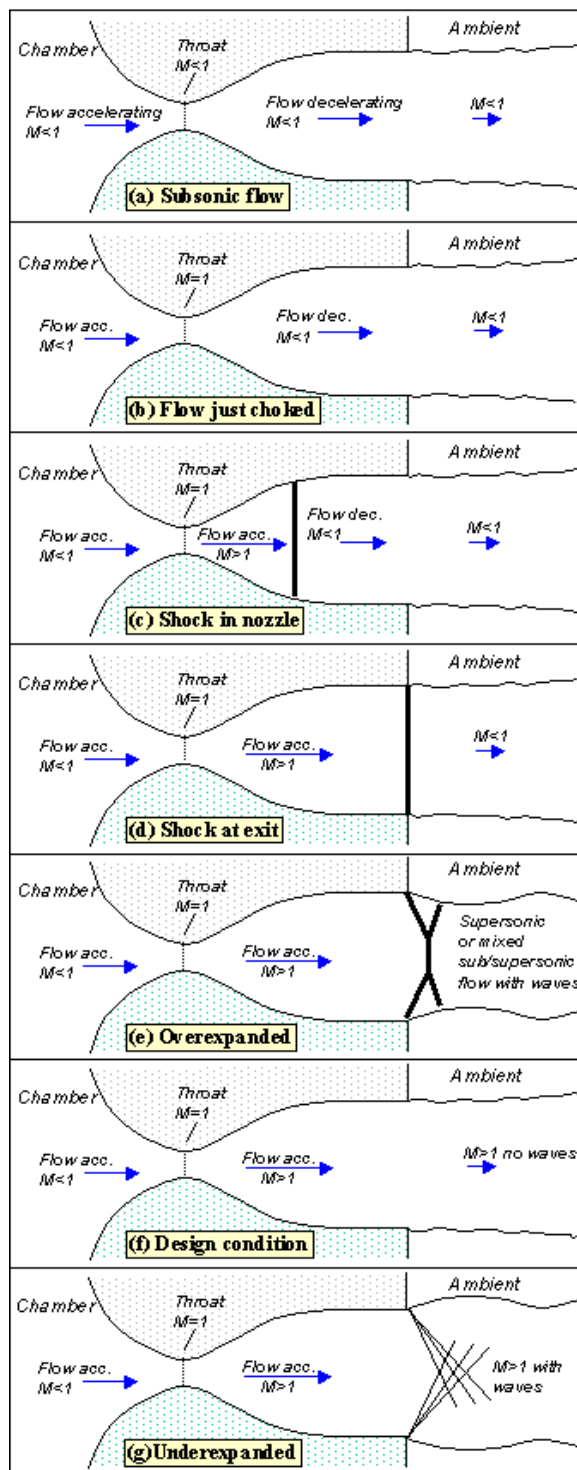


Figure 2-2: Illustrates the jet behaviour with varying back pressures, from [61].

### 2.2.3 Valve flow rate calculations based on empirical equations

The experimental setup in this thesis used a valve to control the hydrogen releases. The valve was the restricting point in the tube system from the reservoir to the nozzle exit. To understand the flow through the system, it is instructive to perform some simple calculations for the actual valve. This section summarises the theory and empirical relations used in the process industry for valve design.

The flow capacity of a valve is given by the dimension and the flow coefficient ( $C_V$ ). This parameter allows for comparison of valves with different design, nominal pipe size and pressure rating. The original definition of the flow coefficient is the flow rate of water in gallons per minute with a differential pressure of 1 psi at a temperature of 60 °F. This corresponds to 0.145 bar and 15.6 °C. It follows that a  $C_V$  of unity corresponds to a flow rate of one gallon per minute under the stated conditions. To accommodate SI units, it is possible to introduce the corresponding parameter  $K_V$ , which is proportional to  $C_V$ :

$$K_V = 0.865 * C_V \quad (5)$$

Since  $C_V$  is the most common characteristic within the process industry, including countries that have adopted the SI system, most vendors provide only  $C_V$ -values in datasheets for valves, and most equations are adapted to imperial units, this thesis will operate with  $C_V$ .

Methods for calculation of both compressible and incompressible fluids are presented many places. Most vendors of valves, and especially those who deliver control valves, provide a manual with equations for estimations of  $C_V$  values. The primary purpose of these manuals is to guide the customer to select the correct valve size and characteristic for their process conditions. A rather comprehensive method is used as basis for this thesis {[60], [64]}. A similar, but a bit simpler method is presented elsewhere {[65, p. Tech-8], [66, p. 19]}.

All handbooks provide alternative equations to adapt to the available information. Among the two preferred handbooks with the most advanced procedures {[60], [64]}, only one provides proportionality constants for different units, including SI derived units [60]. For calculation of volumetric flow based on molar mass for the gas, the following equation could be used:

$$C_v = \frac{q}{N_9 F_P P_1 Y \sqrt{\frac{x}{M T_1 Z}}} \quad (6)$$

where  $N_9$  is a constant based on the desired units (a value of 2240 is suited for calculation in bar,  $\text{Sm}^3/\text{h}$  and K),  $q$  is the volumetric flow rate (in  $\text{Sm}^3/\text{h}$  at  $T = 15.5$  °C,  $p = 1$  atm = 1.013 bara),  $F_P$  is the piping geometry factor<sup>4</sup>,  $P_1$  is the inlet pressure (bara),  $x$  is the pressure drop ratio for the given conditions,  $M_w$  is the molar mass for the gas (g/mol),  $T_1$  is the initial temperature of the gas,  $Y$  is the expansion ratio, and  $Z$  is the compressibility factor. The pressure drop ratio  $x$  is defined as:

$$x = \frac{P_1 - P_2}{P_1} \quad (7)$$

where  $P_2$  outlet pressure from the valve. The expansion ratio  $Y$  is calculated from:

$$Y = 1 - \frac{x}{3F_K X_T} \quad (8)$$

---

<sup>4</sup> The piping geometry factor  $F_P$  accounts for restrictions due to bends, reducers, and other components at the inlet and outlet of the valve. As the setup in this thesis has the same dimension on the adjacent tubing as the valve itself, this value is 1, and the procedure for calculating  $F_P$  is not shown here (can be found in [60], [64]). Notably, and significant deviation from unity of  $F_P$  increases the complexity of the calculations significantly.



where  $X_T$  is an empirical value that gives the pressure drop ratio at which choked flow occurs (for a gas with  $\gamma = 1.4$ ), and  $F_K$  is the ratio of specific heats factor, defined as:

$$F_K = \frac{\gamma}{1.4} \quad (9)$$

Thus, if the actual pressure drop ratio  $X$  is larger than the product of  $F_K$  and  $X_T$ , it must be replaced with that expression in all places it is used in the equations. This implies that the expansion ratio  $Y$  can never become smaller than  $2/3$ , since the last term in Eq. (8) will become  $\frac{X_T F_K}{3X_T F_K} = \frac{1}{3}$  when choked conditions occur.

The compressibility factor  $Z$  describes the deviation between a real gas and ideal gas behaviour at a given temperature and pressure. Compressibility factor above one indicates that the real gas occupies a larger volume or has a higher pressure than the corresponding molar volume of an ideal gas at the given conditions [67, Ch. 1.3.5]. Hydrogen at ambient conditions behaves similar to an ideal gas. As seen in Figure 2-4, the  $Z$ -value for hydrogen is between 1.0 and 1.1 for the temperature and pressure ranges this thesis operates within. A  $Z$ -value of 1.05 is selected for the calculations shown below.

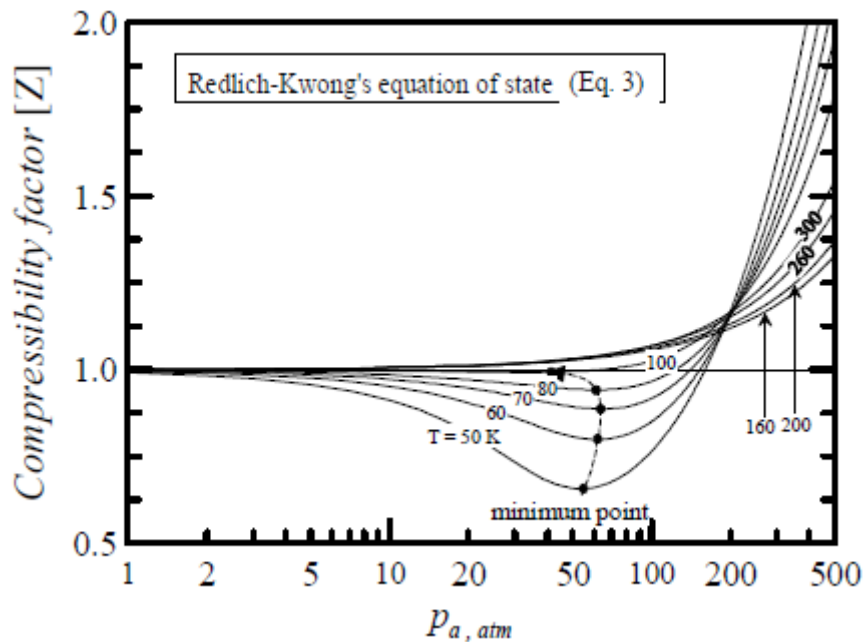


Figure 2-4: Compressibility factor for hydrogen for different isotherms according to the Redlich-Kwong equation of state, from [68].

It follows that two empirical valve-specific values are required for the calculations. The vendor of the  $\frac{3}{8}$ " release valve used in this thesis provided the  $C_V$ -value, but not the  $X_T$ -value. As such, a typical  $X_T$ -value for valves of similar design and dimensions was used. Table appendix 2 . summarises the relevant information for the valve used in this project, including the  $C_V$ -value (0.9) and the stipulated  $X_T$ -value (0.62).

The variables used in these calculations are to some extent depending on each other. In scenarios where the pressure drop ratio and other factors are unknown, it might be necessary with several iterations to achieve sufficient precision. This will be the case if the equations for instance are used to determine the necessary  $C_V$ -value and valve position at given flow conditions, or the pressure drop through a given valve at a given flow. However, for the purpose of the calculations in this thesis, iterations are not

necessary, since it is only necessary to calculate the flow at choked conditions. This is because both the parameter  $X$  in Eq. (7) and the parameter  $Y$  in Eq. (8) are constant under choked conditions.

Figure 2-5 summarises the volumetric flow rates for hydrogen and nitrogen, calculated for various inlet pressures and a fixed outlet pressure of 1 atmosphere according to Eqs. (6), (7), (8) and (9). For ambient exit pressure the flow is choked for all reservoir pressures investigated. Nitrogen has a molar mass of 28 g/mol and a compressibility factor close to 1.0 for the whole pressure range from 0 to 100 bar [69].

Figure 2-5 shows that nitrogen has a much lower volumetric flow rate than hydrogen at the same conditions. The difference in the volumetric flow is proportional to the difference in sonic velocity, according to Eq. (2). The difference in sonic velocity is caused by the differences in molar mass. At 100 bar initial pressure, the flow through the valve will be 1.2 and 0.32 Sm<sup>3</sup>/s for hydrogen and nitrogen, respectively. As both gases have compressibility factors near unity in the relevant pressure range, the nitrogen system will be depressurised slower. However, since nitrogen has significantly higher molar mass compared to hydrogen, the mass flow rate is higher than for hydrogen.

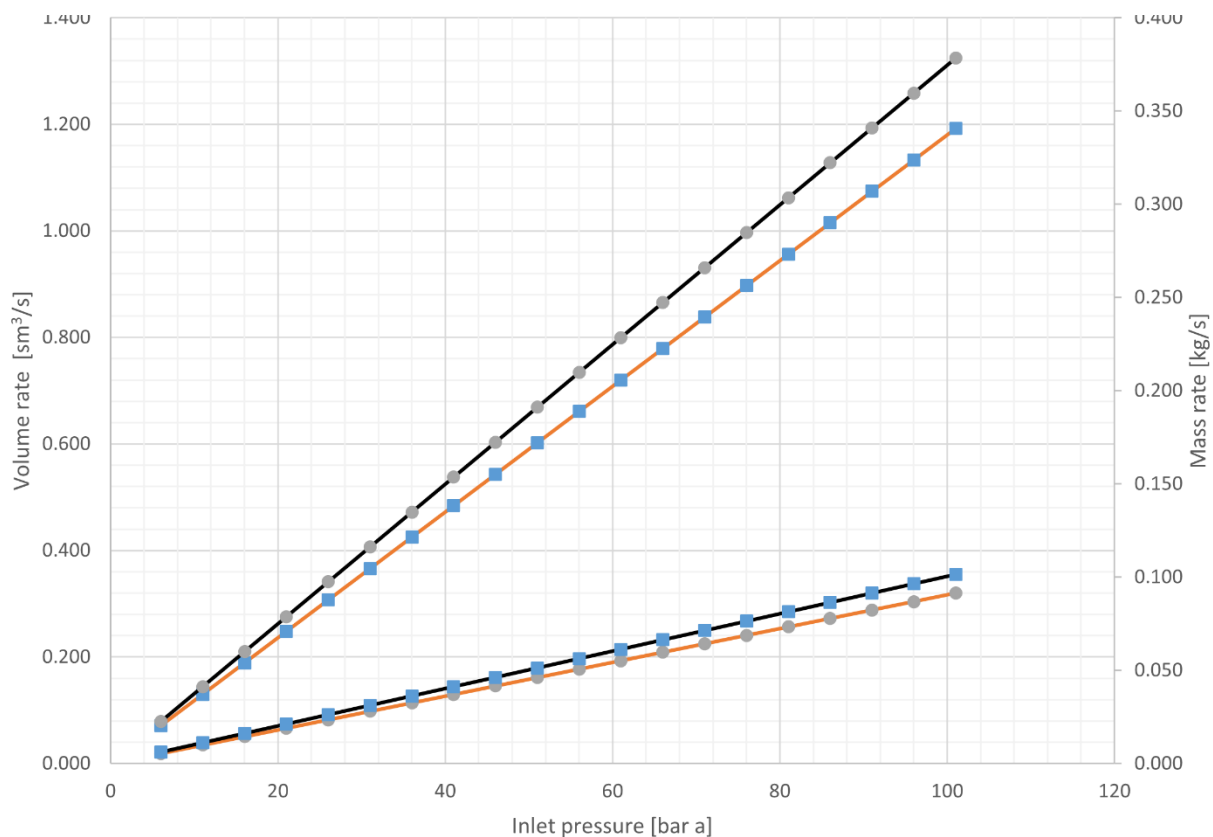


Figure 2-5: The relation between inlet pressure and standard flow rate/mass flow rate for the 3/8" valve that has been procured for this project. Calculations based on a  $C_v$ -value of 0.9 and a stipulated  $X_T$ -value of 0.62. The mass flow for both gases is read on the right axis, while standard volume rate for both gases are read on the left.

#### 2.2.4 Additional restriction in downstream tubing and nozzle

The nozzle used for experiments with releases through valve in this thesis has a length of 126 mm and an internal diameter of 5 mm. It is shown in MECH-02-01. The setup used in these experiments are described in section 4.2.1 and further described in detail in A.2.3 and A.2.4. This nozzle is directly connected to a tubing section with 75 mm length and 5.2 mm ID. The relative length for this arrangement ( $L/D$ ) is 40.

The nozzle arrangement used in the rupture disc experiments is even longer. It has a total length of 216 mm, of which 81.5 mm is downstream of the rupture disc and has an ID of 8 mm. The remaining 134.5 mm has varying ID in the span between five and six millimetres. This gives an accumulated relative length of approximately 36. It is further described in A.2.5.

Due to this long relative length for these two sections, significant pressure losses must be expected. However, as the static pressure at the nozzle exit is neither known, nor possible to measure in the current setup, it is difficult to estimate this pressure loss. Comprehensive calculations or numerical simulation is necessary to get a precise estimate.

However, with a rated pressure drop ratio of 0.62 for the 3/8" valve and a ratio of specific heats factor of 1, the flow across this valve will become choked when the pressure at the valve outlet is  $0.38 \cdot P_1$ . Thus, an initial release pressure of 50 bars will allow as much as 19 bars inlet pressure to the downstream tubing section, and still cause choked flow through the valve.

It is also uncertain if the tubing and nozzle section provide enough divergence to allow supersonic flow at the inside. This must be investigated through dedicated experiments. Ishii *et al.* investigated pulsed jets in air and found that the exit velocity was restricted to Mach 1 [70]. The setup in their experiment was a 70 cm long tube with a 20 mm ID, thus giving a relative length of 35. This is rather similar to the relative length of 40 in this setup. However, they did not have any upstream restrictions, such that the valve in this setup. The upstream restrictions in the valve might act as a converging-diverging nozzle thus allowing supersonic velocity in this section.

Ishii *et al.* also found the following relations between exit velocity and the pressure ratio across the system from the reservoir to the ambient pressure at the outlet  $p_4/p_1$ . These values were outlined for air.

$p_4/p_1 < 4.1$ : subsonic.

$4.1 < p_4/p_1 < 41.2$ : sonic under expanded.

$41.2 < p_4/p_1$ : supersonic under expanded.

Based on previously calculated sonic velocity for hydrogen and calculated mass flow rates at choked conditions through the 3/8" valve, the necessary static pressure to obtain a MACH 1 jet at the ID 5 mm nozzle exit is shown in Figure 2-6. The necessary pressure is shown as a function of mass flow rate and inlet pressure if choked flow through the 3/8" valve occurs, and that this is the restricting factor. The calculations are based on previously calculated values for mass flow and sonic velocity for hydrogen (2), (6), (7), (8) and (9). The conversion to the actual flow rates for the given pressure and temperatures are done with the ideal gas law, without any corrections ( $Z=1$ ).

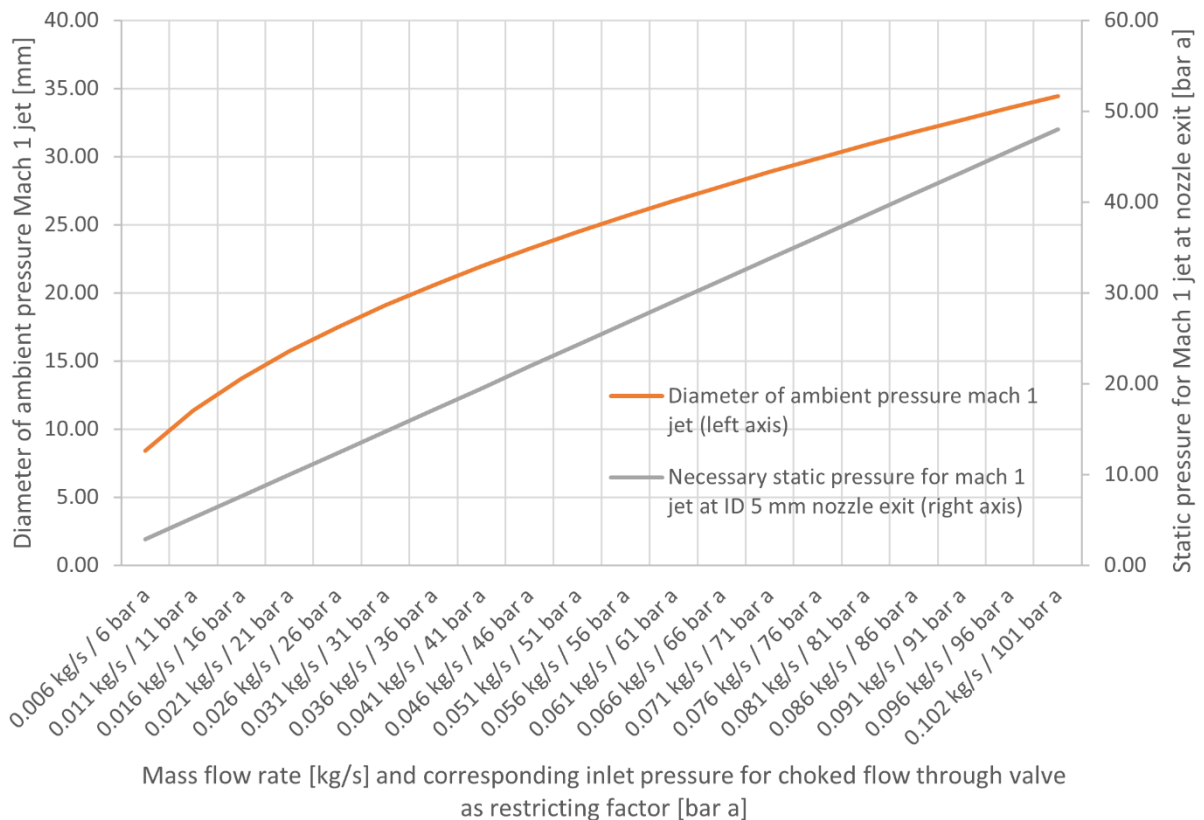


Figure 2-6: Diameter of an ambient pressure and temperature Mach 1 jet, and necessary static pressure to obtain a Mach 1 jet at the nozzle exit for various mass flow rates. The x-axis also shows the corresponding inlet pressure to the valve for choked flow condition

As the results in Figure 2-6 show, the calculated static exit pressure for a velocity of Mach 1 corresponds to approximately  $0.47 * p_1$ , thus giving a necessary static pressure of 24 bars for the calculated choked flow through the  $\frac{3}{8}$ " valve at 51 bar a inlet pressure. These pressure ratios will entail further restrictions to the flow than what occurs in the release valve. The calculated static pressure at the nozzle exit will simply not leave enough differential pressure across the valve to give choked flow. In addition to this exit pressure, a significant pressure drop through the tubing and nozzle must be expected. These calculations

However, if the geometry of system allows the flow to go supersonic, the static pressure at the exit might become low enough to cause choked flow across the valve. The flow will at least become supersonic when the inlet pressure to the tubing and nozzle section (which corresponds to the outlet pressure of the valve) exceeds 41.2 atmospheres [70]. Due to the unknown pressure loss through the tubing/nozzle section, this point along the x-axis is unknown.

It will be a reasonable, but conservative to assume that the flow will become choked through the valve and not be further restricted by downstream pressure losses. This assumption could be used for further estimations in this thesis. Regardless of the pressure at the nozzle exit, the gas velocity has potential of becoming at least sonic, with a probable further increase at the outside as the underexpanded jet expands.

### 2.2.5 Discontinuous flow and shock waves

The reservoir volume in this setup is rather small, at 150 ml. Total volume estimated to 185 ml, as described in 4.2.1. This means that the pressure will deplete rapidly when the release valve is opened, thus never allowing steady-state conditions. As the theory above is mainly intended for steady-state conditions, this aspect will add some extra error margins to the previously shown calculations and assumptions.

Sudden increase in pressure is a prerequisite for the diffusional ignition phenomena. Thus, some degree of shock formation must occur if the combustible mixture should be able to ignite.

### 2.2.6 Volume rate estimations based on pressure change

In case the volume rate is not known nor possible to measure directly, calculations based on the pressure change rate could give coarse estimates of the volume rate. A version of the ideal gas equation modified to include rates is suitable for this:

$$\dot{p}V = \dot{n}RT \quad (10)$$

Where  $\dot{p}$  is pressure change in bar per milliseconds (bar/ms) and  $\dot{n}$  is molar flow rate in mol/ms. The other parameters are used as described earlier.

Eq. (10) could be used to find the molar flow rate based on the measured pressure change. By using this molar flow rate in the same equation with values for standard conditions inserted ( $t=15.5^\circ\text{C}$ ,  $p=1$  atm) a corresponding standard volume flow for this pressure change could be found. The two operations combined will yield the following equation:

$$\dot{V}_s = \frac{p_{system}V_{system}T_s}{p_sT_{system}} \quad (11)$$

In this equation, the subscript “s” specifies that it is the standard condition of the parameter, as described above, while the subscript “system” specifies that it is the value from the system where the pressure change is measured.

## 2.3 Measuring principles

This chapter provides essential theory about the principles that are utilised in acquisition of information from the experiments conducted through this thesis work. Even when “turnkey” systems are used, it is important to have a basic knowledge about the principles. Such knowledge will make the user aware of the strengths and limitations for the equipment and give a stronger basis prior to undertaking installation and adjustment work on the systems. It will also make us more aware of the important aspects to look for during analysis of the data.

### 2.3.1 Shadowgraph visualisation technique

The Shadowgraph technique utilises that the refractive index changes along with changing density in the investigated fluid. The density differences could be induced by change in pressure or temperature

for the same gas, or it could be caused by partial mixing of different gases, creating boundaries where the two different gases meet.

The refractive index  $n$  is the relation between the light speed in vacuum and the light speed through a transparent object or fluid:

$$n = \frac{c_0}{v} \quad (12)$$

Where  $c_0$  is the light speed in vacuum and  $v$  is the light speed through the fluid or object upon which the index is calculated for. The equation shows that the refractive index increases with increasing light resistance (thus reduced velocity) in a fluid. Due to the various velocity, a light beam will change direction when it travels between fluids with different refraction indexes, with an angle that deviate from orthogonal. Snell's law quantifies this change of direction:

$$n_1 * \sin(\alpha_1) = n_2 * \sin(\alpha_2) \quad (13)$$

Where  $n$  represents the refractive index for material 1 and two, and  $\alpha$  represents the angle of attack for the light beam related to the normal of the boundary between the materials in material 1 and 2. Since the angle is defined related to the normal of the boundary, a beam that passes through the medium boundary orthogonally will not change direction. As  $\sin(0) = 0$ , the equation will yield 0 on both sides, independently of the refractive index. An angle that differs from the orthogonal direction, on the other hand, will deviate from its initial angle when it has travelled into the other fluid if the refractive indexes are not identical.

Light from a point light source that has gone through a collimating lens, will keep on in a parallel pattern. This is shown in the first example in Figure 2-7. However, if the light passes through fluid with a refraction index that deviates from the ambient gas or air, the beams will deviate from their initial path. This will give stronger light intensity in some areas of the receiving surface (in the case illustrated in Figure 2-7 this will be the lens, and ultimately the image chip of the camera). Other areas of the receiving surface will receive less light intensity, as the light beams intended to reach that area is curved into another path by varying refraction index. Apart from some of the light near the outer boundary of the lens, all light that has been redirected by changing refraction indexes will hit the receiving surface. This means that the total energy, and thus average light intensity on the receiving end will remain constant, as explained by Davidhazy [71, p. 4].

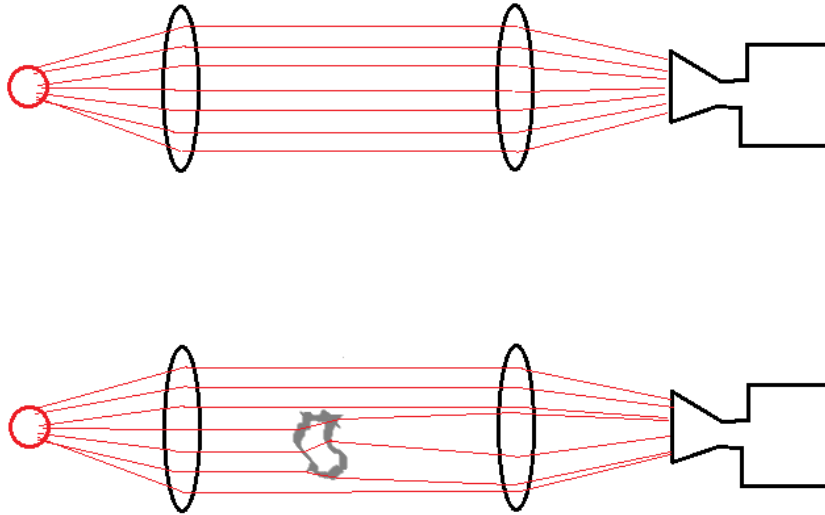


Figure 2-7: Simplified illustration of the Shadowgraph principle. Above: Constant refractive index through the whole investigated area. Below: A cloud of gas with different refractive index compared to its ambience disturbs the light beams, thus redistributing some of the light intensity on the receiving sensor.

As mentioned above, it is the variation in refraction index that alter the direction of the light beams. Variation in refraction index itself will only alter the direction and curvature of the beams. A constant gradient of refraction index would thus just have shifted the whole picture, thus reproduced the light beams with the same relative position at the receiving surface. The variations in light intensity and subsequent patterns on the receiving surface is therefore a result of the change in the gradient of refractive index. In other words, the fluctuations in light intensity that is visible on a shadowgraph system correlates with the second derivative of the refraction index. The refraction index is, as mentioned earlier related to the density of the fluid among other factors. A better description of the principle and physics behind the Shadowgraph are given by Mauger *et al.* [72], Hu [73], Davidhazy [71] and others.

Another important aspect is that the two-dimensional perspective on the Shadowgraph surface does not identify how the light beam has deviated. It is not possible to distinguish between a light beam that has been exposed to a steep refractive index gradient for a short distance or a small gradient for a longer distance. Thus, the picture on the shadowgraph will also correlate to the length of the gradient. This is one of the factors that makes Shadowgraph rather unsuited to quantitative measures [72]. It is at least necessary with proper standards and additional data if this technique should be able to deliver quantitative results.

In a Schlieren system, a significant portion of the disturbed light beams is removed on the “knife” located at the focus point of the so called “field lens”. A Schlieren system will produce more distinct views, and the patterns will correlate with the first derivative of the refractive index (density gradient) {[72], [73]}.

The main benefit with a Shadowgraph system, is that it is relatively simple to assemble and adjust. Schlieren, on the contrary depends on precise adjustment of two mirrors or lenses, in addition to the knife, the light source and the camera or viewing surface. The distances between the components are related to the focal length of the lenses/mirrors used [71].

Many different Shadowgraph setups are available, with various complexity. According to Hu [73], it should be possible to make simple Shadowgraph images without collimated light, and directly onto a surface such as a screen. These simplest and most straightforward setups are often referred to as direct Shadowgraph. Other variants of direct shadowgraph utilise a retroreflective screen in conjunction with

a light source and an ordinary camera located close to each other. Settles *et al.* describe an example of such setup.

This thesis uses a slightly more complex setup, where two telecentric lenses are used. One lens connected to the light source collimates the light while the lens connected to the camera gives it a focus point of infinite distance. This method eliminates the distance-dependent magnification of objects that are found in conventional lenses. In a telecentric lens, equally sized objects at different distances will appear at the same size, on the contrary of both conventional (endocentric) lenses and the human eye [74]. A clear advantage with this system is that edges on physical objects or displayed Shadowgraph patterns will be displayed in the same scale, thus allowing comparison and measurement of sizes directly in the field of vision on the camera.

### 2.3.2 Piezoelectric pressure transducers

Piezoelectric pressure transducers utilise the piezoelectric effect to measure pressure changes. The piezoelectric effect is an effect that causes some crystals to generate electrical charge when they are exposed to pressure or other mechanical forces. The charge is proportional to the amount of force applied. By measuring this charge, it is possible to monitor how the pressure exerted on the piezo element changes.

The piezoelectric effect occurs in crystalline materials without central symmetries [75]. Quartz crystals ( $\text{SiO}_2$ ) are very capable for these purposes, and the transmitters used in this experimental setup is made from quartz [76]. As the electric charge generated in the crystals used in these pressure transducers are rather small, the signal must be amplified with an external power source to become more robust and detectable for logging and control equipment.

The measurements from piezoelectric pressure transducers will drift when exposed to a static load over time [77]. These types of sensors are therefore not suited for long time measurements of stable pressures.

## 2.4 Potential ignition sources for spontaneous ignition of hydrogen-air mixtures

Hydrogen is, due to its properties, easily ignitable for many types of ignition sources. As mentioned in section 2.1, it is classified in gas group IIC and temperature class T1. This means that many ignition mechanisms capable of igniting other combustible gases, will ignite hydrogen as well. And in particular those mechanisms depending on released energy in some form, for instance as sparks. In many cases, less “effort” is needed to ignite hydrogen gas than other gases at similar conditions. This is for instance mentioned as a comment to why a larger number of ignited hydrogen leaks has unidentified ignition sources compared to ignited non-hydrogen leaks [36]. However, hydrogen is not more sensitive to temperature related mechanisms compared to other common combustible gases due to its relatively high auto-ignition temperature. Although the main focus for this thesis has been the diffusion ignition phenomena, several other potential mechanisms has been briefly studied and are presented here:

### 2.4.1 The diffusion ignition phenomena

The theory about the diffusion ignition phenomena is that leaking hydrogen of abrupt character creates a shock wave that is fast and powerful enough to compress the air (or other oxidizer) at the shock wave front. When the air is compressed, the temperature will increase adiabatically. If the wave has enough power, or sufficient confinement is present, the final temperature of the air might exceed the ignition temperature for hydrogen. In order to get ignition, the air at the boundary must be warm enough to make the temperature of the hydrogen air-mixture after diffusive mixing warmer than the auto ignition temperature for the mixture. According to Dryer *et al.* [53] and Wolański and Wójcicki [40], the mixing



process at the boundary between the compressed air is the limiting process. In other words, the conditions must allow the pressure and resulting adiabatic temperature to stay high for enough time to get sufficient mixing of the hot air and the cold hydrogen. However, as stated in most articles investigating this phenomenon, 100  $\mu\text{s}$  is usually enough to get sufficient mixing. The shock wave usually travels faster than the hydrogen boundary, thus producing a growing volume of heated, unmixed air in front of the hydrogen/air mixture. A literature study related to the factors that affect the propensity for this mechanism to occur, is presented in section 3.

### 2.4.2 Reverse Joule-Thomson effect

One of the mechanisms that has been postulated in the literature, is ignition caused by the reverse Joule-Thomson effect. Both Astbury and Hawksworth [36] and Dryer *et al.* [53] mention this. However, both conclude that it is highly unlikely that the Reverse Joule-Thomson mechanism alone is capable of igniting hydrogen under realistic conditions.

All gases that undergo throttling (irreversible, adiabatic expansion, which is isenthalpic [78]) is subject to the Joule-Thomson phenomenon. Maytal and Pfothenauer dedicated a chapter of their book to a thorough explanation of the phenomenon [79]. The adiabatic Joule-Thomson coefficient,  $\mu$ , is defined in the following way [79]:

$$\mu = \left( \frac{dT}{dP} \right)_h \quad (14)$$

The coefficient can be both negative (temperature will increase as pressure is reduced) and positive, depending on the initial temperature and pressure of the gas. The point where the direction changes is called the inversion point. Figure 2-8 shows the inversion lines for some gases. These inversion lines are drawn as the locus of the temperature maximal points on the isenthalpic lines for each gas [19]. The inversion temperature for hydrogen at atmospheric pressure is approximately 193 K [10]. This correlates well with the curve in Figure 2-8.

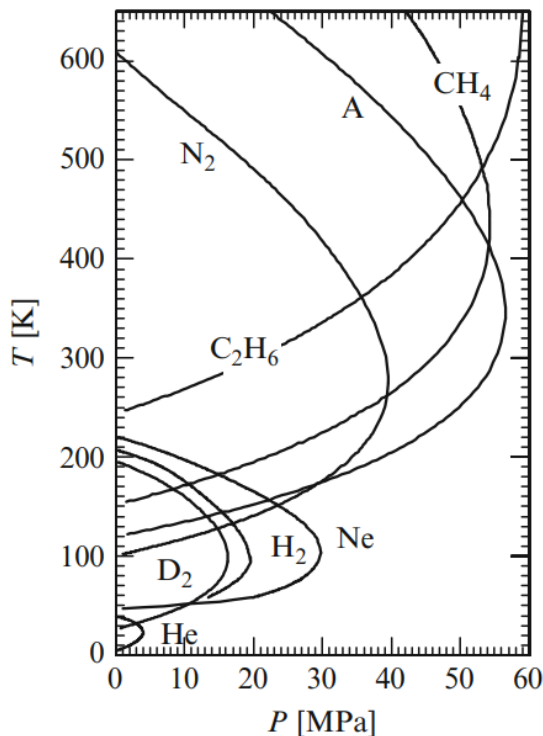


Figure 2-8: The Joule-Thomson inversion lines for some gases in the P-T-plane. The coefficient is positive within the enveloped area. Positive coefficients will cause temperature reduction when gas is expanded with throttling, from [79, Ch. 2.4].

Figure 2-8 clearly shows that hydrogen will have a negative value for the J-T coefficient for all practical applications, except for processes involving liquefaction.

However, the coefficient must be large enough if the reverse Joule-Thomson phenomenon should become a possible ignition source. Michels *et al.* have published a set of tables with thermodynamic properties for hydrogen and deuterium [80]. One of the properties in this publication is the J-T coefficient ( $\mu$ ). As we can see from Table XI in this publication,  $\mu$  is between -0.04 and -0.05 °C/atm for pressures from 200 to 700 atmospheres at room temperature. If the temperature is increased to 150 °C,  $\mu$  is between -0.0492 and -0.0535 °C/atm for that pressure interval.

Therefore, hydrogen at ambient temperature cannot achieve the auto ignition temperature of 585 °C from the Joule-Thomson effect, even at 700 bars initial pressure. A full, perfectly isenthalpic, blow down of hydrogen initially at 1000 bars and 150 °C will give a final temperature of approximately 200°C at ideal conditions. However, temperature increments somewhere between 30 and 50 K depending on initial pressure, might be a contributing factor in an ignition. This temperature increase will reduce the required ignition energy if a spark ignites the mixture and reduce the necessary temperature increase from other heat sources if heat is the ignition source

### 2.4.3 Electrostatic discharges

As mentioned above, hydrogen has a minimum ignition energy (MIE) of only 0.017 mJ for stoichiometric conditions [49]. This is extremely low. According to Astbury and Hawksworth [36], the quenching distance is only 0.69 mm. That means, that a flame front can propagate through a gap as small as 0.69 mm without being quenched. Astbury and Hawksworth mention 3 different types of electrostatic charges with the potential to ignite hydrogen, namely sparks from isolated conductors, brush discharges and corona discharges. A calculated example for an electrostatic discharge from a person's finger with a distance to the object discharged to at quenching distance is shown in the article. The formula for energy in a spark discharge is:

$$E = \frac{1}{2} CV^2 \quad (15)$$

Where C is capacitance and V is the voltage. The capacitance for a human is approximately 100 pF ( $1 \cdot 10^{-10}$  F). The dielectric strength for a stoichiometric mixture of hydrogen and air was interpolated from the values for dielectric strength for air and pure hydrogen and was found to be 26.25KV/cm. (17.5KV/cm for hydrogen\*0.3 and 30KV/cm\*0.7 for air.) Thus, the energy that can potentially be released in a spark discharge when the distance is equal to the quenching distance of 0.69mm, is 0.164 mJ. Almost ten times as much as the MIE.

Brush and corona discharges also have the potential to ignite the mixture. Particles carried in a stream of expanding gas might also generate sparks or electrostatic discharges that have the potential to ignite the gas mixture. In other words, electrostatic discharges in various forms are potent ignition sources, capable of igniting hydrogen-air mixtures if they contain enough energy.

#### 2.4.4 Sudden adiabatic compression

This potential ignition source is described by Astbury and Hawksworth [36]. The main difference between sudden adiabatic compression and diffusion ignition, is that sudden adiabatic compression ignition occurs when a combustible mixture of hydrogen and air is compressed until the temperature is above the self-ignition temperature for that mixture in a confined space. The following expressions can be used to find final temperature after compression based on values for pressure and volume, respectively:

$$T_2 = T_1 \left( \frac{P_2}{P_1} \right)^{\frac{\gamma-1}{\gamma}} \quad (16)$$

$$T_2 = T_1 \left( \frac{V_1}{V_2} \right)^{\gamma-1} \quad (17)$$

where  $\gamma$  is the ratio of specific heats (assumed equal to 1.4 for diatomic gases like hydrogen). By using eq. appendix (16), the final temperature for a hydrogen-air mixture with initial temperature 300K and an initial pressure of 1 bar that is compressed to 200 bar could be calculated to 1363K when compressed ideally and adiabatic. However, this is very unlikely to happen [36]. They cite an experiment done by Pan *et al.* where a temperature increase of only 149K was measured for a compression ratio (initial volume divided on final volume) of 28, that in theory should have a 453K temperature rise. So, ignition by sudden adiabatic ignition is possible, but highly unlikely.

#### 2.4.5 Ignition by hot surface

Hot surfaces will ignite hydrogen if the surface is able to heat the hydrogen to above its auto-ignition temperature. It is also a prerequisite that a sufficiently large volume is heated for the heat generation from oxidation and supplied heat to exceed the heat losses [56, Ch. 2.2.4]. In addition, the hydrogen must be exposed to the heat source for enough time. As hydrogen has relatively high autoignition temperature (585 °C), and hence classified in Temperature class T1, it is not significantly more sensitive to this ignition mechanism compared to conventional fuels.

#### 2.4.6 Ignition by mechanical impacts

Mechanical impacts as a potential ignition source for hydrogen-air mixtures have just been briefly investigated at the end of this thesis work.

Very little information seems to exist about the potential for ignition by impact of particles on objects in general and stainless steel particles on brass objects in particular. Especially for applications where neither particles nor impacted area are preheated. Impact of 5-600  $\mu\text{m}$  aluminium particles carried by an oxygen shock striking on a Monel 400 target preheated to 80°C has been investigated [81]. However, it is uncertain if these results are transferable to the current system, with a completely different combination of shock gas and materials of particles and impinged object.

Potential ignition of hydrogen-air mixtures from friction sparks generated by a grinding wheel has also been investigated, by [82] and others. Due to the elevated temperature of the friction spark particles, the transferability of these results to the conditions in this thesis work is doubtful.

However, the kinetic energy of a particle will at least give an indication about its potential to contribute to an ignition mechanism.

$$E_K = \frac{1}{2}mv^2 \quad (18)$$

Where  $E_K$  is kinetic energy,  $m$  and  $v$  is particle mass and velocity, respectively.

Particles carried by a shockwave could possibly be heated by air between the particle and the bow shock that is generated behind it [56, Ch. 7.3.8]. This mechanism is subject to two competing mechanisms: The friction between the particle and the shock will accelerate the particle, thus eventually reducing the temperature behind it. Small particles will be accelerated larger and therefore receive less heat energy. But on the other hand, the larger particles that receive more energy, also need more energy for the temperature increase. The quantitative effect of this mechanism has not been investigated in this thesis work.

## 3 Literature review

As mentioned earlier, diffusion ignition as a possible ignition source was first introduced and investigated by Wolański and Wójcicki in 1973 [40]. It has later been published many articles that investigate this mechanism, both experimentally and numerically.

### 3.1 Relevant literature and results

#### 3.1.1 Experiments by Wolański and co-workers

The initial experiments by Wolański and Wójcicki were set up with a tube,  $\varnothing$  10mm, connected to a closed spherical chamber [40]. They filled the part of the tube closest to the chamber with hydrogen, and the outer part of a tube contained a mixture of hydrogen and oxygen. The three parts (chamber, driven section and driving section) was separated by two membranes. By igniting the driving section, they shot the hydrogen volume in the driven section into the chamber, which was filled with either air or pure oxygen, depending on the set up. In some of the experiments, they equipped the chamber with a cylinder or piston just opposite of the inlet from the cylinder to make reflected shock waves. These reflected shock waves interacted with the initial shock waves and increased the amplitude of the pressure pulses.

Most of their experiments used hydrogen at an initial temperature of 575 K, as they used the conditions for synthesis gas in ammonia production as basis. They found the minimum velocity of the hydrogen gas necessary to get ignition and the resulting pressure at the closed hydrogen chamber before the leakage occurred. They did this by solving differential equations in a computer, and later verified the results by experiments in the setup described above.

They concluded that it was necessary to have a velocity of Mach 2.8 to get ignition at their initial setup without reflected shock wave. An initial pressure of 38 bars was enough to reach this velocity. If the shock wave is reflected, Mach 1.7 is sufficient, and this can be achieved with an initial pressure of 12 bars.

As Wolański's initial experiments were performed with the hydrogen gas at an initial temperature of 575 K and by releasing it into a completely confined chamber, the results are not representative for most systems used for hydrogen utility. The initial temperature they used, is about 100 K lower than the ignition temperature for the synthesis gas composition [40].

In a later contribution [41], Wolański and Oleszczak used a setup similar to the one used in the original experiment [40]. The main difference is that in this setup, the volume containing the atmospheric air is only partly confined. A membrane that ruptures "almost instantly" after the hydrogen is injected into the visualisation chamber separates it from a downstream dump tank.

Pressurised hydrogen is injected into the visualisation chamber when a rupture disc breaches. A nozzle with various length and diameter is mounted onto the rupture disc holder. They used a nozzle with  $\varnothing$ 10 mm and length 10 mm immediate downstream of the disc, and this was unchanged through all experiments. But the part downstream of this was varied between the experiments.

Lengths from 45 to 95 mm was used, with mostly 10 mm as diameter were used. However, for the 45mm length, they used diameters of 10, 25 and 32 mm. Both 25 mm and 10 mm diameters were tested on the 95 mm length, but only 10 mm were used for 65 mm and 75 mm length. Different pressures were used on all setups, and the results were categorised in "no ignition", "delayed ignition" and "ignition". Delayed ignition is ignition that occurs in the visualisation chamber, and direct ignition will occur within

the extension tube. They used both a high-speed camera, a pressure transducer, and a photodiode in order to detect and categorise ignitions.

The pressure in the visualisation chamber reaches approximately 0.5 bars before the membrane breaches. But as seen in some of the experiments that saw significant time delay between injection of hydrogen and ignition, this does probably not affect the results. In the results with a longer time delay, the shock wave that gave ignition must have been present a “long” time after the breach of the membrane (approximately 10 ms with 65 mm length and ID 10 mm and 7.4 MPa.)

The results were a bit ambiguous, as none of the setups gave a clear pressure limit that gave ignition. On the setup with 95mm length and 10 mm diameter, ignition occurred as low as 51 bars. However, they also did tests at 93 bars without ignition. But Wolański and Oleszczak concluded that longer tubes give a higher repeatability for ignition. Figure 3-1 shows that the critical pressure for ignition in a 10 mm tube is reduced from approximately 77 bars for 45 mm length, to 55 bars for 75 and 95 mm length.

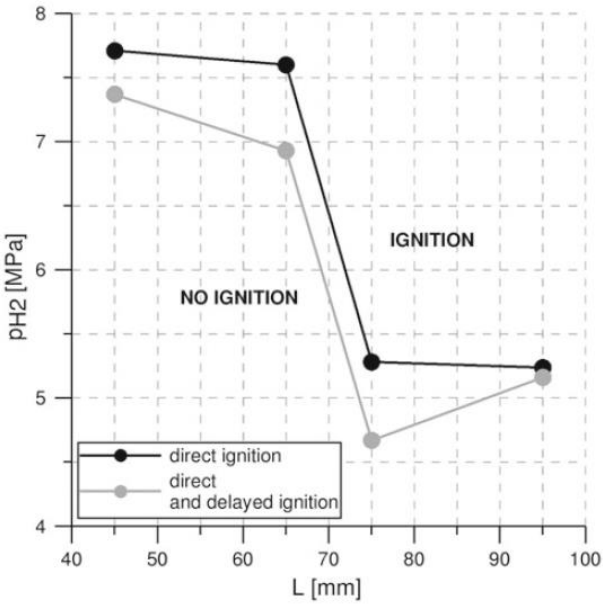


Figure 3-1: The relation between tube length and pressure necessary to get ignition for tubes with 10 mm diameter, from [41].

Figure 3-2 show the results from all experiments performed on Ø 10 mm tube. The results are ambiguous, as results with not ignited, delayed ignition and direct ignition are mixed and scattered through the whole pressure range. But there is a clear tendency towards that tube lengths of 75 and 95 mm will give ignition at a lower pressure than shorter tube lengths.

Figure 3-3 shows how the results from experiments done with 45 mm tube lengths and different diameters. As for Figure 3-2, results with the three different outcomes are mixed and scattered along the pressure range. The differences between the diameters are not easy to interpret, so Wolański and Oleszczak concludes that the diameter is insignificant. However, all except one of the results with direct ignition occurred with 10 mm diameter, so the repeatability seems to be better at the smallest diameter. Wolański and Oleszczak also point at this.

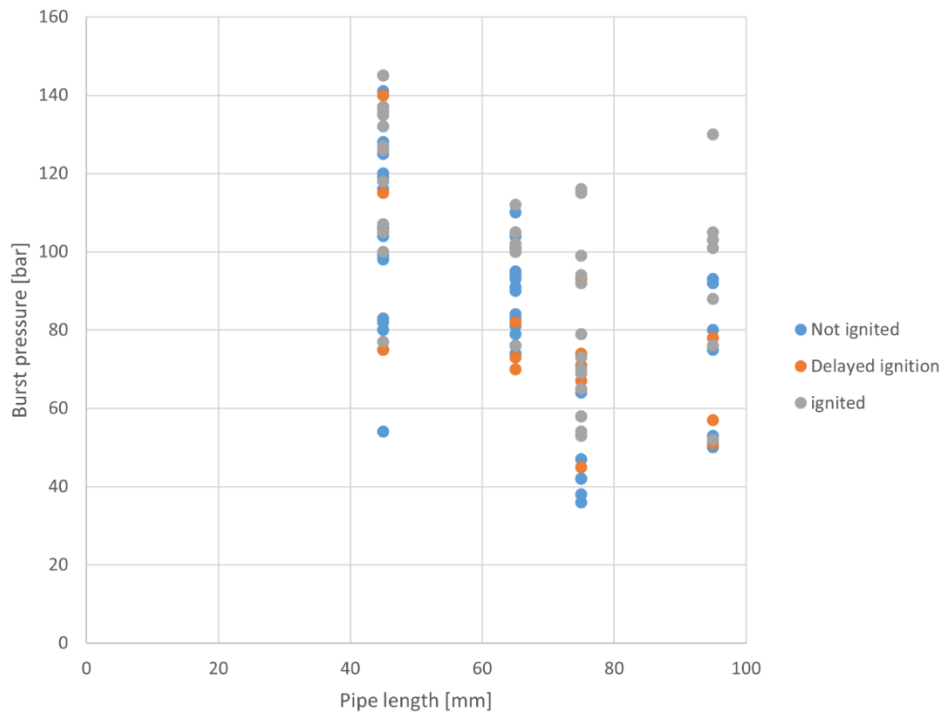


Figure 3-2: Results from experiments with ID 10 mm tubes from Wolański and Oleszczak. Pipe length related to burst pressure for the three scenarios; not ignited, delayed ignition and direct ignition for the experiments performed with  $\varnothing 10$  mm pipes at different lengths.

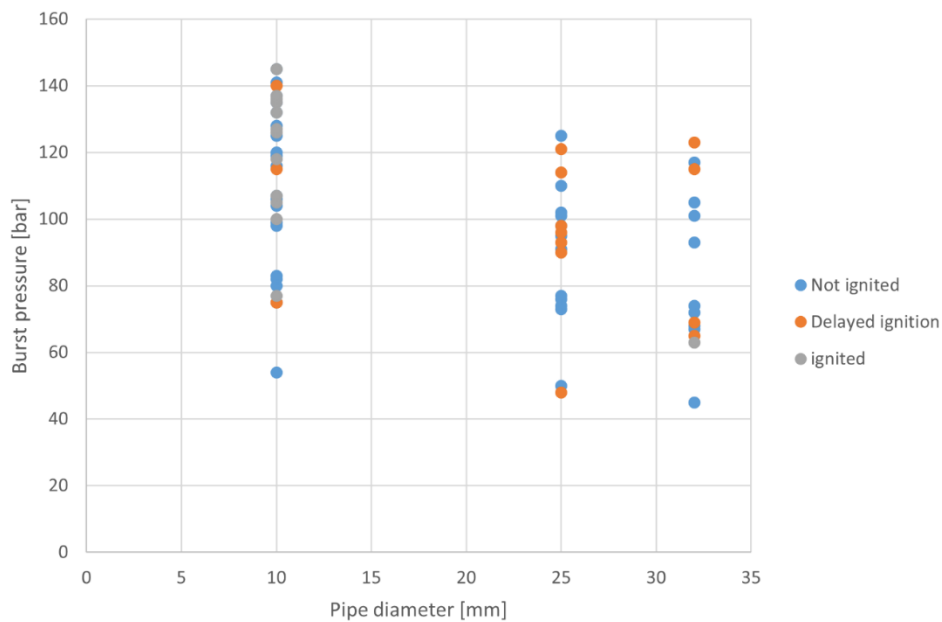


Figure 3-3: The results for 45 mm pipe lengths of different diameters from experiments conducted by Wolański and Oleszczak. The results for  $\varnothing 10$  mm are the same as those presented in Figure 3-2 for 45 mm pipe length.

Most articles that investigate the diffusional ignition phenomenon have a very similar setup. But unlike the setup in the two articles credited Wolański, most experimental setups use a tube that is completely open in one end. Pressure transmitters (PT) and photodiodes are usually located at various lengths of the tube. The photodiodes and PT's are usually placed with one PT and one photodiode at the same tube length, but diametrically opposite of each other.

### 3.1.2 Experiments by Dryer and co-workers

Dryer *et al.* [53] describe their experimental setup as a system where conventional rupture discs were used. They used commercially available models as well as discs they produced themselves. The volume of the system upstream of the disc was varied between the experiments in the span from 0.25 to 2.25 by changing the number of connected steel tanks, as well as varying the length of the tubing. They found out that variations in the upstream volume had very little impact on the test results, as the bleed down time was much larger than the time scale for ignition for all volumes.

Two different types of burst disc and holders was used initially. The “T-type” and the “B-type”. The T-type had orthogonal holes downstream of the disc. Because the T-type made it difficult to modify the downstream geometry, it was only used for a few experiments.

Dryer *et al.* performed over 200 experiments. They did not get ignition for pressures below 20.4 atm., and neither for pipe lengths below 3.81 cm nor pressures below 56.6 atm. Without any geometry downstream the rupture disc, ignition never occurred for the tested pressures up to 113 atm. They also found that ignition did not occur in tube lengths above 300 cm and pressures below 55.4 atm. If some of the volume ignited in an early stage of the release through such long tubes, it always quenched before the exit.

Although no spontaneous ignition was observed for geometries consisting of one piece of tube with length under 10.16 cm, ignition was possible with shorter lengths than that, if the length consisted of several tubes joined together. The unions have some internal shapes that probably enhances the mixing between the expanding hydrogen and air.

Dryer *et al.* [53] concluded that further work in this area “... *should include much higher pressures, different failure diameters and downstream geometries, as well as consideration of boundary failures into open air along with shock interactions with surrounding obstruction in close proximity to the boundary failure*”.

### 3.1.3 Experiments by Jiang, Pan, Wang and co-workers

Jiang, Pan, Wang and co-workers {[83], [84], [85]} used a 3-litre tank, connected to a rupture disc with unspecified diameter. Their set up could get different total tube length by changing three spools with equal length, joined together with two joints. Between the three spools of equal length and the rupture disc, there was a segment with a length of 65 mm. Downstream from the last of the three equal spools, was a tube with 55 mm length. The length of the three variable tubes varied from 60 to 960 mm, giving a total length between 300 and 3000 mm for Wang *et al.* [84]. Before and after each of the three spools with variable length, they placed a pair of pressure transducer and photodiode, giving a total of 4 pairs. These sensors were used to give measurements of shock wave velocity, ignition point and shock wave strength. Figure 3-4 summarises the results from Wang *et al.*, indicating a critical point at tube length 1500 mm and ignition for pressures down to 37 bar.



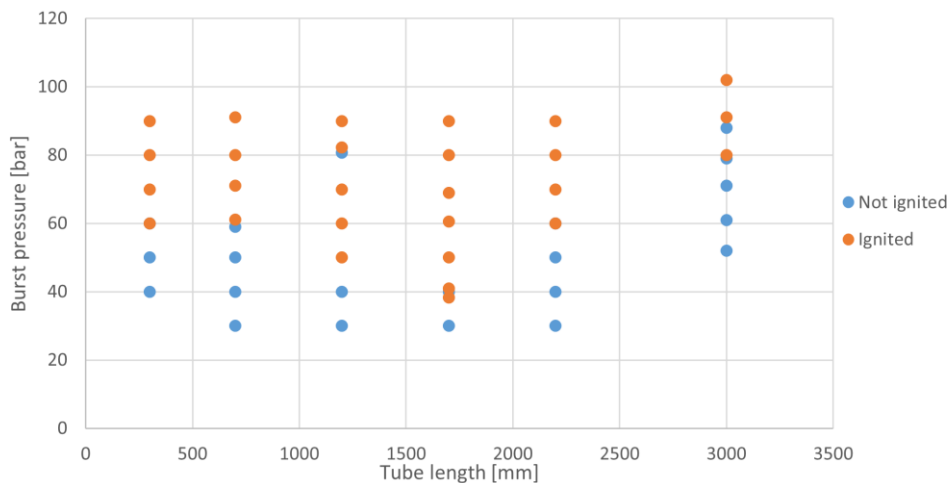


Figure 3-4: The results for Wang *et al.*, from [84]. The tube diameter for all experiments is 10 mm.

Jiang *et al.* used a constant length of 2200 mm in their experiments, but they varied the diameter between 10 and 15 mm. They found that the larger diameter gave higher probability for ignition compared to the smaller one at the same burst pressure. They discuss a few reasons that might explain this. For example, the attenuation rate was lower for the 15 mm tube lower compared to the 10 mm. So even though the shock wave had higher initial speed in the 10 mm tube, the larger attenuation rate gave a more rapid slowdown in the smaller tube. The 15 mm tube could therefore maintain a strong compression wave for a longer duration. The increased volume in the 15 mm tube also aids the mixing between hydrogen and air, thus creating a larger volume of combustible mixture.

Pan *et al.* use a similar experimental design as Wang *et al.* [84]. But all their experiments use tubes with 10 mm ID, and the length varies from 300 to 2200 mm. Figure 3-5 illustrates that the results were rather ambiguous when focusing on tube length for ignition and non-ignition results. The focus in the article is comparison of shock wave intensity at different burst pressures and flame development at the tube exit (after ignition has already occurred). Pan *et al.* concluded that shock wave velocity was strongly correlated to burst pressure. Probability of formation of ball flame at the exit and the size of this was also strongly correlated to release pressure. They could not find an obvious relation between tube length and the flame parameters investigated.

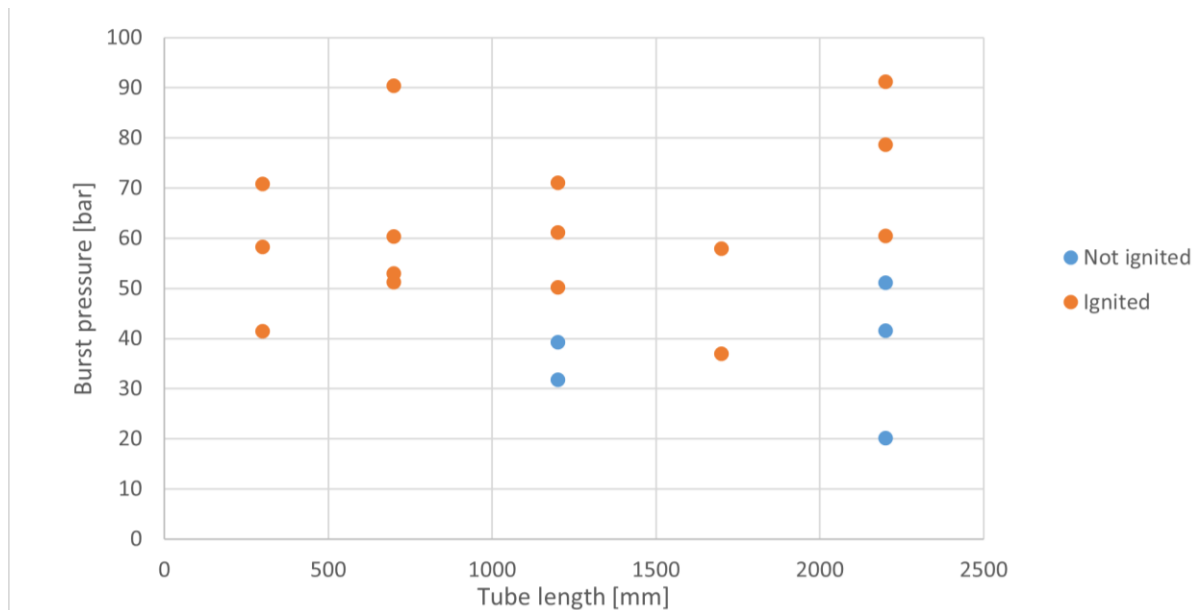


Figure 3-5: The results for the experiments conducted by Pan et al.

### 3.1.4 Experiments by Golub and co-workers

Golub and co-workers investigated the diffusional ignition phenomenon both experimentally and numerically {[86]-[87]}. The latter contribution [87] included both numerical simulations and experiments. In the simulations, the pressure was varied between 150 and 400 bars, and the diameter of the hole from 1 to 4 mm, at an initial temperature of 300 K. The simulations showed that the hole diameter had to be more than 3 mm if sustained combustion should occur. Some cases gave an ignition that was quenched after a short time. This was for instance the case for 200 bar initial pressure and 2 mm hole diameter (at 300 K). The same experiment with 400 K initial hydrogen temperature gave sustained combustion.

The experimental setup used a tube with ID 5 mm and lengths from 95 to 185 mm. It had a confined volume of pressurised hydrogen separated from the tube by a rupture disc. The volume of the pressurised hydrogen reservoir was approximately 0.045 litres (45 ml). Only one photodiodes and one pressure transducer, placed 50 mm from the outlet of the tubes, were used to detect ignition and measure pressure waves. The results showed a clear dependency on tube length for ignition to occur. A 95 mm tube required 80 bar initial pressure to give self-ignition, 140 mm required approximately 52 bar, and a 185 mm tube only needed 40 bar for ignition to occur.

The experimental setup in the second paper [86] was similar to that in the first [87], but with tube length 65 mm in addition to 95, 140 and 185 mm. This study also included a few tests without any tubes at all, as well as a series of tests with a rectangular shaped tube with cross section 2 mm × 10 mm. The rectangular tube had practically the same cross-sectional area as the ID 5 mm tube (20 mm<sup>2</sup> vs. 19.64 mm<sup>2</sup>). The rectangular tube was only tested for one length (183 mm), but with three pairs of photodiodes/pressure transducers, located at 43, 93 and 143 mm downstream from the rupture disc.

Because the results presented in the first paper [87] were similar to the results for the same conditions in the second paper [86], Figure 3-6 and Figure 3-7 only summarise the results from the latter [86]. The results show a strong correlation between tube length and the burst pressure for the circular tubes. For the rectangular tube, the position where ignition occurs gets closer to the rupture disc as the pressure increases. None of the results indicate that the pressure required for ignition increases when the tube exceeds a certain length. However, this might be because the experiments did not include sufficiently long tubes to identify a critical point.

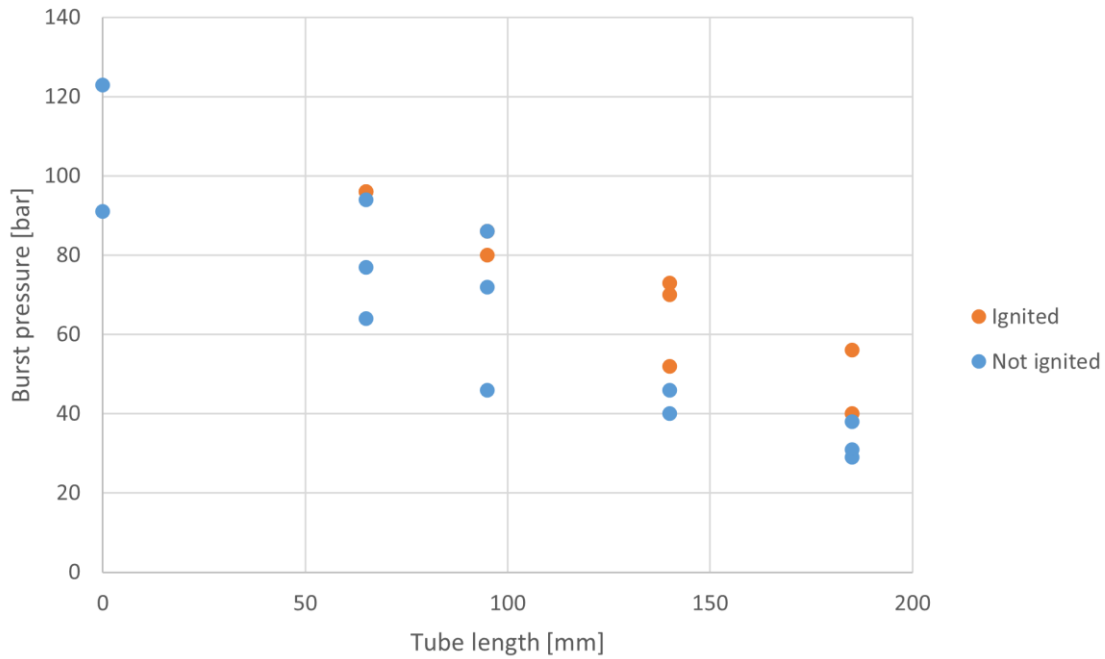


Figure 3-6: Results for circular tubes, from Golub *et al.* [86].

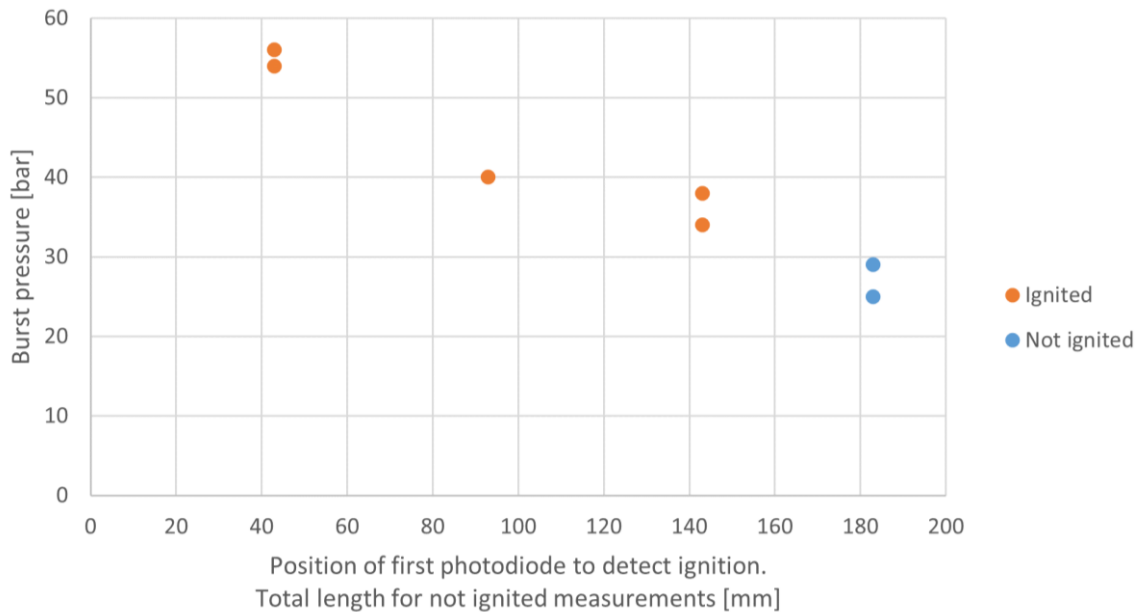


Figure 3-7: Results for the rectangular tube, from Golub *et al.* [86]. The tube length is identical for all experiments, and the x-axis represents the position of the first photodiode that detected the ignition. The x-axis value for tests without ignition is set to the total tube length (183 mm).

### 3.1.5 Experiments by Mogi and co-workers

Mogi *et al.* performed experiments with both  $\varnothing$  5 and 10 mm tubes {[88]-[89]}. They used a setup that was very similar to those seen in the other articles mentioned already, with pipe lengths from 3 to 500 mm [88], and from 3 to 300 mm [89].

They used diaphragms made of a Polyethylene terephthalate (PET) film [88] as well as conventional brass and copper diaphragms [89]. By changing the thickness of the PET film, they were able to get the desired burst pressure for each experiment. A purpose-built measurement tube with a length of 200 mm

and a diameter of 10 mm was used on some of the experiments to get ignition data. This test tube had 5 pairs of photodiodes and piezoelectric pressure transmitters. The article does not clearly state in which experiments (or in how many of them) the measurement tube was used.

The results can be seen in Figure 3-8 below. They divided their results in 3. “No ignition”, “failed ignition” and “ignition”. “Failed ignition” means that ignition is observed, but the flame is quenched before the available gas is combusted. In Figure 3-8 this expression is replaced with “ignition, not sustained”, as this better describes the event.

They distinguished between not sustained ignition and full ignition by using a high speed camera at the outlet of the tube [89]. By wetting the inner wall of the tube with a 1% solution of  $\text{Na}_2\text{CO}_3$ , they made the flames visible for the high-speed camera. Although high-speed camera was also used [88], it is not mentioned if  $\text{Na}_2\text{CO}_3$  solution was also used in these experiments. However, when the measurement tube was used [88], the photodiodes could probably detect ignition without the presence of this solution.

Their conclusion in both studies is that ignition is not likely to occur for short pipe lengths or no pipe at all, and that the probability increases with increasing pipe length. However, based on the graphical presentation of their results below it should be possible to assume the following: When the pipe length exceeds an unspecified, critical point, the required pressure starts to increase. This agrees with results found in many other articles presented in this document. The results from the first study [89] was included in the figures in the second paper [88]. But as these earlier results show the same as the more recent ones, they have been omitted in Figure 3-8.

The results show that most experiments with 10 mm pipe is conducted at lower pressures than for the 5 mm pipe. This might indicate that a lower pressure is required to get ignition for a wider pipe diameter. At least until a certain, critical diameter that is not found in this article. However, it also seems that a larger part of the experiments on 10 mm diameter lacks ignition compared to the case for 5 mm. So maybe the difference in required pressure per diameter is not as large as the first impression might indicate.

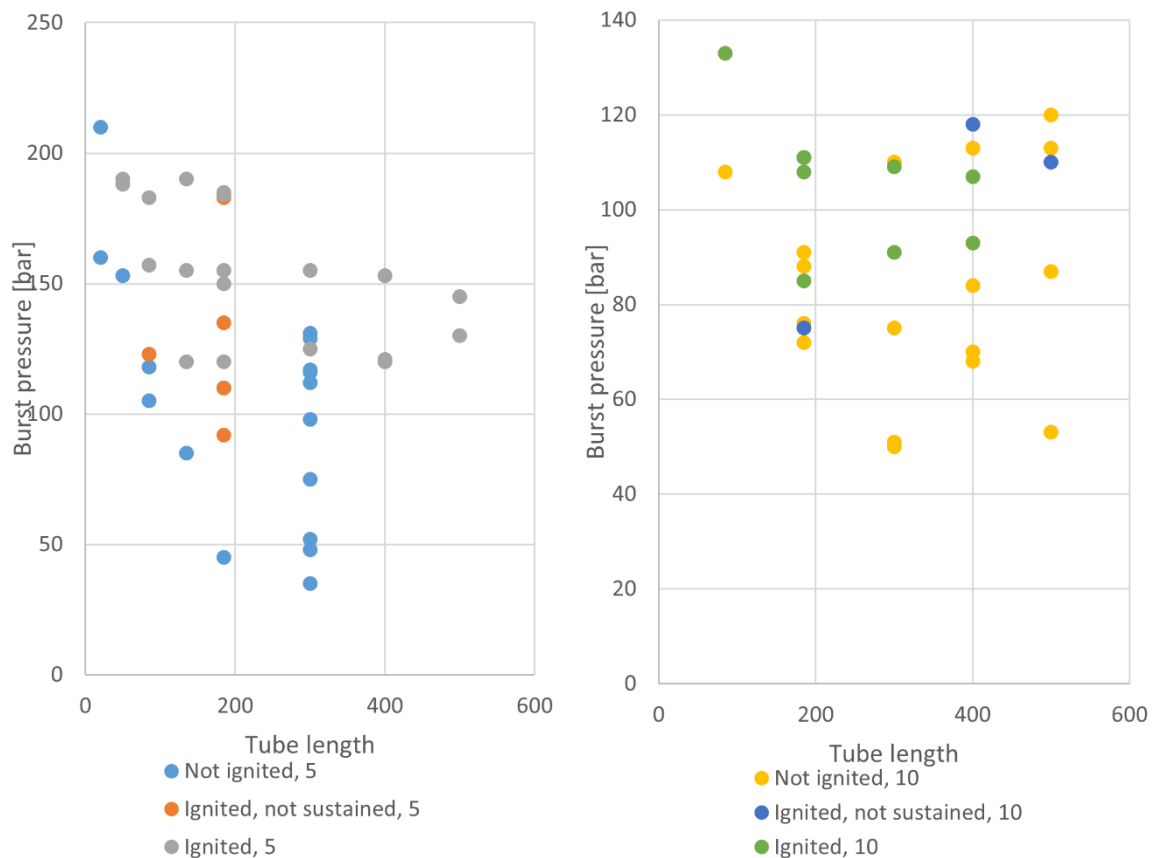


Figure 3-8: Data for 5 mm pipe (left) and 10 mm pipe (right) in Mogi *et al.* [88].

### 3.1.6 Numerical simulations by Liu and co-workers

Many articles mentioned so far include comparisons of experiments and numerical simulations. Liu *et al.* presented simulations without any accompanying experiments [90]. The main difference between this work and most other contributions concerning the diffusion ignition phenomenon, is that Lie *et al.* simulated releases of hydrogen directly into an open space. Section 3.2 presents some other examples of numerical studies of releases into an ambient atmosphere {[91]–[93]}.

Liu *et al.* used direct numerical simulation (DNS) with a grid resolution of 10  $\mu\text{m}$ , for three different cases: leakage of hydrogen to the atmosphere at initial pressures 10, 40 and 70 MPa [90]. The diameter of the leakage point was 1 mm in all cases. The case with 100 bar initial pressure resulted in a maximum temperature of approximately 450 K, but no local combustion was detected. Local combustion in the simulation was recognised by increased concentration of OH molecules (or ions or radicals), which is an intermediate product in hydrogen combustion.

The results from the simulations with 400 and 700 bar were similar. The plots for 400 bars presented in the article show that the maximum temperature increased from 2  $\mu\text{s}$  (1400 K) to 10  $\mu\text{s}$  (1750 K). The highest temperature at 2  $\mu\text{s}$  occurred at the front of the shock wave (caused by the adiabatic compression of the air), whereas the maxima at 10  $\mu\text{s}$  occurred at the contact surface region where hydrogen and compressed air is partly mixed, indicating that the increased temperature is caused by combustion. This was confirmed by the simulated mass fraction of OH $^-$  at 10  $\mu\text{s}$ . Longer distance from the leakage to the shock wave front and larger temperature are the most considerable differences between the experiments with 400 and 700 bars. The difference in the amount of energy released in the two experiments is probably the reason for this.

Even if ignition was observed at an early stage, the combustion was quenched relatively fast for both 400 and 700 bar scenarios. Liu *et al.* proposed two different mechanisms that might cause this quenching:

1. The flame is blocked from evolving, as it will be constantly in front of the hydrogen gas, where the reactants are partly mixed. The temperature maximum is at the shock wave front. As it will be a significant distance between the area with enough mixing and enough temperature, the flame front will not meet a combination of ideal temperature and ideal concentration. Without this combination, the flame front is not able to evolve into a full ignition.
2. The second explanation they proposed, is that when the combustion goes along, an increasing amount of H<sub>2</sub>O will be formed as a product of the combustion. The product will accumulate between the hydrogen and air zone and avoid mixing. This can eventually quench the flame.

The overall conclusion in this article is therefore that sustained ignition cannot occur if high pressure hydrogen is released into air through a trajectory free of obstacles and confinement. But as they have only simulated with 1 mm opening, they cannot exclude that a larger hole might cause sustained ignition even if no obstacles or confinement is present. This is also commented by Golub *et al.* [87].

## 3.2 The effect of rupturing behaviour on ignition

Many articles imply that the way the rupture disc opens, will affect the results. Some articles are even entirely dedicated to this variable.

### 3.2.1 Experiments by Golovastov and Bocharnikov

Golovastov and Bocharnikov used a setup with a confined volume of pressurised hydrogen, separated from an ID 18 mm 60 mm long tube that had two pairs of photodiode and piezo electric pressure transducers for one part of their experiments [94].

Along the axis of the tube, they had a photomultiplier and a light diode. The photomultiplier was located behind a transparent part of the pressurised container and looked towards the light diode that was placed at the open end of the tube. As the rupture disc opened, an increasing amount of light from the diode reached the photomultiplier. In this way, it was possible to determine the rupture rate. The sensor in the tube could determine shock wave and ignition properties for the different rupture characteristics. By using different materials and thickness in their rupture discs, they got different rupture rates.

Variations in rupture rate determined in which of the three modes the shock wave was formed: 3-step, 2-step or 1-step. Figure 3-9 illustrates the differences between the three modes, showing pressure readings at 10 and 50 mm together with readings from the photodiode at 50 mm and the reading from the photomultiplier at an x-axis showing synchronised time. The rate of pressure change ( $dp/dx$ ) is determined with the dashed triangle found in each figure.

According to Figure 3-9, the 3-step mode does not give ignition, whereas the 2-step mode gives ignition with approximately 15-20  $\mu$ s delay from the pressure maxima at the second wave step. The 1-step mode gives direct ignition, as the pressure maxima at 50 mm is detected simultaneous as the flame front passes this point.

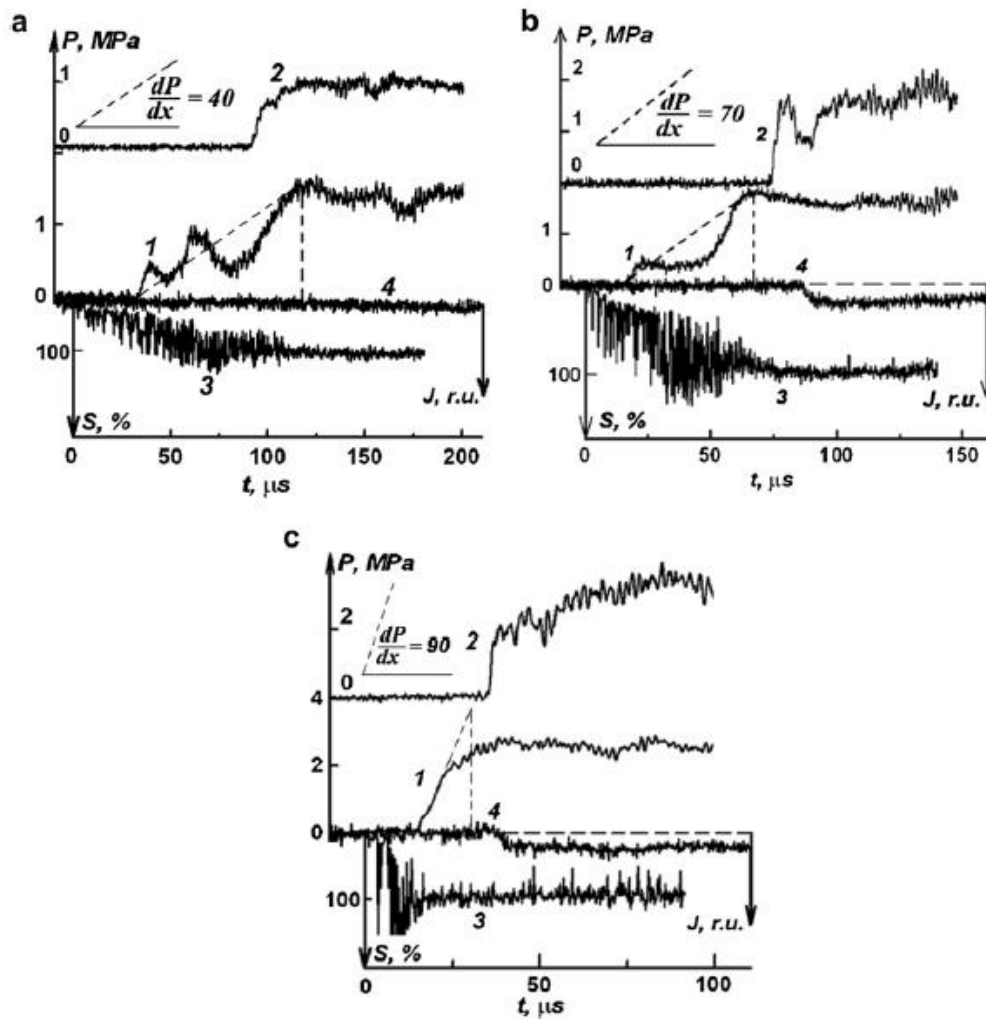


Figure 3-9: Different modes of shock wave formation upon rupture of a diaphragm. A is a 3-step mode, b is 2-step mode and c is 1-step mode. 1=pressure reading at 10 mm, 2= pressure reading at 50 mm, 3=reading from photomultiplier (shows how open the diaphragm is) and 4= reading from the photodiode at 50 mm (qualitative indication of ignition), from [94].

The experiments by Golovastov and Bocharnikov also show an almost proportional correlation between rupture rate and ignition delay ( $\tau$ ) [94]. They used a tube of  $\varnothing$  5 mm and 185 mm length for this experiment. Their results indicate that the initial hydrogen pressure does not considerably affect the delay. This is shown when rupture rate is plotted against ignition delay for different experiments, as in Figure 3-10.

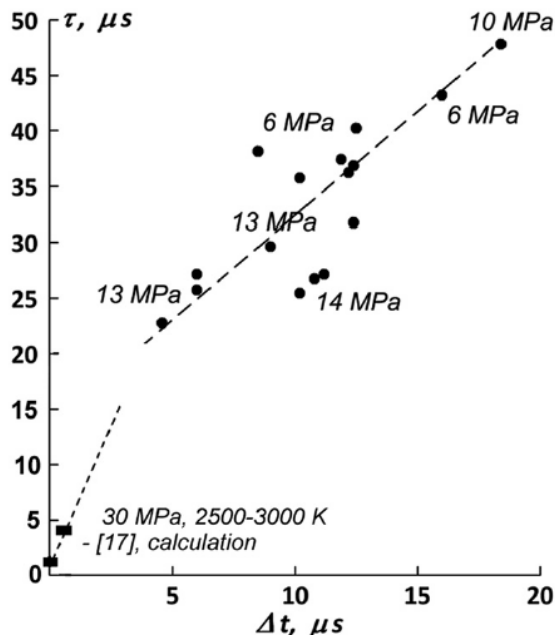


Figure 3-10: Show the relation between rupture rate ( $\Delta t$ ) and ignition delay ( $\tau$ ). As the dotted trendline indicates, it is a linear relation between them, from [94].

### 3.2.2 Experiments by Kaneko and Ishii

Kaneko and Ishii [95] investigated how rupture rate affected ignition. They used rupture discs made of aluminium, brass and copper with thickness of 0.2, 0.4 and 0.5 mm. By making cross shaped scores in the diaphragms with a length of 11 mm and depth from 30 to 160  $\mu\text{m}$ , they could adjust the burst pressure and rupture characteristics as desired. The setup was otherwise like that used by Gong *et al.*, with a tube length in the range of 80 to 350 mm with  $\text{Ø}$  10 mm. A high-speed camera and a xenon lamp located behind observation windows at opposite sides of the diaphragm along the axial direction was used to log the opening behaviour of the rupture disc.

Their experiments reveal a proportional relation between burst pressure and diaphragm thickness divided by diaphragm diameter. This is shown by the following formula:

$$P_r \propto \frac{\delta}{D} \quad (19)$$

where  $\delta$  is the thickness of the diaphragm, or the thickness in the pit of the scored line (total thickness of diaphragm minus scoring depth),  $P_r$  is the rupture pressure, and  $D$  is the diameter of the diaphragm.

There is a clear correlation between diaphragm thickness and shock wave speed (which again affect required pressure to get ignition). As an aluminium diaphragm needs a larger thickness to withstand the same pressure as a diaphragm made of copper or brass, the first one will give a slower rupture rate than the latter, and thus a slower shock wave speed and higher required ignition pressure.

### 3.2.3 Experiments by Gong and co-workers

Gong *et al.* investigated the effect of burst disc opening ratio, opening pattern, as well as how the shock wave pressure affect the probability for ignition using an experimental setup with a 360 mm tube of 15 mm internal diameter {[96]-[97]}. The opening ratio was defined as the diametrical relation of the actual opening and the full diameter of the burst disc [97]:

$$\chi = \frac{D}{D_0} \quad (20)$$



where  $\chi$  is the opening ratio,  $D$  is the actual opening diameter of the rupture disc, and  $D_0$  is the maximum opening diameter of the rupture disc. Gaskets with various internal diameters were inserted between the rupture disc and the tube to alter the opening ratio. The investigations showed that the opening ratio has a large impact on the shock wave pressure.

Gong *et al.* were not able to achieve spontaneous ignition for any cases with  $\chi = 1/2$  or lower, even at the maximum tested burst pressures which were around 90 bars for all opening ratios. Their results showed a shock wave pressure of 8.8 bars at the maximum tested pressure of 87.1 bars with an opening ratio of  $1/3$ . Even at this pressure, the shock wave pressure was lower than the shock wave pressure for the lowest tested burst pressure with an opening ratio of 1. This opening ratio gave 9.4 bars of shock wave pressure for 19.5 bars bursting pressure.

The potential effects induced by different opening patterns and rates were not given any attention at all in this article [97]. However, the other article by Gong *et al.* from 2019 focuses a lot on how these factors affect the shock wave pressure [96].

By introducing relative dimensions, they were able to compare scenarios that involved tubes in different sizes [96]. One of the relative parameters was relative length of tube, which is defined as tube length divided by tube diameter. Dimensionless burst and shock wave pressure was described as the burst or shock wave pressure, respectively, divided by the atmospheric pressure. They also used an equation for estimating the diaphragm opening time. The equation was first presented by Drewry and Walenta [98].

$$t = k \left( \frac{\rho \delta D}{P_b} \right)^{\frac{1}{2}} \quad (21)$$

where  $t$  is the burst disc opening time and  $\rho$  is the density of the burst disc material.  $\delta$  is the thickness of the burst disc, while  $D$  is the diameter of it,  $k$  is a calibration constant that is different for different materials and applications, it must be determined by experiments. Based on the results from experiments performed by Kaneko and Ishii [95], Gong *et al.* found that a value of 2.68 is suitable for aluminium and 1.57 for copper. These constants are valid when standard SI units are used for all factors in the equation. Gong *et al.* also found that the  $k$ -value for Drewry and Walenta's initial estimates from 1965 for 302 stainless steel burst disc is 2.4 when converted into SI units [98]. Wen *et al.* uses a value of 0.91-0.93 as  $k$ -factor in their article from 2009, which also presents Eq. (21) [92]. However, the material of the disc is not specified in this article.

Gong *et al.* investigated how different dimensions and conditions from previous work {e.g. [88], [95], [87], [99], [100]} affected the ignition probability. The relation between the mean Mach number and the initial pressure ratio showed, as expected, that a larger pressure ratio gave a higher mean Mach number. They also plotted the dimensionless shock wave pressure against the "derived dimensionless parameter" and found a proportional relation between these two properties. The derived dimensionless parameter is the dimensionless burst pressure multiplied by the ratio of the characteristic time (the time needed for the shock wave to travel a distance equal to the tube diameter) divided by the calculated opening time. These parameters are presented in relation to Eq. (22) below.

The authors then used their own data in addition to data from some of the sources mentioned above in a scatter plot with the derived dimensionless parameter on the y-axis and the dimensionless tube length on the x-axis. The results were also marked with "ignition" or "no ignition". Based on this plot, they found empirical correlation for the trend line at the boundary between ignition and no ignition:

$$\left(\frac{P_b}{P_a}\right)\left(\frac{D}{U_s t}\right) = 22.3\left(\frac{L}{D}\right)^{-0.58} \quad (22)$$

where  $P_a$  is the atmospheric pressure,  $U_s$  is the shock wave speed and  $L$  is the length of the tube. The other parameters are the same as in Eq. (21). The left side of the equation is altogether referred to as the “derived dimensionless parameter”.

### 3.2.4 Numerical simulations by Wen, Xu and co-workers

Xu *et al.* and Wen *et al.* have conducted a few studies that investigate how the rupture rate will affect the probability for ignition. They have also published an article that investigates how different release pressures and tube lengths affect the probability for ignition, just like many other researchers have also done.

An article published in 2008 refers to a numerical study of a system consisting of a pressurised reservoir and a piece of ambient atmosphere [91]. Unlike most other studies of this phenomenon, the hydrogen stream from the rupture point is not led into a semi-confined or congested space. Liu *et al.* also simulated leakage into an open space [90] (section 3.1.6)

In the study, they simulated different scenarios with 300 bars, 3 mm rupture diameter and 273 °K at the pressure reservoir upon rupturing. Various rupture rates were investigated in this setup, using 0, 0.3, 0.6, 0.9 and 1.2  $\mu$ s from closed to fully open. Their results showed that rupture rate is a key parameter for spontaneous ignition. Decreased rupture time gives a more extensive shock wave which increases the probability for spontaneous ignition.

Even with the relatively large volumes of pressurised hydrogen available upstream the leakage point, the shock waves generated through a gradual opening never reached the same intensity as a sudden rupture at the same conditions reached. However, rupture times of 0.3 and 0.6  $\mu$ s gave sufficient shock wave intensity to generate ignition, according to figures showing OH mass fractions at different times after the rupture. However, the case with 0.6  $\mu$ s had just some small areas where combustion occurred. The areas were not large enough to give a sustained combustion.

Another article by Wen *et al.* published in 2009 presents a more traditional numerical setup for investigating the diffusion ignition phenomenon, with a volume of pressurised hydrogen connected to a tube filled with ambient air [92]. The pressure cylinder and tube are only separated by a diaphragm with a thickness of 0.1 mm. The initial temperature was 293 K in all experiments. The tube ended in a section of ambient atmosphere. To avoid shock waves from reflecting in the “upstream wall” of this ambient environment and disturb the formation of vortices at the tube outlet, the tube exit had 8 mm offset into the ambient environment.

The article used 1D simulations for initial investigation of the phenomenon. Their results showed much lower values for shock velocity and temperature than the corresponding results from 2-D simulations. Wen *et al.* think the reason for this is that reflected shock waves give a significant contribution to the overall shock severity, and these are not taken into account in a 1D simulation.

An experiment with 5  $\mu$ s delay, 150 bar initial pressure 6 cm tube length and 3 mm tube diameter was used as a basis for comparison in the evaluation of four different variables. Namely rupture time, tube length, tube diameter and rupture pressure. They did only change the value they were investigating in each experiment.

The overall conclusions in brief words, were as follows:

1. Shorter rupture time gave more rapid temperature increase, but all cases gave approximately the same maximum temperature. The ignition delay increased along with increased rupture time.
2. Increased tube length produced a better developed flame at the tube outlet, thus producing a more robust ignition.
3. Increased tube diameter gave longer ignition delay for the same length.
4. Ignition delay had a strong dependency on initial pressure. This is in line with most other authors findings. While the basis experiment with 150 bars as earlier mentioned had a delay of 9  $\mu\text{s}$ , the 100-bar experiment gave 12  $\mu\text{s}$  delay, while the 50 bar setup had as much as 45  $\mu\text{s}$  delay. The huge gap between the delay for 50 and 100 bar experiments, could indicate that the pressure must overcome a threshold to be able to initiate diffusion ignition. This is also proposed in other research works, for instance by Oleszczak and Wolanski [41] .

An article from Xu *et al.* from 2008 evaluates aspects related to the development of the mixing zone through the tube, as well as how the flame propagates (or not) downstream of the tube [93]. The article is based on numerical simulations of a  $0.5^\circ$  sector of a tube, at initial pressures ranging up to 100 bars, with the majority of experiments with 70 bars initial pressure. Initial temperature was 500 k for all experiments.

As molecular diffusion rate is inversely proportional with pressure, high pressures within the tube might increase the time until sufficient amount of combustible mixture is present in the boundary between the displaced air and the expanding hydrogen. It will also reduce the supply of fuel and oxidant to the flame front in the boundary, thus reducing the probability for a sustained combustion. The article also mentions turbulence that occurs in the under expanded jet at the tube outlet, and as a general consequence of the expansion of the gases. The turbulence will contribute to mixing the gases, providing a larger volume rate of available combustible gases for flame front. If the combustion should be able to develop from the small flames at the boundary between the gases to a stable flame, these phenomena are crucial.

### 3.3 The effect of obstacles and angles in the tube

Different groups of researchers have investigated how different shapes in the tubing downstream of the rupture disc affect the propensity for ignition.

#### 3.3.1 Experiments by Pan and co-workers

This group of researchers have earlier conducted research with straight tubes. This work is summarised on page 29 in this thesis. In their study from 2020, they investigated three different L-shaped tubes, as well as a straight tube for comparison [101]. All four tubes had the same total length of 836 mm and ID of 10 mm, but length upstream and downstream of the angle was altered for the L-shaped tubes. The upstream lengths were 230, 423 and 616 mm. Their experiments showed a correlation between critical burst pressure (the lowest pressure resulting in spontaneous ignition) and length from burst disc to angle. Shorter distances gave lower critical pressures, but the correlation was non-linear. All L-shaped tubes could produce ignitions at lower pressures than the straight tube, but the difference between the straight tube and the tube with an angle located at 616 mm was minimal.

### 3.3.2 Experiments by Gong, Duan, Sun and co-workers

This group of authors have contributed on a number of articles that investigate angle and other obstructions in the tubes. Other authors have also contributed on these articles, but the three names mention in the heading are listed on all articles mentioned in this section.

In an article from 2017, they investigate how different angles in a 360 mm ID 15 mm tube affect the probability for spontaneous ignition [102]. They investigated angles of 150, 120, 90 and 60°, all located 120 mm away from the rupture disc. The angles were defined so that a straight tube would have been denoted as 180°. The tube was equipped with three pairs of photodiodes and pressure transducers, located 90, 180 and 270 mm away from the rupture disc. A reservoir of 0.44 litres was pressurised to pressures between roughly 20 and 100 bars in the different experiments.

Their results show that a steeper angle could produce ignition at lower pressures. Ignition occurred as low as 21.5 bars in the 60° tube, and approximately 35 bars for the 120° and 150° tubes. Increased pressures made the ignition detectable closer to the rupture disc. Ignition was detected already at the first pair of instruments at 90 mm at burst pressures of 31.4, 52.9, 67.1, 73.8 and 75.9 bars for 60° to 150° and straight tube, respectively. Another interesting observation from this work, was that all except one of the experiments that produced ignition were also able to propagate the ignition out to the exhaust chamber.

An article from 2016 investigated how changes in the cross-section of the tube affected the ignition probabilities [103]. This setup used the same 0.44 reservoir volume, 360 mm tube length and initial ID of 15 mm [102]. They investigated local and permanent contractions and enlargements. The local contractions and enlargements used a 30 mm section of either 10 mm or 20 mm ID, starting at 120 mm. The ID was returned to 15 mm after the temporary change. The permanent contractions and enlargements altered the ID to either 10 or 20 mm from 120 and through the remaining tube length.

Their results showed that local enlargement and contraction as well as permanent contraction could produce ignitions at significantly lower pressures than a comparable straight tube. Their theory was the shock wave was partially reflected on the forward-facing surfaces at the contractions, and that this enhanced the total intensity of the shock waves, thus reducing the critical pressure for ignition. The local enlargement has a “forward facing surface” at the point where the ID returns to its initial value.

However, as also permanent enlargement of the tubing section gave lower critical pressure than the corresponding straight tube, this reflected shock wave cannot be the only reason.

A more recent article, published in 2019 investigates how restrictions inserted into the tube affect the propensity for ignition [104]. They used a tube with ID 15 mm and 400 mm length, and four pairs of pressure sensor/photodiodes distributed at 80 mm intervals. Obstacles were inserted between 240 and 320 mm downstream of the rupture disc. Seven obstacles with spacers between them were used in the “obstacle package”. The obstacles had a metal cross where two steel “beams” intersected at the centre of the tube. Both spacers and obstacles had a significant annular thickness, thus reducing the remaining ID of the tube. The spacers had an axial thickness of 4 mm, while the obstacles were 2 mm, giving a total length of 38 mm for the obstacle package.

The article describes three different ignition mechanisms:

- a) Ignition occurs upstream of the obstacles. This is the mechanism that will ignite the mixture in a tube without obstacles. The probability for such ignitions will increase as the burst pressure increases. The ignition position will also move closer to the burst disk as pressure increases
- b) The second mechanism described is a small ignition at a position upstream of the obstacles. This ignition is quenched, but the turbulence generated as the incident shock wave travels through the obstacles, will give a second ignition downstream of the obstacles. The reason for why the initial

ignition is quenched, is either that all available combustible hydrogen/air mixture is consumed or that the leading shock wave does not provide enough energy to maintain a sufficient temperature to develop the flame.

- c) The third mechanism is where ignition first occurs downstream of the obstacles. The mixing of hydrogen and air as the shock wave passes the obstacles will aid this mechanism. Ignition might also occur upstream of the obstacles afterwards due to the reflected shock waves.

Despite the increased turbulence, and in some cases reduced critical burst pressure, for the tube with obstacles, the authors conclude that the obstacles do not improve the flame development outside of the tube.

The authors also published a numerical study based regarding this matter [105]. They used an 18-step chemical reaction mechanism for the hydrogen/air mixture. Their setup consisted of a 15 mm ID tube of 360 mm length, with a 90° bend located 120 mm downstream from the rupture disk (identical to the variant with 90° [102]). The rupture disk was simulated with a initially closed plane with 15 mm diameter, which opened in ten steps, starting with the centre part. The duration of this opening process (from the first to last annular section of the plane) was estimated with Eq. (21). They used an initial temperature of 300 K.

The mesh size varied from 0.8 mm adjacent to the burst disk, to 10 mm in the high-pressure storage tank, which was a 40 mm ID tube with 240 mm length. The tube corner also had 0.8 mm mesh.

The normal shock wave was capable of initiating ignition upstream of the tube bend if the pressure was large enough. This occurred with 91 bars initial pressure.

The release with 21.6 bars initial pressure ignited due to the reflected shock waves. Ignition occurred two places independent of each other. The first ignition was located upstream of the bend, when the reflected shock wave from the outer tube wall after the angle interacted with the remaining shock waves and increased pressure after the initial release flow/shock wave. The second ignition occurred close to the inner wall in the tube section downstream the bend, in the area where the reflected shock wave from the outer tube wall hit the inner wall with an angle.

Due to the reflected shock waves downstream of the tube bend, even the 21.6 bars scenario achieved a relative robust ignition in that part of the tube section.

Three different ignition mechanisms were presented:

1. Ignition occurred due to the heating of the hydrogen/air mixture along the tube wall caused by the normal shock wave travelling away from the burst disk. This mechanism caused ignition in straight tube sections without obstacles, illustrated in Figure 3-11 *a*) below.
2. After the shock wave had been reflected in the outer wall, a part of the shock wave was reflected towards the rupture disk and reservoir. It interacted with the flow coming from the reservoir. This shock wave interference in combination with transformation of kinetic energy into internal energy (heat) could cause ignition, illustrated in Figure 3-11 *b*) below.
3. Some of the hydrogen flowed close to the inner tube wall in the part of the tube downstream of the tube bend. This hydrogen stream easily mixed with the air in the downstream part of the tube. The reflected shock wave from the outer tube wall will have a curvilinear shape, and some of this shock hit the hydrogen/air mixture in the proximity of the inner tube wall, illustrated in Figure 3-11 *c*).

Both mechanisms 2 and 3 occurred in experiments with as low as 21.6 bar initial pressure.

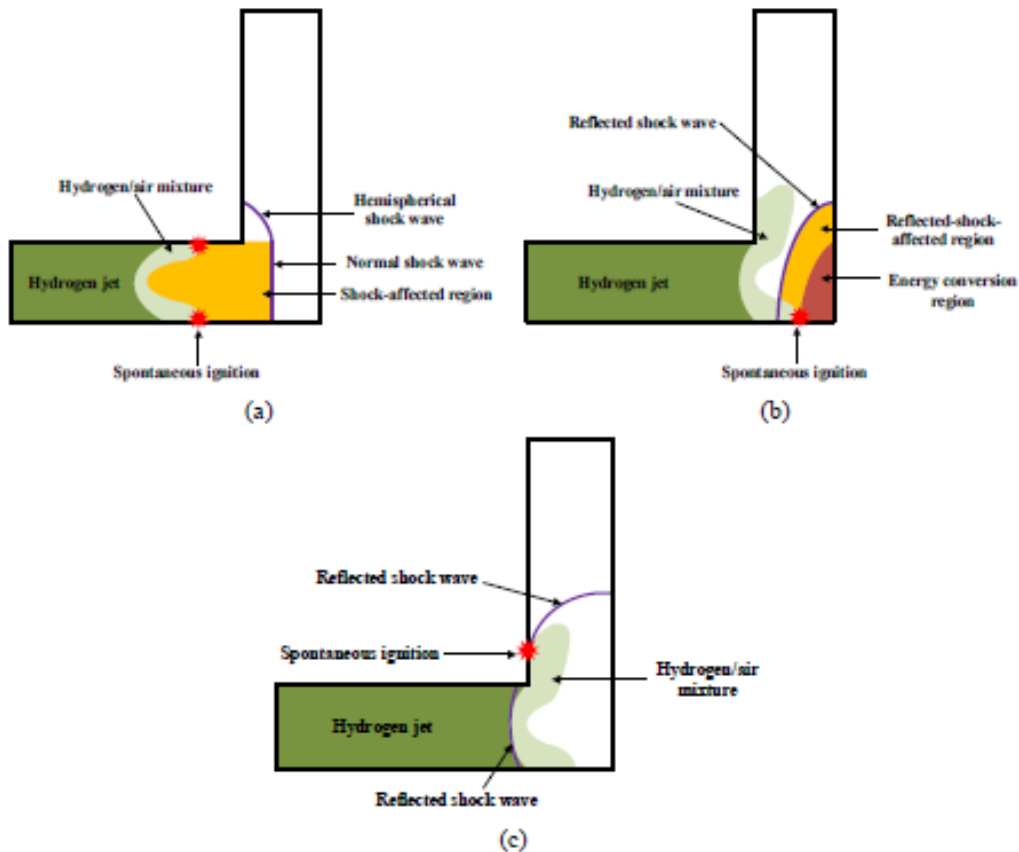


Figure 3-11: Illustration of three different ignition mechanisms identified by Gong *et al.* [105], from the article.

### 3.4 The effect of modified atmosphere

Gong *et al.* investigated the effect of adding hydrogen to the atmosphere in the tube downstream of the burst disc [106]. They used a setup with a 360 mm long tube with inner diameter 15 mm tube and pairs of piezoelectric pressure transducers and photo diodes located 90, 180 and 270 mm downstream from the rupture disc, similar to the experiments from the same group presented above. The difference from the experiments presented above was that the 360 mm tube had an additional line connected to it, for displacing the gas in the tube with premixed gas from a mixing system. The tube was isolated from the open exhaust chamber with three layers of paper to keep the premixed concentration until the disc had ruptured without affecting the pressure conditions.

The study included releases into atmospheres with 5, 10, 15 and 20 vol.% hydrogen in air. The temperature of the shock wave decreased by 6 % for 20, compared to 0 vol.% hydrogen with a shock released from an initial pressure of 60 bars. This factor alone would reduce the propensity for ignition. Figure 3-12 shows that the addition of hydrogen to the ambient air vastly reduces the critical burst pressure for ignition: a 20 vol.% hydrogen-air mixture reduces the critical pressure from 43.7 bar to less than 17.9 bar.

The same setup was used to evaluate the effect of adding carbon dioxide to the air in the tube downstream of the burst disc [107]. Figure 3-12 shows that an increase in the CO<sub>2</sub> concentration from 0 to 15 vol.% increased the critical pressure from 43.7 to 64.1 bar.

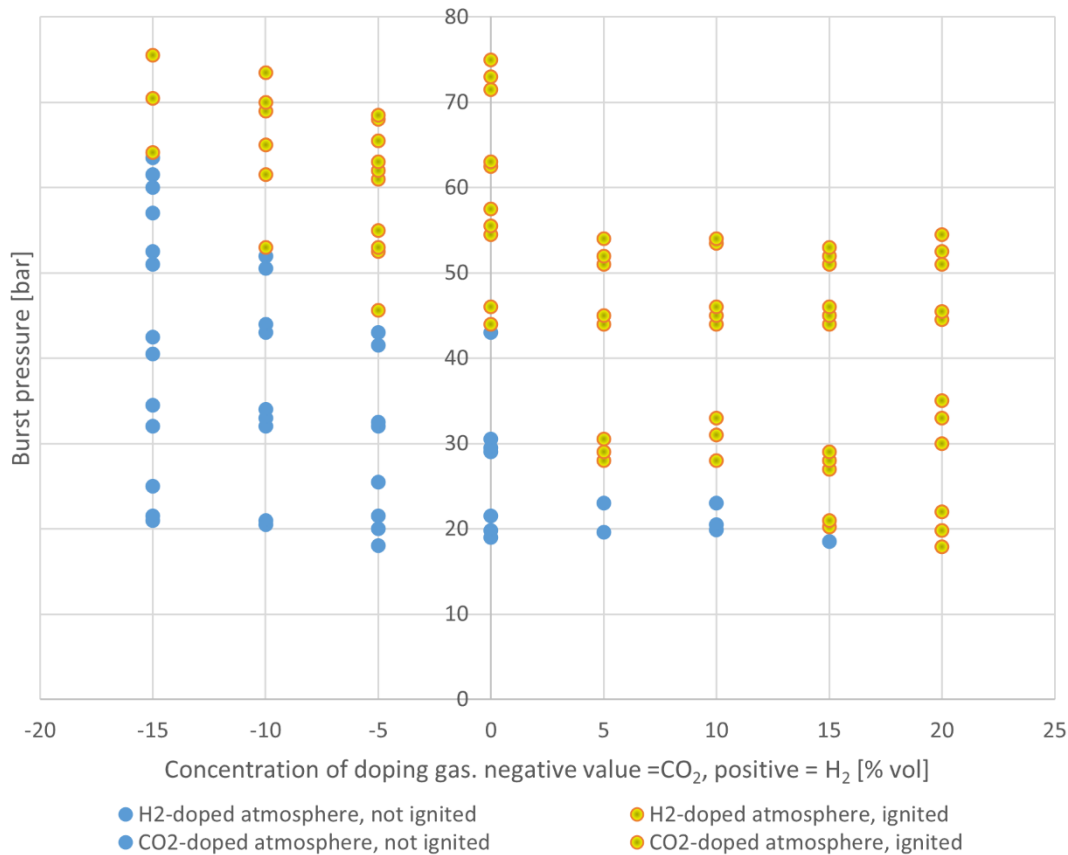


Figure 3-12: The effect of doping the atmosphere in the tube with either CO<sub>2</sub> or H<sub>2</sub>, based on data from [107]. The x-axis use negative values for CO<sub>2</sub> concentrations, to distinguish the different doping gases.

### 3.5 Main characteristics from the literature review

The articles presented above indicate that a lot of factors affect the probability for diffusion ignition to occur after abrupt releases of hydrogen. The criticality of the different parameters has not been quantitatively evaluated, but their direction of impact has been evaluated. It should be possible to obtain a certain qualitative understanding based on the findings.

- Tube length – Increased length reduces the critical burst pressure – up to a certain point, where the critical pressure starts to increase with increasing length. It thus appears to exist a critical tube length that will give the lowest possible required burst pressure for a given set of conditions.
- Tube diameter – Tube diameter also seems to affect the critical burst pressure. However, it seems to be less critical than tube length. A critical value seems to exist also for tube diameter.
- Tube diameter and – length seems to correlate with each other; thus it might be the relative length (L/D) that actually correlates. An example of a such potential correlation is shown in Eq. (22).
- Changed concentration in the downstream gas seems to have a large impact on the critical pressure. Hydrogen present in the ambient atmosphere prior to the rupture reduces the critical pressure necessary to create ignition. If the downstream ambient atmosphere contains CO<sub>2</sub> on the other hand, the critical burst pressure increases.
- Angles and obstructions within the tube seems to reduce the critical pressure. Steeper angles and larger obstructions give lower critical burst pressures.

- Rupture rate is also important. Faster rupture rates, thus decreasing opening times for the burst discs, tend to decrease the critical pressure.

Data based on results in most of the experiments presented in this chapter, as well as some others that are only indirectly presented above, were compiled in an attempt to visualise correlations and dependencies. A total of 987 experiments were included in this collection. Some of them were based on graphic reading of figures in the articles, while others were found in tables. The following figures include data from various sources {[41], [83]–[89], [95]–[97], [99], [101]–[104], [106]–[109]}.

Figure 3-13 summarises most experiments performed with straight tubes. The burst pressure is plotted against the relative tube length. The results are divided in three categories, as most articles have done this. The “partially ignited” category includes different variations of experiments where ignition is observed at some stage in the release, but not sustained. The definition of “ignited” varied among the articles but was generally classified as ignitions that were strong enough to be detected at the end of the investigated area.

As the plot clearly shows, these results are way too ambiguous to make it possible to draw any certain conclusions. It seems that the lowest burst pressures are achieved for a relative length around 25, but this could also be because the experiments around this relative length was distributed among relatively few articles, and that they observed low critical pressures due to factors not shown here.

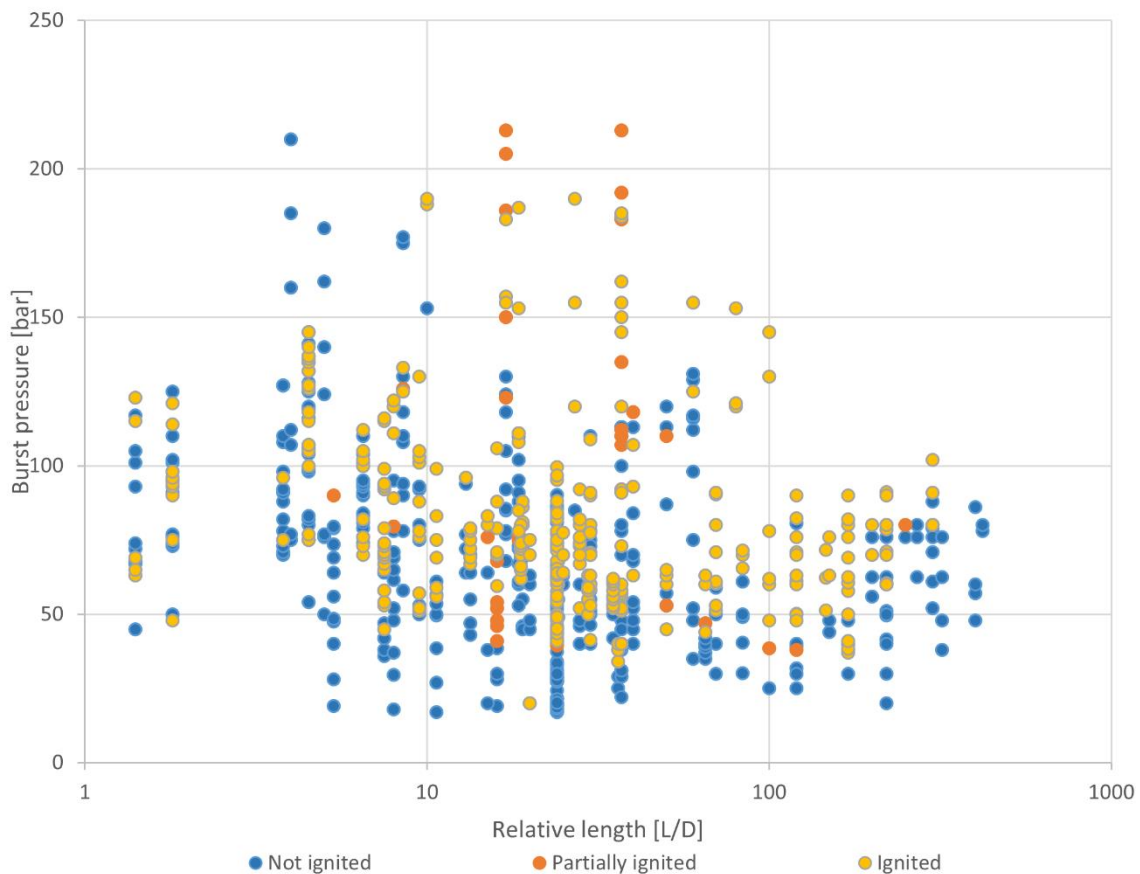


Figure 3-13: Scatter plot of experiments with straight tubes. Burst pressure plotted against relative tube length.

Figure 3-14 and Figure 3-15 show the results with the most common tube diameters, namely 10 and 15 mm as a function of the absolute tube lengths. The longest tube lengths are excluded to make the figures easier to study in the area where most experiments have been conducted. These figures are also rather ambiguous. However, it seems that the critical pressure for ID 15 mm decreases with length all the way up to 360 mm. Unfortunately, no experiments were made with slightly longer tube lengths. Further



experiments with tube lengths from 400-700 mm could have revealed a possible critical tube length for this internal diameter.

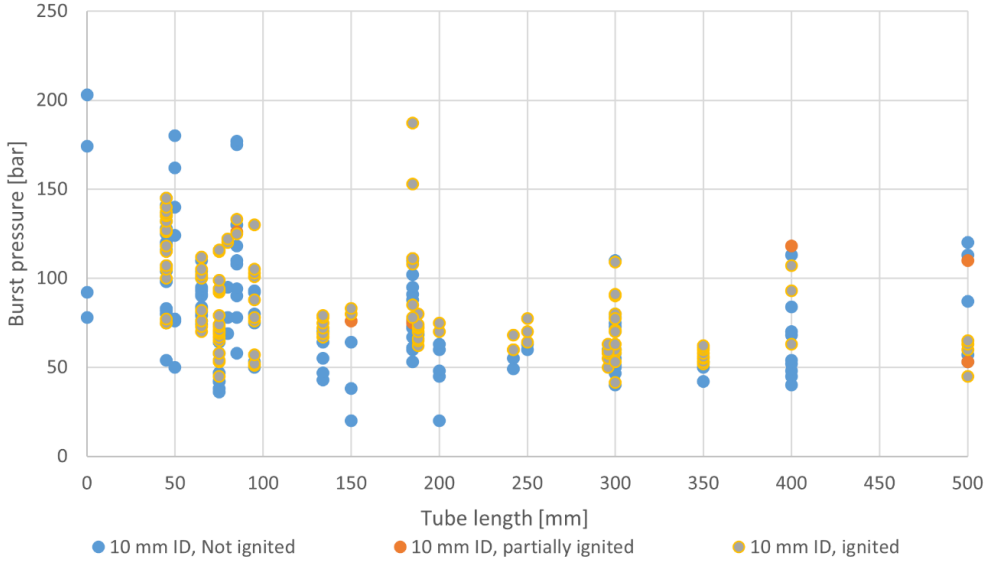


Figure 3-14: Scatter plot of results from experiments with ID 10 mm tubes in various lengths.

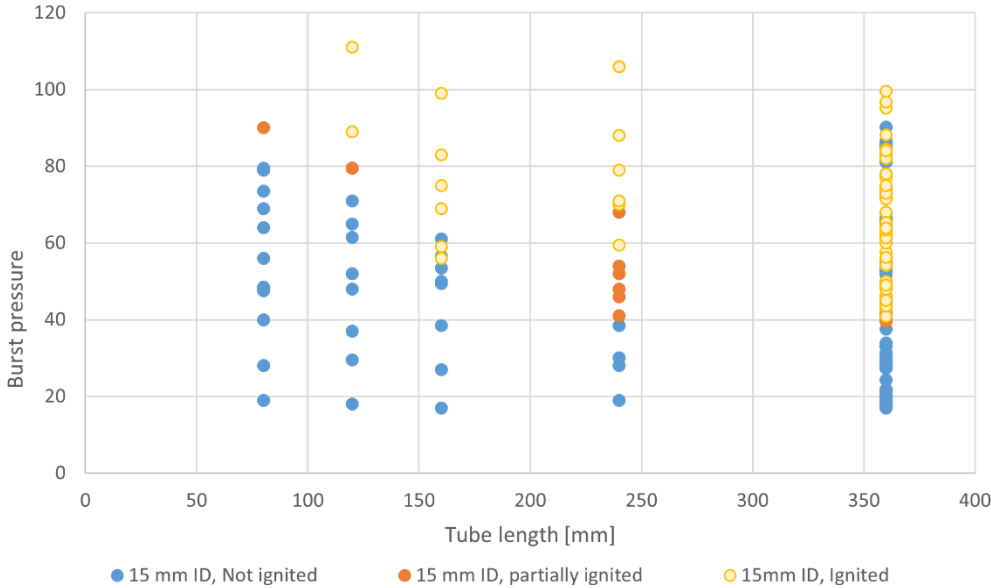


Figure 3-15: Scatter plot of results from experiments with ID 15 mm tubes in various lengths.

## 4 Experimental work

### 4.1 Purpose of experiments

The diffusion ignition phenomenon was investigated through the literature review, and many parameters appear to affect the propensity for this phenomenon to occur upon abrupt high-pressure hydrogen

releases. A summary of these parameters is given in section 3.5. However, most of the experiments followed roughly the same path: Hydrogen at relatively high pressures were released from a reservoir and into an open-ended tube of various diameter and length. The release occurred upon the burst of a rupture disc. Parameters that were altered were, for instance, tube length and diameter, burst pressure, if obstacles or bends were present within the tube, and if yes – the extent of their complexity.

Despite large variations for these parameters and others, the investigated area was rather small. The experiments in this thesis were designed to investigate this phenomenon in a wider context.

- We replaced the rupture disc usually found in these experiments with a fast, air-actuated valve to investigate the propensity for diffusion ignition to occur when the release is developed in a fundamentally longer time scale than provided by a rupture disc.
- We added an object at the outlet of the open-ended tube to reflect potential shock waves back towards the jet outlet, thus increasing the total shock wave intensity.
- We also did experiments with rupture discs. This was mainly done for two reasons:
  - Validate this experimental setup against literature experiments with rupture discs. Similar results at similar conditions indicate that the results are comparable also for experiments without rupture discs.
  - Investigate how the presence of “Obstruction objects” in front of the tube outlet affected the results for rupture disc leakages.

## 4.2 Experimental equipment

This section describes the functionality of the experimental equipment used in this thesis. Technical specifications that are of importance for the results are elaborated. Also, the instrumentation and its capacity and limitations are described here. The design and construction of the equipment consumed a large amount of the available time and resources during this project. Appendix A provides a more detailed description about the components to better reflect the effort put into this work. Details about the progress and possible future improvements and extensions to the equipment are provided in appendix B. The level of details in these appendices could also become very useful if this setup should be developed further, modified, or replicated at a later occasion.

### 4.2.1 Mechanical equipment

The mechanical part of the setup is roughly divided in two parts: the high-pressure hydrogen system and the explosion chamber with its belonging blowdown pipe. The main components are indicated on the picture in Figure 4-1 and Figure 4-2. A more thorough description of the components, how they were designed and their specifications are provided in appendices A.1, A.2 and D.

#### High-pressure hydrogen system

The high-pressure reservoir is connected to both hydrogen and nitrogen gas bottles with individual pressure regulators. The nitrogen were used for leakage testing as well as to dilute and displace hydrogen before disassembly of the system, as mentioned in 4.3, 4.4.1 and 4.5. A connection block machined from a piece of stainless steel provide enough branches for the connected lines, plus a spare connection. The “front end” of the connection block is connected to the pressure reservoir with a short tube length. The piezoelectric transducer is installed in the opposite end of the connection block to give a straight line from the valve, through the pressure reservoir to the transducer, thus optimising responsiveness. The  $\frac{3}{8}$ ” release valve is located immediately below the explosion chamber, and as the flow turns 90° degrees in the valve, the gas flows vertically when it enters the explosion chamber. Figure 4-2 shows the valve.

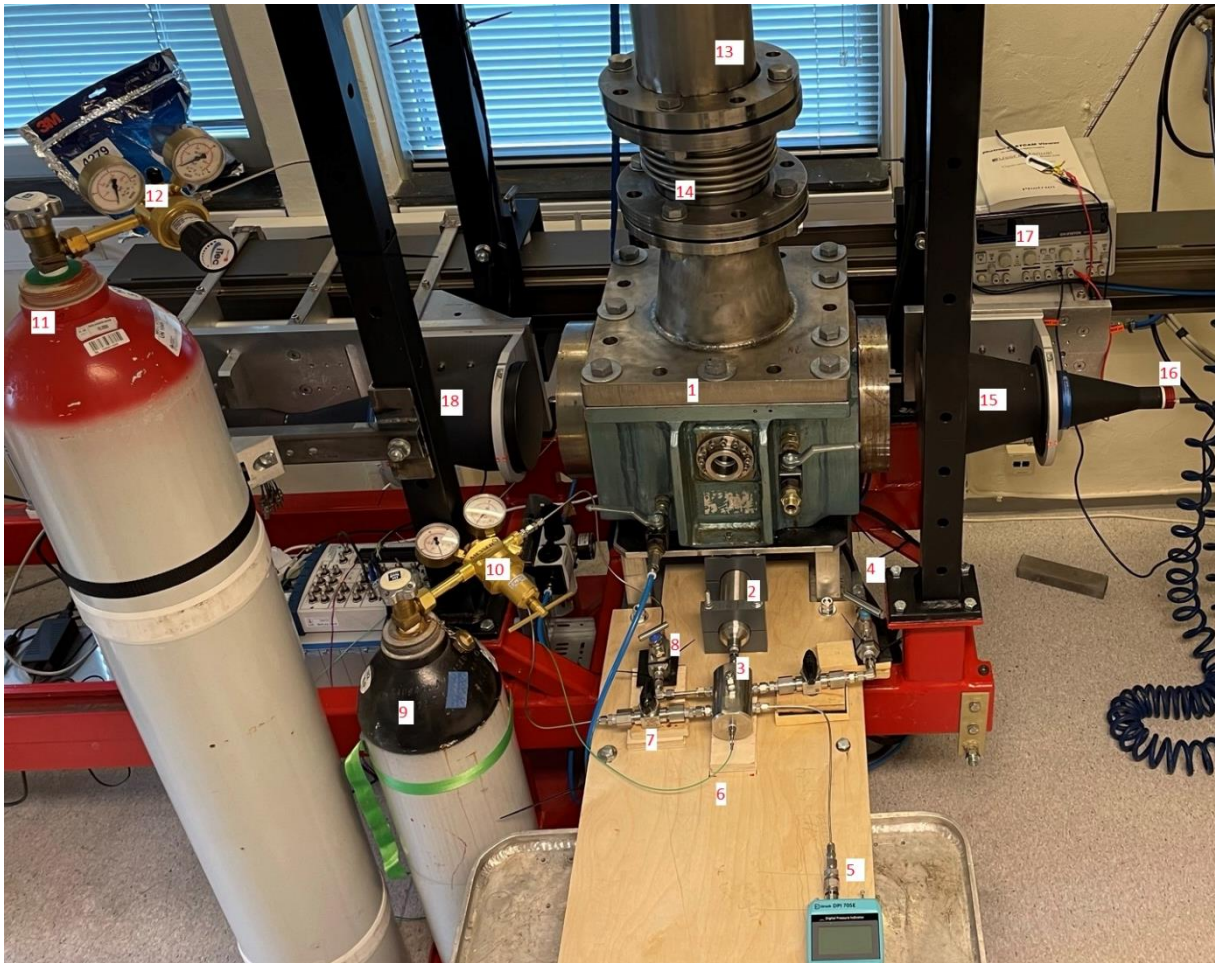


*Figure 4-1: Overview of the main components of the experimental setup: 20-litre explosion chamber (1), 150-ml pressure reservoir (2), connection block (3), backup depressurisation line with isolation valve and throttle valve (4), digital manometer (5), piezoelectric pressure transducer (6), isolation valve from hydrogen supply (7), isolation valve from nitrogen supply (8), nitrogen bottle (9), nitrogen regulator (10), hydrogen bottle (11), hydrogen regulator (12), blowdown pipe (13), axial compensator (14), telecentric lens, light source side (15), light source (16), power supply for light source (17), and telecentric lens, camera side (18).*

In addition to the 150 ml reservoir, the confined volume upstream of the release valve before release consist of approximately 350 mm  $\frac{1}{8}$ " tubing, 400 mm  $\frac{1}{4}$ " tubing and 200 mm  $\frac{3}{8}$ " tubing and internal cavities in the connection hub, which both have an ID around 5 mm. This gives a total volume of about 161 ml, but it is fair to anticipate that cavities not accounted for above results in a total volume of approximately 175 ml.

The entrance to the explosion chamber goes through an aluminium flange equipped with threading that corresponds to the fitting parts on the high-pressure system, thus facilitating a gas tight perforation. The nozzle or nozzle assembly for burst disc experiments is attached in the opposite end of the flange. Both the upstream and downstream tubing sections on the release valve is 75 mm long with an ID of 5.2 mm.

Industrial hydrogen with grade 5.0 was used in all tests. It has a purity of 99.999 %.

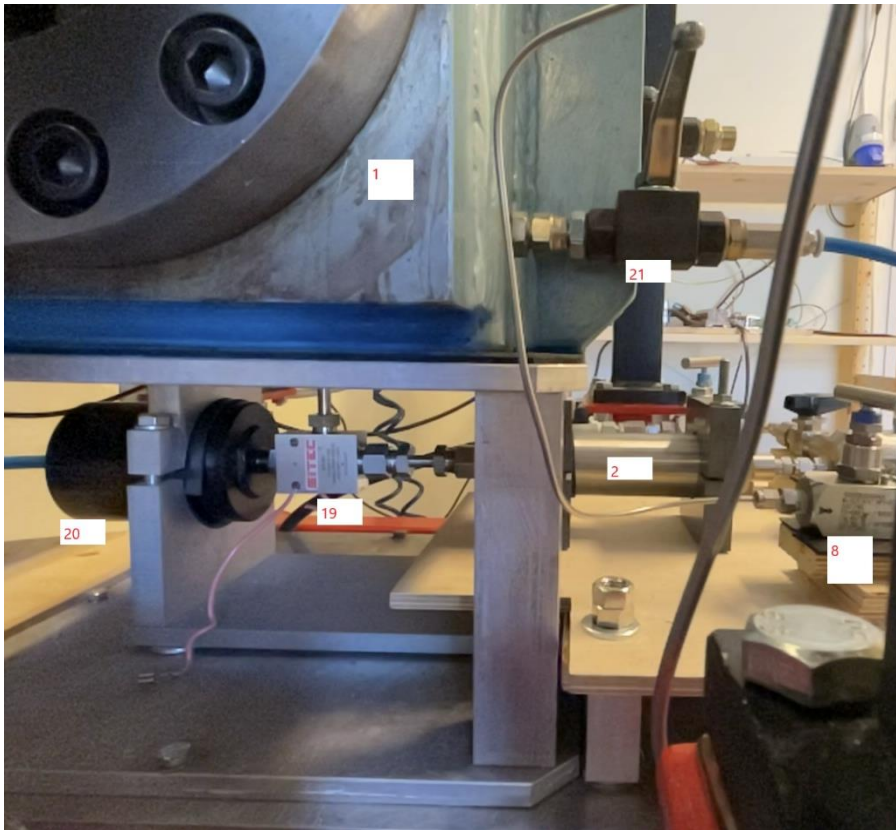


Figure 4-2: The high-pressure release valve (19) with actuator (20), the 20-litre explosion chamber (1) and the 150-ml pressure reservoir (2), isolation valve from nitrogen supply (8), and valve with permanent air supply for flushing of chamber (21).

### Nozzles

Two different types of nozzles were used in this experimental work. Both assemblies, including the release valve, are shown in MECH-03-02. In addition to that, the nozzles and related component made “in house” during this project is shown with more details in MECH-02-02. One of the nozzles is open with an internal diameter of 5 mm. This brass nozzle, made specifically for this project, was used for the experiments where time scales caused by valve opening were investigated. It seals directly against the tube end coming up from the release valve, as it has the opposite oriented taper shape than the tube end. This nozzle alone is 126 mm long. The combined length from the release valve outlet to the nozzle exit is 205 mm, and the relative length is 40, when the respective ID of 5.0 and 5.2 mm for the nozzle and tubing is considered.

The nozzle assembly used for rupture disc experiments consist of the same 75 mm tubing that is present in the other assembly, in addition a commercially available rupture disc holder and a brass nozzle attached at the outlet of the disc holder. The assembly installed in the explosion chamber is shown in Figure 4-3. As the tube end and the disc holder have the same orientation of the taper shape and are not designed to be connected directly together, a “joint sleeve” made from stainless steel is placed between them within the flange.

The assembly has an overall length of 216 mm from the release valve to the nozzle exit. From the rupture disc to the outlet, the distance is 85 mm. This assembly have various ID’s in the different sections, but the whole section downstream of the rupture disc has an ID of 8 mm. The upstream section has ID’s between 5 and 6 mm, while the orifices have “free pass” ID’s of 6.35 mm. This gives an opening ratio ( $\chi$ ) approximately 0.8.



Figure 4-3: Rupture disc assembly installed in the explosion chamber (ID at nozzle exit = 8 mm).

When the different ID's are considered, the upstream section has a relative length of about 25.4, while the downstream section has 10.6. The variations in ID in the upstream section introduce some obstacles to the flow path in the boundary between the different diameters.

#### Obstruction objects

Different obstruction objects are mounted in front of the nozzle exit to reflect shock wave back towards the outlet. Three different obstruction objects were made for this project. They were all made from brass. Additionally, the holding rod used to attach the objects to the explosion chamber was used alone as an obstruction object in some experiments. Both the threaded and the straight end of this rod have been used. All obstruction objects as well as the holding rod are shown in MECH-02-01.

Figure 4-4 and Figure 4-5 show the three obstruction objects (OO), denoted "A", "B" and "C" in the drawings, documentation, and meta data for the experiments. They are all made from a cylinder-shaped piece of brass with an OD of 31.8 mm. The length from top of the object and down to the part of the obstruction object located farthest away from the nozzle exit is just above 40 mm for all objects independently of their shape.

- Obstruction object A has a semi-circular shape with a radius of 13 mm. The edges of the object is extended 1.7 mm below the centre of the semicircle.
- Obstruction object B has a square shaped cut out, with a width of 23.7 and a height of 15.4 mm.
- Obstruction object C is flat, thus with a circular shaped plane directed towards the nozzle exit.
- The connection rod has an OD of 13 mm. The threaded end has a 26 mm long section with M12 threads.

All objects, including the connection rod were polished before they were used for the first time. However, as Figure 4-4 shows, A and C have a rather rough surface. For object A, this was due to

vibrations in the milling machine when the shape was milled out. For object B, it was due to poor access to the narrower part of the structure in the polishing machine.



Figure 4-4: Obstruction objects A, B and C, respectively.



Figure 4-5: The straight end of the connection rod.

#### 4.2.2 Instrumentation

The experimental equipment is equipped with various instruments and control equipment to allow control and monitoring of the experiments. This equipment is explained in detail in appendix A.3. It is also shown graphically in the drawing IFD-01-01.

- Piezoelectric pressure transducer in the HP reservoir and explosion chamber.
- Conventional pressure transducer in the HP reservoir. Not connected to the acquisition system.
- High-speed camera with telecentric lenses and light source that produce shadowgraph footage of the point of impact.
- Pneumatic system to actuate the release valve.
- Signal amplifier for piezoelectric transducers and data acquisition module

The essential components are shown in Figure 4-1, Figure 4-2 and Figure 4-6. A description of the principles for pressure transducers is found in 2.3.2.

### Piezoelectric pressure transducers

The piezoelectric transducer in the HP reservoir is, as mentioned above, mounted in the connection block with a location and orientation that gives a straight line into the pressure reservoir. This is done to ensure as fast response as possible. Approximate distance between the piezo transducer and the closest end of the reservoir is 16 cm. 46 cm is the distance between the transducer and the inlet to the release valve.

The transducer in the explosion chamber is mounted in the side wall of the chamber, 60 mm above the vertical centre and 30 mm from the edge of the side wall. This gives an approximate distance of 200 mm from the nozzle outlet, depending on the configuration. The angle between the jet vertical “jet flow line” and the transducer is 60 degrees. The narrow part of obstruction objects A and B will thus partially shelter from direct approaches of possible reflected shock waves from the centre of the obstruction objects.

An amplifier is used to transform the signal from the minor capacity difference initially measured, to a more useful voltage signal. The magnitude of the amplification is decided by the necessary pressure range for the transducers. Section 4.8.1 describes the settings used in this setup. The amplifier is triggered by a signal from the data acquisition module, thus limiting drift off before the experiment is conducted.

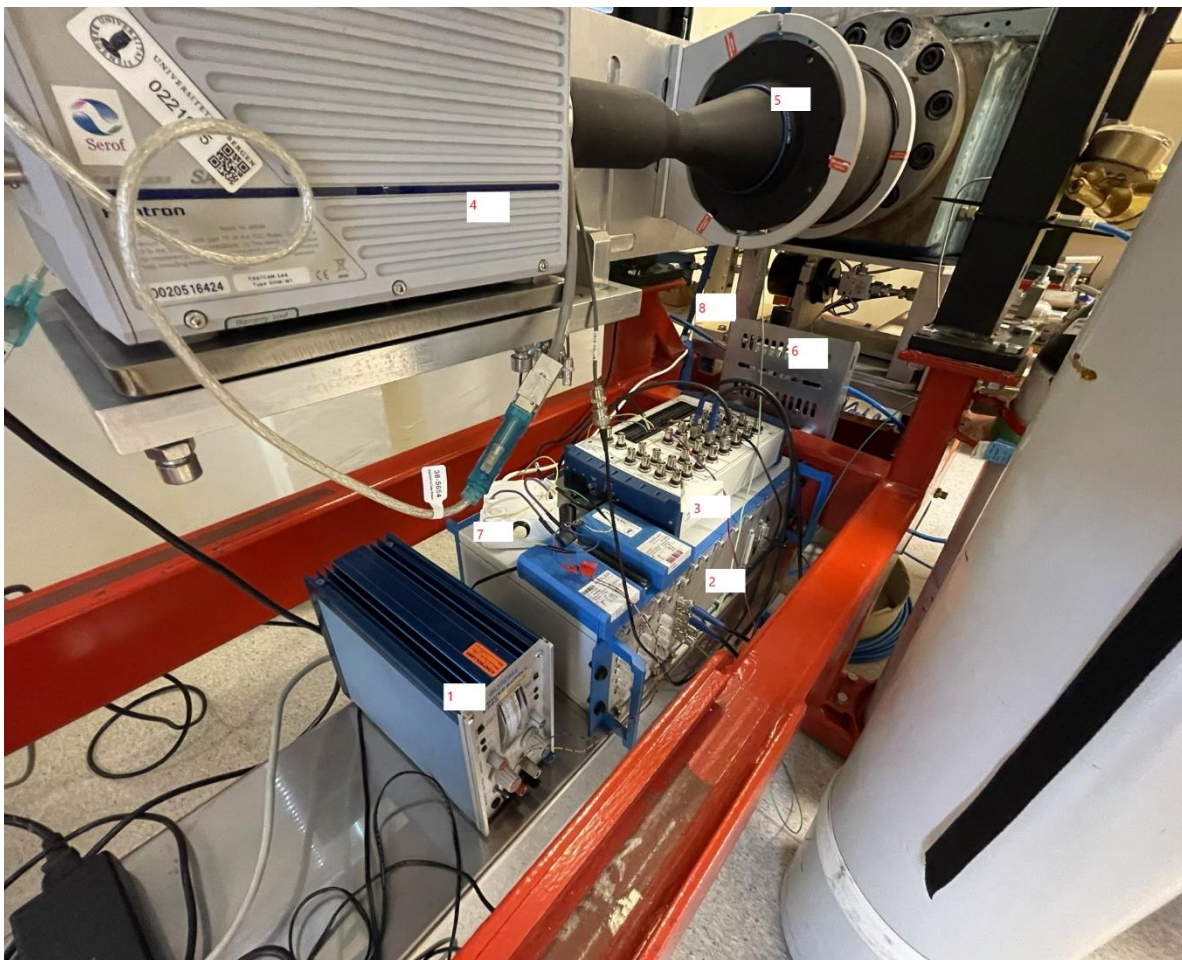


Figure 4-6: External power source to release valve solenoid (1), amplifier for piezoelectric transducers (2), data acquisition module (3), high-speed camera (4), telecentric lens, camera side (5), pressure regulator for instrument air, hidden behind cable tray (6), manual control of solenoid for release valve (7), and solenoid valve for release valve, hidden behind wooden bracket (8).

A conventional digital pressure transducers is installed in the HP system to allow monitoring of the pressure on a continuous basis. This was for instance necessary during pressurisation of the system to get more precision than provided by the coarse manometers on the pressure regulators. This digital transducer measures absolute pressure.

#### High-speed camera and lenses

The high-speed camera and its corresponding lenses are installed to view the area where the release and impact on obstruction objects occur. It is equipped with a telecentric lens. This in combination with another telecentric lens equipped with a point light source at the opposite side of the chamber form a shadowgraph system. Shadowgraph pictures enable observation of shock waves, hydrogen gas and jet discs. Theory about the principles is presented in section 2.3.1.

The camera, a Phantom SA4, records in black and white, at a maximum resolution of 1024x1024 for frame rates up to 3600 fps. 768x768 is available at 6750 fps. The camera communicates directly with the computer, and the footage from the experiments is viewed and processed directly in the belonging software. This software is used to set up the camera before recording, initiate recording and process the footage afterwards. Further details about the camera settings and processing methods used in this project are given in section 4.8.1.

## 4.3 Safety considerations in design and experimental work

Storage and handling of compressed hydrogen imply hazards, partly due to the relatively high pressure, but in particular due to the large amount of chemical energy that could be released in the event of loss of containment followed by immediate or delayed ignition. Some of the safety-related properties of hydrogen are particularly challenging, including the ignition sensitivity, the wide flammability range, and the high reactivity. At the same time, this aspect represents the main motivation for the present study. This section outlines the safety measures incorporated in the experimental work, including design considerations and procedures.

### 4.3.1 Inherent safety features in the design

- The volume of the high-pressure reservoir is kept low; a 150 ml reservoir plus a small volume in adjacent tubing.
- In all tubing sections where high flow was not an important aspect related to the experiments, a tubing with  $\frac{1}{8}$ " OD is used. The ID of this tubing is only 1.5 mm, this limits the potential of a leakage either directly on the tubing or in downstream equipment.
- All components on the high-pressure system had a higher design pressure than the maximum available pressure on the gas bottles; a sudden pressurisation of the system to full bottle pressure would therefore not entail any danger.
- No possibilities for physical isolation of the blowdown pipe. At least not without substantial effort. Thus, no risk for dangerous pressure build-up following hydrogen release and possible subsequent ignition into an erroneously closed explosion chamber and blowdown pipe.
- Two independent possibilities for depressurisation of the high-pressure section to safe location: Either through the conventional release valve, or via manual valves and a hose into the blowdown pipe. The latter alternative is referred to as "backup depressurisation line" in the drawings and documentation.
- The used materials, mostly stainless steel 316 and some carbon steel, are well suited for hydrogen service in the pressure range they are exposed to.
- The location of the lab provided a certain level of inherent safety; the buoyancy properties of hydrogen made the rooftop location ideal, as a hydrogen leakage would rapidly flow away from



potential dangers on ground and building level. This location at the top of the building also reduced the consequences of structural damages from an eventual explosion.

- A permanently connected nitrogen bottle with regulator enabled easy displacing of combustible hydrogen gas from the HP system before any work that required splitting of the system.
- Permanently connected air supply to the explosion chamber enabled displacing of un-combusted hydrogen and combustion products before splitting of the blowdown pipe.

#### 4.3.2 Procedural safety features

- Checklists and procedures were made to ensure that important safety related actions were made before, during and after sessions of experimental work. These procedures are attached in appendix C.
- The blowdown pipe exit was located at a rather inaccessible point at the rooftop. In addition to this, the area near the outlet was also blocked with barrier tape during the experiments.
- The doors from the laboratory and out to the rooftop as well as the door from the hallway were kept open during experiments and other types of work that increased the potential for leakage. Two open doors in addition to the pressure provided from the HVAC system in the building provided a substantial air flow through the room, thus diluting potential leakages.
- The gas bottles were always kept closed at the bottle valve, except the short times when the system was pressurized.
- Thorough commissioning and leak testing before hydrogen was introduced – as described in section 4.4.
- The computer where the experiments were set up and initiated from stood a fair distance away from the experimental equipment. It was also placed so that the person controlling the computer could get into a corner behind the fireproof gas bottle cabinets with just a small step back from the computer. The 10 second delay from initiation of the experimental sequence to the actions occurred also made it easy to leave the room if this was considered necessary.

## 4.4 Commissioning activities

After the experimental setup was assembled according as described above, several tests were performed to ensure that the system was safe and ready for operation.

### 4.4.1 Leakage tests

Leakage tests were performed in steps, adapted to the progression in the commissioning and experimental work. The purpose of these tests was to verify that the experimental setup was leak tight at all stages of the experimental work. A leak tight system is a prerequisite for safe handling of hydrogen. Thus, proper leak testing is an important tool to ensure the safety of all involved parties.

#### Initial low-pressure test with air

After assembly, air was temporarily connected to the HP system in the location where the backup depressurisation line is usually connected. Air was used for safety reasons, as the low pressure on the plant air system would cause less damage than the high pressure provided by the nitrogen bottle. Even though this nitrogen pressure was controllable through the regulating valve, it was inherently safer to use a pressure source with lower potential.

The system was pressurised up to the available air pressure of approximately 7.6 bars. Then all potential leakage points; threaded connections and fittings were coated in a rich soap/water-mixture. Due to its polarity properties, a soap film will produce bubbles if air flows through it. This method made it easy to spot even minor leakages that was undetectable through sound and feeling. Figure 4-8 shows an example

of a minor leakage found with bubbling soap film. Minor leaks were sealed by applying more torque to the fittings.

When no further leakages could be observed through soap bubbles, a holding test was performed to ensure that the system was properly sealed. This test would also indicate internal leakages through the valves, as this would give a significant pressure decrease without visible external leakages. The test was performed by pressurising the system to the maximum available air pressure, then isolating the air supply and waiting approximately ten minutes.

#### **Initial high-pressure test with nitrogen**

After the system had proved to be tight at low air pressures, nitrogen at higher pressures were introduced to the system. The procedures with soap bubble and holding tests were repeated with a nitrogen pressure of 100 bars, which was the maximum available. Experiments with nitrogen were then performed, as further described in 4.5.

#### **Leakage test before first introduction of hydrogen**

Prior to first introduction of hydrogen, the full setup was leakage tested with nitrogen. As the hydrogen tubing was not connected until the initial nitrogen tests was finished, a complete leakage test of the hydrogen supply system was not feasible earlier. The full system was leakage tested with nitrogen, flowed in the opposite direction into the hydrogen system, all the way to the closed bottle valve. The volume was confined according to the valve positions in Figure 4-7. The hydrogen pressure regulator (01-PCV-101, as shown on P&ID-01-01) was set to a higher pressure than the maximum test pressure to ensure that it remained open during the full test. Then nitrogen was supplied into the system, thus streaming the opposite direction into the hydrogen system, all the way to the closed bottle valve.

At this point, all potential leakage points were coated with soap film once again. When no leakages could be observed, a 30-minute holding test was performed.

After the leakage test with nitrogen, the system was pressurised with hydrogen in a controlled manner. Then, a similar holding test was conducted with hydrogen. The results for both nitrogen and hydrogen holding tests are shown in appendix B.2.

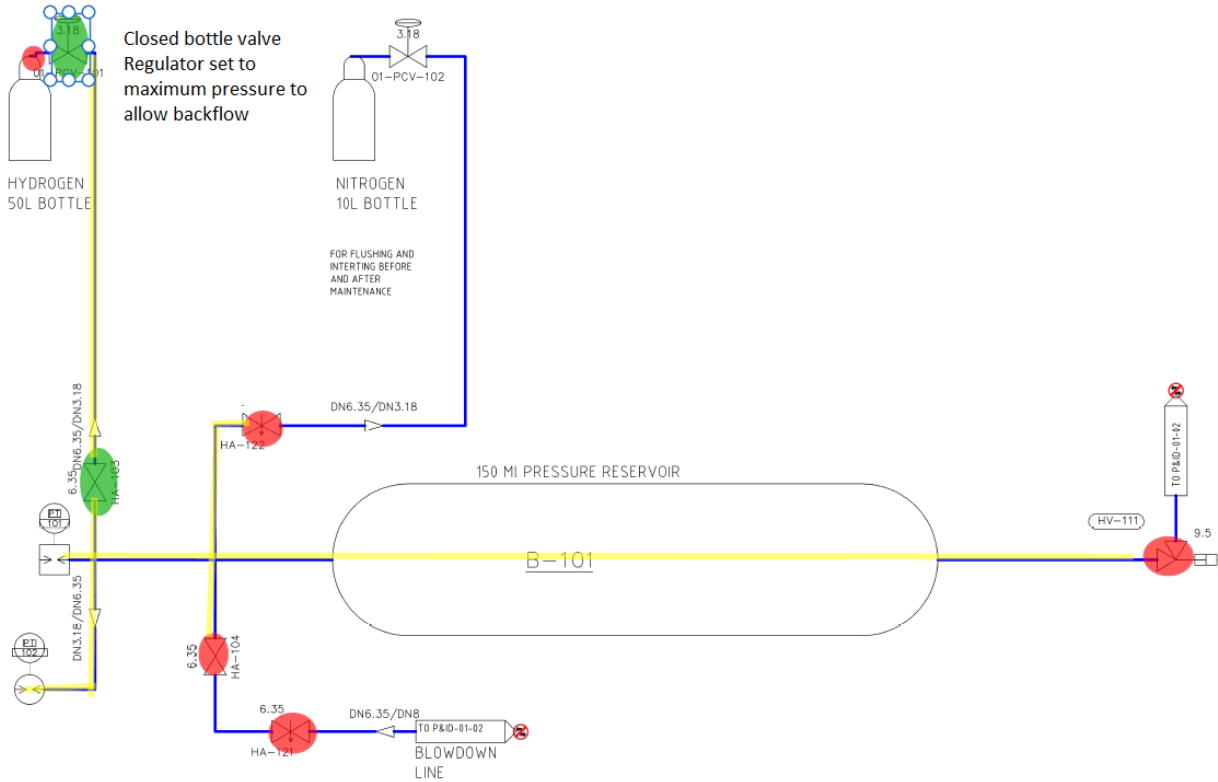


Figure 4-7: The line-up used for both full and simplified leak tests. The yellow marking indicates the volume included in the leak test, red marking indicates closed valves, green marking indicate that the valve should be open. The drawing is based on a section of P&ID-01-01.

### Simplified leak tests

Throughout the experimental phase, some minor modifications to the high-pressure system were occasionally required. For instance, when the hydrogen gas regulator was replaced by a needle valve to allow higher pressures than the regulator could deliver. After each of these modifications, a simplified leakage test with 100 bar nitrogen were conducted with a holding time of at least 5 minutes. The confined volume for these tests were as shown in Figure 4-7.



Figure 4-8: An example of two minor leakages identified with bubbling soap film at approximately 100 bar nitrogen pressure.

#### 4.4.2 Initial setup and verification of instrumentation

After the Initial low-pressure test with air, the instrumentation were set up and adjusted, and a few “dry runs” with only air pressure were performed to see that the valve opened when it should, and that both the camera and the piezoelectric amplifier was triggered by the signal in the test sequence. An initial assessment of the timing for these recordings were also made. It was verified that the *Test logger* program produced a readable file with correct meta data and logged values.<sup>5</sup> It was also verified in this stage that the camera images had decent quality, and that cropping, and storage of this footage worked as intended. Section 4.8.1 describes the selected settings for timing, measuring ranges, etc.

By holding a lighter against the nozzle exit in the open chamber in an attempt with low pressure air, the camera’s ability to show visible flames as well as density gradients were tested. Section 5.1 presents and discusses the results from the tests.

### 4.5 Reference tests with nitrogen through the release valve

After the assembly, a series of experiments with nitrogen were performed. This ensured a proper functional testing of the setup, but most important – it gave a series of videos and pressure data for nitrogen jets with different release pressures. These could later be compared to hydrogen jets under identical pressure and obstructing object conditions. All experiments were done with obstruction object A at 13.6 mm distance. A total number of 14 experiments were conducted with nitrogen – at pressures between 11.6 and 101.1 bar $a$ .

All these experiments were performed following the same procedure. The only difference was which pressure the system was pressurised to before the release. The first step when the system was pressurised, was to open the isolation valve from the nitrogen supply into the system (HA-122 on P&ID-01-01).

---

<sup>5</sup> Low pressure air release only resulted in significant changes in the values from the transducer mounted in the HP-reservoir, but live values from only one transducer was sufficient to verify the functionality of the program and its output.

Then, the bottle valve was opened, before the system pressure was gradually increased by adjusting the regulator until the desired pressure was achieved. Then, a final verification of settings and recording equipment was done before the experiment was initiated. Settings related to the instrumentation is described in 4.8.1.

## 4.6 Testing with hydrogen through the release valve

The main batch of experimental work was related to investigation of hydrogen releases in a longer time frame. This was done by conducting experiments where hydrogen was released through an air actuated needle valve, usually referred to as “the release valve”. With some exceptions, all these experiments were conducted with obstruction object A. Three different distances between the object and nozzle were investigated, namely 7.9, 13.6 and 19.5 mm. In addition to these experiments, a small series were also made where the threaded end of the connection rod was used as obstruction object. Another series without any obstructions were also done.

Pressures between 10 and 166 bara were investigated, but the full pressure range was only investigated for obstruction object A at 13.6 mm distance. The other objects and distance settings were primarily investigated in the range near the maximum available regulator pressure of 100 bars. Four out of 43 experiments with hydrogen and release valve were conducted without the regulator. The regulator was replaced with a needle valve during these experiments. Pressures up to the available bottle pressure at the time were investigated in these experiments.

It was not necessary with any mechanical work between each experiment, if obstruction object type and position remained unchanged. Thus, all experiments with the same obstruction object conditions were, as far as possible, done successively.

The explosion chamber was flushed with air from the permanently connected air supply between each experiment. This was done to dilute and displace hydrogen and potential combustion products from the last experiment. The HP reservoir was also flushed between each experiment to remove potential air that could have diffused into the system through the release valve at the end of its opening cycle during the experiment. The flushing was done by first pressurise the system to a few bars, then depressurise it through the backup depressurisation line.

After this, the system was pressurised to the desired pressure. After a verification of the settings on the recording equipment as well as valve positions on the setup, the next experiment was triggered. To ensure precise and safe methods, the checklists presented in appendix C were followed.

Parts of the operation described in 4.7 were conducted when the obstruction object itself or its position had to be changed. But it was not necessary to loosen and remove the lid to get access to the obstruction object. Figure 4-9 and Figure 4-10 show the state of the blowdown pipe when the obstruction objects were accessible through the pipe on the chamber lid.



*Figure 4-9: The lid of the 20-litre explosion vessel and the blowdown pipe, with the axial expansion joint removed.*



*Figure 4-10: The connection rod installed in the transverse steel beam – the socket wrench operates the set screw fixing the connection rod to the beam.*

## 4.7 Experiments with hydrogen release through rupture discs

A total number of 14 experiments with rupture disc were conducted. In these experiments, the release was initiated upon the burst of a rupture disc, resulting in an abrupt leakage with subsequent shock waves. The purposes of these experiments are described in section 4.1. A nozzle assembly that included a rupture disc holder were inserted instead of the conventional hydrogen nozzle. This is described in section 4.2.1. The release valve was also used in this experiment to time the bursting of the rupture disc, thus ensuring that the event was recorded in the data acquisition system.

The rated rupture pressures for these discs were altered; five had 100 bars, five had 80 bars and the remaining four had 50 bars. A variety of obstructions and distances were also used, Obstruction objects A, B and C in addition to a few experiments with either no obstructions, or the straight side of the connection rod. The distance to the obstruction objects was altered in the range between 10 and 30 mm. To get as much information as possible from each of the few experiments that were conducted, the setup for each experiment was determined through ongoing assessments as observations were made.

As a result of the design, the blowdown pipe and explosion chamber lid had to be partially dismantled to replace the rupture disc between each experiment. This was done by disassembling the flanges in each end of the axial compensator and remove this. The bolts in the flange in the opposite end of the first pipe spool also had to be loosened, but not removed. A jack strap supported the weight of this pipe spool during the whole operation. Figure 4-9 show the setup at this point. After the axial compensator was removed, the bolts in the chamber lid were removed, and the chamber lid was lifted partly aside, thus

providing space to operate a socket wrench on the burst disc holder as well as cleaning the lenses and removing any debris with pressurised air.

With a new rupture disc in place, the next step was to flush the system all the way up to the rupture disc to displace possible contaminating air that could have entered the small volume between the closed release valve and the rupture disc after the previous experiment. This flushing was performed by locking the release valve open, and then pressurise the system to approximately 30 bars, before the volume was depressurised to ambient pressure via the backup depressurisation line. This operation was repeated three times to ensure that the potential level of contaminating air was negligible.

After the last depressurisation, the system was once again pressurised to approximately 30 bar before the release valve was closed, thus leaving 30 bar in the segment between the valve and the rupture disc. This was done to have as large and consistent molar volume present in the HP-reservoir in each experiment. Although the volume between release valve and rupture disc was small, this pre-pressurising of the segment reduced the pressure drop in the reservoir from the valve opening was initiated until the disc burst.

The reservoir was pressurised to 100 bars for all experiments where 50 and 80 bar discs were used. But when the 100 bar discs were used, the pressure was increased to max available bottle pressure, which was between 170 and 180 bars at the time these experiments were conducted. As for the experiments with more than 100 bars with the valve-only setup described in section 4.6 above, the regulator was replaced with a needle valve to facilitate these elevated pressures.

## 4.8 Data recording and interpretation

### 4.8.1 Camera and transducer settings

The frame speed on the high-speed camera was adjustable. In this project, 3600 fps was used for experiments where release through the valve alone was investigated. 3600 fps corresponds to time increments of 0.27 ms. This was the fastest frame speed that allowed maximum resolution of 1024x1024 pixels. Each recording had a duration of 1.515 seconds at the selected frame speed, thus producing 5457 frames in each recording. Shutter time was set to correspond to the full frame duration to give as much light in the pictures as possible. Some details about the used setup are shown in the meta data presented “on screen” in Figure 4-11.

For experiments with rupture discs, a faster frame speed was used. The selection of frame speed for these experiments were a compromise between field of vision and light intensity on one side and time steps between the frames on the other. Most of the rupture disc experiments were performed with a frame speed of 6750 fps, which corresponds to 0.15 ms per frame. On this setting, the camera delivered recordings of 1.43 seconds, containing 9701 frames [110]. This velocity allowed a resolution of 768x768 pixels, which covered an acceptable area around the nozzle exit and obstructing objects. Further details about interpretation methods are given in 4.8.2 and additional details about the camera and corresponding software are given in appendix A.3.2.

The “Test logger” program provided the opportunity to trigger the different components individually at suitable times during a common sequence triggered manually by the test personnel. The settings presented in Table 4-1 were used for all experiments:

For the pressure recordings, both the sample rate and the recording duration could be adjusted in the “Test logger” program. Further details about this program are provided in appendix A.3.5. A sample rate of 100 000 Hz and duration of 2 seconds were used in this project, producing a total of 200 000 samples for each of the two piezo electric transducers and the indicator for valve actuation for each experiment.

As Table 4-1 shows, there was a 100 ms time difference between the initiation of the amplifier to the time when the recording started. This was done to avoid that potential noise generated during the initialisation affected the logged results.

Table 4-1: Start times and duration for the actions initiated in the experimental sequence on "Test logger".

Description of activity	Activity start	Activity end
Test sequence (manually initiated by test personnel)	0	15
Initiation of amplifier for piezoelectric readings	9.8	11.8
Data acquisition active	9.9	11.9
Camera recording <sup>6</sup>	9.9	11.9
Activation of release valve	10.0	12.0

Both piezoelectric transducers had a range from 0-250 bars. However, use of the full available pressure range for the transmitters would give unnecessary low resolution for transducers that could not possibly be exposed to such high pressures. By adjusting the amplification through the amplifier, it was possible to achieve higher resolution for the logged data, as a wider span of the available voltage signal was used. Table 4-2 shows the used ranges for this project. As the table show, the transducer in the explosion chamber was initially set to a relatively wide range. This range was eventually narrowed down when experience about pressure development for ignited leakages was obtained.

Table 4-2: Measuring ranges for the pressure transducers

Location	No. of experiments	Pressure range [bar]
Explosion chamber, piezoelectric transducer	1-69	0 - $\pm 20$
	73	0 - $\pm 2$
	74-87	0 - $\pm 3$
HP-reservoir, piezoelectric transducer	All experiments	0 - $\pm 200$
HP-reservoir, digital manometer	All experiments	0 - 200

#### 4.8.2 Measurements and interpretation on the high-speed images

The software used to control the high-speed camera had a built-in tool to make measurements on the pictures. The tool initially measured in pixels. The program also had a built-in calibration function to convert pixel counts to distance measurements. Since the camera was equipped with a telecentric lens, the relation between pixels and distance was constant independent of the distance between the object and the lens. The diameter of the hydrogen nozzle was used to calibrate this function, as it had a constant value of 12 mm, as annotated in MECH-02-01. 12 mm corresponded to 177 pixels in the picture frame, as shown in Figure 4-11. The conversion was done manually in most cases based on the same method as the built-in conversion. Both methods gave satisfying precision.

---

<sup>6</sup> The duration of the camera recording is dependent on the selected frame speed and other factors that are adjusted directly in the camera software. Thus, the camera will not end the ongoing recording when the triggering signal is ceased. In the currently used setup, the recording nevertheless ends before the trigger signal ceased.



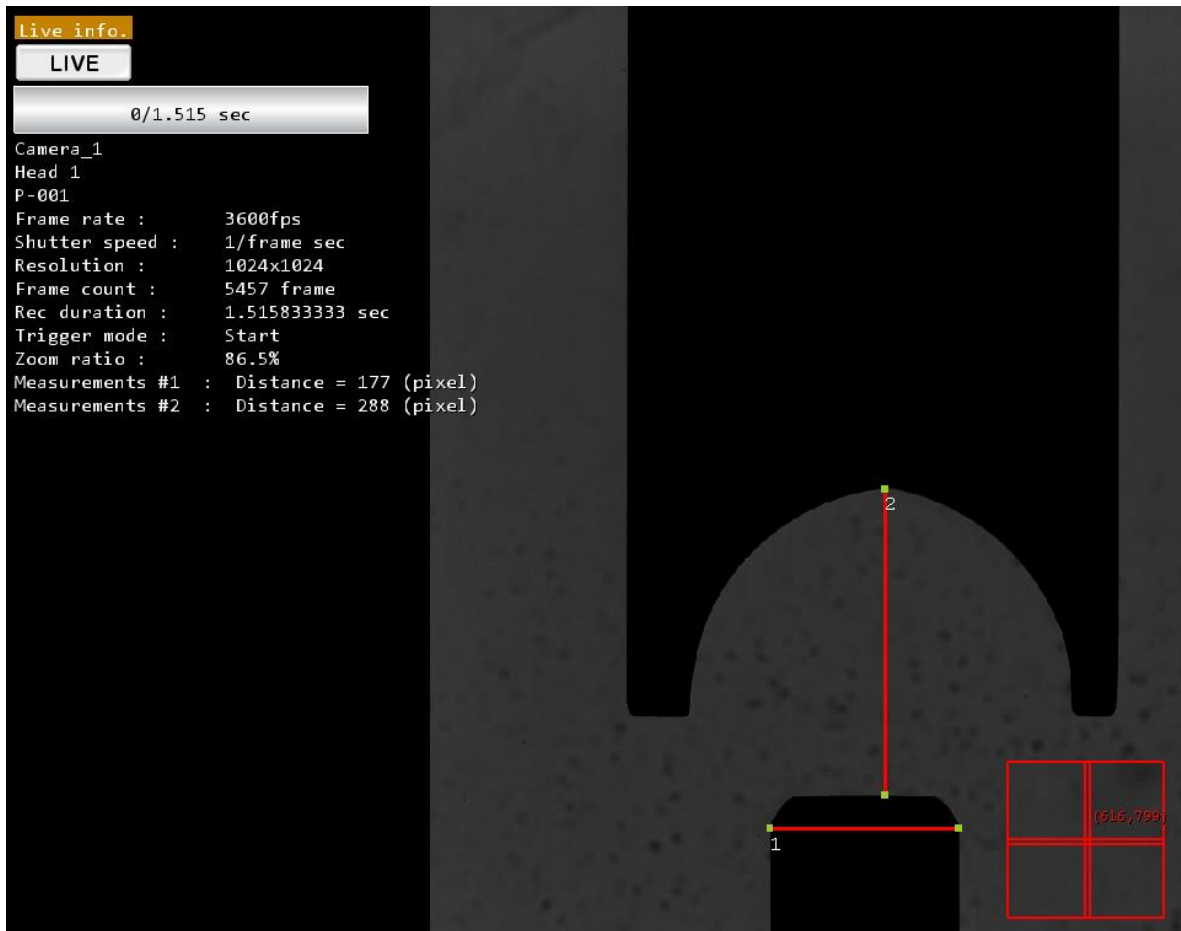


Figure 4-11: An example of the built-in measuring tool in the camera software. The 12 mm nozzle fills 177 pixels of the picture frame. The marker tool shown in the lower right corner enhances the picture beneath, thus making it easier to define precise endpoints.

To compensate for a slightly darker picture at 6750 fps compared to the footage with 3600 fps, a built-in tool in the camera software called *High dynamic range* (HDR) was used on its most moderate setting. This tool enlightened the dark sections of the pictures.

HDR and the described measurements were the only tools in the PFV 4 software that were used systematically. Visual interpretation of the footage was the primary analysis method. Relevant parts of the recording were watched multiple times at low replay speed to look for signs of ignition and map the jet development.

In addition to this, a script for analysis of the pictures in MATLAB was also used. This script helped to highlight the gradients in a single picture or a selected sequence of pictures from the recording. The gradients, initially shown as variations in the grayscale of the picture was coloured according to a colour code scheme in this MATLAB script. The script produced a conventional 2D figure with only boundary outlines as well as a movable 3D representation of the picture.

### 4.8.3 Calculations and plotting based on data from piezo electric sensors

The *Test logger* program used to control the experiment generated a .txt file from each experiment, containing all sample points from the two piezo electric transducers in addition to the voltage signal used to monitor release valve opening. The data were organised in separate rows. A script based on JavaScript programming language were used to convert these files to .csv format and add a column with timestamps for each row of datapoints as this was missing in the data produced by the *Test logger* program.

Further processing and preparation of the data as well as comparison and visualisation (plotting) were done with Pandas and matplotlib, which is packages available to the Python programming language. The programs were run on a Jupyter Notebook, which allowed development and execution of code from the same window. The following parameters were calculated based on the initial data:

- Pressure difference calculations for running 1 ms intervals were done for the pressure in the reservoir. This pressure difference served as a simple indication of the slope of the reservoir pressure curve. The difference pressure values were added as a new column to the data frame that originated from the .csv file generated above. The differences were assigned to the middle of their span. Thus, each slope value showed the difference between the pressure measured 0.5 ms later and 0.5 ms earlier than the time of the pressure value on the row it was assigned to. The calculation was done in a script where a function, called “slopeadder” looped through all rows in the file, calculated the difference and appended it to a list. To avoid errors for the 50 first and last columns of the file for which one of the compared indexes did not exist, an IF condition sets the difference value for these rows to zero. When the function had looped through all the rows, the generated list was appended as a new column to the initial data frame based on the .csv-files. The new, extended data frame was saved as a separate .csv file, thus leaving the source file unchanged. The “slopeadder” function was called up from a for-loop that looped through a specified list of files for efficient data treatment for all experiments.
- A simple function found the lowest (e.g. highest negative value) value in the pressure difference column. It returned both the value of this largest difference as well as its timestamp and the logged pressure in the reservoir at this moment. It also returned the time for when the release valve was initiated. This script worked on a single, manually specified file at the time.
- Another program added two columns to the data frames it processed. One column showed the current pressure in the reservoir for each row. This value was calculated by subtracting the minimum value in the column from the current value at the current row. The minimum value should ideally correspond to the difference between the initial pressure and the atmospheric pressure in absolute pressure. Thus, the calculated pressure difference corresponded to the current (over)pressure in the reservoir [barg]. The other column contained the corresponding standard volume flow rate for the calculated pressure difference on each row, based on Eq. (11). These two columns were made in a separate function for each. The “pressureadder” function made the column with current pressure in the same manner as the “slopeadder” function described above but did not need an IF function to omit first and last 50 rows. A function called “calcflow” calculated the volumetric flow rate in the exact same way as for “pressureadder” described above. The new extended data frame with two new columns was saved as a new file. Both functions were called up from a for-loop that treated all files in a specified list. This program was only used on the datasets from a few experiments where it was of interest to evaluate these values.
- A number of different plots were produced to analyse different aspects about the experiments. These plots were generated in matplotlib, also through Jupyter Notebook. The formatting was adjusted for each case to make the plots as informative as possible. The same method was also used for the single 3D-plot that was generated.

# 5 Results and discussion

## 5.1 Visibility of gases and flames

Section 4.4.2 describes some initial tests conducted to verify that the images had sufficient quality and that the shadowgraph system was able to detect variations in pressure and gas density. Figure 5-1 and Figure 5-2 shows the result from the test with a lighter.

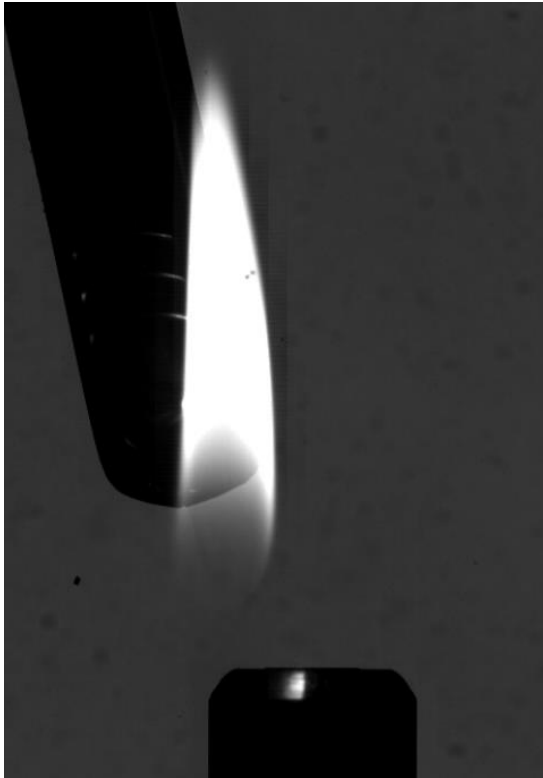


*Figure 5-1: The flame from a lighter visualised by the shadowgraph system and the high-speed video camera.*

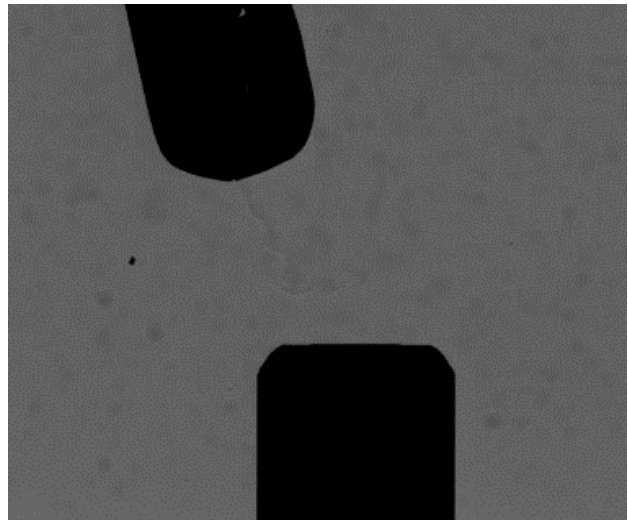


*Figure 5-2: Unignited gas from the lighter visualised by the shadowgraph system and the high-speed video camera..*

Figure 5-1 shows that the laminar diffusion flame from a lighter is clearly visible on the shadowgraph pictures. The lighter gas was also visible in unignited state, as seen in Figure 5-2. It might be a bit hard to see, but the figure shows a lighter gas flow with a shear layer that forms vortices. Unfortunately, it was a lot of background noise in these early experiments. The background noise is seen as darker spots in the open parts of the camera field. However, the shear layer was easy to detect on a moving film due to its movement compared to the static background noise.

As nitrogen has a density very close to the mixture density for the ambient air, it was not visible on the shadowgraph pictures unless it had pressure gradients caused by jet structures or similar.

Unignited hydrogen on the other hand, was visible on the system as it is much lighter than the ambient air. However, the hydrogen did not look like the lighter gas in Figure 5-2, at least not when released with high velocities as it was in this thesis work. Hydrogen produced instead a cloud with a wave pattern similar to the shadows of waves displayed at the seabed below clear, shallow water. This observed pattern was most likely because all cases with released hydrogen in this thesis work was of turbulent character, thus gave uneven mixtures at the boundary between the hydrogen and ambient air. The pattern is observable on Figure 5-11 as a cloud that encapsulates the nozzle and obstruction object. At the

moment displayed in the figure, the cloud seized the lower half of the picture. A yellow dotted line indicates the boundary, but the boundary has a smoother transitional character.

Observations made later in the experiments indicate that flames were visible as large scaled gradients with a turbulent pattern. This is for instance showed in Figure 5-18. The flames were also moving fast in the video recordings. However, they were not differentiating in colour, as the lighter flame in Figure 5-1 is. As the flames looked similar as other pressure gradients expect from their size, it is possible that marginal, unsustained ignitions was not possible to detect.

A possible explanation to why the flames observed during the experiments appeared so differently compared to the lighter flame, could be that hydrogen combustion emits less light in its combustion compared to hydrocarbons due to low concentration of particles and soot. A lower amount of emitted light in combination with a more distributed combustion caused by the turbulence and premixed character thus resulted in weaker and more diluted illumination.

## 5.2 Flow rates and jet properties

The experiments yielded a lot of information about flow rate and jet characteristics. Even though this was not the primary objective to investigate in this thesis work, a study of these data and comparison to literature and empirical calculations when possible – could give a useful indication of the behaviour of the hydrogen during abrupt releases.

### 5.2.1 Calculated flow rates compared to empirical flow values

The flow rate through the release was calculated based on the running one ms pressure difference in the pressure reservoir, as described in section 4.8.3. The calculations were based on Eqs. (6), (7), (8). Current inlet pressure was also calculated based pressure differences observed throughout the experiment, as explained in section 4.8.3. In order to get an overview of the potential in the release, the maximum flow rate was found for all experiments. Figure 5-3 shows the flow rate plotted against current upstream pressure for all experiments, including those with nitrogen. The figure also contains the calculated flow at choked conditions through the  $\frac{3}{8}$ " valve, for nitrogen and hydrogen flow.

Maximum flow correlates well to the pressure it occurs at, which is illustrated by the trendlines and the corresponding  $R^2$  values. The proportional fit for the rupture disc experiments is disturbed by the outlier experiment 73, observed as the most intensive result both regarding volume rate and pressure. This outlier is further discussed in section 5.6.

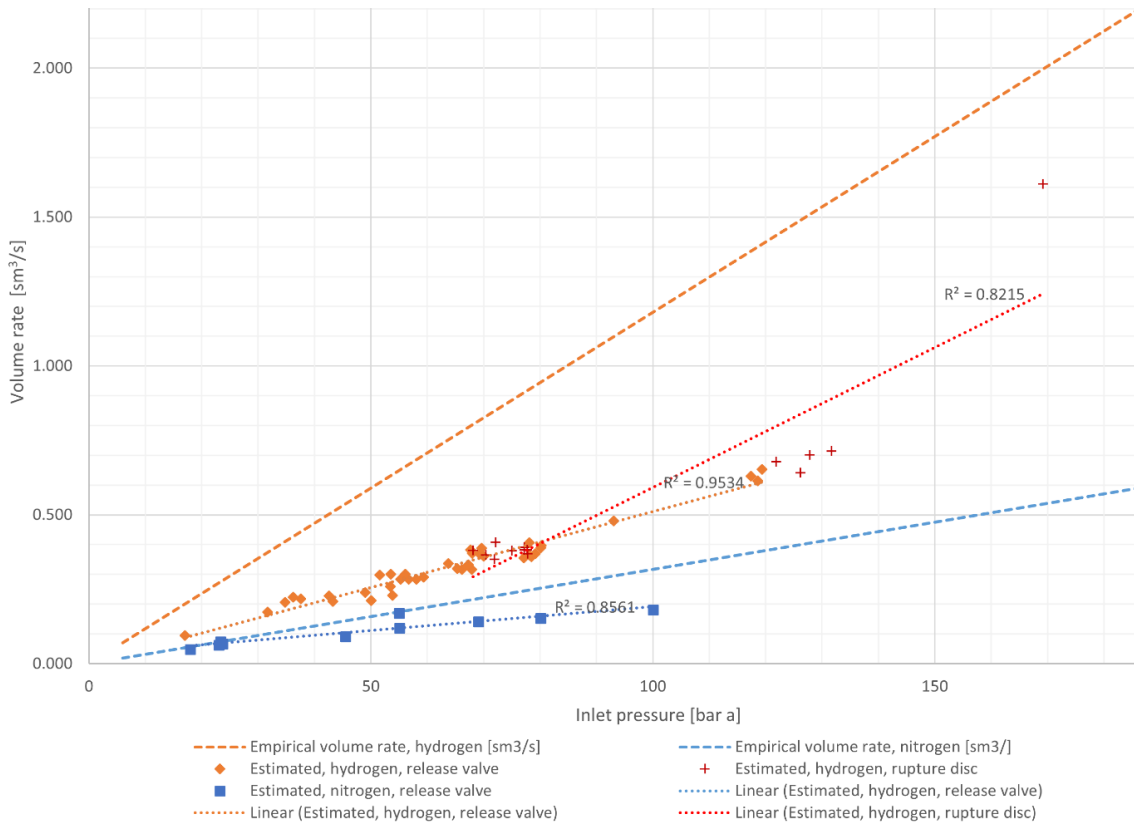


Figure 5-3: Calculated flow for the moment maximum pressure change rate in all experiments. Compared with empirical values for choked flow conditions in the 3/8" valve. The lines with empirical values are from Figure 2-5.

Figure 5-3 also shows that the observed maximum flow rate correlates to the empirical values for choked flow. However, the observed maximum for hydrogen seems to be only 40 % of the value for the empirical flow rate at the corresponding pressure. For nitrogen, this relation seems to be approximately 67 %.

Calculated volumetric flow rates for the full duration of the experiment is plotted for some selected hydrogen experiments in Figure 5-4. Experiments with release valve as well as rupture discs are included in the plot:

- Test 42: Release valve experiment with 104 bara initial pressure
- Test 73: Rupture disc experiment with a 100 bar rated disc, and 179.7 bar a initial pressure. This was an outlier experiment, which is further discussed in 5.6.
- Test 74: Rupture disc experiment with a 100 bar rated disc and 177.5 bar a initial pressure.
- Test 85: Release valve experiment with 166.4 bara initial pressure.

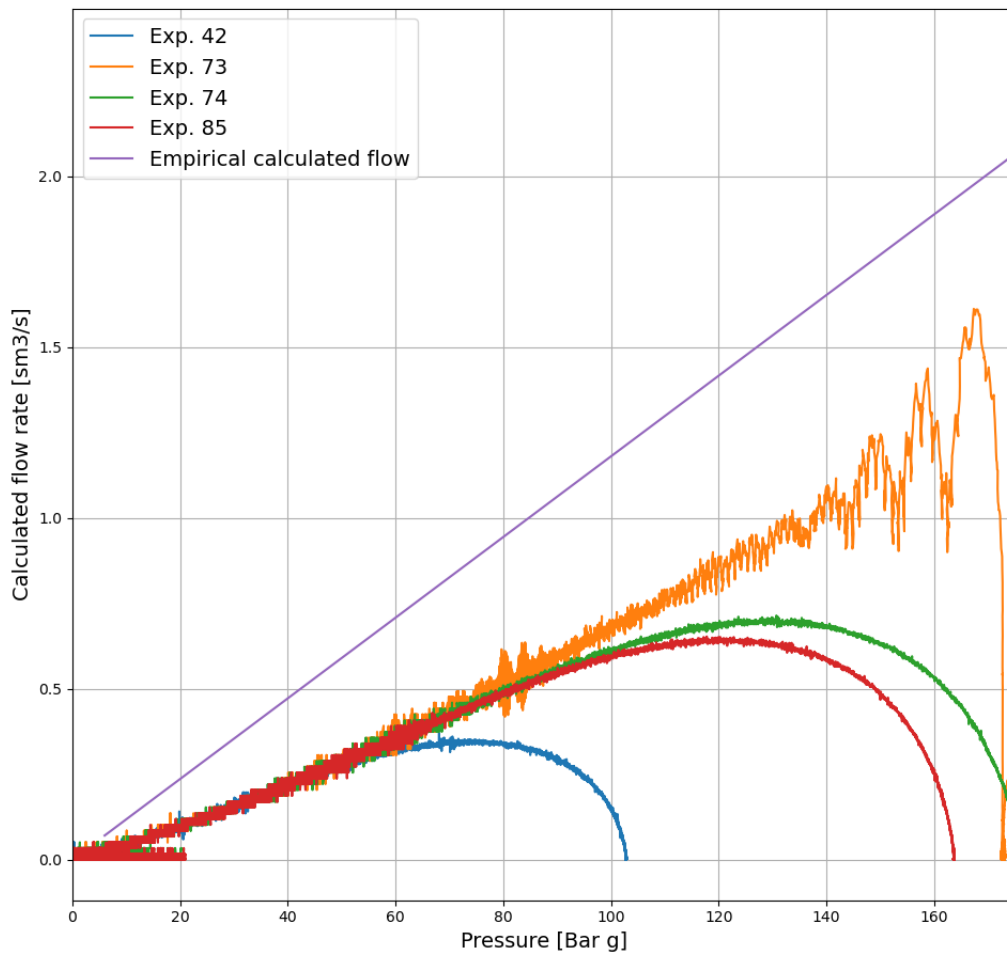


Figure 5-4: Flow rates calculated based on pressure gradient in the hydrogen reservoir for some selected experiments. The curve with empirical values for choked flow through the  $\frac{3}{8}$ " valve is added for comparison. Empirical values initially found in Figure 2-5.

Figure 5-5 shows the calculated volumetric flowrate for the full duration of experiment 25, which was a nitrogen experiment with an initial pressure of 101 bara. The trendline for empirical calculated flow at choked conditions is included for reference.

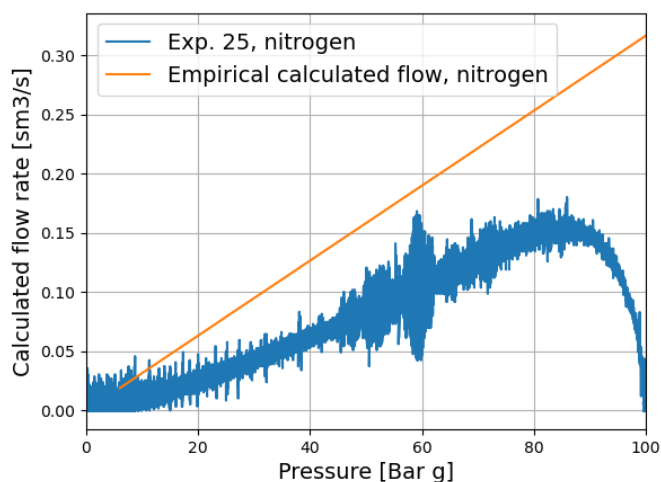


Figure 5-5: Flow rates calculated based on pressure gradient in reservoir for a nitrogen experiment. The curve with empirical values for choked flow through the  $\frac{3}{8}$ " valve, from Figure 2-5 is added for comparison.

The linear section of all flow rate trends in Figure 5-4 seems to correspond to slightly above 50 % of the empirical calculated value at the same pressure. The linear section of the nitrogen trend seems to correspond to just below 60 % of the empirical values.

#### Transducer drift-off apparent in the hydrogen plot

The part of the plots in Figure 5-4 that show increasing pressures at nearly zero flow was caused by drifting values from the piezoelectric transducers at the end of the logging. As the plot show the full datasets, and not only section with significant flow values, the drift-off is visible in the plot. The transducer drift-off appeared to increase throughout the experimental work, so that the latest experiment, such as the shown Test 85, showed up to 20 bar pressure increase after the minimum value had occurred. However, the absolute values of the minimum pressures at the end of the depressurisations corresponded well to the logged initial pressure for each experiment. Thus, it is evident that drift off was not a problem in the interesting parts of the logging.

As the flow rates are calculated based on the absolute value on the pressure difference, transducer drift off at the tail of the plot could yield falsely displayed flow rates. However, the pressure gradients in the drifting section of the plots were small. A 20 bar drift during some 1.7 seconds should be easy to single out from even the tail of the depressurisation, which typically last for 300 ms with a significantly larger pressure difference.

#### Influence of valve opening time on maximum flow rates

It is possible that the definite opening time of the valve affected these results. The reduced valve opening probably limited the flow rate in the initial stage of the release, when the release had its largest potential. This factor could also explain why the maximum values for the nitrogen experiments correlates better with the empirical values than the maximum hydrogen values, as shown in Figure 5-11. The nitrogen depressurisation typically lasted three times as long as hydrogen cases at similar initial pressure. As a consequence of that, the remaining pressure when the valve reached fully open position was larger in the hydrogen cases.

The difference is visible on the figures as well, as the part of the plots that deviates from linearity on the highest pressures are much larger in Figure 5-4 (except from the outlier Test 73) compared to the plot in Figure 5-5. The differences between hydrogen and nitrogen releases are further described in 5.2.4.

### Deviations between calculated and measured flow rate values

The results show that estimated flow rates based on measured pressure development deviates from the preliminary calculated values for choked flow through the applied  $\frac{3}{8}$ " valve. However, it is a clear linear correlation between these two. Pressure based calculations seems the yield flow rates with about half the magnitude of the preliminary calculated flow rates. This deviation could be caused by one or a combination of several factors:

- Restrictions downstream of the release valve could entail that the flow is not choked through the valve: Both the nozzle assemblies used in these experiments had lengths above 200 mm. This, in combination with ID around 5 mm for parts or the full length probably entailed a large pressure drop during the release. This pressure drop could have added enough restrictions to the system to reduce the flow rate compared to the choked flow through the valve alone.
- The stipulated  $X_T$  value used in the empirical calculations might be too high: As rated pressure drop ratio ( $X_T$ ) was not known for the valve used in this setup, it was stipulated based on values for similar valve constructions. If the used value of 0.62 is higher than the actual pressure drop ratio during choked flow in this valve, the equations will give too high flow rates compared to the actual results.
- The method used for estimation of flow rate based on the measured pressure in the reservoir might be inaccurate:  
The conversion from pressure gradients to volumetric flow rates is an approximation based on expected volume change for a given change in amount of gas, paired with presumed proportionality between observed pressure gradients and change in amount of gas in the system. This method has not been validated against a known flow, and its precision is therefore not known. It might give erroneous results. However, at small increments of time and pressure as in this application, I expect it to yield decent estimations of the actual flow.
- The pressure recordings might not have sufficient responsivity and accuracy: The pressure recorder is located at the opposite end of the system compared to the release valve. Its deliberately located at the opposite end of the outlet in the connection block, thus providing a "free line of sight" between the transducer and the outlet. Nevertheless, the system volume in combination with distance might reduce the responsiveness of the measurements significantly. However, this kind of reduced responsiveness should not affect the measurements too much in the "steady" stage of the release. During this stage, the pressure depletion at the location of the transducer should match the depletion at the outlet, with a near constant delay. Thus, insufficient responsiveness in pressure measurements could probably result in an apparently slower initial increase in rate, but should not affect the "steady state" part of the measurements too much. Furthermore, figures presented elsewhere in this section show that the transducer responds fast. Figure 5-22 does for instance show that the transducer can pick up oscillations with a period of just above 1 ms. The amplitude of these oscillations is too small to make it visible directly on the large scaled pressure plot, but it is visible on the pressure difference plot. Thus, the combination of reservoir volume and shape and transducer location should be responsive enough to produce reliable values with regards to flow rate calculations.

### 5.2.2 Jet structures and jet development

The shadowgraph system enabled observation of jet development through the releases. Despite different initial pressures, obstruction object type and distances, the observed jets had many similarities. The main differences were the size, clarity and duration of the observed structures. Some elements were only visible on the most vigorous jets.

Figure 5-6 shows a timelapse of the jet development in Test 85, which was an experiment where hydrogen was released through the release valve alone, from an initial pressure of 166.4 bara. Obstruction object A was located at a distance of 13.6 mm from the nozzle exit.



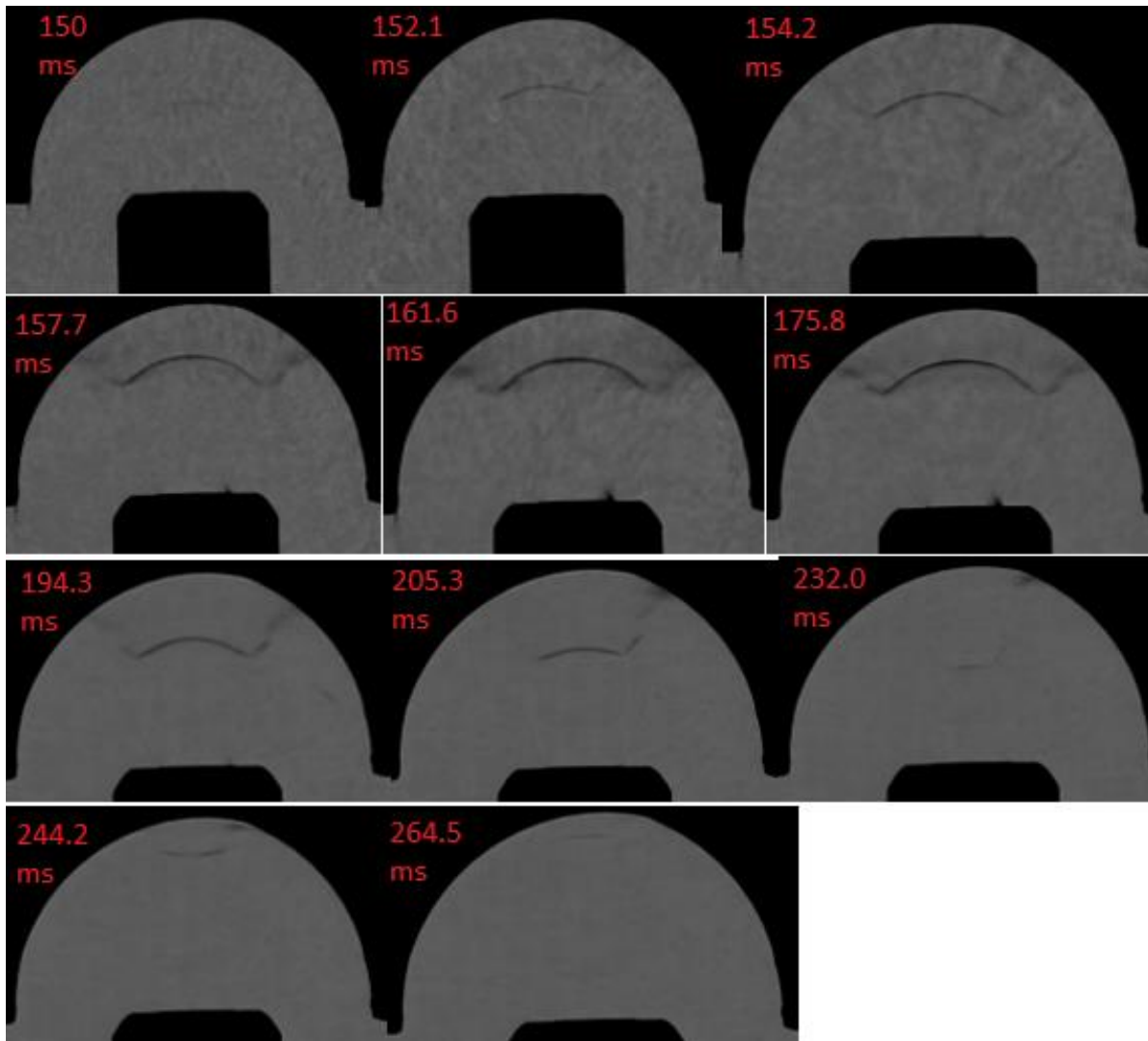


Figure 5-6: Timelapse of jet development in Test 85. 166.4 bara initial pressure and 13.6 mm between the nozzle exit and the top of obstruction object A.

The following list describes the development of the jet in Figure 5-6, but except from the timestamps, this description is universal for most jets.

- 1) 150 ms: Hydrogen has been released and is visible as a turbulent pattern. The jet structure has not started to develop yet.
- 2) 152.1 ms: A “jet disc” has developed just above the middle of the free distance. Its width is currently 6-7 mm.
- 3) 154.2 ms: The disc has developed further, and now has a semi-circular shape that corresponds to the shape of the obstruction object. It has moved further away from the nozzle exit.
- 4) 157.7 ms: The jet has increased in strength. It is almost as wide as the nozzle diameter, and the gradient that goes from each end of the jet disc and up to the obstruction object (oriented orthogonally on its impact point on the OO) is now visible. Structures at the boundary of the nozzle exit is also starting to develop.
- 5) 161.6 ms: The jet is at its strongest. Shear layers from the nozzle exit boundary to the outer end of the jet disc is visible. Oblique oriented pressure gradients oriented from the nozzle exit boundary and inwards in the jet flow is also barely visible.
- 6) 175.8 ms: The jet is starting to deteriorate, but the disc appears wider now than in previous picture.

- 7) 194.3 ms: The jet is deteriorating. It is narrower and a bit closer to the nozzle exit. Shear layers and oblique shock waves are almost completely gone.
- 8) 205.3 ms: The jet is further deteriorating. It has moved closer to the nozzle exit and is narrower.
- 9) 232.0 ms: The jet disc is now barely visible, and it has moved down to approximate halfway between the nozzle exit and the OO.
- 10) 244.2 ms: Immediately after the initial jet disc has disappeared, an apparently new disc appears much closer to the obstruction object. This was typical for all tests with obstructions.
- 11) 264.5 ms: The “new” disc is now almost completely gone.

The mentioned shear layers are visible in Figure 5-7 which is a detail picture of the picture shown with 161.6 ms timestamp in Figure 5-6. The conical shaped structures start at each side of the nozzle exit. The outer pressure gradients will be visible all the way up to the jet disc if the jet is strong enough. Many pressure gradients are visible along the curvature of the nozzle, and the most inward gradients are almost joined together in the centre of the jet.

Jet structures were in general more visible on nitrogen releases, as further discussed in section 5.2.4. Thus, the shear layers are easier to see on the left side of Figure 5-12.

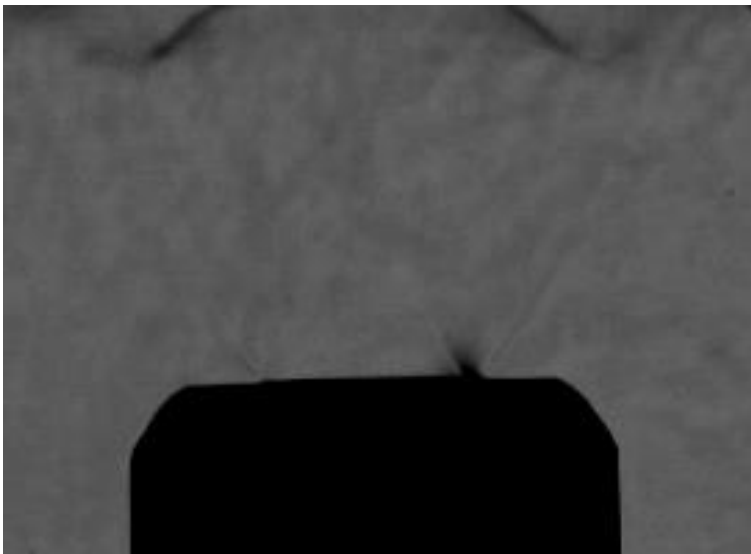


*Figure 5-7: Detail picture of shear layers in Test 85 at 161.6 ms.*

A jet disc was also visible in tests without any obstruction. It was, however, much weaker than the jet structures observed with obstructions present. Figure 5-8 shows a timelapse of the disc development in Test 65, with initial reservoir pressure 107.1 bara. Unfortunately, there is a significant amount of background noise in these pictures that makes the disc harder to see. Nevertheless, a very thin disc can be observed in the figure. The development followed the same pattern as the other jets; the disk was established some milliseconds after hydrogen was first observed. It then increased in strength, and also moved further away from the nozzle exit. The disc was 12.9 mm away from the nozzle exit at its strongest. After that, it started to deteriorate in strength and move back towards the nozzle exit.

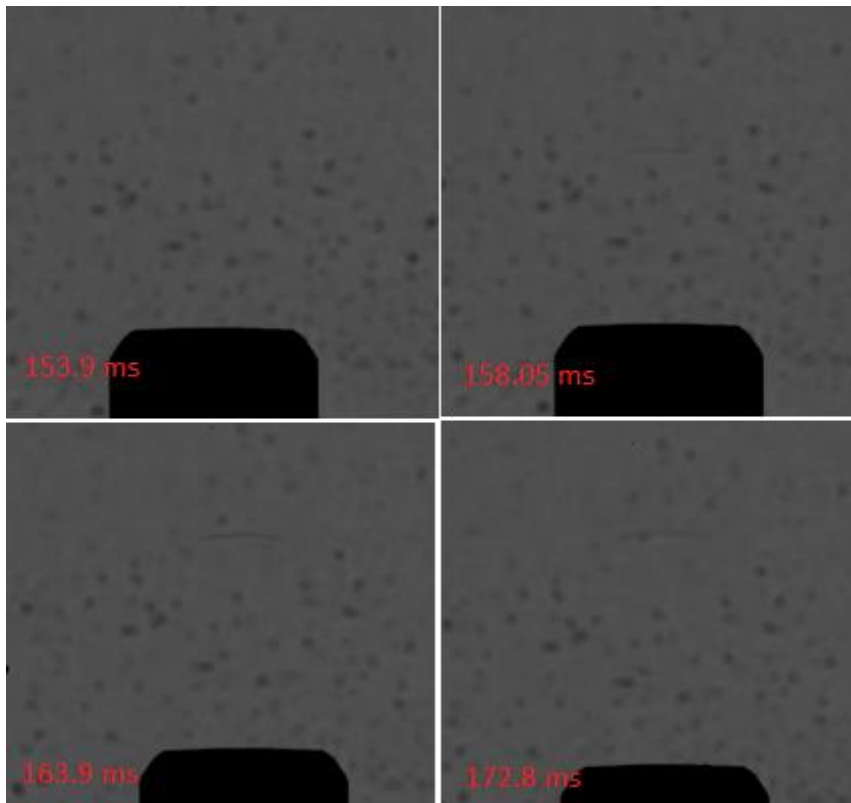


Figure 5-8: Timelapse of Test 65. 107.1 bara initial pressure and no obstructions.

#### Reflections regarding the observed jets compared to the literature

The jets observed in these experiments followed a very similar pattern. Even when no obstructions were present, a jet structure could be observed. Test 85, which was one of the tests with the highest initial pressure was selected as an example to explain the typical behaviour. This was primarily as the different elements become more apparent in a stronger jet, thus is easier to see on a static picture. However, both the inward and outward pointing pressure gradients originating from the nozzle exit, were only visible on the strongest jets.

The strongest jets look very similar to the underexpanded jet shown in Figure 2-3. Based on this similarity, it is a slight chance that the observed structures are expanded jets. The inward facing gradients at the nozzle exit looks similar to the oblique expansion waves in the jet stream, while the outward pointing shear layers looks like the flow boundaries on the jets illustrated in Figure 2-1, Figure 2-2 and Figure 2-3.

If the observed jets are underexpanded jets, then the disc structure observed in practically all experiments is a Mach disc. According to the literature, the Mach disc occurs at the location where the gas reaches sonic velocity on its transition from initial supersonic velocity near the nozzle exit, to subsonic velocity farther away from the nozzle.

However, the presence of the obstacles in most of these experiments might give a completely different situation than the pictured underexpanded jet. Due to the reflected flow from the surfaces on the obstruction object, it is likely that the pressure increases across the observed disc. This is in agreement with the description of Figure 2-3 by Molkov [63]. However, it is quite the opposite of the explanation given to the case referred to as underexpanded jet from the textbook by Anderson [59] and the applet by Devenport [61] and in the explanation of case *e*) in Figure 2-2. According to the terminology used there, the observed jet behaves as an overexpanded jet, where a pressure increase occurs over the Mach disc when the velocity transits into the subsonic area after initial supersonic velocity.

The fact that jet discs are also visible on cases without nearby obstruction enhances the theory that the observed discs are Mach discs. The observed disc in this case cannot be produced by pressure gradients caused by increased static pressure near the obstructions alone, which could be the case for the disc upstream of the obstruction objects. When the jet is able to produce a Mach disc at free-flowing condition, it should also be capable of producing overexpanded jets in more constrained conditions. Although the weak appearance of the discs in the free-flowing jets make them hard to interpret.

In future work, it would be of interest to investigate jet behaviour at even higher initial pressures to better observe the behaviour on larger and clearer jets. As nitrogen jets were generally easier to see, as discussed in section 5.2.4, it would also be interesting to perform experiments without obstructions where nitrogen is released. Further investigations should also look into if the transverse beam at 120 mm downstream of the nozzle exit affects the jet behaviour.

### 5.2.3 Jet development in experiments with rupture disc

The burst disc experiments developed a full jet structure between two picture frames, in other words in less than 0.15 ms. Figure 5-9 illustrates this for Test 74. This experiment had an initial pressure of 178.5 bara and a rupture disc with a rated burst pressure of 100 bars. Some of the experiments did not show a fully developed jet in the first picture, but this might have been because the release has been initiated shortly before the picture was captured. Thus, giving an actual time difference of much less than 0.15 ms between the release and the pictured partially developed jet. It did appear to be a certain correlation between the degree of development in the first picture of the jet and typical intensity-controlling parameters such as obstruction object type and distance. However, this correlation was weak.

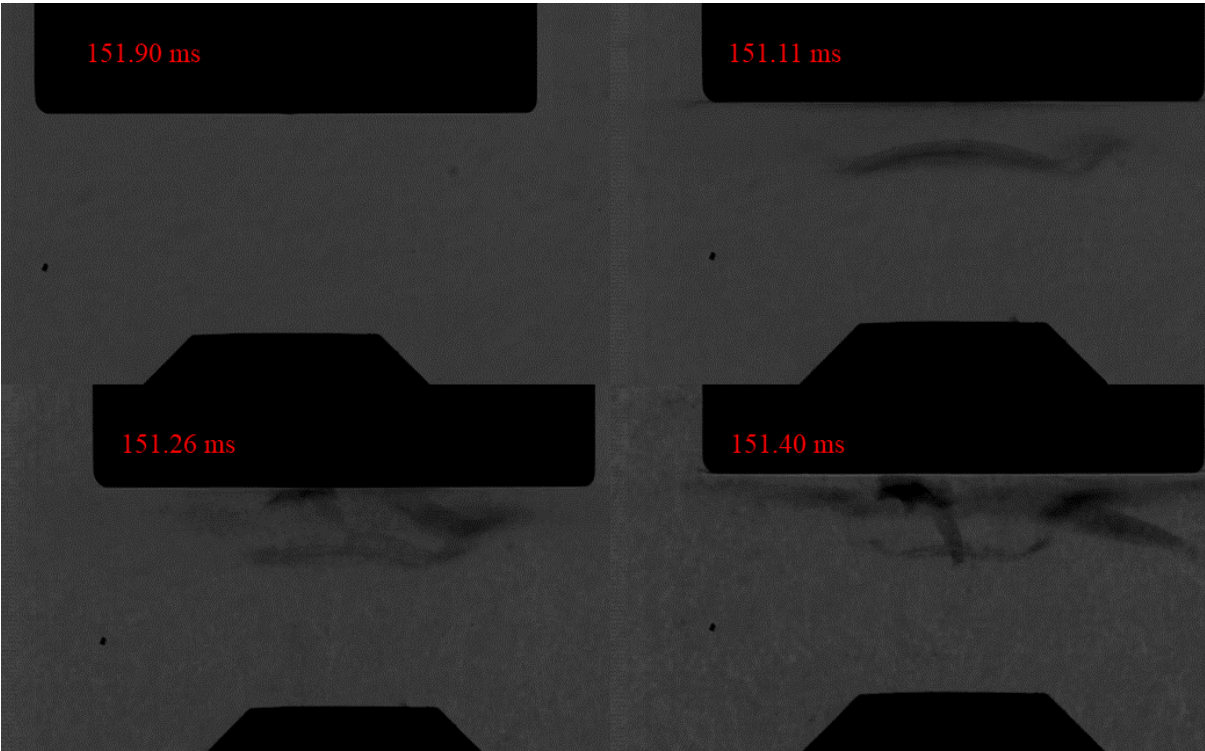
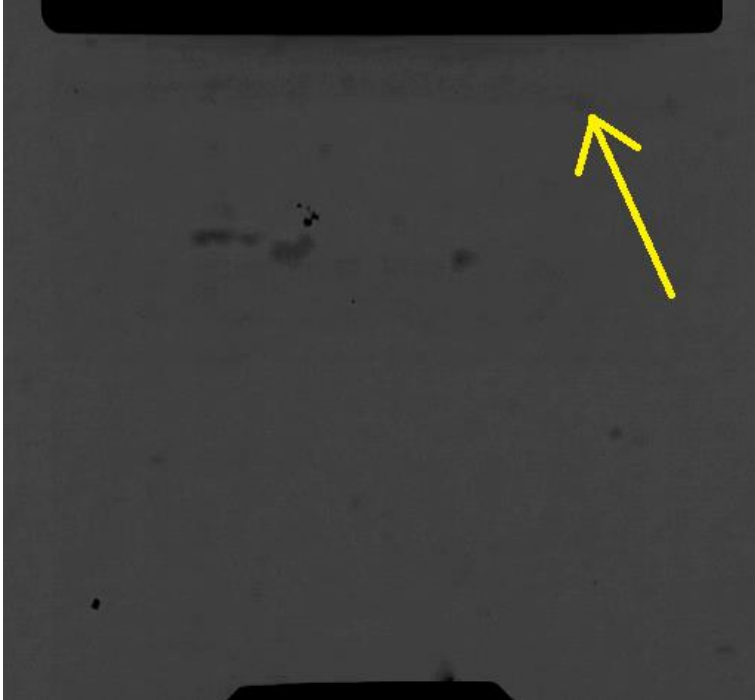


Figure 5-9: Jet development in the initial phase of Test 74. 100 bar rupture disc, initial pressure of 178.5 bar.

The behaviour of the first structure to appear in the rupture disc experiments was a bit indistinctive. In some cases, the structure behaved like the jet structures observed in the release valve experiments, but at a much shorter lifespan. These structures seem to be standing shock waves. In other tests, the initial structure looked like a shock wave. This is the case for the structure shown in Figure 5-10, which is

from Exp. 79 that had an 80-bar rupture disc OO C located at 30 mm distance. The structure is unfortunately hard to see due to poor image quality but is indicated with an arrow. It has a semi-circular shape with large radius, very close to the obstruction object. It was completely disappeared in the next picture frame, in the contrary to the initial structures seen in most other experiments that typically remained for a few pictures, thus 0.5 ms or more.



*Figure 5-10: Potential shock wave at the beginning of the release from Test 79.*

After the initial fast development, the observed jets deteriorated very quickly compared to the case with release valves. It completely disappeared in some cases. The structures might have been sustained during the whole release in some of the cases where ignition occurred, but was in that case concealed by flames or severe turbulence, thus not possible to see. However, a jet structure reappeared in most cases after a while, and these structures behaved identical as the jets in the tests with release valve when the jets had passed their peak intensity.

A possible explanation for this behaviour is that the initial rupture produces a strong, conventional expanded jet. But as the pressure downstream of the release valve quickly declines towards the conventional “steady state” release situation after release, the flow eventually becomes too weak to sustain an expanded jet structure. After a while, the needle valve has opened more, and the flow is once more able to produce the jet structure. After this, the jet behaves exactly as from a depressurisation through the release valve alone.

Given the importance of the shock waves in the diffusion ignition mechanism, it is likely that shock waves similar to those in Figure 5-9 was produced in most experiments with rupture disc, but not visible on camera. Another possibility is that the observed “short lived” conventional jet structures occurred abrupt enough to behave as a shock wave. Higher frame speeds are necessary to investigate this aspect in more detail.

Although the ignition seems to occur immediate after the release in all experiments it occurs, and the propensity for ignition should therefore not be affected by the restrained flow rate after 0.5 ms or so with large flow rates. However, it cannot be concluded from these observations that the restrained flow is not reducing the propensity for ignition.

#### 5.2.4 Comparison of nitrogen and hydrogen

A series of tests with obstruction object A at 13.6 mm distance were conducted with both hydrogen and nitrogen. These experiments are described in sections 4.5 and 4.6. This identical setup provided the opportunity to compare the behaviour of these gases, both related to blowdown rates and jet formation. Figure 5-11 shows a comparison of an experiment with nitrogen (Test 25) and hydrogen experiment at similar initial pressure (Test 42). The hydrogen test had an initial pressure of 104 bara, while the nitrogen had 101.1 bara. The figure shows that it took about 180 ms (140 to 320 ms on the figure) to fully depressurise the hydrogen system. The nitrogen depressurisation took about 600 ms. (140-740 ms on the figure).

The maximum slope in the reservoir pressure, given as 1 ms pressure difference, was calculated to -2.18 bar per milliseconds (bar/ms) for the hydrogen release, at 161.7 ms after the start of the recording. The corresponding value for the nitrogen test was -1.06 bar/ms at 159.3 ms. For both experiments, the released gas was initially detected at 154 ms. Simple calculations done with Eq. (11) indicate that these values correspond to volume flow rates 0.38 Sm<sup>3</sup>/s for hydrogen and 0.18 Sm<sup>3</sup>/s for nitrogen.

The pressures at the moment of maximum slope were 68 bars for hydrogen and 86 for nitrogen. The expected volumetric flow at choked conditions in the 3/8" valve for these inlet pressures according to Eqs. (6), (7), (8) is 0.272 and 0.80 Sm<sup>3</sup>/s for nitrogen and hydrogen, respectively. Thus, the calculated flow corresponded to about 66 and 47 % of the expected flow rates for nitrogen and hydrogen, respectively.

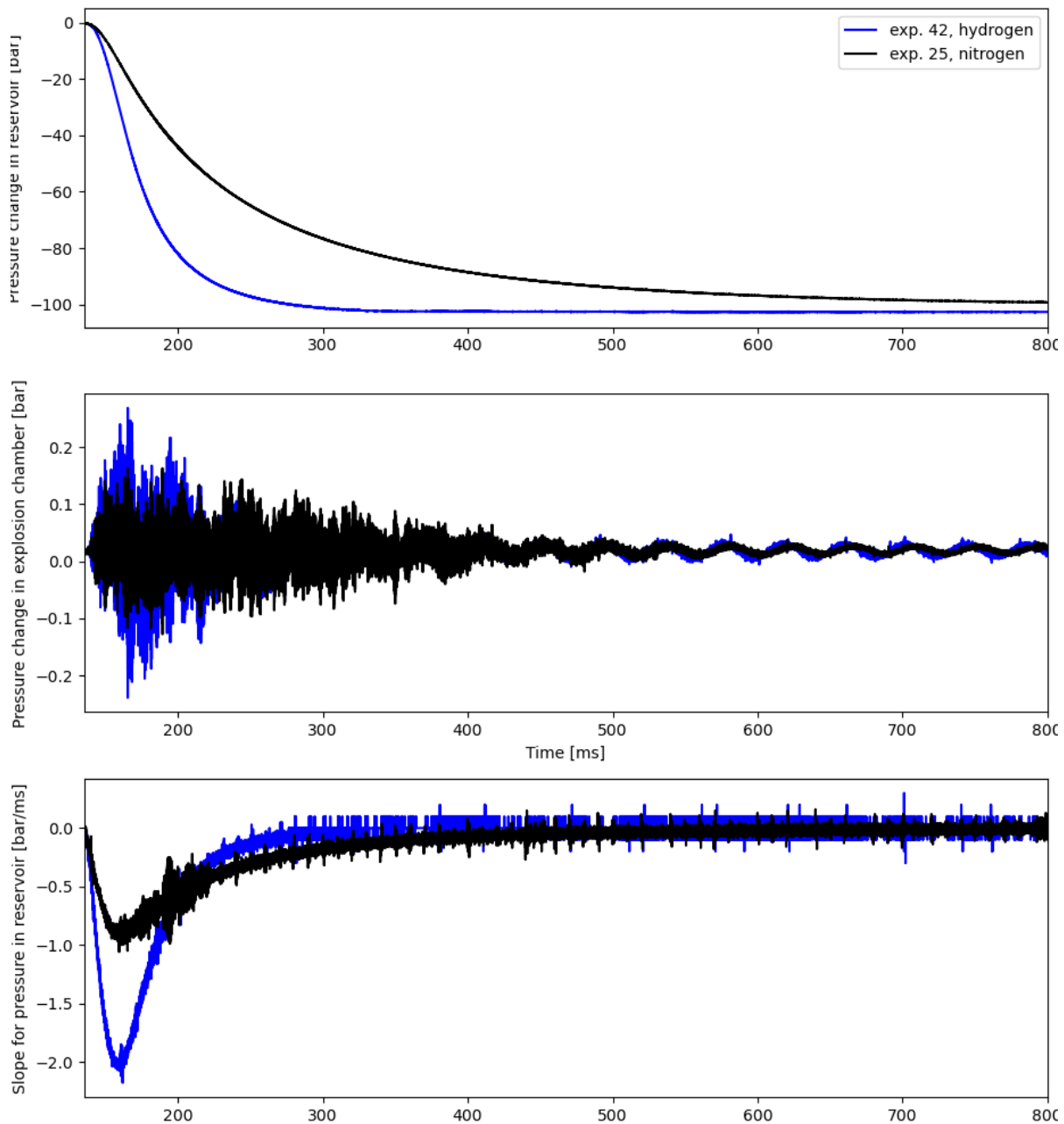


Figure 5-11: Trends from reservoir and explosion chamber for Test 25 with nitrogen and Test 42 with hydrogen. Both experiments had approximately 100 bars initial pressure, and obstruction object A was installed at a distance of 13.6 mm. The x-axis in all plots starts at  $t=135$  ms.

As discussed in 5.2.1, it seems like the peak flow rate occurred before the release valve was fully open. The time scale of the hydrogen release is much shorter than for nitrogen. Thus, the effect related to the valve's moving time will appear stronger for the hydrogen experiments. This seems to be a plausible explanation for why the actual hydrogen flow rate at peak flow rate deviates more from the expected, empirical calculated value, than the corresponding nitrogen case. Figure 5-3 shows that this systematically occurs for all experiments.

Nitrogen yields much more visible jet structures, despite that its initial density is not visible on shadowgraph, while the lighter hydrogen gas is. This is very visible in Figure 5-12, which shows the jet structures in Test 25 and 42 at their peak intensity. Both nitrogen jet was bigger and appeared clearer than the hydrogen jet. The maximum diameter for the hydrogen jet was 8.8 mm, while the nitrogen jet was 11.9 mm at its widest.

A possible explanation for this difference in jet appearance might be that the lower sonic velocity for nitrogen causes supersonic transitions to occur at lower intensity than for corresponding hydrogen jets. However, this effect was expected to be at least partially equalised by the lower release rates for nitrogen. The reason for this difference between the gases must be further investigated if this is of interest for future experiments.

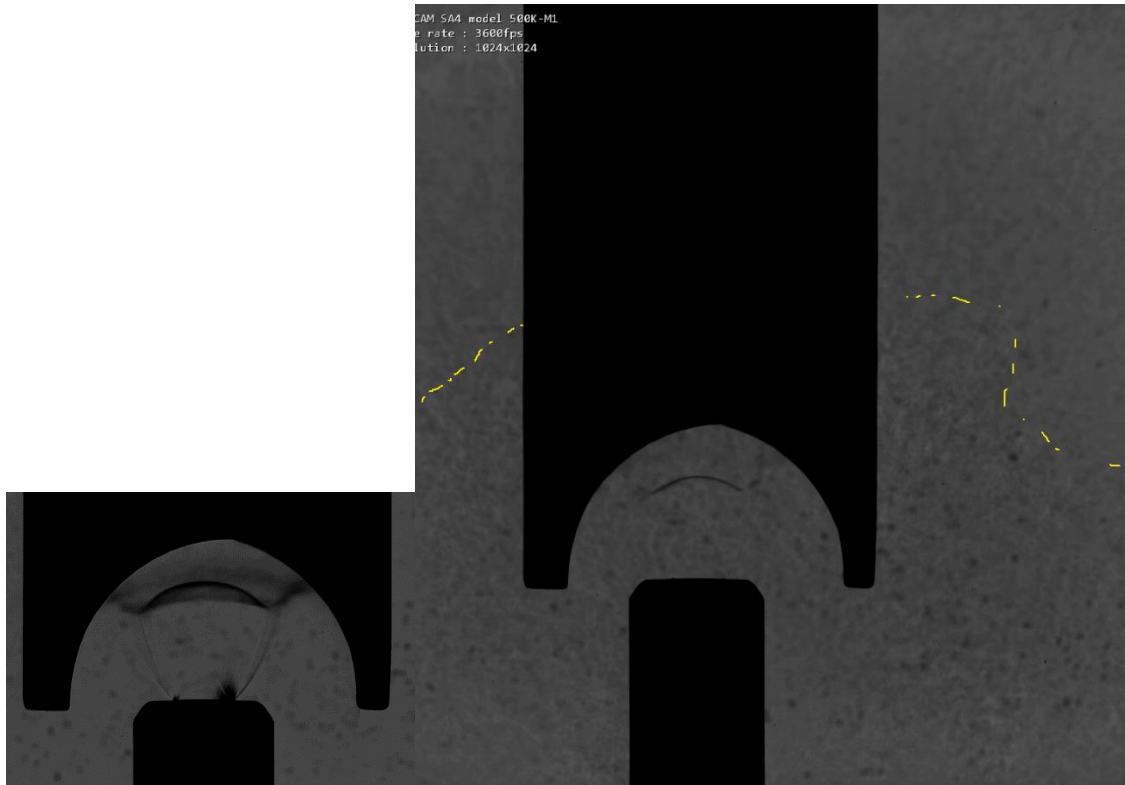


Figure 5-12: Test 25 (nitrogen) at 170.1 ms (left) and Test 42 (hydrogen) at 172.2 ms (right). Both pictures present the jet at the peak intensity. The yellow dotted line to the right marks the approximate position of the hydrogen-air boundary.

### 5.2.5 Time delay for valve opening and asynchronous time stamps

The recording is supposed to start 100 ms before the release valve is initiated, as described in 4.8.1. A closer look at logged values for initiation of the release valve reveals that initiation usually occurred around 80 ms into the pressure recording. This deviation from the expected 100 ms might be because of delays in the initialisation of the data acquisition. Timestamps for valve opening are shown in appendix E together with other types of meta data for the experiments.

Peak flow rate was detected at around 148-160 ms for most experiments, thus a relative time difference of 75-80 ms from the valve was triggered. This relative time decreased slightly with higher release pressures. This relative time includes all time-consuming aspects of the valve opening process as well as the travel time from the upstream side of the valve to the nozzle exit.

Detected peak flow rate and relative time do not give any indication of the position of the valve at this moment. Similar relative time from valve initiation to peak flow rate for hydrogen and nitrogen despite the different release rate indicate that the valve opening is the dominating parameter in the initial phase of the release.

Released gas was usually observed around 150 ms on the camera recording. Maximum size of the jet usually occurred at 160-170 ms for most experiments. The time stamp between the camera and pressure recordings are not synchronised, but they are both started 100 ms before the valve is initiated. As the



working principle of the camera entail that it keeps already stored footage when triggered, it should not have much delay from triggering to the first picture stamped at 0.0 ms. This recording principle is further described in appendix A.3.2. Based on the deviation between expected and measured triggering time for the valve and this camera feature, it could be assumed that time stamp on the camera is 10-20 ms ahead of the time stamp in the pressure recordings.

It is as mentioned earlier that the valve is not fully open when the maximum flow rate occurs. Both camera recordings and pressure plots indicate that peak rate occurs about 20 ms after flow is first detected. Neither camera recordings nor pressure log give information that could tell anything about when the valve is sufficiently open to allow full flow, but it should be reasonable to assume that it uses between 30 and 60 ms from fully closed to fully open position.

If further experiments are conducted with release valve at a later stage, we should attempt to get more precise measurements of the transition time for the valve. Optical methods could be used, with a light source and a light detector (photodiode or similar) on each side of the valve. The detected light intensity will increase along with the valve opening until it stabilises at an intensity associated with fully open position. However, this method will require that the valve is disconnected from the upstream and downstream systems. The method is therefore incapable of investigating how different initial pressures affect the opening time. This aspect would also be interesting to investigate.

### 5.3 Results from experiments with release valve alone

A total of 43 experiments with hydrogen released through the release valve was conducted in this project. Figure 5-13 gives an overview of these the initial pressure, obstruction object and distance from nozzle to object.

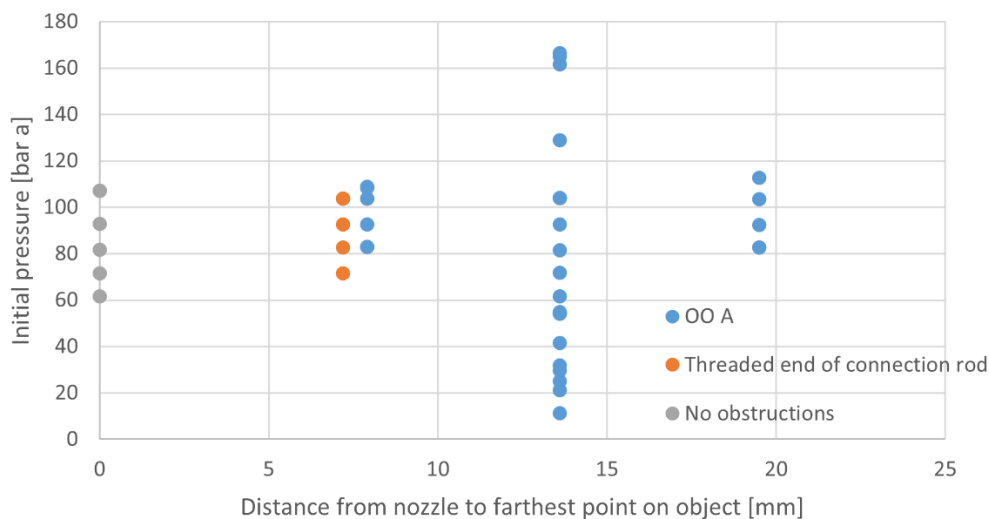


Figure 5-13: All experiments with hydrogen release through release valve.

The pressures in the explosion chamber during some of the experiments where obstruction object A was inserted at 13.6 mm distance is shown in Figure 5-14. It shows experiments with a distribution of initial pressures from 24.9 bar a to 166.4 bar a. In addition to the experiments shown in this figure, Test 42 with 104 bar a initial pressure is shown in Figure 5-11.

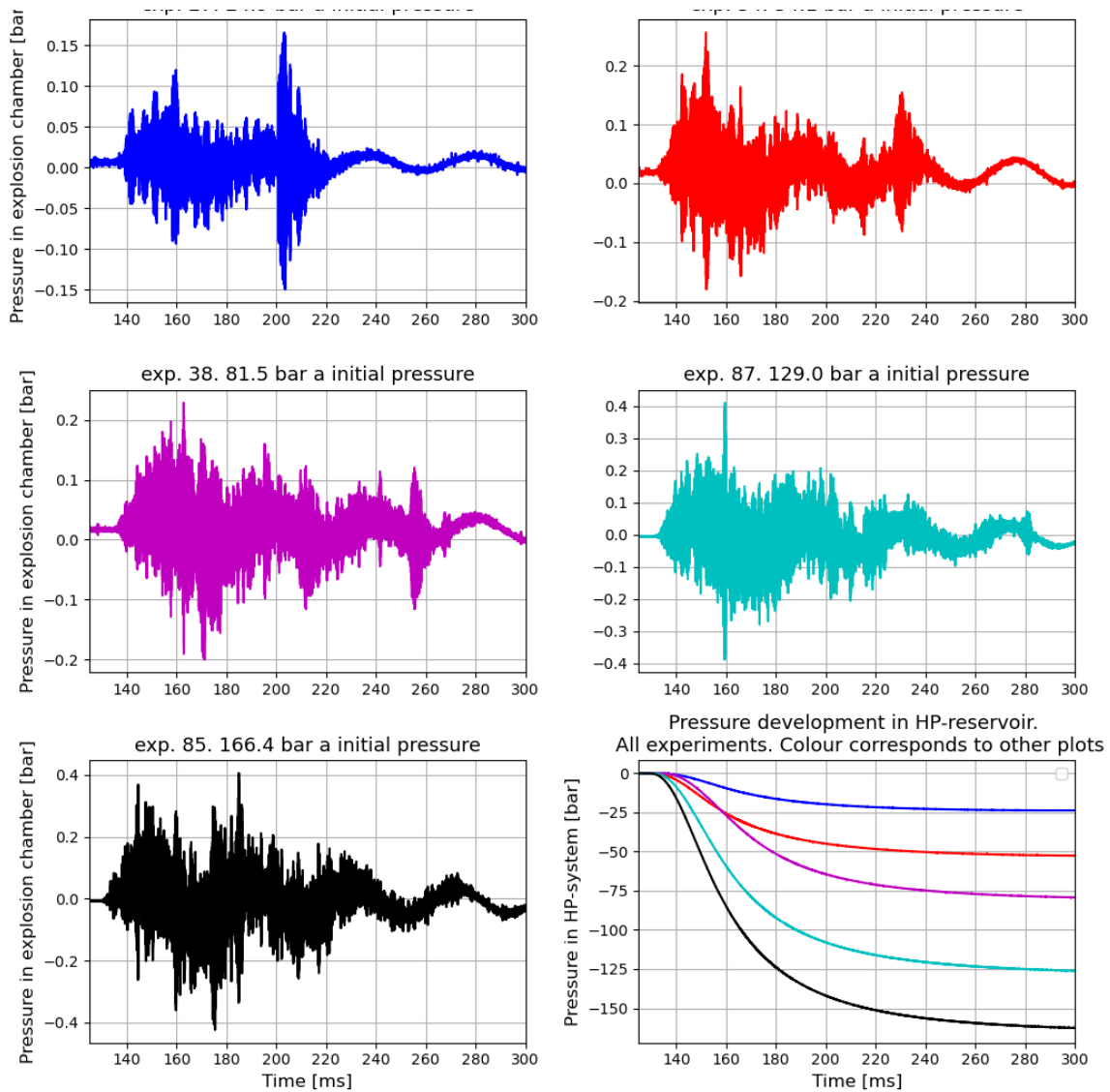


Figure 5-14: Pressure in explosion chamber for experiments with hydrogen released through valve. All experiments had OOA at 13.6 mm distance.

None of these experiments resulted in detectable ignition. Neither explosion chamber pressure, shadowgraph footage or sound and appearance in the room during the release gave any indications that ignition occurred. However, it is still a slight possibility that ignitions occurred at some point but was extinguished before it was detectable with the current instrumentation. Experiments conducted with improved instrumental setup will therefore be of interest. Photomultipliers at strategic locations could be able to detect unsustained ignitions. However, the current setup is sufficiently sensitive for the purpose in these experiments, as it was sensitive enough to detect sustained ignitions. Sustained ignitions are most interesting to detect, as these ignitions with subsequent explosions have a realistic damage potential.

Despite that ignition was never detected in these experiments, it is still possible that it could occur at higher pressures. Hydrogen releases through valves should therefore be investigated at pressures up to well above what is commercially available in the public domain. The pressures in this setup was limited by the available bottle pressure, but an improved setup with a pressure booster would allow significantly higher pressures.

# 5.4 Results from experiments with rupture discs

A total number of 14 experiments with rupture discs were conducted. Figure 5-15 gives a graphical overview of how these experiments were distributed with regards to object type, rated burst disc pressure and distance to object. The experiments are also presented with essential details in Table 5-1.

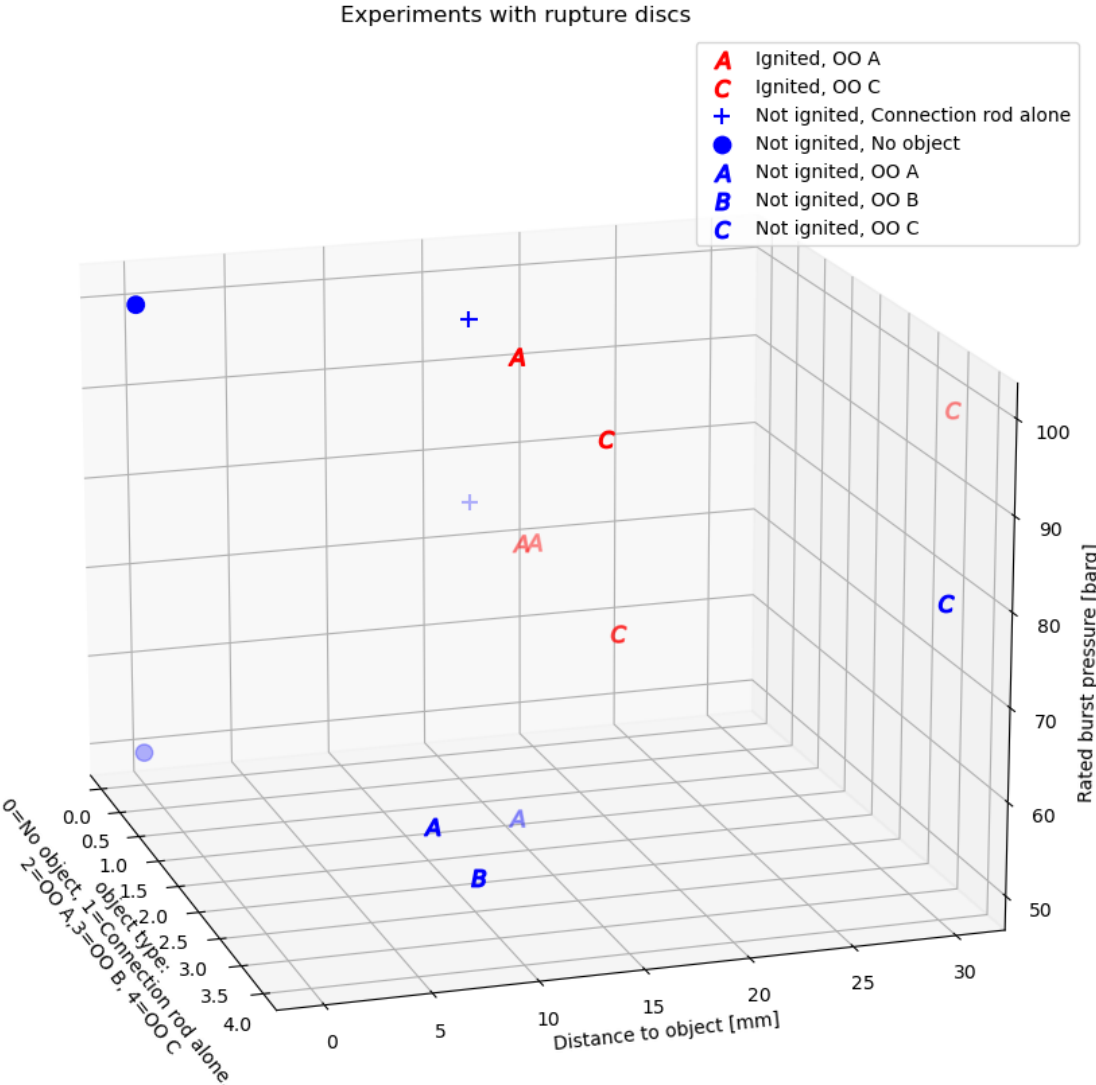


Figure 5-15: Visualisation of rated burst pressure, object type and distance to object for all rupture disc experiments.

Six out of the 14 experiments resulted in ignition. Ignition was easy to detect, as it was evident in several different parameters. Figure 5-16 shows two examples of this: The ignitions and subsequent explosions were easy to see through the visualisation windows. Condensed water was also present in the explosion chamber after the ignited releases. Condense appeared on the visualisation windows immediate after the experiment. In some of the shadowgraph-recordings, the condense on visualisation windows reduced visibility before the depressurisation was finished. In addition to this, the temperature at the 2.6 mm thick blowdown pipe increased significantly due to the produced heat from the combustion. After the most vigorous ignitions, it was almost not possible to rest the hand against pipe at the warmest point just above the axial compensator.

Table 5-1: Essential data about rupture disc experiments.

Test no.	Initial pressure [bara]	Obstruction object	Distance to OO [mm]	Rated burst pressure [bar]	Ignition
66	105.1	None	0	50	No
67	106.8	OO A	15.25	80	Yes
70	103.1	OO A	14.4	50	No
73	179.7	OO A	14.4	100	Yes
74	177.5	OO C	13.8	100	Yes
75	176.6	OO C	30.2	100	Yes
76	176.1	None	0	100	No
77	176.3	Rod only	14.4	100	No
78	106.3	OO C	14.4	80	Yes
79	107	OO C	30	80	No
80	104	Rod only	14.4	80	No
81	104.4	OO A	14.6	80	Yes
82	103.5	OO A	10.2	50	No
83	103	OO B	10.1	50	No

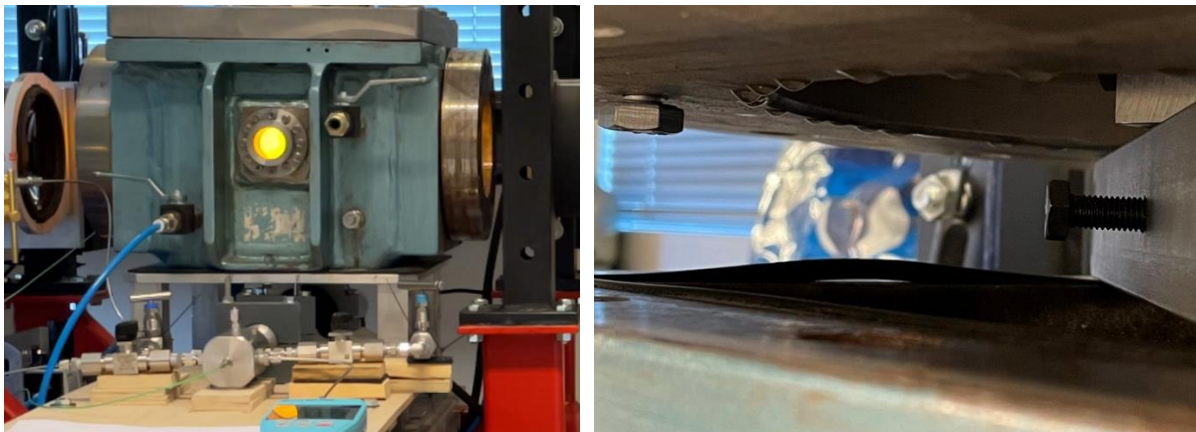


Figure 5-16: Evidence of ignition. Visible combustion/explosion through the visualisation window during Test 73 (left). Condensed water as a product of combustion under the chamber lid after an experiment (right).

Ignition was also visible on the shadowgraph images. Figure 5-17 show a comparison of Exp. 75 where ignition occurred and Test 79 where ignition did not occur. Both experiments were done with OOC at approximately 30 mm distance, but Test 79 had a 80 bar rupture disc, compared to the 100 bar disc in Exp. 75. These figures are generated through a MATLAB-script that was intended to enhance gradients in the pictures. The flames were visible in the conventional camera recordings from all ignited experiments. Figure 5-18 shows the flame propagation for the first five milliseconds after release in test 78. This appearance of the flame gradients and development with respect to time was typical for most ignited experiments.

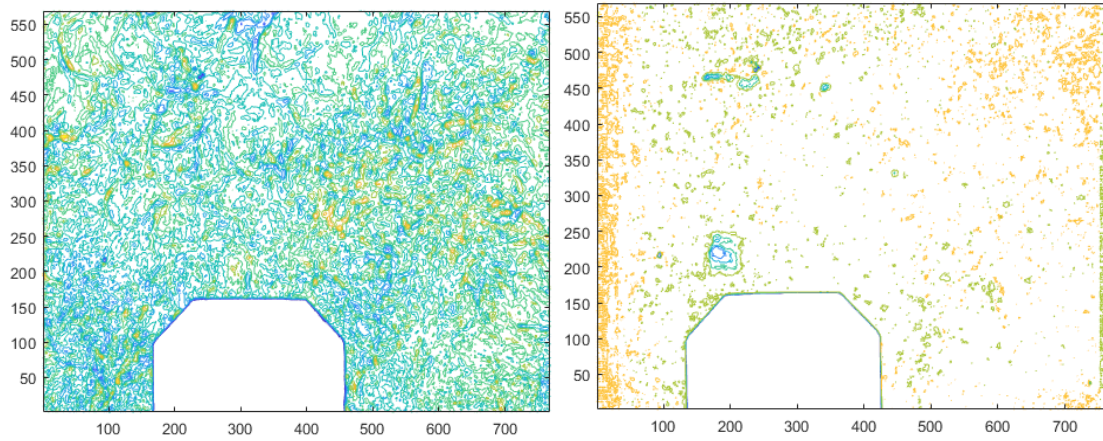


Figure 5-17: Illustrations generated with MATLAB for Test 75 at 152.2 ms (left) and Exp. 79 at 157.1 ms (right).



Figure 5-18 Timelapse for explosion development in a typical ignited test. Example shown is test 78.

#### 5.4.1 Rupture discs – 50 bars

Four experiments were conducted with rupture discs that had rated burst pressures of 50 bar  $\pm$  10 %. All experiments had 100 bar initial upstream pressure. Ignition did not occur on any of these experiments. As shown in Figure 5-19, none of the experiments yielded more than 0.2 bar overpressure in the

explosion chamber. In the two last experiments, Test 82 and 83, the obstruction object was moved even closer to the nozzle exit in an attempt to get ignition, but it did not make any difference. This were the only experiments with rupture discs with shorter distances than the “standard 14.4 mm.

Test 83 was also the only experiment during the whole project were OO B was used. It was used to investigate if the results were different compared to Test 82 with OO A. All other factors except from the type of obstruction object was similar between these two experiments.

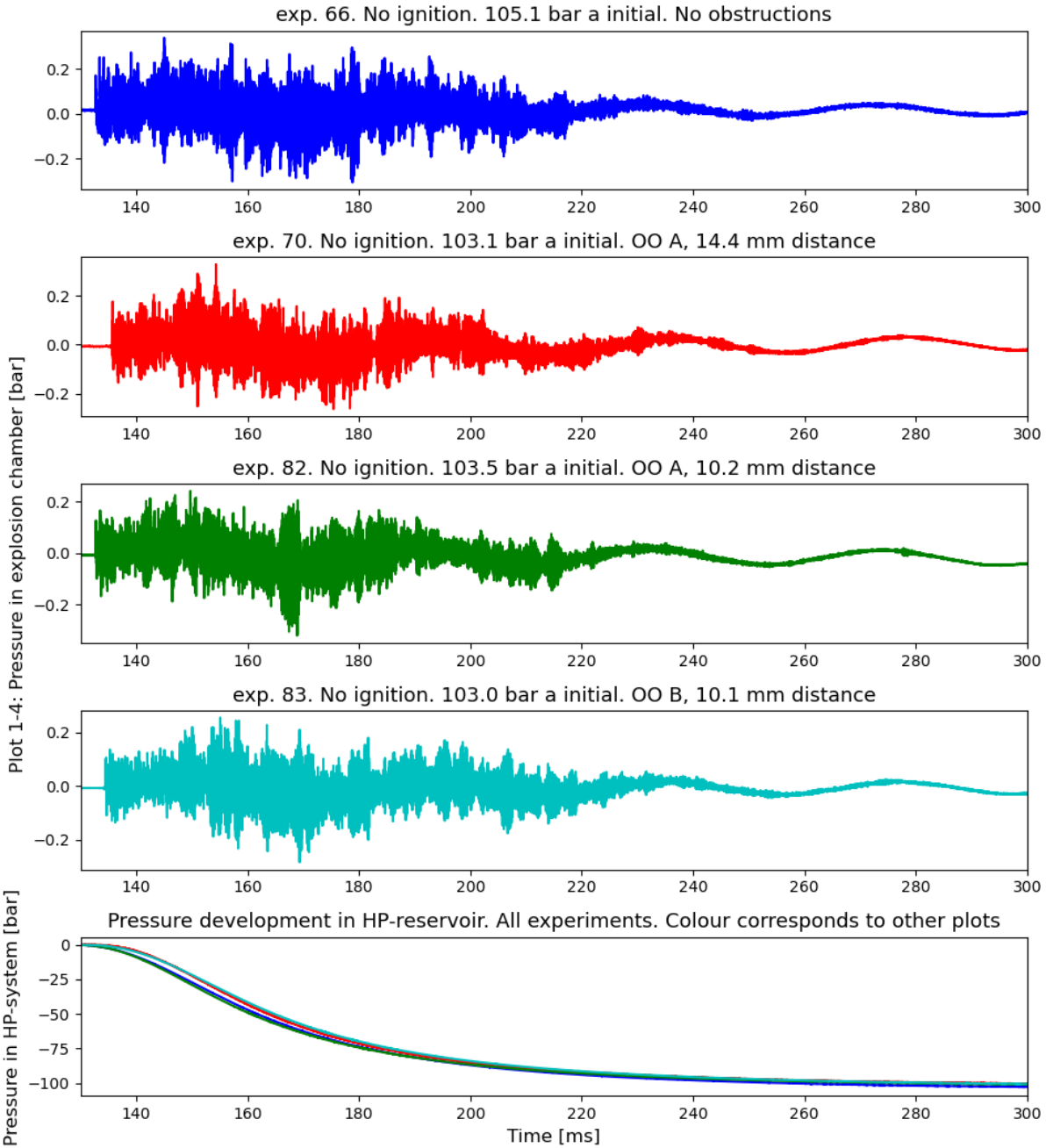


Figure 5-19: Plots for pressure in explosion chamber for all four experiments with 50 bar rupture discs.

### 5.4.2 Rupture discs – 80 bars

Five experiments were conducted with rupture discs that had rated burst pressure of 80 bar ± 10 %. The initial pressure upstream of the release valve was 100 bar in all tests. Three of the tests resulted in ignition. Common for these experiments, was that the distance to the objects were below 15 mm. Figure

5-20 show the pressure plots for the explosion chamber pressures during the experiments. It shows a significant difference between the experiments that ignited compared to unignited experiments. Test 78 gave peak pressures up towards 1 bar, but the trend in the oscillating plot seems to peak just below 0.6 bar. The corresponding values for Test 67 and 81 that also ignited, was just above 0.4 bars.

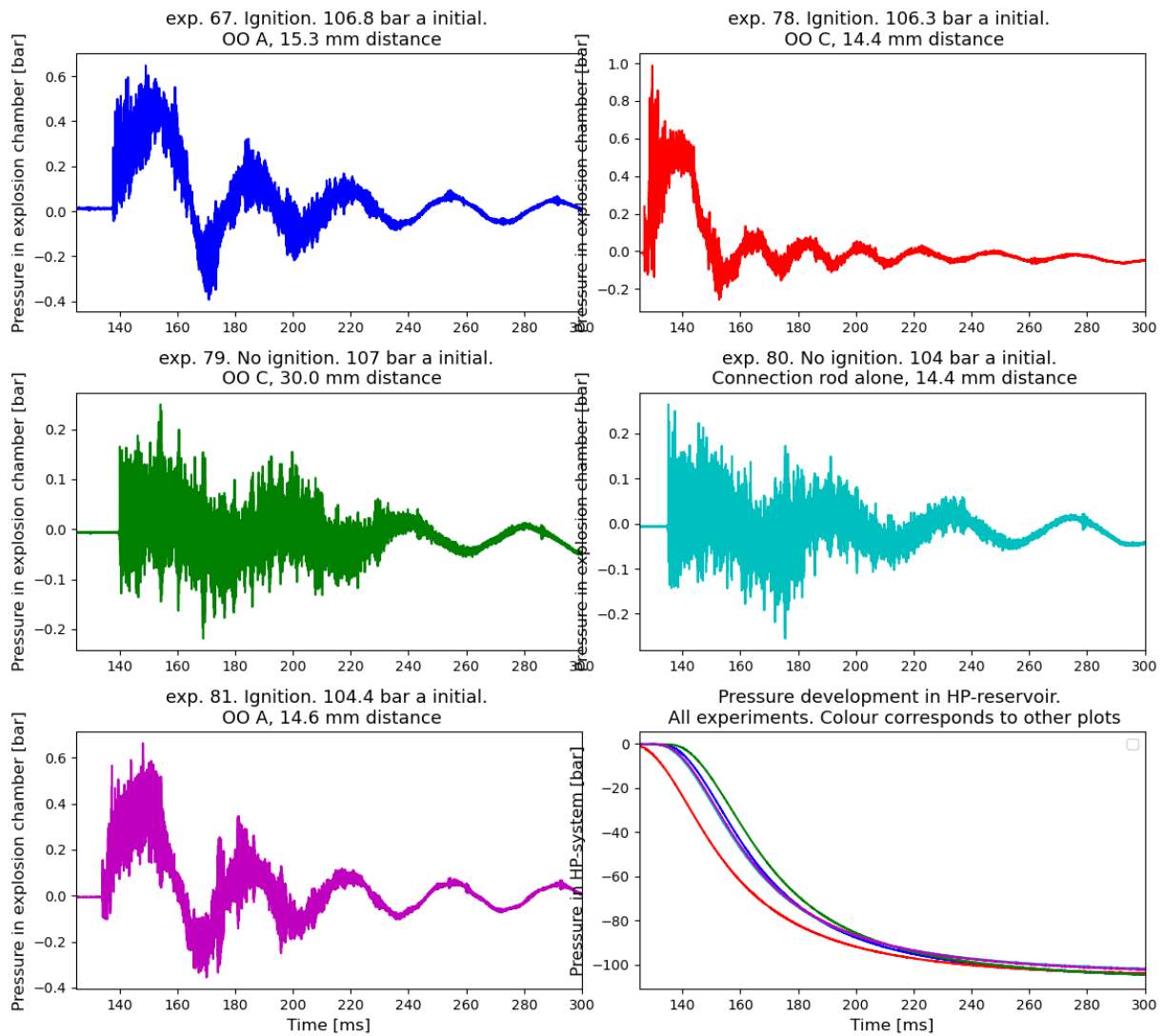


Figure 5-20: Plots with pressure in the explosion chamber for all experiments conducted with 80 bar rupture discs.

### 5.4.3 Rupture discs – 100 bars

A total of five tests were conducted with discs that had rated burst pressures of  $100 \pm 10\%$ . In addition to the five tests where successful release occurred, another four unsuccessful attempts were made before the first successful release. These unsuccessful attempts, namely test no. 68, 69, 71 and 72 had initial pressures of 106.0, 105.6, 124.8 and 164.7 bara, respectively, were performed with the same particular disc. The successful attempt with the same disc, test number 73, had an initial pressure of 179.7 bara, thus 68.7 bars above the rated burst pressure, including error margin.

Figure 5-21 shows a plot of the resulting explosion chamber pressures and reservoir pressure for these five tests. Three experiments gave ignition. These three had in common that that one of the obstruction objects were used. The experiments conducted with either the connection rod alone or no obstructions, did not give ignition. The figure shows that test no. 73 produced a maximum pressure up towards 1.5.

However, as this rupture disc was an outlier, it yielded results that are not directly comparable with the other experiment among these discs. Further details and observations from this test are discussed in section 5.6. The maximum pressure for the two other tests were approximately 0.8-0.9 and 0.7 barg for test no. 74 and 75, respectively. As for all the explosion chamber pressure plots, the noise level made exact determination of realistic maximum pressures a bit difficult.

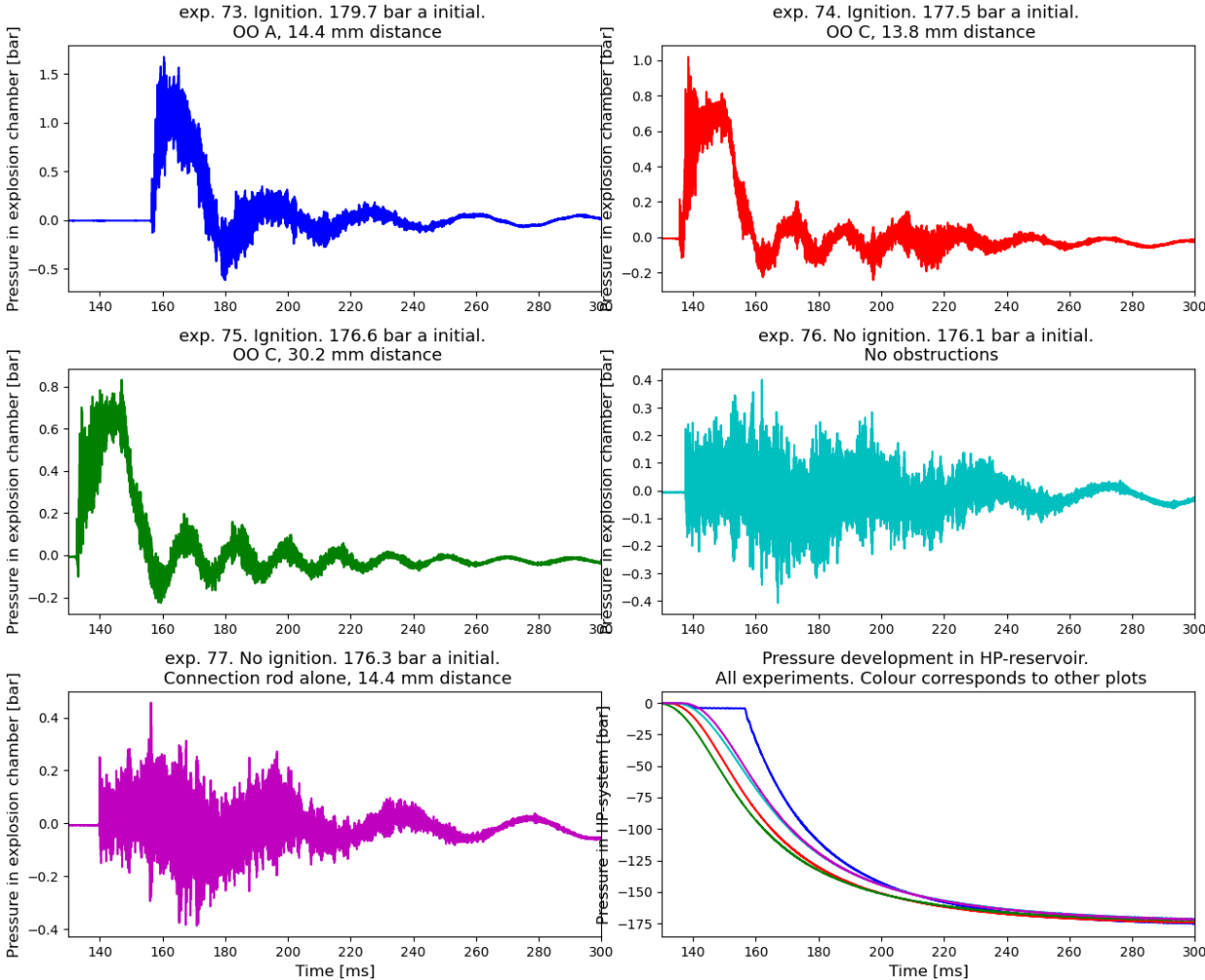


Figure 5-21: Plots for pressure in explosion chamber for all experiments with 100 bar rated rupture discs.

All the failed attempts happened as mentioned on the first 100 bar disc that was tried. Maximum available hydrogen pressure was used for the four remaining discs with 100 bar rupture pressure to avoid additional failed releases. Initial pressures just marginally above the rupture pressure for a disc entailed the risk of giving delayed releases. Delayed releases entailed a risk of not being recorded. Given the limited number of rupture discs available in this project and their unit cost, this would have been very undesirable. However, there were no indications on the pressure data from the other tests that such high initial pressure was necessary.



## 5.5 Evaluation of different obstruction objects and distances

As none of the experiments performed with release valve resulted in ignition, this part of the thesis work did not provide any particularly useful information about the influence of different obstruction objects and their distances. Nevertheless, the high-speed footage gave a qualitative indication of the potential based on the size and appearance of the jet at different obstacle conditions. The overall impression after these tests, was that the obstruction object A, which was the only one tested in the release valve experiments, was much more efficient than the much narrower connection rod. Although the connection rod also yielded jet discs, they were both smaller and more unstable than the discs produced at similar conditions with OO A in place. As mentioned earlier, jet discs were also produced in the absence of any obstructions, but these discs were much weaker.

Distance also affected the size of the disc. Increased distances gave weaker discs. But the shortest distance of 7.9 mm did not appear much stronger than the distance corresponding to the radius of the semi-circular shape.

During the rupture disc experiments, a rather wide variety of objects and distances were investigated. In these experiments, both the observed jet intensity and whether ignition occurred was indicators for the efficiency of the applied object/distance combination.

The semi-circular OO A appeared to give more powerful pressure interactions than the flat OO C. This is in line with the preliminary expectations, as the semi-circular shape should be able to reflect the jet back towards a concentrated point. It was not possible to distinguish these objects based on ignition results, but this might be because the conditions where both these objects were tested was not marginal enough to disclose the differences. It would have been of interest to test OO A at 30 mm distance with both 80 and 100 bar burst discs. When these tests were conducted with OO C, ignition only appeared with the 100-bar disc.

OO B was only used in one experiment, with 10 mm distance and a 50 bar rated disc. This object had a vertical wall on each side of the 2d plane observed through the camera. When assessing this test and object, it is important to remember that none of the tests with 50 bar rated discs resulted in ignition. Some interesting shock interactions occurred near the corners between the horizontal surface directed towards the nozzle exit and the vertical side walls. OO A was tested at the same distance and pressure, and it appeared as the total amount of pressure interactions was slightly larger with the OO B applied, compared to OO A. Thus, it would be interesting to evaluate this object or other shapes with right angles in future experiments.

Variations in distance yielded difference in ignition results. OO C did, as mentioned above, give ignition at 30 mm distance with a 100 bar disc, but not with an 80 bar disc at the same conditions. It is likely that an equivalent critical distance exists for all other object/pressure combinations that are capable of producing ignition

None of the experiments with either connection rod alone or no obstructions, produced ignitions, not even with 100 bar rupture discs. However, the connection rod was only tested at one distance, 14.4 distance. OO C, which practically is the same shape but with a larger diameter than the rod, produced ignition at similar distance and pressure conditions as the connection rod did not. It thus appears that the connection rod at the tested distance did not provide enough area to reflect shock waves to give ignition. Further tests at shorter distances should therefore be conducted

## 5.6 The “outlier” Test 73

Test 73 gave some unique results. Its burst pressure appeared to be significantly higher than any other experiments. All other parameters, such as pressure measurements, camera footage and also sound and appearance during the release indicated that this test was something different than the other.

### 5.6.1 Pressure behaviour

Figure 5-22 shows plots for reservoir pressure, pressure in explosion chamber and pressure gradient for reservoir pressure as running 1 ms difference. It is shown at a shorter time interval than the corresponding plots in Figure 5-21. The Y-axis in the reservoir pressure plot is also magnified to better show details in the initial phase of the release. The corresponding plots for test 74, which gave ignition with more ordinary behaviour, is included for comparison.

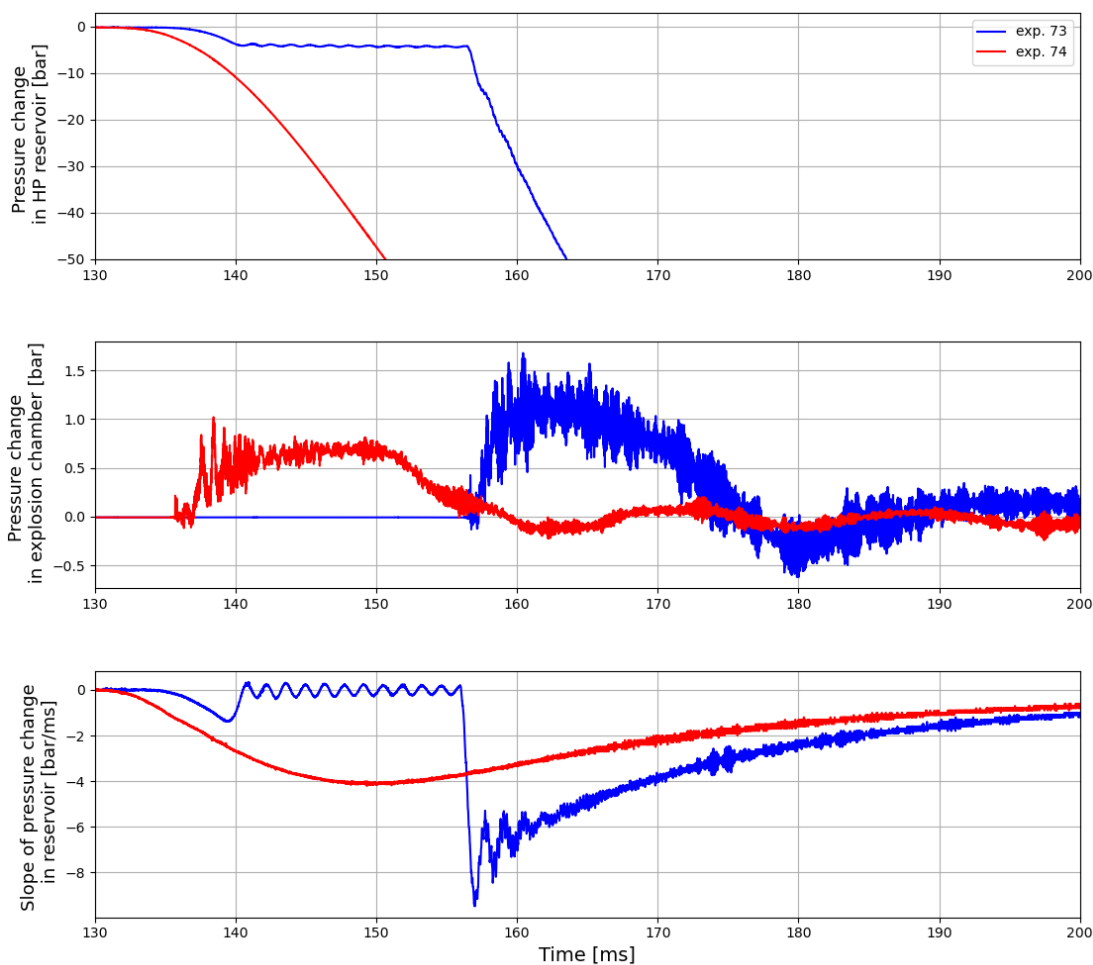


Figure 5-22: Comparison of recorded pressure data for Exp. 73 and Exp. 74. Above: Pressure in the HP reservoir. In the middle: Pressure in the explosion chamber. Below: Running 1 ms pressure difference for the reservoir pressure.

At about 140 ms, where a continuous pressure decline is started for test 74, only a slight pressure decrease is seen in test 73. The pressure stabilises at around 175 bars and remains stable for almost 20 ms before a very rapid pressure decrease occurs. A possible explanation for the observed behaviour, is that the initial pressure decrease was caused by the opening of the valve. As the disc did not rupture, the pressure equalised at the common pressure for the full volume including the section between the valve and disc. During the delay time, the valve continued its transit towards open. Thus, it had substantially

larger flow capacity when release finally occurred, compared to the conventional releases. This is the plausible explanation for the much faster release rate in the initial phase of this release compared to the others. The peak rate in this release was 9.5 bar/ms, compared to about 4 bar/ms for the other 100 bar rated discs.

The plot also shows that small oscillations with a period of just above 1 ms and an amplitude of 0.25 bar. The oscillations were probably generated when the initial flow through the release valve was reflected by the closed rupture disc. The pressure slope plot also shows a damped oscillation in the phase of the release when the rate declined from its maximum. Such oscillations were not visible on the slope plots from the other experiments. These oscillations are more difficult to explain than the previous, but they might have been caused by effects related to the abrupt and large flow out of the HP-system. Maybe expansion waves that propagated into the HP-system?

### 5.6.2 Observations from high-speed footage

The shadowgraph-images also revealed some atypical behaviour in test 73 compared to the other tests. Figure 5-23 (left) shows a white cloud-like area that appeared before any pressure gradients were visible. The cloud represented a distinct difference compared to the background shown in the first phase of the recording, so it must be related to the release. In the subsequent picture frame, a fully developed jet structure was visible. A very bright spot was also visible at the top of the semi-circular obstruction. The bright spot could be the point of ignition, but this is hard to determine based on the limited information from these pictures.

In this experiment, the initial abrupt jet structure did not fade away as in the other experiments. This was probably because the release valve was more open when this release occurred than in the other tests. Thus, it allowed a substantial higher flow when the initial pressure in the nozzle had exited and the system converged towards the steady-state choked condition.

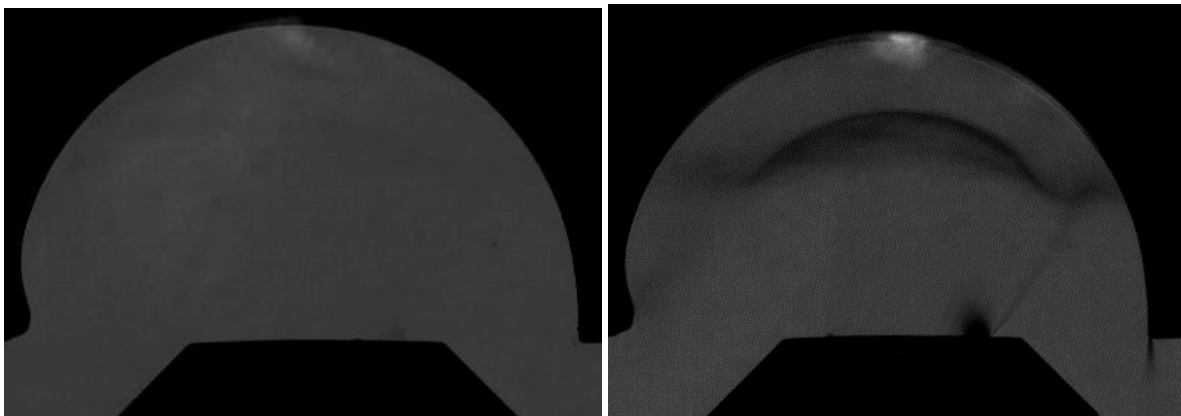


Figure 5-23: Abnormall white area and spot at the initial phase of the release in test 73.

The large difference between the release rate and jet behaviour in this experiment compared to the other, indicates that it would be beneficial to use a setup that is not depending on a release valve for further investigations of rupture disc releases.

## 5.7 Possible ignition sources

### 5.7.1 Diffusion ignition mechanism

The opening time for the release valve is estimated to 30-60 ms from closed to practically fully open with regards to flow properties. This estimate is outlined in 5.2.5.

Literature indicates rupture disc opening times between a few and above 20  $\mu\text{s}$  [94]. However, the instruments in this setup are neither intended nor capable to measure the opening times experienced in these experiments. A fully developed jet develops as fast as, or faster than the time corresponding to the interval between two pictures. This interval is just below 150  $\mu\text{s}$  in at the applied 6750 fps speed. Thus, it is reasonable to assume that the rupture discs also open to nearly fully open position in a shorter interval than this.

The difference between the opening time for the valve and a rupture disc is then between two and three orders of magnitude. This is a substantial difference, and a plausible explanation for why ignition repeatedly occurred at in the rupture disc experiments, but never in the release valve experiments.

Some literature based on numerical analysis indicate that the opening time of the rupture disc should be down towards 0  $\mu\text{s}$  before diffusion ignition could occur repeatedly [91]. The time scale for the opening in this project is not known in detail but it appears to be below 150  $\mu\text{s}$  (and most likely significantly less). Jet structures also appear to be both abrupt and powerful. Thus, it is possible that the diffusion ignition phenomena causing the observed ignition.

Nevertheless, it is hard to differentiate the jet behaviour and magnitude in a release that resulted in ignition from another that did not give ignition. But with relatively long intervals between the pictures and limited quality in the pictures itself, it is hard to see the mechanisms in detail. Thus, it could be that the jet structures in the ignited releases are stronger than some unknown threshold even though this is not detectable on the pictures.

### 5.7.2 Ignition by impact of debris from the rupture discs

This potential ignition mechanism was not discussed prior to the experiments but was revealed during the experiments. Debris of the rupture discs was observed as they impacted the obstruction object in all experiments. The typical chain of events for these impacts, are shown in Figure 5-24. The objects travelled through the visible area in less than the time difference between two pictures. The objects also leave a trajectory in the pictures, as the shutter speed is too slow to pinpoint the debris to an exact location. As shown on Figure 5-25, the impacts also leave visible marks in the obstruction objects. Although only OO C is shown in the figure, the same marks were found on all obstruction objects, including the end of the connection rod.

Other pictures of tests without obstructions showed that pieces of debris had travelled through the whole viewing area of the camera during a single picture. This corresponded to a velocity of *at least* 176 m/s. This velocity could be used as a conservative estimate for the kinetic energy in the debris. As the debris is affected by gravity in the vertical releases, and also has a certain mass that must be accelerated during the short distance from the disc location to the impact area, the objects are not likely to attain the same velocity as the released gas. Nevertheless, sonic velocity of hydrogen could be used as a high estimate of the kinetic energy.

As almost nothing of the material that covered the opened section of the disc remained attached to the burst disc body, much more debris than the collected amount was released during the experiments. An opened rupture disc is shown in Figure 5-25 together with a photo of the collected pieces of debris.

Some of these pieces was later found inside the explosion chamber. The collected pieces were weighed on a weight with display capacity to show resolution of  $10^{-4}$  g, however, the accuracy and repeatability of the weight were not known.

Based on the mass of the particles and the estimated velocities, the kinetic energy of the particles has been calculated with Eq. (18). Mass data and calculated values for kinetic energy are presented in Table 5-2.

Table 5-2 Weight and estimated kinetic energy for the collected debris

Number of pieces collected	Description of debris	Approximate mass per piece [mg]	High estimate for energy [mJ]	Low estimate for energy [mJ]
1	Almost a complete disc	11.8	9971	182.8
4	Medium sized	3.0-5.0	2535-4225	46.5-77.4
2	Small	1.0-2.0	845-1690	15.5-31.0
4	Very small	< 1.0	<845	<15.5

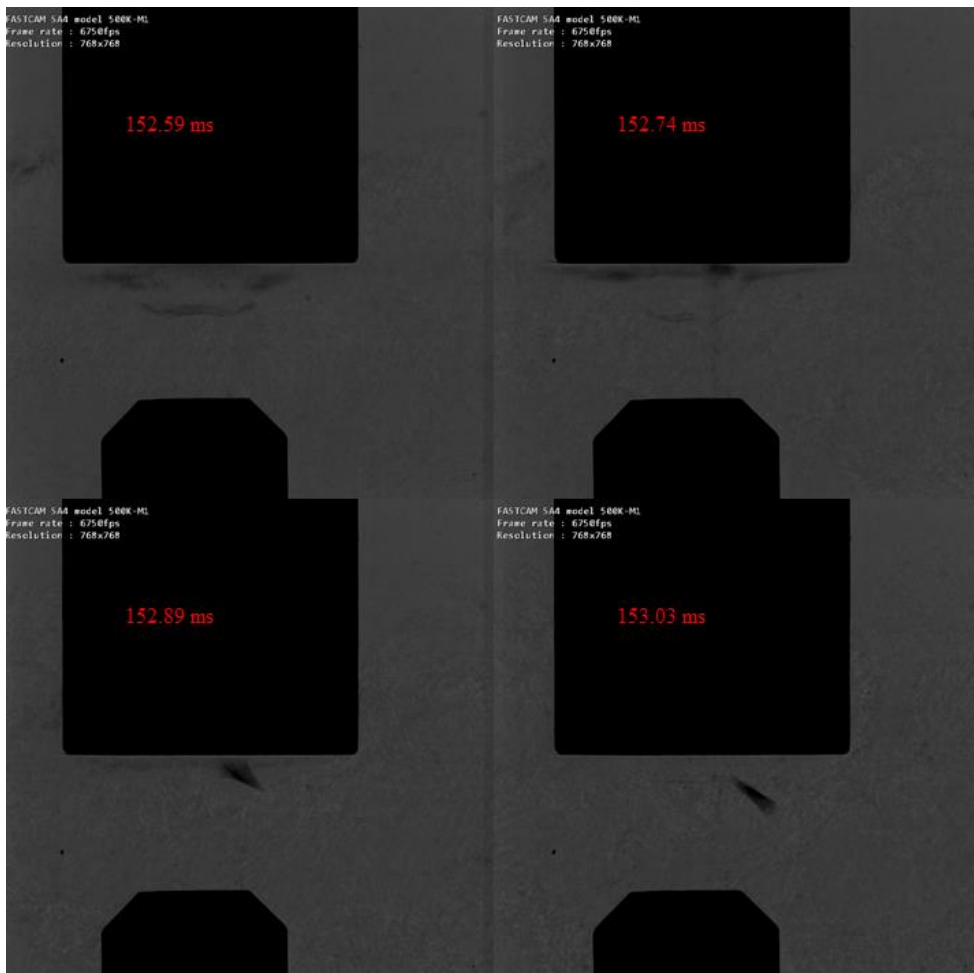


Figure 5-24 Timelapse for a typical impact between debris from the rupture disc and the obstruction object.



Figure 5-25 Grooves in OOC caused by impacts from debris (left). An open rupture disc (middle). Collected debris from all experiments. Thumbtack for size reference (right)

Not much information exists about particle impact on surfaces without preheating as ignition source. No relevant literature was found about this issue, but as this potential ignition mechanism was first observed at the end of the thesis work, literature survey in this topic was not a part of the initial scope. However, as mentioned in 2.4.6, particle impact as ignition source has been considered possible in other contexts. Mechanisms for shock-heating of particles are also described.

Based on the low amount of information about this potential mechanism, it is not likely that the impact from the debris alone was the ignition source in these tests, but it cannot be excluded. However, impacts of particles in combination with heating effects might have the potential to ignite the hydrogen-air mixtures.

Much more knowledge is needed before this potential ignition mechanism could be rejected. Both further literature surveys within topics related to this, and modified experiments should be conducted to obtain sufficient knowledge about this. By using rupture discs that does not release debris, it should be possible to efficiently decide if this mechanism is possible. Such discs could for instance be made with thicker materials with grooves to achieve desired burst pressure. Such discs should leave a number of opened petals still attached to the rupture disc frame instead of releasing debris particles into the flow. However, such rupture disc designs are likely to give increased rupture times [96]. This change must be considered along with the potential for impact ignition if the propensity for ignition changes with new disc design.

## 5.8 Repeatability and uncertainty

Several tests with identical pressure and obstruction conditions were conducted for the conditions that was considered to have the highest propensity for ignition. As such, it is possible to determine with high degree of certainty that ignition cannot occur at conditions that are less vigorous than those investigated here. Some work remains to ensure repeatability on all boundary conditions. But given the observations from the experiments, it is more important to expand the investigated area with increasing pressures and more capable combinations of obstruction objects and distances, than investigating repeatability for the conditions already investigated.

Because of the limited number of available rupture discs, evaluation of uncertainty was not prioritised for these experiments. However, some of the tests were similar enough in their conditions to give some indications of repeatability for the highest release pressures and shortest distances. However, when the investigated area has been further extended in future experiments, repeatability evaluations by conducting multiple experiments with identical conditions must be prioritised.

The qualitative nature of the objectives in this thesis resulted in a low focus on quantitative uncertainties. Uncertainties were for instance not calculated for the pressure recordings, even though this would have been possible with the available information about the transducers and amplifier. However, due to the oscillations in these data, it might be a complicated process to calculate the uncertainty.

## 6 Conclusions

Propensity for spontaneous ignition upon abrupt releases of high-pressure hydrogen has been investigated. Two different setups were used to investigate releases initiated in widely different time scales. The effect of obstructions with various shapes, sizes and distances impinged by the jet was also evaluated. Pressures between 10 and 175 bar was investigated, along with obstructions located between 7.2 and 30.2 mm away from the nozzle outlet. Releases through rupture discs were well investigated in earlier work, but not in combination with obstruction objects at the outside of the nozzle. No previous work has been found about propensity for ignition during releases through fast acting valves.

Both setups produced jet structures both with and without obstructions present. The jet structures appeared to be expanded jets. Some uncertainty exist about whether it was overexpanded or underexpanded jets.

A pneumatically actuated valve with an estimated opening time of 30-60 milliseconds (ms) was used to investigate releases that developed at a millisecond-scale. A 205 mm nozzle arrangement with ~5 mm inner diameter was used in conjunction with this valve. The influence of a semi-circular obstruction in front of the nozzle exit at distances varying from 7.9 to 19.5 mm, and pressures between 10 to 165 barg was investigated. Additional test with a narrower obstruction at 7.2 mm distance or no obstruction at all were also conducted at pressure ranges from 60 to 100 bars. A total of 43 experiments were conducted with release valve and various obstruction and pressure combinations.

None of the investigated combinations using the release valve resulted in ignition.

Rupture discs with rated burst pressures of 50, 80 and 100 barg ( $\pm 10\%$ ) were used in conjunction with the release valve to investigate releases that developed at a microsecond-scale. All the rupture disc pressure A 215 mm nozzle arrangement with shifting inner diameters between 5 and 8 mm was used in conjunction with the discs.

- Six out of 14 experiments resulted in immediate ignition.
- None of the tests with 50 bar rupture discs resulted in ignition
- Rupture discs with 80 and 100 bar rupture pressure resulted in ignition in the presence of an obstruction at sufficiently close distance.
- Shorter distances between the nozzle exit and the obstruction increased the possibility for ignition
- Rupture discs with high pressure in combination with obstructions at short distances gave repeated ignitions. Although too few tests were conducted to draw any definite conclusions regarding this.

The ignition source was not identified with absolute certainty in these tests. Two different ignition sources were plausible:

- Diffusion ignition caused by interactions between shock waves from the nozzle exit and reflected shock waves from the obstructions. Diffusion effects could also have occurred within the nozzle arrangement in addition to the observed shock waves at the outlet.
- Kinetic energy release upon impact between the obstruction and debris originating from the collapsed rupture disc.

Among these two mechanisms, diffusion ignition is the most probable.



## 7 Suggestions for further work

Based on the findings and limitations in this thesis work, some essential aspects are suggested for further investigations

Although ignition never occurred with releases through fast acting valves in this setup, it would be of great interest to investigate such releases at higher pressures. As 1000 bar hydrogen systems are commercially available, the mechanism should be investigated up to at least this pressure. A wider range of obstruction objects and distances should also be investigated in order to identify potentially dangerous designs near potential hydrogen leakage points. Efforts should also be made to find combinations of valves, actuators and instrumentation that yields faster opening times than the setup used in this setup. As such, the large difference in time scale between the current valve setup and rupture disc applications could be investigated.

More experiments should be conducted with rupture discs. A wider range of combinations of obstruction objects, distances and pressures should be investigated to quantify the critical conditions for ignition. The current setup for rupture disc experiments depends on the release valve to initiate rupture and trigger the instrumentation. Future work should try to identify if the intermediate reduction in flow rate due to the definite opening time of the valve affects the propensity for ignition at marginal conditions.

The instrumentation should be improved in future tests. Faster frame rates are necessary to identify the ignition source in tests where ignition occurs. More piezoelectric transducers at various locations should be used to ensure a better understanding of the shock waves and jet development. Proposed locations are inside the release nozzle, at or near the impact point on the obstruction objects and at different locations in the cavity surrounding the obstruction. Photodiodes should also be added to the instrumental setup. Photodiodes in combination with pressure transducers might be able to detect marginal or intermittent ignitions.

# References

- [1] H. Ritchie and M. Roser, “Energy - Our World in Data,” *Our world in data*, 2015. <https://ourworldindata.org/energy#how-much-energy-does-the-world-consume> (accessed Oct. 26, 2020).
- [2] BP, “Statistical Review of World Energy,” 2020. Accessed: Oct. 25, 2020. [Online]. Available: [www.bp.com/statisticalreview](http://www.bp.com/statisticalreview).
- [3] BP, “Energy Outlook 2020 edition,” 2020. Accessed: Oct. 25, 2020. [Online]. Available: <https://www.bp.com/content/dam/bp/business-sites/en/global/corporate/pdfs/energy-economics/energy-outlook/bp-energy-outlook-2020.pdf>.
- [4] DNV GL, “Energy Transition Outlook 2020 - A global and regional forecast to 2050,” 2020. [Online]. Available: <https://eto.dnvgl.com/2020/index.html>.
- [5] International Energy Agency, “World Energy Outlook 2020 – Analysis - IEA,” *World energy outlook 2020*, 2020. <https://www.iea.org/reports/world-energy-outlook-2020> (accessed Oct. 26, 2020).
- [6] United Nations - Department of Economic and Social Affairs - Population Division and United Nations, “World Population Prospects 2019 Highlights,” 2019. Accessed: Jul. 27, 2021. [Online]. Available: [https://population.un.org/wpp/Publications/Files/WPP2019\\_Highlights.pdf](https://population.un.org/wpp/Publications/Files/WPP2019_Highlights.pdf).
- [7] H. Kharas and K. Hamel, “A global tipping point: Half the world is now middle class or wealthier,” 2018. Accessed: Oct. 26, 2020. [Online]. Available: <https://www.brookings.edu/blog/future-development/2018/09/27/a-global-tipping-point-half-the-world-is-now-middle-class-or-wealthier/>.
- [8] H. Kharas, “The unprecedented expansion of the global middle class - an update,” 100, 2017. Accessed: Jan. 23, 2019. [Online]. Available: [https://www.brookings.edu/wp-content/uploads/2017/02/global\\_20170228\\_global-middle-class.pdf](https://www.brookings.edu/wp-content/uploads/2017/02/global_20170228_global-middle-class.pdf).
- [9] Climatewatch, “Global historical emissions,” *Historical GHG emissions*. [https://www.climatewatchdata.org/ghg-emissions?breakBy=sector&chartType=area&end\\_year=2016&gases=all-ghg&start\\_year=1990](https://www.climatewatchdata.org/ghg-emissions?breakBy=sector&chartType=area&end_year=2016&gases=all-ghg&start_year=1990) (accessed Dec. 14, 2020).
- [10] International energy agency, “Global CO2 emissions in 2019,” 2020.
- [11] University of East Anglia, “Data (CRUT).” <https://sites.uea.ac.uk/cru/data> (accessed Dec. 30, 2020).
- [12] N. L. Bindoff *et al.*, “Chapter 10 - Detection and attribution of climate change: From global to regional,” in *Climate Change 2013: The Physical Science Basis. IPCC Working Group I Contribution to AR5*, vol. 9781107057, Cambridge: Cambridge University Press, 2013, pp. 867–952.
- [13] United Nations, “United nations framework convention on climate change - home page.” <https://unfccc.int/> (accessed Dec. 31, 2020).
- [14] United Nations Framework Convention on Climate Change (UNFCCC), *The Paris agreement - treaty*. 2015, p. 27.
- [15] M. R. Allen *et al.*, “SPECIAL REPORT Global warming of 1.5°C Chapter 1 Framing and context,” in *IPCC special report: Global warming of 1.5 C*, 2018, pp. 49–92.
- [16] J. Rogelj *et al.*, “SPECIAL REPORT Global warming of 1.5°C Chapter 2 Mitigation pathways

- compatible with 1.5°C in the context of sustainable development,” in *IPCC special report: Global Warming of 1.5 °C*, 2018, pp. 93–174.
- [17] H. Blanco *et al.*, “The Future of Hydrogen,” Paris, France, 2019.
- [18] J. Aarnes, M. Eijgelaar, and E. . Hektor, “Hydrogen as an energy carrier,” 2018. [Online]. Available: <https://www.dnvgl.com/oilgas/download/hydrogen-as-an-energy-carrier.html>.
- [19] IEAGHG and C. K. Preston, “The CCS Project at Air Products’ Port Arthur Hydrogen Production Facility,” Cheltenham, UK, 2018. Accessed: Jun. 06, 2021. [Online]. Available: <https://ieaghg.org/publications/technical-reports/reports-list/9-technical-reports/956-2018-05-the-ccs-project-at-air-products-port-arthur-hydrogen-production-facility>.
- [20] A. Frassoldati, T. Faravelli, and E. Ranzi, “A wide range modeling study of NO<sub>x</sub> formation and nitrogen chemistry in hydrogen combustion,” *Int. J. Hydrogen Energy*, vol. 31, no. 15, pp. 2310–2328, Dec. 2006, doi: 10.1016/J.IJHYDENE.2006.02.014.
- [21] U.S. Department of energy, “Hydrogen Storage | Department of Energy.” Accessed: Jul. 27, 2021. [Online]. Available: <https://www.energy.gov/eere/fuelcells/hydrogen-storage>.
- [22] A. Hoffrichter, “HYDROGEN AS AN ENERGY CARRIER FOR RAILWAY TRACTION,” University of Birmingham, Birmingham, 2013.
- [23] International Maritime Organization, “INITIAL IMO STRATEGY ON REDUCTION OF GHG EMISSIONS FROM SHIPS,” 2018. Accessed: Aug. 01, 2021. [Online]. Available: <http://www.imo.org>.
- [24] T. Førde, “Grenser flyttes med verdens første hydrogenferge - Tu.no,” *Teknisk ukeblad*, Mar. 08, 2021.
- [25] T. Stensvold, “Den første hydrogenfergen kommer til Norge i november - Tu.no,” *Teknisk ukeblad*, Aug. 19, 2020.
- [26] Enova, “Neste år kan Finnøysambandet få hydrogenferje,” *Press release*, p. 3, Jan. 15, 2021.
- [27] T. Stensvold, “Wilhelmsen med hydrogenskip i rute mellom Stavanger-Kristiansund - Tu.no,” *Teknisk ukeblad*, 2020.
- [28] McKinsey & Company, Fuel Cells and Hydrogen 2 JU, and Clean Sky 2 JU, “Hydrogen-powered aviation,” 2020. doi: 10.2843/471510.
- [29] Statkraft, “Hydrogenproduksjon og grønt stål i Mo industripark,” *Press release*, Jun. 03, 2020.
- [30] M. Valestrand, “Hydrogen skal erstatte kull i Tyssedal,” *Nor. Energi*, vol. 96, no. 2, pp. 20–23, 2019, Accessed: Jun. 08, 2021. [Online]. Available: <https://energiogklima.no/nyhet/tizir-sikter-pa-gront-hydrogen/>.
- [31] Hybrit, “Hybrit - research project 1, work package 4 hydrogen-based reduction of iron ore.” <https://www.hybritdevelopment.se/> (accessed Jun. 08, 2021).
- [32] H21, “H21 North of England,” 2018. Accessed: Jun. 08, 2021. [Online]. Available: <https://h21.green/projects/h21-north-of-england/>.
- [33] International energy agency, “Energy Technology Perspectives 2020,” 2020. Accessed: Jun. 07, 2021. [Online]. Available: [www.iea.org/t&c/](http://www.iea.org/t&c/).
- [34] M. Rausand and I. B. Utne, *Risikoanalyse - teori og metoder*. Trondheim: Tapir Akademisk forlag, 2009.
- [35] M. E. Paté-Cornell, “Quantitative safety goals for risk management of industrial facilities,” *Struct. Saf.*, vol. 13, no. 3, pp. 145–157, Mar. 1994, doi: 10.1016/0167-4730(94)90023-X.

- [36] G. R. Astbury and S. J. Hawksworth, "Spontaneous ignition of hydrogen leaks: A review of postulated mechanisms," *Int. J. Hydrogen Energy*, vol. 32, no. 13, pp. 2178–2185, Sep. 2007, doi: 10.1016/J.IJHYDENE.2007.04.005.
- [37] U. von Pidoll, E. Brzostek, and H. R. Froechtenigt, "Determining the incendivity of electrostatic discharges without explosive gas mixtures," *IEEE Trans. Ind. Appl.*, vol. 40, no. 6, pp. 1467–1475, Nov. 2004, doi: 10.1109/TIA.2004.836303.
- [38] R. Reider, H. J. Otway, and H. T. Knight, "An unconfined, Large-volume hydrogen/air-explosion," 1971. Accessed: Oct. 13, 2019. [Online]. Available: <https://ntrs.nasa.gov/archive/nasa/casi.ntrs.nasa.gov/19710000041.pdf>.
- [39] J. Bond, *Sources of Ignition: Flammability Characteristics of Chemicals and Products*. Elsevier Ltd, 1991.
- [40] P. Wolanski and S. Wojcicki, "Investigation into the mechanism of the diffusion ignition of a combustible gas flowing into an oxidizing atmosphere," in *14th symp. on combustion, Pittsburgh, PA, the combustion inst*, 1973, pp. 1217–1223.
- [41] P. Oleszczak and P. Wolanski, "Ignition during hydrogen release from high pressure into the atmosphere," *Shock Waves*, vol. 20, no. 6, pp. 539–550, Dec. 2010, doi: 10.1007/s00193-010-0291-x.
- [42] Ludwig-Bölkow-Systemtechnik GmbH, "Press Release 2021: Record number of newly opened hydrogen refuelling stations in 2020 - H2Stations.org." 2021, Accessed: Jul. 27, 2021. [Online]. Available: <https://www.h2stations.org/press-release-2021-record-number-of-newly-opened-hydrogen-refeulling-stations-in-2020/>.
- [43] J. Sakamoto, R. Sato, J. Nakayama, N. Kasai, T. Shibutani, and A. Miyake, "Leakage-type-based analysis of accidents involving hydrogen fueling stations in Japan and USA," *Int. J. Hydrogen Energy*, vol. 41, no. 46, pp. 21564–21570, Dec. 2016, doi: 10.1016/J.IJHYDENE.2016.08.060.
- [44] J. A. Løkke, "The Kjørbo incident," 2019.
- [45] A. P. Harris and C. W. San Marchi, "Investigation of the hydrogen release incident at the AC Transit Emeryville Facility (Revised)," Livermore, CA, 2012. Accessed: Oct. 03, 2019. [Online]. Available: <https://prod-ng.sandia.gov/techlib-noauth/access-control.cgi/2012/128642.pdf>.
- [46] T. Skjold, "On the strength of knowledge in risk assessments for hydrogen systems," in *13th international symposium on Hazards, Prevention, and Mitigation of industrial explosions*, 2020, pp. 72–84.
- [47] Hydrogen tools, "Basic Hydrogen Properties." <https://h2tools.org/hyarc/hydrogen-data/basic-hydrogen-properties> (accessed Jun. 09, 2021).
- [48] G. Cui, Z. Li, and C. Yang, "Experimental study of flammability limits of methane/air mixtures at low temperatures and elevated pressures," *Fuel*, vol. 181, pp. 1074–1080, 2016, doi: 10.1016/j.fuel.2016.04.116.
- [49] "Minimum Ignition Energy (MIE)." <http://explosionsolutions.co.uk/110411020.pdf> (accessed Oct. 11, 2019).
- [50] The engineering toolbox, "Heat of combustion." [https://www.engineeringtoolbox.com/standard-heat-of-combustion-energy-content-d\\_1987.html](https://www.engineeringtoolbox.com/standard-heat-of-combustion-energy-content-d_1987.html) (accessed Apr. 03, 2020).
- [51] V. Babrauskas, *Ignition Handbook: Principles and applications to fire safety engineering, fire investigation, risk management and forensic science*. Issaquah, WA, USA: Fire science publishers, 2003.
- [52] J. G. Speight, *Rules of thumb for petroleum engineers*. Hoboken, NJ, USA: John Wiley & Sons, 2017.

- [53] F. L. Dryer, M. Chaos, Z. Zhao, J. N. Stein, J. Y. Alpert, and C. J. Homer, “Spontaneous ignition of pressurized releases of hydrogen and natural gas into air,” *Combust. Sci. Technol.*, vol. 179, no. 4, pp. 663–694, Mar. 2007, doi: 10.1080/00102200600713583.
- [54] A. A. Konnov, A. Mohammad, V. R. Kishore, N. Il Kim, C. Prathap, and S. Kumar, “A comprehensive review of measurements and data analysis of laminar burning velocities for various fuel+air mixtures,” *Prog. Energy Combust. Sci.*, vol. 68, pp. 197–267, Sep. 2018, doi: 10.1016/J.PECS.2018.05.003.
- [55] European Committee for Electrotechnical Standardization (CENELEC), “Explosive atmospheres - Part 0: Equipment - General requirements.” Brussels, 2018.
- [56] R. K. Eckhoff, *Explosion hazards in the process industries*, Second edi. Gulf professional publishing, 2016.
- [57] Willi Automation & control, “Selection of explosion protected equipment for hazardous locations-hazardous-zone-t1-t2-t3-t4-rate-zone0-zone-1-zone-2-zone-3 - Wili Co., Ltd - Thermo Controls.” <https://www.wili.com.vn/knowledge/119-hazardous-zone-t1-t2-t3-t4-rate-zone0-zone-1-zone-2-zone-3> (accessed Jul. 24, 2021).
- [58] Health and safety executive, “Hazardous Area Classification and Control of Ignition Sources.” Accessed: Jul. 24, 2021. [Online]. Available: <https://www.hse.gov.uk/comah/sragtech/techmeasareacclas.htm#references>.
- [59] J. D. Anderson, *Modern compressible flow*, 3rd ed. New York, NY: McGraw-Hill, 2004.
- [60] Fisher Controls International LLC, “CONTROL VALVE HANDBOOK Third Edition,” 2001.
- [61] W. J. Devenport and Y. Wang, “Nozzle Applet,” *Virginia Tech*, 2001. <http://www.engapplets.vt.edu/fluids/CDnozzle/cdinfo.html> (accessed Jan. 20, 2021).
- [62] HyResponse, “LECTURE. Unignited hydrogen releases, their prevention and mitigation,” in *Educational materials: hydrogen safety basics for First Responders*, HyResponse.
- [63] V. Volkov, “Fundamentals of Hydrogen Safety Engineering 1,” in *Fundamentals of Hydrogen Safety Engineering*, Bookbon learning, 2012, p. 216.
- [64] Flowserve Valtek, *Flowserve Valtek Control Valve Sizing & Selection Manual*. 1994.
- [65] Butech, “Technical information,” *Butech Catalog chapter*, Erie, Pennsylvania, USA, p. 11.
- [66] Autoclave Engineers, “Valves, Fittings and Tubing Medium and High Pressure Condensed Catalog,” *Autoclave brochure*, Wexford, Republic of Ireland, p. 20, 2017.
- [67] M. Helbæk and S. Kjelstrup, *Fysikalsk kjemi*, 2nd ed. Bergen, Norway: Fagbokforlaget, 2006.
- [68] S. Matsuo, S. Koyama, J. Nagao, and T. Setoguchi, “Flow characteristics of high-pressure hydrogen gas in the critical nozzle,” p. 5.
- [69] J. E. Jensen, W. A. Tuttle, R. B. Stewart, H. Brechna, A. G. Prodell, and Brookhaven national laboratory, “Section VI. Properties of nitrogen,” in *Selected cyogenic data notebook*, Volume 1., J. E. Jensen, W. A. Tuttle, R. B. Stewart, H. Brechna, and A. G. Prodell, Eds. Brookhaven National laboratory, 1980, p. 45.
- [70] R. Ishii, H. Fujimoto, N. Hatta, and Y. Umeda, “Experimental and numerical analysis of circular pulse jets,” *J. Fluid Mech*, vol. 392, pp. 129–153, 1999, doi: 10.1017/S0022112099005303.
- [71] A. Davidhazy, “Introduction to shadowgraph and schlieren imaging,” 478, 2006. Accessed: Jul. 08, 2021. [Online]. Available: <http://scholarworks.rit.edu/article/478>.
- [72] C. Mauger, L. Méès, M. Michard, A. Azouzi, and S. Valette, “Shadowgraph, Schlieren and interferometry in a 2D cavitating channel flow,” *Exp. Fluids*, no. 6, pp. 1895–1913, 2012, doi:

10.1007/s00348-012-1404-3i.

- [73] H. Hu, "Lecture # 07: Flow Visualization techniques: Shadowgraph and Shadowgraph and Schlieren." Accessed: Jul. 08, 2021. [Online]. Available: <https://www.aere.iastate.edu/~huhui/teaching/2010Sx/AerE343L-AerE311L/Lecture-notes/Lecture-07-Notes.pdf>.
- [74] Opto Engineering, "Telecentric lenses - Opto Engineering." <https://www.opto-e.com/basics/telecentric-lenses> (accessed Jul. 09, 2021).
- [75] Ø. Grøn and J. Sandstad, "piezoelektrisitet – Store norske leksikon," *Store Norske Leksikon*. 2020, Accessed: Jul. 13, 2021. [Online]. Available: <https://snl.no/piezoelektrisitet>.
- [76] Kistler Instrumente AG, "Data sheet, Type 701A." p. 2.
- [77] Kistler Instrumente AG, "Manual: Test & measurement - pressure." p. 64, 2020.
- [78] "Adiabatisk prosess – Wikipedia." [https://nn.wikipedia.org/wiki/Adiabatisk\\_prosess](https://nn.wikipedia.org/wiki/Adiabatisk_prosess) (accessed Oct. 17, 2019).
- [79] B.-Z. Maytal and J. M. Pfotenhauer, "The Joule-Thomson Effect, Its Inversion and Other Expansions," in *Miniature Joule-Thomson Cryocooling*, New York, NY: Springer New York, 2013, pp. 39–72.
- [80] A. Michels, W. de Graaff, and G. J. Wolkers, "Thermodynamic properties of hydrogen and deuterium at temperatures between  $-175^{\circ}\text{C}$  and  $150^{\circ}\text{C}$  and at pressures up to 2500 atmospheres," *Appl. Sci. Res.*, vol. 12, no. 1, pp. 9–32, Jan. 1964, doi: 10.1007/BF03184744.
- [81] M. W. Crofton, P. T. Stout, M. M. Micci, and E. L. Petersen, "Particle-Impact Ignition Measurements in a High-Pressure Oxygen Shock Tube," in *28th International Symposium on Shock Waves*, 2012, pp. 301–306, doi: 10.1007/978-3-642-25685-1\_46.
- [82] A. Y. Shebeko, Y. N. Shebeko, A. V. Zuban, and N. V. Golov, "Experimental Investigation of the Ignition of Combustible Gas Mixtures by Friction Sparks," *Combust. Explos. Shock Waves*, vol. 54, no. 3, pp. 264–274, Jun. 2018, doi: 10.1134/S0010508218030024.
- [83] Y. Jiang *et al.*, "Pressure dynamics, self-ignition, and flame propagation of hydrogen jet discharged under high pressure," *Int. J. Hydrogen Energy*, vol. 44, no. 40, pp. 22661–22670, Aug. 2019, doi: 10.1016/J.IJHYDENE.2019.03.268.
- [84] Z. Wang *et al.*, "Experimental study on spontaneous ignition and flame propagation of high-pressure hydrogen release through tubes," *Int. J. Hydrogen Energy*, vol. 44, no. 40, pp. 22584–22597, Aug. 2019, doi: 10.1016/J.IJHYDENE.2019.06.188.
- [85] X. Pan *et al.*, "Experimental Investigation of the Self-Ignition and Jet Flame of Hydrogen Jets Released under Different Conditions," *ACS Omega*, vol. 4, no. 7, pp. 12004–12011, Jul. 2019, doi: 10.1021/acsomega.9b01214.
- [86] V. V. Golub *et al.*, "Mechanisms of high-pressure hydrogen gas self-ignition in tubes," *J. Loss Prev. Process Ind.*, vol. 21, no. 2, pp. 185–198, Mar. 2008, doi: 10.1016/J.JLP.2007.06.012.
- [87] V. V. Golub *et al.*, "Shock-induced ignition of hydrogen gas during accidental or technical opening of high-pressure tanks," *J. Loss Prev. Process Ind.*, vol. 20, no. 4–6, pp. 439–446, Jul. 2007, doi: 10.1016/J.JLP.2007.03.014.
- [88] T. Mogi, Y. Wada, Y. Ogata, and A. K. Hayashi, "Self-ignition and flame propagation of high-pressure hydrogen jet during sudden discharge from a pipe," *Int. J. Hydrogen Energy*, vol. 34, no. 14, pp. 5810–5816, Jul. 2009, doi: 10.1016/J.IJHYDENE.2009.04.079.
- [89] T. Mogi, D. Kim, H. Shiina, and S. Horiguchi, "Self-ignition and explosion during discharge of high-pressure hydrogen," *J. Loss Prev. Process Ind.*, vol. 21, no. 2, pp. 199–204, Mar. 2008, doi:

10.1016/J.JLP.2007.06.008.

- [90] Y.-F. Liu, N. Tsuboi, H. Sato, F. Higashino, and A. K. Hayashi, "Direct numerical simulation on hydrogen fuel jetting from high pressure tank," *Proc. 20th Int. colloquium Dyn. Explos. React. Syst.*, Accessed: Sep. 26, 2019. [Online]. Available: [https://www.researchgate.net/profile/Yunfeng\\_Liu10/publication/269204462\\_Ignition\\_of\\_Hydrogen\\_Suddenly\\_Leaked\\_from\\_a\\_High\\_Pressure\\_Tank/links/5bb19029299bf13e605968ec/Ignition-of-Hydrogen-Suddenly-Leaked-from-a-High-Pressure-Tank.pdf](https://www.researchgate.net/profile/Yunfeng_Liu10/publication/269204462_Ignition_of_Hydrogen_Suddenly_Leaked_from_a_High_Pressure_Tank/links/5bb19029299bf13e605968ec/Ignition-of-Hydrogen-Suddenly-Leaked-from-a-High-Pressure-Tank.pdf).
- [91] B. P. Xu, J. X. Wen, S. Dembele, V. H. Y. Tam, and S. J. Haworth, "The effect of pressure boundary rupture rate on spontaneous ignition of pressurized hydrogen release," *J. Loss Prev. Process Ind.*, vol. 22, no. 3, pp. 279–287, May 2009, doi: 10.1016/J.JLP.2008.07.007.
- [92] J. X. Wen, B. P. Xu, and V. H. Y. Tam, "Numerical study on spontaneous ignition of pressurized hydrogen release through a length of tube," *Combust. Flame*, vol. 156, no. 11, pp. 2173–2189, Nov. 2009, doi: 10.1016/j.combustflame.2009.06.012.
- [93] B. P. Xu, L. El Hima, J. X. Wen, S. Dembele, V. H. Y. Tam, and T. Donchev, "Numerical study on the spontaneous ignition of pressurized hydrogen release through a tube into air," *J. Loss Prev. Process Ind.*, vol. 21, no. 2, pp. 205–213, Mar. 2008, doi: 10.1016/J.JLP.2007.06.015.
- [94] S. V. Golovastov and V. Bocharnikov, "The influence of diaphragm rupture rate on spontaneous self-ignition of pressurized hydrogen: Experimental investigation," *Int. J. Hydrogen Energy*, vol. 37, no. 14, pp. 10956–10962, Jul. 2012, doi: 10.1016/J.IJHYDENE.2012.04.070.
- [95] W. Kaneko and K. Ishii, "Effects of diaphragm rupturing conditions on self-ignition of high-pressure hydrogen," *Int. J. Hydrogen Energy*, vol. 41, no. 25, pp. 10969–10975, Jul. 2016, doi: 10.1016/J.IJHYDENE.2016.04.211.
- [96] L. Gong, Q. Duan, J. Sun, and V. V. Molkov, "Similitude analysis and critical conditions for spontaneous ignition of hydrogen release into the atmosphere through a tube," *Fuel*, vol. 245, pp. 413–419, Jun. 2019, doi: 10.1016/j.fuel.2019.02.064.
- [97] L. Gong, Q. Duan, J. Liu, M. Li, K. Jin, and J. Sun, "Effect of burst disk parameters on the release of high-pressure hydrogen," *Fuel*, vol. 235, pp. 485–494, Jan. 2019, doi: 10.1016/j.fuel.2018.08.044.
- [98] J. E. Drewry and Z. A. Walenta, "Determination of diaphragm opening-times and use of diaphragm particle traps in a hypersonic shock tube," University of Toronto, 1965.
- [99] N. Kitabayashi, Y. Wada, T. Mogi, T. Saburi, and A. K. Hayashi, "Experimental study on high pressure hydrogen jets coming out of tubes of 0.1–4.2 m in length," *Int. J. Hydrogen Energy*, vol. 38, no. 19, pp. 8100–8107, Jun. 2013, doi: 10.1016/J.IJHYDENE.2012.10.040.
- [100] K. Yamashita, T. Saburi, Y. Wada, M. Asahara, T. Mogi, and A. K. Hayashi, "Visualization of spontaneous ignition under controlled burst pressure," *Int. J. Hydrogen Energy*, vol. 42, no. 11, pp. 7755–7760, Mar. 2017, doi: 10.1016/j.ijhydene.2016.06.240.
- [101] X. Pan *et al.*, "Experimental study on pressure dynamics and self-ignition of pressurized hydrogen flowing into the L-shaped tubes," *Int. J. Hydrogen Energy*, vol. 45, no. 7, pp. 5028–5038, Feb. 2020, doi: 10.1016/j.ijhydene.2019.11.161.
- [102] L. Gong, Q. Duan, Q. Sun, K. Jin, and J. Sun, "Effects of the geometry of downstream pipes with different angles on the shock ignition of high-pressure hydrogen during its sudden expansion," *Int. J. Hydrogen Energy*, vol. 42, no. 12, pp. 8382–8391, Mar. 2017, doi: 10.1016/j.ijhydene.2017.02.025.
- [103] Q. Duan, H. Xiao, W. Gao, L. Gong, and J. Sun, "Experimental investigation of spontaneous ignition and flame propagation at pressurized hydrogen release through tubes with varying cross-section," *J. Hazard. Mater.*, vol. 320, pp. 18–26, Dec. 2016, doi: 10.1016/j.jhazmat.2016.08.005.

- [104] P. Li, Q. Duan, L. Gong, K. Jin, J. Chen, and J. Sun, "Effects of obstacles inside the tube on the shock wave propagation and spontaneous ignition of high-pressure hydrogen," *Fuel*, vol. 236, pp. 1586–1594, Jan. 2019, doi: 10.1016/J.FUEL.2018.09.120.
- [105] L. Gong *et al.*, "Numerical study on the mechanism of spontaneous ignition of high-pressure hydrogen in the L-shaped tube," *Int. J. Hydrogen Energy*, vol. 45, no. 56, pp. 32730–32742, Nov. 2020, doi: 10.1016/j.ijhydene.2020.08.267.
- [106] L. Gong *et al.*, "Spontaneous ignition of high-pressure hydrogen during its sudden release into hydrogen/air mixtures," *Int. J. Hydrogen Energy*, vol. 43, no. 52, pp. 23558–23567, Dec. 2018, doi: 10.1016/j.ijhydene.2018.10.226.
- [107] L. Gong, Q. Duan, J. Liu, M. Li, K. Jin, and J. Sun, "Experimental investigation on effects of CO<sub>2</sub> additions on spontaneous ignition of high-pressure hydrogen during its sudden release into a tube," *Int. J. Hydrogen Energy*, vol. 44, no. 13, pp. 7041–7048, Mar. 2019, doi: 10.1016/j.ijhydene.2019.01.197.
- [108] L. Gong, Q. Duan, L. Jiang, K. Jin, and J. Sun, "Experimental study of pressure dynamics, spontaneous ignition and flame propagation during hydrogen release from high-pressure storage tank through 15 mm diameter tube and exhaust chamber connected to atmosphere," *Fuel*, vol. 182, pp. 419–427, Oct. 2016, doi: 10.1016/j.fuel.2016.05.127.
- [109] Q. Duan, H. Xiao, W. Gao, L. Gong, Q. Wang, and J. Sun, "Experimental study on spontaneous ignition and flame propagation of high-pressure hydrogen release via a tube into air," *Fuel*, vol. 181, pp. 811–819, Oct. 2016, doi: 10.1016/j.fuel.2016.05.066.
- [110] Photron Limited, "Fastcam SA4 High-speed imaging system," *Photron datasheet*. Tokyo, Japan, Accessed: Jul. 08, 2021. [Online]. Available: <https://www.highspeedimaging.com/photron-fastcam-sa4/>.
- [111] T. Skjold, "SELECTED ASPECTS OF TURBULENCE AND COMBUSTION IN 20-LITRE EXPLOSION VESSELS Development of Experimental Apparatus and Experimental Investigation," The University of Bergen, 2003.
- [112] Belman AS, "Catalogue - Expansion joints." Belman AS, Esbjerg, Denmark, p. 504, [Online]. Available: <https://www.belman.com/download/>.
- [113] SITEC-Sieber Engineering AG, "High-pressure components catalogue." Accessed: May 20, 2021. [Online]. Available: <https://www.sitec-hp.ch/en/Willkommen>.
- [114] SITEC-Sieber Engineering AG, "Email-correspondance Sitec-Sieber valve vendor." p. 1, 2020.
- [115] Parker Hannifin Corporation, "Parker Needle Valves Catalog, 4110-NV." 2019, Accessed: May 21, 2021. [Online]. Available: [www.parker.com/ipdus](http://www.parker.com/ipdus).
- [116] Norsk olje og gass, "Fittings og small bore tubing systemer," Norsk olje og gass, 2020. Accessed: May 23, 2021. [Online]. Available: <https://www.norskoljeoggass.no/globalassets/dokumenter/drift/hc-lekkasjer/handboker/handbok-fittings-og-small-bore-tubing-systemer---03.04.2020.pdf>.
- [117] Hy-Lok Corporation, "Hy-Lok tube fittings catalogue." p. 76, 2017.
- [118] The engineering toolbox, "ANSI B1.20.1 - NPT - American National Standard Taper Pipe Threads." [https://www.engineeringtoolbox.com/npt-national-pipe-taper-threads-d\\_750.html](https://www.engineeringtoolbox.com/npt-national-pipe-taper-threads-d_750.html) (accessed May 25, 2021).
- [119] The engineering toolbox, "ISO 228 - Pipe Threads where Pressure-tight Joints are not made on the Threads." [https://www.engineeringtoolbox.com/iso-228-pipe-threads-d\\_2037.html](https://www.engineeringtoolbox.com/iso-228-pipe-threads-d_2037.html) (accessed May 25, 2021).
- [120] Aventics, "Catalog: Series CD07." p. 176, 2020, [Online]. Available:



<https://www.emerson.com/en-au/catalog/aventics-sku-5772075280>.

- [121] Photron Limited, “Photron Fastcam Viewer software– Photron.” <https://photron.com/photron-support/> (accessed Jul. 18, 2021).
- [122] I. B. Kalvatn, “Experimental investigation of the optical measurement method for detecting dust and gas flames in a flame acceleration tube,” University of Bergen, 2009.
- [123] T. Skjold, D. Castellanos, K. L. Olsen, and R. K. Eckhoff, “Experimental and numerical investigation of constant volume dust and gas explosions in a 3.6-m flame acceleration tube,” *J. Loss Prev. Process Ind.*, vol. 30, no. 1, pp. 164–176, Jul. 2014, doi: 10.1016/J.JLP.2014.05.010.

# Appendices

# A Technical and functional description

The experimental setup can roughly be divided in the following sections:

- Explosion chamber and blowdown pipe.
- High-pressure hydrogen system
- Instrumentation and logging systems
- Structural supports

The sections are partly integrated, and the categorisation above is based on the functionality of the different parts of the system. Figure appendix 1 gives an overview of the most important components of all sections except the support structures section.

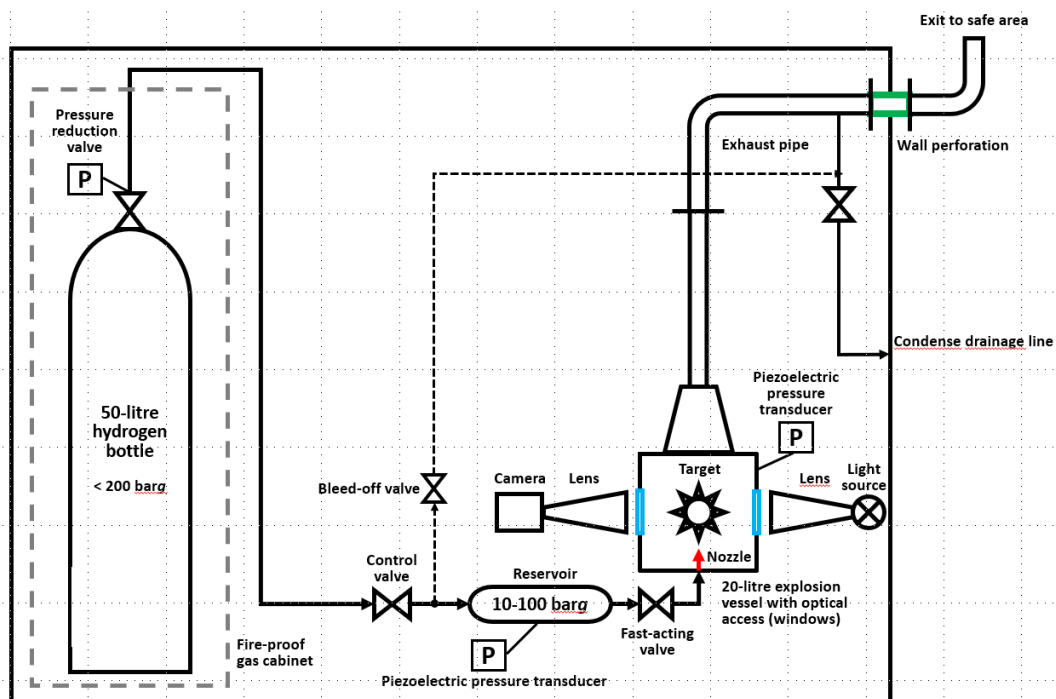


Figure appendix 1 Shows a brief overview of the experimental setup. The most important parts of the blowdown pipe, high pressure hydrogen system and instrumentation are shown.

## A.1 Explosion chamber and blowdown pipe

This system is designed to provide a safe volume to conduct explosion experiments in atmospheric pressure air. The experiments are conducted inside the explosion chamber, which is directly connected to an open blowdown pipe. Exhaust gases from combustions and explosions are thus led to a safe location. The system is shown on a piping and instrumentation diagram (P&ID), namely P&ID-01-02.

### A.1.1 Explosion chamber

The experiments were conducted in the explosion chamber. This chamber is a 20-litre cubical vessel that was initially built for constant volume explosion experiments with dust mixtures. The initial design and purpose is described elsewhere [111, Ch. Appendix B]. With a cubical shape and an internal volume

of 20 litres, the dimensions are 271 mm in each direction ( $\sqrt[3]{20 \text{ dm}^3}$ ). The chamber is equipped with the following utilities:

- 2 Visualisation windows
- 2 Equipment flanges
- 8 Threaded ports; different sizes.
- Bottom flange

Two circular visualisation windows with a diameter of 140mm are located at opposite walls. The windows are aligned with the same vertical and horizontal position on each side, thus providing a line of sight through the vessel that is perpendicular to the walls with the windows. A clear line of sight through the vessel is a prerequisite for visual observation techniques like Schlieren and Shadowgraph. In this project, Shadowgraph was used, and the two lenses were aligned with each other on each side of the vessel.

The two remaining side walls are equipped with two smaller flanges suitable for various equipment, one on each side. Their outer diameter is 82.2 mm, and they are mounted with 12 M8 bolts. These flanges are also aligned so that the line dragged through the centre of each flange lies perpendicular to the side walls it is perforating. Depending on the design of the flanges, these ports can serve a vast difference of purposes. They have for instance earlier been used for electric arc ignition. This was done by mounting one electrode in each flange. The end point of each electrode was separated by a sufficient air gap in the middle of the vessel, thus giving short circuit at the appropriate voltage. Other purposes for these flanges could include additional visualisation windows, for instance used for ignition detection with photo diode.

A total of 8 threaded ports are distributed on the two side walls with the small flanges. They have different dimensions, for instance ½” pipe threads and M14x1.25 [111, Fig. B-8]. They can be used for different purposes, for instance gas filling when a modified atmosphere is required. or flushing. In this project, one of the ports was connected to a hose with compressed air used to flush the vessel after each experiment to dilute and displace remaining uncombusted gas or combustion products. A piezo electric pressure transducer was mounted in one of the other ports, providing a “neutral” measurement of the pressure development during the experiments.

In the centre of the bottom of the vessel, there is another flange. The hole in the vessel has a diameter of approximately 40.5 mm, while the outer diameter of the flange is 100 mm. The centre of the flange is elevated 30 mm, corresponding to the thickness of the bottom of the vessel, thus giving a relatively planar surface in the bottom of the vessel. The flange is drilled and threaded with M20x1.5. With this threading, the flange will work as the fitting side of the medium-pressure fitting system used, thus enabling interconnection between the high-pressure hydrogen system and the vessel. The sealing principles and layout in this interconnection is further described in A.2.3 and A.2.6.

## A.1.2 Chamber lid

The square shaped lid on the vessel is fastened with 16 M20 bolts. Sealing between the lid and the vessel is ensured by an O-ring immersed in a groove in the vessel body. The circular opening in the lid has an internal diameter (ID) of 210 mm, and a concentric reducer is integrated (welded) to it. At the lower end of the reducer, the outer diameter (OD) is 219.1 mm, while it is 168.3 mm at the top. This corresponds to a nominal diameter (DN) 200 and DN 150 ISO (both nominal pressure 16 bars (PN16)), respectively. A conventional DN 150 PN 16 flange is located at the top of the reducer.

A piece of steel is mounted on the underside of the lid, right across the 210 mm exit hole. Its purpose is to secure the obstruction object. This object, which can be changed to evaluate how different shapes affect the scenario, is fastened to a brass rod with OD 13 mm. Outer M12 threads at the end of the rod is attached to corresponding inner threads on the obstruction object. The brass rod is lead through a hole

at the center of the steel beam and secured with a set screw. The steel beam is attached to the vessel lid with one M12 screw on each side of the 210 mm exit hole. Further descriptions of the obstruction objects are given in A.2.3.

### A.1.3 Blowdown pipe and utilities

The blowdown pipe is made from two spools of DN 150 mm pipe with 2.6 mm wall thickness. One 90° bend is welded into each spool. Their bending radius, measured at the centreline of the pipe equals 1.5 times the nominal pipe diameter. This means that the bending diameter (for a 180° turn, still at the centreline) equals three times the nominal pipe diameter.

The first bend changes the direction of flow from upwards to horizontal (westwards). The last bend changes the direction towards the wall with the wall perforation (southwards). The total length of the blowdown pipe, from the top of the vessel to the outer end of the wall perforation is approximately 2.6 metres measured along the centreline. The calculated volume, including the part with increased cross-sectional area at the vessel lid is calculated to approximately 56.2 litres.

All joints between the spools and components are made by DN 150 PN 16 flanges. However, two different types of flanges are used. Some are of the conventional fixed type, while others are slip-on flanges. These slip-on flanges are pressed against a neck that is welded to the pipe spool. They can be rotated and – to a certain extent – deviate from the radial plane. As the measurements and also construction work itself had relatively wide tolerances, a certain amount of flexibility was necessary when the spools were installed in their final position. These loose flanges provided some of the flexibility.

In addition to that, the setup contained an axial expansion joint located between the vessel lid and the first pipe spool. The compensator has a “pipe wall” made from multiple layers of steel, shaped with bellows. An illustration is shown in Figure appendix 2. The expansion joint can be compressed or elongated 24 mm in each axial direction. It can also take up 3 mm movement in the radial direction. However, the compensator cannot take up more movement than what corresponds to full movement along one of the axes.

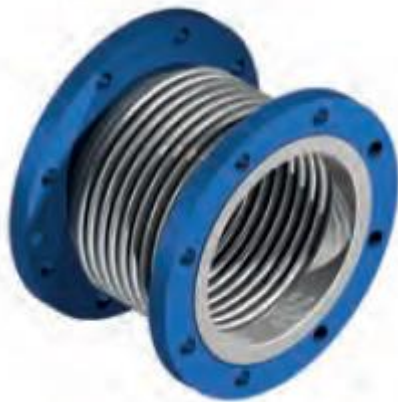


*Figure appendix 2 An illustration of the type of axial expansion joint used in this setup, from [112, p. 95].*

The horizontal stretch of the pipe, and especially the pipe spool that has its full length in the horizontal direction, is intended to have a slight slope towards the wall outlet. A sustained slope in the correct direction will avoid condensed water to flow down to the explosion vessel, but rather to flow towards the outside. Condensed water is expected due to factors explained in A.5. A specific slope has not been defined in the design and manufacturing process, so the actual slope depends on the remaining tolerances during the assembly.

At a later occasion, an upward pointing finish will be mounted to the pipe outlet at the outside, thus preventing drainage through the exhaust pipe outlet. A socket wall outlet (sockolet) is therefore welded onto the underside of the exhaust pipe at the straight pipe section between the wall perforation and the last 3D bend. A sockolet is a short pipe piece with a significantly smaller diameter than the main pipe. It is shaped to fit perfectly to the outer surface of the main pipe. The main pipe is perforated corresponding to the internal diameter of the sockolet. The sockolet used here has  $\frac{3}{4}$ " tapered "pipe threads". The drainage is done through a low-pressure hose, routed to the outside through a cable perforation in the wall, just above the floor. A ball valve above the hose will avoid hydrogen release through this hose.

A branch is connected to the sockolet above the isolation valve towards the drainage hose, so it can fulfil an additional purpose along with providing the possibility for drainage, namely a safe blow down of the high pressure (HP) hydrogen system. A high-pressure hose is routed from the HP hydrogen system to this socket, thus providing a possibility to bleed off the hydrogen pressure without using the fast-acting valve into the explosion vessel. This is a safety measure in case any problems should occur prior to the release in an experiment. Another safety measure is that there is no valve between the high-pressure hose and the branch connected to the blowdown valve. It is thus not possible to leave the high-pressure hose pressurised. The operation of the hose is done through valves located at the high-pressure hydrogen system, near the hose connection.

#### A.1.4 Wall perforation

The interior of the wall perforation is a piece of straight pipe; thus, it will work as a small pipe spool with respect to the blowdown functionality. There are no pipe supports in this end of the blowdown pipe, and the only pipe support on the whole segment is located at the opposite end of the last spool compared to the wall perforation. The wall perforation thus needs to hold approximately half the weight of the last pipe spool. This comes in addition to its own mass and also probably a large portion of the weight of the future vertical "chimney spool" at the outside of the wall.

A conventional PN 16, DN 150 type flange is welded onto the inner end of the pipe spool in the wall perforation. However, to be able to pass the component through the hole in the wall, a purpose-built narrow type of flange was welded onto the outer part of the pipe. This flange had an outer diameter of only 228 mm, compared to 285 mm for a conventional PN 16, DN 150 type flange. As this narrow flange did not allow the use of bolts as wide as a standard flange, it was equipped with 12 x M12 bolts. And as the back side of the flange is inside the wall, the flange had threaded holes. This is a significant deviation compared to the 8 x M20 bolts with nuts on each side of the joint (free holes in both flanges) used on the other flanges in the system.

The perforation was fastened to the wall using two steel plates, one on each side of the wall. The plate on the inside was welded to the pipe thus providing a sealed connection between the outside of the pipe and the surrounding plate. The outer plate had a hole with slightly larger inner diameter, just enough to let the custom-made flange (OD 228 mm) pass through. Both plates have a thickness of 10 mm and outer measures of 420 x 420 mm. An M16 threaded rod in each corner squeezes the two plates together.

As the wall was slightly wider than expected a 20 mm nylon spacer with 13.2 mm free holes was added at the outside of the custom flange. The outer surface of the spacer was a few millimetres outside of the plate, allowing the flange on the future "chimney spool" to be wider than the other flange. The flange intended for this spool has already been made and has an outer diameter of 300 mm.

The inside of the wall is covered a 35-45 mm layer of metal reinforced Styrofoam for insulation, coated with a thin layer of concrete. This insulating material is soft. To avoid pushing the plate on the wall perforation through the concrete "coating" and Styrofoam, a 45mm diameter section around the threaded rods are removed and replaced with plastic spacers. This will transfer the forces applied on the threaded rods to the solid brick wall instead of the soft Styrofoam. The diameter of this spacer is approximately

40 mm while the length is approximately 45 mm. To provide sealing and insulation around the wall perforation, the gap between the steel plate and the wall is sealed with proper sealant for outdoor and indoor environments. The gap between the hole in the outer steel plate and the custom flange that passes through it, is also sealed. The cavity between the square shaped hole in the wall and the penetrating pipe is filled with insulation foam.

## A.2 High-pressure hydrogen system

A high-pressure hydrogen system holds a small volume of hydrogen at the desired pressure before the experiment is conducted. This system is designed with components with various pressure rating, but all components are rated for higher pressure than the maximum pressure in a gas bottle (approximately 200 bars). The layout is shown in a piping and instrumentation diagram (P&ID-01-01), which is included as an appendix in this thesis. A section of this P&ID is also shown in Figure appendix 3.

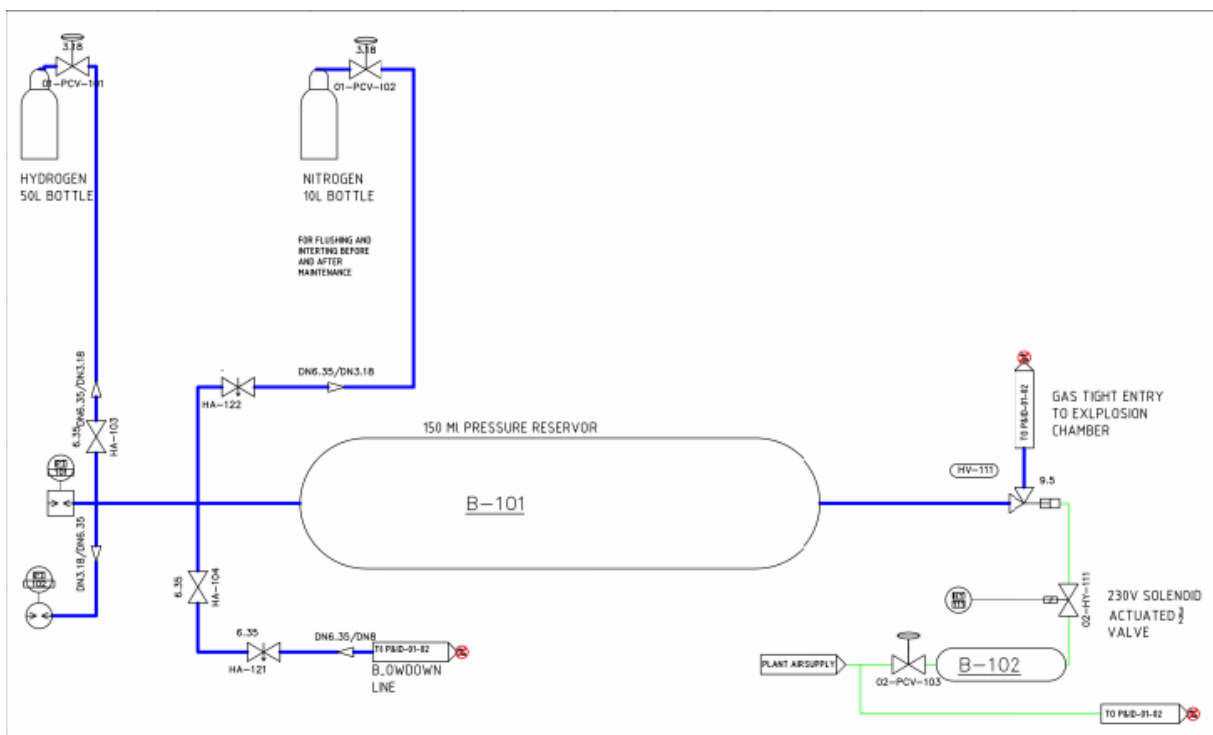


Figure appendix 3 A section of P&ID-01-01, showing the high-pressure hydrogen system for illustrational purposes. The P&ID can be seen in a more convenient size elsewhere in this thesis.

The system can roughly be divided in the following sections:

- Filling, monitoring and backup depressurisation
- Pressure reservoir
- Release tubing with actuated valve

### A.2.1 Filling, monitoring and backup depressurisation

The segment upstream of the pressure reservoir fulfils all purposes related to pressurisation, pressure monitoring and backup depressurisation. The system looks spacious in the P&ID, but all branches on this side of the pressure reservoir is made in one solid block of stainless steel. This block is equipped with 6 ports with internal ¼” National pipe threads (NPT) and one port with internal M10x1 threads. The NPT threaded ports are equipped with adapters to a two-ferrule compression fitting system to allow flexible connection of adjacent tubing lengths and components. All needle and ball valves in this system

have internal NPT threads in each end. The outlet from the hydrogen pressure regulator also has internal NPT. NPT-to-tubing adapters are used to join these components into the fittings system. Two different adapters are used, depending on the distance between the components and other aspects; the tubing side of the adapter could have either a fitting body, or a small tubing piece, thus acting as the tubing end in a fitting. More details about these connections systems are given in A.2.6.

A hydrogen bottle with a corresponding pressure regulator 01-PCV-101 is connected to the system to fill the system before each experiment. 01-PCV-101 has a maximum outlet pressure of 100 bars, and this will be the operational limit of the current system. However, as mentioned earlier, all components have a design pressure that exceed the maximum available bottle pressure. So, a possible failure of 01-PCV-101 will not damage the system.

Before initial use and prior to splitting of the system, a nitrogen bottle with corresponding regulator 01-PCV-102 can be used to flush the system. When nitrogen is used before introduction of hydrogen after maintenance, its role is to dilute oxygen in the system. This process is called inerting. When the system is purged with nitrogen after experiments and before splitting, on the other hand, the purpose is to dilute remaining hydrogen in the system and this operation is called gas freeing. Both operations are performed to avoid unintended mixing of air and hydrogen within and outside the system.

Two different pressure transducers are used upstream of the pressure reservoir. PT-101 is a conventional digital pressure reader which reads absolute pressure. It will be used as a reference when the pressure is adjusted before experiments and is not connected to the control system. The reading from this instrument will also be added to the details about the experiments as the initial pressure for the experiments. PT-102 is a piezo-electric transducer connected to the logging system. More detailed descriptions of these instruments and their principles are given in A.3 and 2.3. The piezo transducer is installed in the port at the back end of the “connection block”. When the pressure drops in the reservoir (and the rest of the system) the pressure decrease will propagate back to the transducer without having to pass any angles or bends. In addition, the short length of the connection block as well as the tubing between it and the reservoir will reduce unnecessary delays in the measurements.

1/8” (3.18 mm) tubing is used from both gas bottles to the connection block, as well as from the connection block to PT-101, the conventional pressure reader. The tubing has a wall thickness of 0.033”, which gives an ID of only 1.5 mm. Fast flow is not necessary in these sections, thus using small tubing is acceptable from an operational point of view. Smaller tubing is safer, as the accumulated volume with pressurised gas is smaller and the leakage rate in case of a burst in the tubing or corresponding fittings will be smaller. The remaining parts of the system where a larger flow rate is required, is equipped with 1/4” (6.35 mm) tubing. The 1/4” tubing sections are from different vendors and project, thus have various wall thickness. However, the wall thickness is at least 0.028”, giving a maximum ID of approximately 5 mm. All tubing dimensions are denoted in mm on the P&ID’s, as shown in Figure appendix 3.

## A.2.2 Pressure reservoir

The project has procured pressure reservoirs in three different sizes: 150, 300 and 500 ml. The 150 ml reservoir was the preferred choice. This is mostly because the smallest reservoir will produce the smallest volume of combustible gas-mixture. Before the setup was properly tested, this was the safest approach. With three different sizes available, it was possible to investigate how the initial hydrogen volume will affect the probability of ignition and the violence of the resulting combustion or explosion. However, this was not investigated in this thesis work.

All reservoirs are “cigar shaped” with one internal threaded 1/4” NPT connection in each end. Two different ports make it possible to locate the reservoir as close as possible to the release valve and point of investigation. If the reservoir only had one port, both filling and release line would have to be connected to the same tubing section, resulting in increased number of tube lengths and junctions along



the route from the reservoir to the release valve. Both OD and design pressure are equal for all cylinders; namely 48 mm and 344 bars. Different lengths accommodate the various operating volumes.

### A.2.3 Release section and obstruction objects

This section is made as short and simple as possible to give a short distance from the reservoir to the nozzle within the explosion chamber. A small tubing section connects the pressure reservoir to the release valve, and another small tubing section connects the downstream side of the release valve to the entry point in the explosion chamber. The direction of flow changes 90° from horizontal to upwards in the release valve.

A medium pressure fitting system is used for the entire release section. This is because these components can withstand very large pressures. The lowest design pressure is 1000 bars, some of the components has much more. The system can therefore be used for experiments where the pressure is increased with a pressure booster. Such experiments might be desirable, as described in B.3.1. A closer description of the principles for this fitting system is given in A.2.6.

Two different sizes could be used in this section: either 3/8" (9.53 mm) or 1/4" (6.35 mm). The release valve is also unique for each dimension. The intention is to use only one dimension at the time for simplicity. But if mixing of sizes is necessary for some reason, a reducing union could be used to join different sized components. In addition to the possibility for variations provided by two different sizes, tubing sections with different internal diameters and lengths could be used as well. However, changing dimension or tubing lengths will require some changes in the support layout, which is generally described in A.4.3. Table appendix 1 gives an overview of the different variations of tubing pieces available.

*Table appendix 1: An overview of the available variations of OD, ID and length for the tubing pieces to the release section*

Outer diameter [inches (mm)]	Internal diameter [mm]	Length [mm]	Numbers in stock [#]
3/8" (9.53)	5.2	75	2
3/8" (9.53)	5.2	100	2
3/8" (9.53)	5.2	200	1
3/8" (9.53)	3.2	75	1
3/8" (9.53)	3.2	100	1
3/8" (9.53)	1.6	100	2
1/4" (6.35)	2.4	65	1
1/4" (6.35)	2.4	100	1
1/4" (6.35)	1.6	65	1
1/4" (6.35)	1.6	100	1

A brass nozzle is mounted on the inside of the explosion chamber. The nozzle is shown in MECH-02-01. This is the last part of the high-pressure hydrogen system. When the hydrogen leaves this nozzle, it enters the explosion chamber with its atmospheric pressure. The nozzle has an overall length of 126 mm and reaches approximately 96 mm above the "floor" in the explosion chamber, which is sufficient to reach the height of the visualisation windows in the chamber. The layout in the chamber is further described in A.1.1. The internal diameter in the nozzle is 5 mm, which corresponds to the largest available internal diameter in the 3/8" tubing.

None of the tubing pieces have an ID of exactly 5 mm, thus, an abrupt change in ID will occur at the joint between the tubing and the nozzle, either reducing or increasing the available cross section,

depending on the selected tubing. As the largest tubing was the primary choice, the change resulted in a surface orthogonal to the direction of flow, yielding a potential for reflected shock waves within the nozzle.

The obstruction object is mounted from the top of the explosion chamber and its vertical position is adjustable to give the preferred distance to the nozzle. Internal M12 threads in the obstruction objects are connected to corresponding external threads on the connection rod. This threaded solution makes it easy to change between different types of objects to evaluate how different designs affect the results. Further details of the mounting system are given in A.1.2.

### A.2.4 Release valve

The release valve is of the needle valve type. These valves are well suited to handle large differential pressures in small dimensions. It is angled 90°, thus changing the direction of flow in the gas. As the entry point to the explosion chamber is vertical, but the rest of the system must be horizontally oriented due to space limitations below the chamber, this is a convenient solution. Figure appendix 4 shows the construction of the needle valve and its actuator.

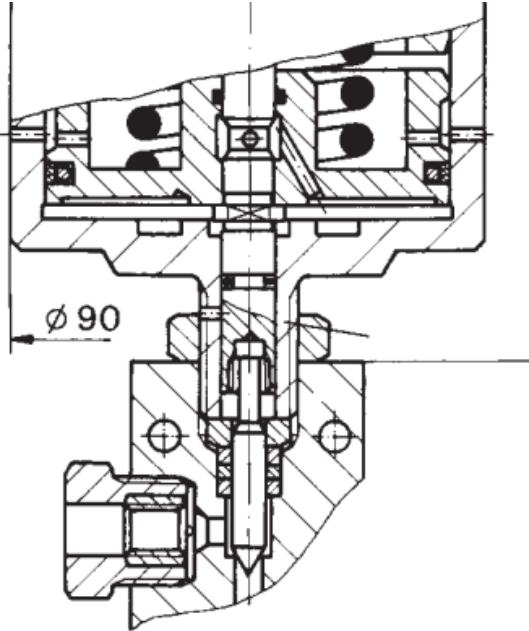


Figure appendix 4 Shows a cross sectional drawing of the needle valve with actuator used as release valve in this experimental setup, from [113, Ch. 710.03].

Another aspect that favours the selection of a 90° valve more than a “flow through” needle valve is that the latter contains two 90° angles. This is clearly shown in Figure appendix 5. Because of this, the 90° valve used in this project has a 50% higher flow capacity, measured in flow coefficient ( $C_v$  value) compared to an equally sized valve of the “flow through” construction. The  $C_v$  values for the two valves are given in Table appendix 2.

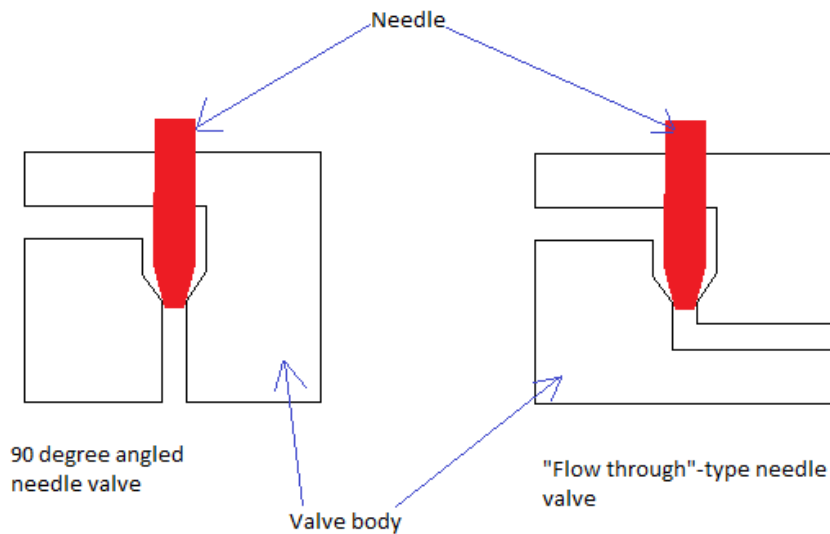


Figure appendix 5 The left illustration shows the generic layout of a 90° needle valve, while the illustration to the right shows a “flow through” type needle valve. The illustration clearly shows that the flow must pass two 90° bends in a typical “flow through” needle valve.

As mentioned above, one needle valve is procured for each of the two stocked tubing dimensions. Apart from the size, they are constructed equally. Some differences do however occur at their actuators. Due to the increased size of the 3/8” valve, the actuator must apply a larger force to move the needle. To be able to deliver more force with the same air pressure and external diameter on the piston actuator, it is of a double-piston type<sup>7</sup>. Both actuators are normally closed. A spring forces the needle towards the closed position, while instrument air pressure counteracts the spring force to open the valve. Air supply is connected through a G 1/8” port at the “top” of the actuator. The opening time is estimated by the vendor to 60-80 ms for the smallest valve [114].

In this experimental setup it is desirable with high flow rate from the reservoir to the point of investigation. Flow characteristics is thus an important parameter in the setup. Theory about flow characteristics,  $C_v$  and  $X_T$ - values and estimates are given in 2.2. As shown in Table appendix 2, the 3/8” valve has  $C_v$  value of 0.9, which is more than 8 times more than the corresponding value for the 1/4” valve.

As the value  $X_T$ - values are not provided by the vendor for these valves, it is not possible to calculate exactly the maximum flow rate through them. However, rated pressure drop ratios given for similar valve constructions could be used to make reasonably accurate estimates. A needle valve with similar size and construction (3/8” tubing, 5.8 mm orifice) but lower design pressure (413 bars, instead of 1000 bars for the valves in these project) has for instance a rated pressure drop ratio of 0.62 at a  $C_v$  of 0.92. A valve relatively similar to the 1/4” valve (2 mm orifice, but 1/8” fitting connection instead of 1/4” NPT) and 345 bar design pressure had an  $X_T$  value of 0.63 for a  $C_v$  of 0.14 [115, p. 5]

<sup>7</sup> Two pistons operating “in series” on the same stem with an enclosed ambient pressured chamber in between

Table appendix 2: Properties for the two different release valves procured for this project.

Tubing dimension [inches (mm)]	Orifice diameter [mm]	C <sub>v</sub>	Rated pressure drop ratio for similar designed valves	Pressure rating [bar]
¼" (6.35)	2	0.105	0.63	1000
¾" (9.52)	5	0.9	0.62	1000

The valves are designed to withstand flow and differential pressures in both directions. But in this project, they are oriented so that the pressure is at the sharp end of the needle. In other words, the pressure reservoir is connected to the port at the bottom of the drawing in Figure appendix 4. This is done for two reasons: The most important is that when the differential pressure is applied towards the sharp end of the needle the hydrogen pressure will provide the largest net force towards the opening direction of the needle. The applied force is equal to the hydrogen pressure multiplied by the net area in the direction of travel.

On the ¾" valve, the needle has a diameter of 6 mm, while the internal diameter of the seat it is sealing against seems to be 5 mm. Thus, the hydrogen will press on a 5 mm diameter surface, plus an unknown part of the annulus where the needle is in contact with the seat. When pressure is applied in the opposite direction, it will maximum exert a net upward force on annulus section of the needle which is in contact with the seat, but most likely even less than that. If 100 bars of pressure are applied in the direction chosen in this experiment, it will provide a force in the opening direction of at least:

$$100 * 10^5 * \frac{\pi}{4} * 0.005^2 = 196.3 \text{ N}$$

The force provided by applying the same pressure in the opposite direction is:

$$100 * 10^5 * \frac{\pi}{4} * (0.006^2 - 0.005^2) = 86.4 \text{ N}$$

Both calculations assume an internal diameter of the seat of 5 mm, which could not be confirmed.

The last reason for the selected direction of flow, is that extensive and destructive modifications is necessary to make sufficient space for the downward facing actuator.

### A.2.5 Rupture disc assembly

An alternative setup was made to facilitate experiments with rupture discs. A rupture disc holder, called *safety head*, from the same vendor as the other medium pressure fitting parts. This holder replaced the hydrogen nozzle at the inside of the explosion chamber. However, as both the safety head and the tubing had the same "tubing end termination" with an outward facing 58° tapered surface, it was necessary to make a "joint sleeve" to achieve a sealed connection between them. This sleeve was made from 316L stainless steel and had an outer diameter that fitted well within the M20 threads in the flange.

The safety head was shorter than the hydrogen nozzle used for experiments with only the release valve. To reach a sufficient height so that the camera did not have to be adjusted a new brass nozzle was made and placed on the discharge side of the safety head. The discharge side of the safety head had internal G ¾" BSP threads. Booth the "joint sleeve" and the rupture disc nozzle are shown in MECH-02-02 The full assembly for the rupture disc experiments are shown alongside with the assembly for the valve-only experiments on MECH-02-03.

Discs with four different rupture pressures was procured for these experiments: 25, 50, 80 and 100 bars. All discs had the same outer diameter and "frame thickness", as well as internal free flowing diameter. The material thickness and quality at the rupture segment was different to accommodate the different rupture pressures.

The release valve was used also during the rupture disc experiments. This was to be able to trigger the camera and the piezo electric transducers in the moment the disc ruptured. If the section upstream of the disc had been pressurized directly from the gas bottle until it ruptured, it would have been hard, if not impossible to time the recording. Instead of this, the release valve was kept closed while the reservoir was pressurized to a pressure well above the rupture pressure for the disc. Then the system was triggered in the same way as for experiments with the valve alone. When the valve opened, the gas flowed through it and increased the pressure upstream of the disc. The disc then ruptured when sufficient pressure had been reached.

It is also a safety aspect related to the use of the release valve to trigger the experiment: pressurising the full volume upstream of the rupture disc without a delimiting valve until it ruptures would require an open bottle supply at the moment of rupture. This would allow gas to flow directly from the gas bottle to the explosion chamber until the valve is manually closed by test executors.

## A.2.6 Connection systems

Several different connection systems are mentioned in the previous chapters. This chapter gives a summary as well as a description of their sealing principle. The following systems are mentioned:

- Two ferrule compression fitting system
- Collar and gland nut high-pressure fitting system
- NPT tapered threads
- ISO parallel pipe threads (G)

### **Two-ferrule compression fittings system**

This principle is very common for all gas systems at moderate pressures. According to a handbook published by *Norwegian oil and gas*, an interest organisation for upstream oil and gas companies with activity on the Norwegian continental shelf, more than 30 different vendors deliver systems based on this principle [116]. These designs typically have pressure ratings up to 10k psi (690 bar). The system used in this project is designed to a maximum pressure of 770 bars for 1/8" tubing and 717 bars for 1/4" [117].

These systems have, as their name indicates, two ferrules. The different components are shown in Figure appendix 6. When the fitting is initially installed, the nut is tightened so that the front ferrule is swaged onto the tubing thus creating a gas tight connection. Further tightening will push the tapered front ferrule towards the opposite tapered inside of the fittings body. The contact between the ferrule and the body becomes gas tight and provides the actual sealing in the fitting. The back ferrule enters within the front ferrule and causes it to expand. This provides the radial force necessary to get proper sealing between the front ferrule and the body. The tapered shape of the body causes the swaging process, as it pushes the front end of the ferrule into the tubing wall when the nut is tightened.



*Figure appendix 6 The components in a two-ferrule fitting before installation. Name of the components on the tubing, from left to right, nut, back ferrule, front ferrule, and body, from [116, p. 13].*

Due to the swaging of the front ferrule onto the tubing, the installation is irreversible. This means that the nut cannot be removed from the tubing after its initial installation (unless the opposite end of the tubing is free from any fittings). The ferrules cannot be reused after the tubing has been cut. If the distance from a bend to the tubing end turns out to be slightly too long, the section with the ferrules must be removed. As the distance from the tubing end to the back end of the back ferrule is quite a few centimetres, the whole tubing section must be replaced or modified if the excessive length is smaller than the required distance to swage on new ferrules. Due to this irreversibility, the group procured plentiful of spare ferrules in case mistakes in the building led to the need of replacing them.

Although many of these two ferrule systems have very similar design on the components, they are generally not interchangeable. It is therefore important to ensure that all components are from the same vendor. If the facility has fittings from more than one vendor at different locations at the plant, the risk of unintended mixing increases. It is also important to avoid mixing millimetre and inch-sized tubing and fittings from the same vendor. Many mm- fittings are almost equally sized as an inch-sized fitting. 10 mm is for instance very close to  $\frac{3}{8}$ " (9.52mm) and 6 mm is close to  $\frac{1}{4}$ " (6.35 mm). However, the differences are big enough to make it hard to achieve a proper sealing. To avoid mixing of components of mm and inch-size, most vendors differentiate these components with machined features, such as extra shoulders, collars or grooves {[116], [117]}. These marks will not fade due to wear and weather, as paint or text marking would.

### **Collar and gland nut high-pressure fittings system.**

The collar and gland nut principle is common among medium and high-pressure fitting systems. These systems have design pressures from approximately 700 bars and upwards. Material thickness plays an important role for the design pressure. The  $\frac{3}{8}$ " size used in this project is for instance delivered in three different internal diameters; 1.6, 3.0 and 5.0 mm. This corresponds to design pressures of 10 000, 7000 (4000 for some components) and 2000 (1000 for valves) bars respectively [113, Ch. 720.00; 720.01; 710.03].

The main difference between this system and the two-ferrule compression fitting system is that the axial end of the tubing is the sealing surface in this system, instead of an external ferrule. Figure appendix 7 shows the different parts of the fitting system used in this project, with names. A  $60^\circ$  conical shape in the fitting body seals against a  $57-58^\circ$  conical shape at the front end of the tubing. The difference in angle between the two surfaces ensures that the only contact point in a fitting prior to tightening, is the very front edge of the tubing which touches a point at the cone close to the hole in the fitting body. When the fitting is tightened, the material will undergo slight elastic deformation so that the contact surface becomes a bit larger [113, Ch. 720.00]. Due to the difference in angle and the desired initial contact surface at the front edge of the tubing, the ID of the fitting body must be slightly narrower than the diameter at the front edge of the conical shape of the tubing.

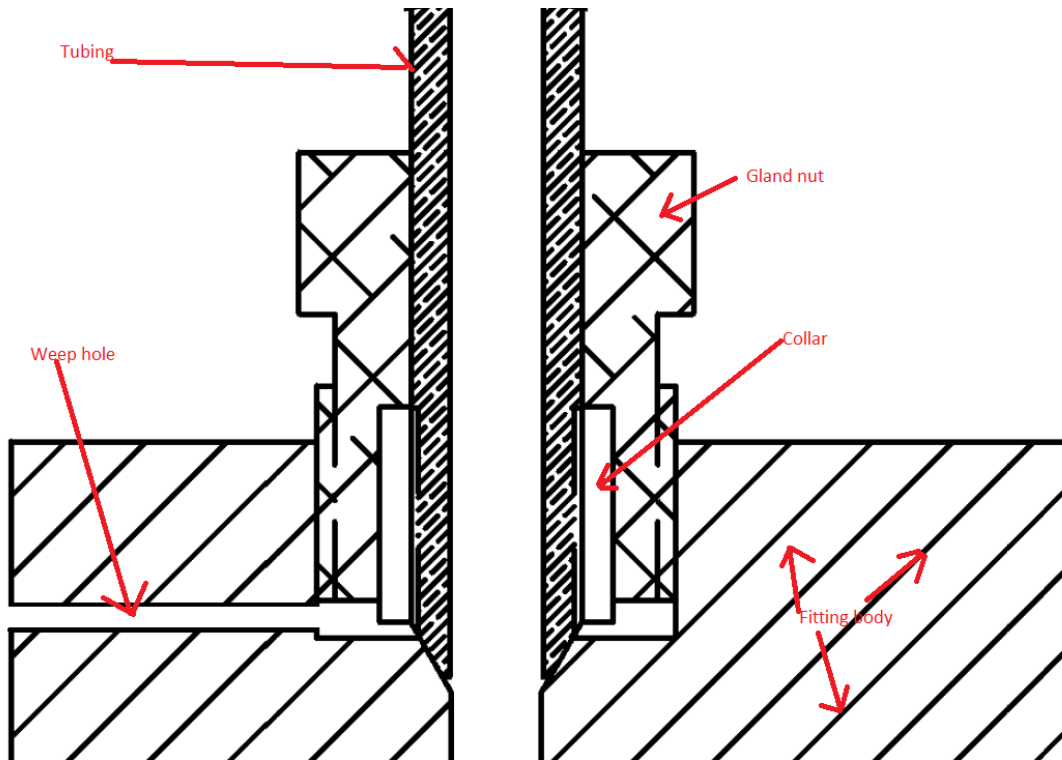


Figure appendix 7 A cross sectional drawing of the high-pressure fitting system used in this project. The black arrows on the drawing indicates where the forces are applied when the fitting is tightened.

As the sealing is provided at the front end of the tubing, the collar does not have to seal. Its only purpose is to transfer the axial force from the gland nut to the tubing, thus ensuring that sufficient force is applied at the sealing connection between the tubing and the fitting body. The collar is left hand threaded. This is necessary, as a right-hand thread collar would have followed the gland nut when it is tightened thus unscrewing itself. This would have made it difficult, if not impossible, to get the proper axial pressure between the fitting body and the tubing.

Unlike a compression fitting system, installation of this fitting is reversible. The threaded collar could be removed at any time if necessary. It is also possible to remake the sealing surface or shorten the tubing length without remaking the whole fitting. The left-hand threaded section can be threaded in as small lengths as necessary, and the same goes for the conical shape at the tubing end.

If the sealing surface has a leakage or the fitting by mistake is loosened while the tubing is pressurized, pressure would leak into the cavity between the fitting body and the gland nut. As the gland nut has a much larger area in the axial direction than the part of the tubing normally exposed to pressure, the force on the threads at the collar and gland nut might become unacceptable. Especially if the leak rate through the coned sealing surface is larger than the leak rate along the threads. To avoid any danger related to this issue, the fitting body has a weep hole. The weep hole will lead an eventual leakage away from the cavity thus avoiding pressure build up.

As for two-ferrule compression fitting, it is important to avoid mixing components from different manufacturers of collar and gland nut fittings, despite similar size and construction.

### NPT tapered threads

As mentioned above, most components in the filling system upstream of the pressure reservoir as well as the reservoir itself, has internal NPT threads. NPT stands for *National Pipe Thread* and is an American standard of threading which is common in the American industry and also the oil and gas-industry globally. The standard includes both parallel and tapered threads, but it is the tapered version that is most common. The thread is defined in ANSI B.1.20.1 [118].

The tapered shape will create sufficient strong force in the radial direction to seal off when the joint is tightened properly. However, it is necessary to use either tape or liquid thread sealant to get a gas tight connection. The sealant/tape will also lubricate the metal which reduce the probability of seizing the parts together on the threads. Seizing is caused by local friction-generated heat, which adheres the two components together. Factors that increase the risk of seizing is lack of lubrication, tightening with uneven motions, tightening too hard, damaged threads or surfaces as well as many other factors.

An important note about the sizing of these threads, is that the denoted size refers to its “trade size”, and not its nominal diameter on the threads. In other words, the diameter used to name the threads is in the vicinity of the ID for a naturally corresponding pipe size. As a rule of thumb, the nominal thread OD for NPT is approximately ¼” inch larger than the denoted size. A ¼” NPT has for instance a nominal OD of approximately 13.7 mm (0.54”). As the thread is tapered, the diameter will vary. The table values for diameter thus often refer to the diameter at the third or fourth thread.

NPT threads are used in most of the components like pressure reservoirs and valves in this system. NPT thus works as a universal connection between different sealing systems and standards.

### **ISO parallel pipe threads (G)**

This thread system is used a few places on this experimental setup, for instance on the air hose connections, as well as on the connection to the backup depressurization hose. This standard of threads is identified by various designations in different standards, such as ISO 228 and BSPP (British standard pipe parallel) [119]. It is also often denoted with G followed by the trade size in inches. For instance, G 1/8”.

Parallel threads will not seal on the threads in the way that tapered threads do. The sealing surface is therefore on axially oriented surfaces on the outside of the threaded section. It is also necessary to use a sealing ring to get a properly sealed connection. The sealing ring could be either full metal or a soft seal type with a rubber layer. Either way, the ring is softer than the material in the two parts that is joined together. When the connection is tightened, the sealing ring is compressed so that it seals the space between the two components. It is not necessary to use tape or sealant on these connections.

In this project, G threads are used extensively in the instrument air system. The digital manometer connected to the filling and monitoring system (described in A.2.1) also has G threads, but an adapter is used to allow connection to the two-ferrule compression fitting system. Some of the fittings near the backup depressurization hose also uses G threads.

## **A.3 Instrumentation and logging systems**

The instrumentation and logging system fulfils many purposes. It consists of the measuring devices; pressure transducers and high-speed camera and instrumentation air used to control the hydrogen release valve. The interface used to define the experimental sequence and extract the information is also part of this system. Also, the components used for amplifying and signal treatment between the computer and the measuring components are included in this system. The system could be divided in the following parts:

- Pneumatic control system
- High-speed camera and belonging optics
- Piezoelectric pressure transducers and amplifier
- Data acquisition module
- Computer program (HMI)

Most of the instrumentation, except the pneumatic control system is shown in detail on IFD-01-01.



### A.3.1 Pneumatic control system

As mentioned in A.2.4, the valve that releases hydrogen from the high-pressure hydrogen system and into the explosion chamber, is operated with instrument air. This means that a proper system for air treatment and preparation is necessary. The air system is included on P&ID-01-01, and the relevant section of this P&ID is also shown in Figure appendix 8.

The air system has the following main components:

- Pressure regulator valve with water separator (02-PCV-103)
- Air reservoir (B-102)
- 230V solenoid actuated 3/2 valve (02-HY-111)
- 8 and 10 mm plastic air hose with corresponding quick release connections

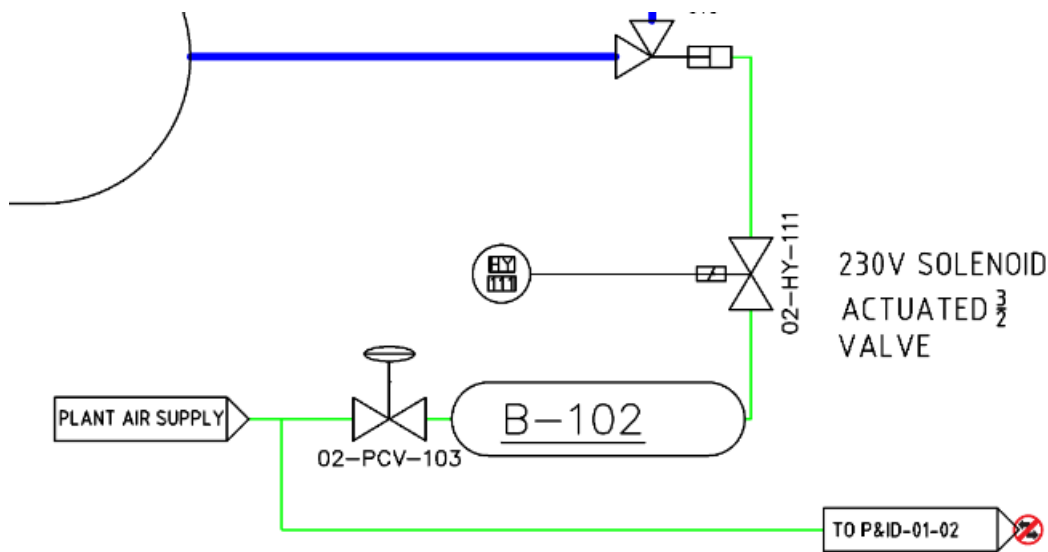


Figure appendix 8 A section of P&ID-01-01, showing the plant air system

Compressed air is delivered from the IFT-buildings internal system for compressed air and has a pressure of approximately 8.5 barg. A 8 mm plastic hose with an approximate length of 3 m is connected to the quick release connection mounted at the wall. A branch is added near the end of this section; thus, both the release valve and the explosion chamber are fed from this line. The air supply to the explosion vessel is shown on P&ID-01-02. A section of this drawing is shown on Figure appendix 9.

The air hose is connected to one of the threaded ports described in A.1.1, through a ball valve. This line is intended for flushing the chamber and blowdown pipe to remove moisture and combustion products before and after experiments. As the compressed air, even at the state delivered from the "net", has more stable properties than the outdoor air, the uncertainty related to varying air conditions due to changing weather, could be reduced.

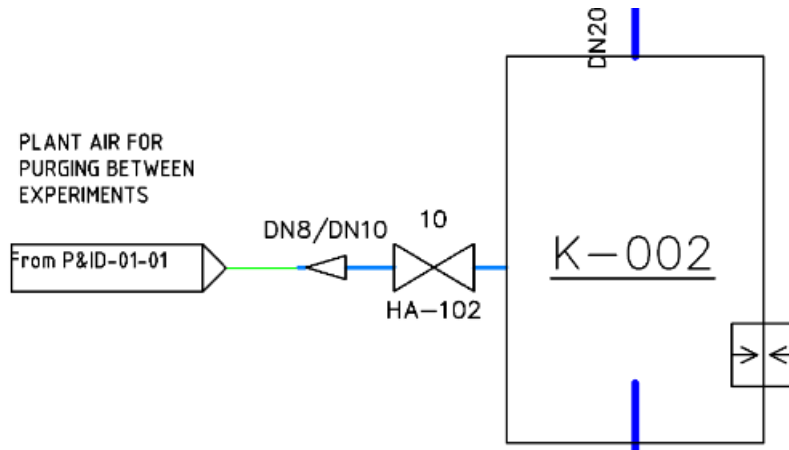


Figure appendix 9 Shows a section of P&ID-01-02, where compressed air is connected to the explosion chamber

### Pressure regulator with water separator

The last leg in the branch connection continues into a pressure regulator, denoted 02-PCV-103 on the P&ID. This regulator has several functions. First, it contains a manual 3/2-valve that allows the downstream segment to be isolated from the air supply and depressurised. It also has a water separator with an automatic drain valve. (The valve at the bottom of the separator body opens when a sufficient liquid level is present). The pressure regulator has an adjustment range from 0.5 to 8 bars and is equipped with an analogue manometer to monitor the adjusted pressure. In this setup, the pressure is adjusted to maximum. This is to allow as large mass flow as possible into the hydrogen release valve when it is opened, thus minimising the opening time. Observations during the installation work suggest that an air pressure of approximately 7 bars is necessary to allow the hydrogen release valve to fully open when it is depressurised. As mentioned in A.2.4, the hydrogen pressure will aid the opening, thus reducing the needed air pressure in line with increasing hydrogen pressure.

### Air reservoir

Downstream of the combined regulator and water separator is the air reservoir. This reservoir has a cylindrical shape and has support brackets welded on to it. It was initially built for another experimental setup. The net volume is unknown but is in the vicinity of 100-150 ml. The reservoir is equipped with an analogue manometer with a range from 0 to 25 barg. Each end of the cylinder is equipped with a port that has G 1/4" internal threads. Thus, the supply from the regulator and the delivery to the solenoid valve is connected in opposite ends. The reservoir and its layout can be seen in Figure appendix 10

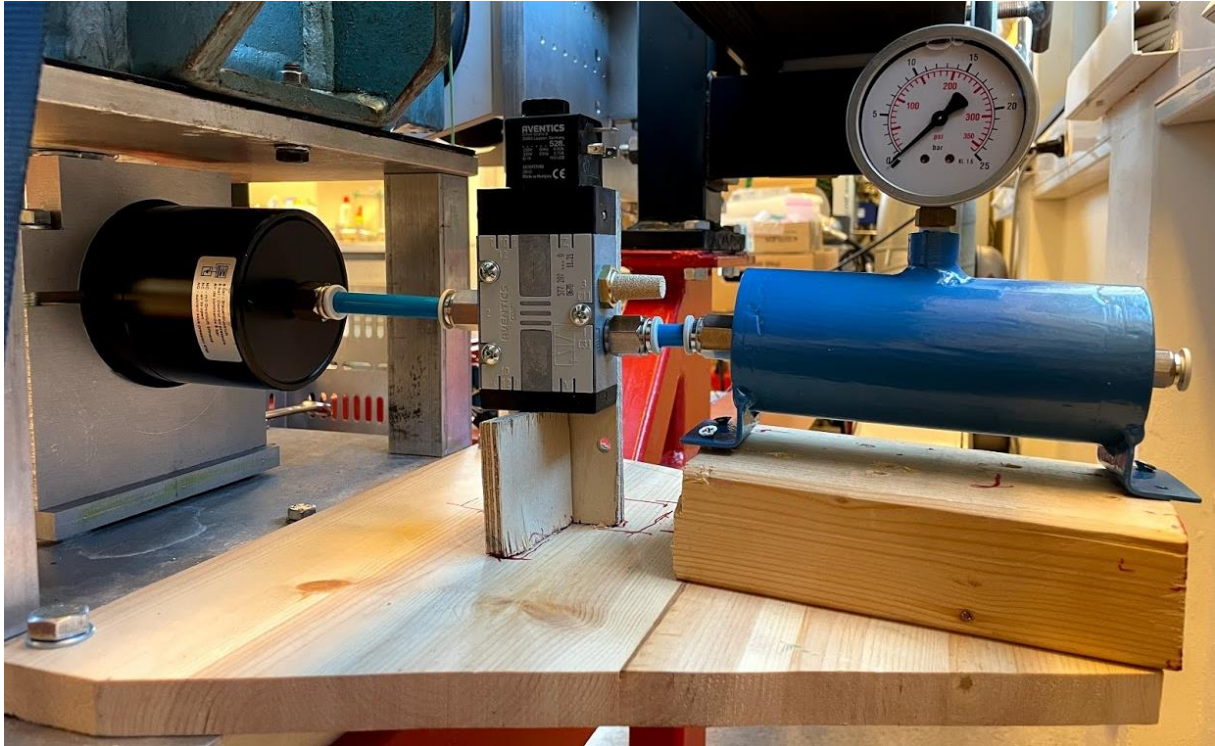


*Figure appendix 10 Shows the actuator of the hydrogen release valve, as well as the 3/2 solenoid and the instrument air reservoir*

### **230V solenoid actuated 3/2 valve**

The 230V actuated solenoid valve is located immediate downstream of the air reservoir. When selecting the valve type, the focus was to find a valve with as high flow rate and as fast reaction time as possible. The selected valve has a nominal flow rate of 1400 l/min. Properties for the selected valve is presented in Table appendix 3. The nominal flow rate is defined as the flow through the valve when the inlet pressure is 6 bars and the differential pressure across the valve is 1 bar [120]. A normally closed configuration is selected, meaning that the attached solenoid must be energised to open the valve. A manual switch on the valve allows the valve to be locked in open position without power supply. This is handy if the valve must be kept open during preparation work where the electric control system is disconnected.

Reaction time or opening time is also an important factor. This information was stated as “typical switch-on time” by the selected valve vendor. Switch on-time is mostly dependent the solenoid, thus the fastest available solenoid for this type of valve was selected. It has a switch-on time of 25 ms and a switch-off time of 45 ms. The latter property is unimportant in this application.

Both 230 V AC and 24 V DC supplied solenoids were available, with similar range of power outputs and switch-on times throughout the product range. 230V AC was selected because the connection to the control system was already built with a relay that had 230V power supply from the grid. Properties related to power consumption for the selected solenoid are shown in Table appendix 3.

Table appendix 3: Key properties for the selected pneumatic solenoid valve.

Property	Value	Unit
Product name	Aventics CD07 3/2 valve	–
Nominal flow rate	1400	l/min
Configuration	Normally closed	–
Solenoid voltage	230	V
Activation power	5.6	VA
Holding power	4.8	VA
Switch-on time	25	ms
Switch-off time	45	ms

Both larger flow rates and faster reaction times than the selected 1400 l/min and 25 ms were available, but not simultaneously. The selected combination was the best fit for this purpose.

### Optimisation of air flow

The hose lengths between the air reservoir, solenoid valve and hydrogen release valve are kept as short as possible to reduce restrictions. To make this possible, all components are aligned vertically so that their inlet and outlet ports have the same elevation. This layout allows tube lengths as short as a few centimetres. In addition to that, the tubing diameter is increased to 10 mm for both sections downstream of the air reservoir.

One of the major restrictions in this system, is the inlet port on the hydrogen release valve. Its internal threaded connection port with G 1/8" gives a significantly lower cross-sectional area than the 1/4" ports in all other components. In addition to the initially low cross sectional-diameter of the fitting, it was equipped with an internal hex used for either disassembly of the fitting itself, or to install the fitting in places with insufficient space to use the external hex shape. This internal 4 mm hex shape was drilled out with a 5.8 mm drill. Figure appendix 11 shows the difference between this modified version and the original.



Figure appendix 11 The difference between an original G1/8" fitting for 10 mm hose and the modified version used for this application that was drilled with 5.8 mm

### A.3.2 High-speed camera and belonging optics

The test setup was equipped with a Photron Fastcam SA4 high-speed camera in the version with 8 GB internal memory. This camera does only record in black and white. Its maximum resolution is 1024x1024, but it is only capable of recording this resolution at up to 3600 fps. The maximum frame rate of 500 000 fps is available with 128x16 resolution.

The shutter speed is individually adjustable between the full duration of each frame and 1  $\mu$ s. Increased frame rate and/or shutter speed produce darker pictures in addition to earlier mentioned reduced resolution. With the provided memory, the camera is capable of recording 1.51 seconds with 3600 fps at 1024x1024. 6750 fps records at 768x768 have a duration of 1.43 seconds.

When the camera is in record mode, it is continuously recording and overwriting the oldest frames, thus keeping a constant record for the available duration on the selected frame speed and resolution. When the record is triggered, by a manual action from the associated program A.3.5. or via a dedicated “triggering signal” from a data acquisition module (DAQ) or another device capable of delivering such signal. The triggering signal can define both start, centre, and end of recording, depending on what will produce the best suited recording based on the used setup.

In this thesis, the camera was set up to be triggered from a digital output signal from the DAQ unit as described in A.3.4, and the trigger signal defined the start of the recording.

The camera is connected to a Opto Engineering TC16M120 telecentric lens. The distinct properties of telecentric lenses are briefly described in section 2.3.1. The camera and lens combination give a field of view of approximately 70x70 mm at max available resolution.

At the opposite side of the explosion chamber, another TC16M120 lens is attached to a Opto Engineering LTCLHP120-r light source. The telecentric lens collimates the light before it passes through the explosion chamber and is received in the telecentric lens at the camera side. This light source has a peak wavelength of 630 nm, thus producing a red light. It is supplied with 12V 350mA DC current from an external, adjustable power supply. The lenses, light source and camera is aligned in a support system that is further described in A.4.2.

### A.3.3 Piezoelectric pressure transducers and amplifier

The setup is equipped with two piezoelectric transducers, one located in the high-pressure hydrogen system, placed in the connection block on the opposite side of the outlet to the reservoir. This location is selected to avoid angles, thus providing as fast response to pressure changes as possible. The other pressure transducer is located in the explosion chamber. It is attached to the upper port on one of the sides of the chamber. The distance from the nozzle exit to the transducer is approximately 200 mm, and the angle towards the transducer is 60° deviated from the jet exit line.

The transducer in the explosion chamber is a Kistler 701A, while the transducer in the HP reservoir is a Kistler 601CAA. They both have a measuring range from 0 to 250 bars, but the physical size and the sensitivity is different. Essential values are presented in Table appendix 4 below {[76], [77, p. 19]}. The 601CAA transducer is assembled to the connection block with a 6423B00 connection hub and a 6503C0A adapter. The outer thread on the adapter is M10x1, and the connection block were built to fit this adapter.

*Table appendix 4: Selected properties for the piezoelectric pressure transducers used in this project.*

Parameter	Kistler 601CAA	Kistler 701A
Sensitivity [pC/bar]	-37	-80
Range [bar]	0-250	0-250
Diameter on sensor [mm]	5.55	9.5

The signal from both transducers is amplified in a Kistler 5064D amplifier mounted in a 2853B chassis. The output signal from the amplifier is -10 - +10 V. The amplification was individually adapted to match the used pressure range in the system. The transducer in the HP reservoir is set with a pressure range of  $\pm 200$  bars (=0.5 volt/bar) while the transducer in the explosion chamber is set up with a range of  $\pm 3$  bar (3.33 volt/bar). It was initially set up to a range of  $\pm 20$  bars, but the range was narrowed down after experience about the pressure development in ignited experiments were obtained. As the actual measured property from the transducers are nC, the relation between the output and input signal to the amplifier will have the form V/nC.

The 2853B chassis has an input used to “trigger” the recording. When the recording is triggered, the amplified output value is reset to zero, and pressure changes given as input values to the amplifier after this point will be presented as changes in the amplified voltage signal. In this thesis, the “trigger” signal is connected to the data acquisition module as described in A.3.4 below.

Details about the settings used on the logging side of the equipment are also given in section 4.8.1 in the Experimental work section.

### A.3.4 Data acquisition module

A National instruments USB-6259 data acquisition (DAQ) module is used to control the instrumentation as well as to acquire and transfer the recorded data. This device uses a USB interface towards the PC that the experiments are controlled from, and the results are sent to. Digital output (DO) ports are used to trigger the connected equipment. These ports transmit a 5 V signal once they are activated. The analogue input ports are connected to the Kistler amplifier and receive the amplified pressure recording signals, as described in A.3.3.

In addition to that, one analogue input (AI) port is used to record the exact time for activation of the release valve. This is done by connecting an AI port to a DO port that is triggered simultaneously as the DO port used to activate the valve. Thus, the acquisition card produces a logging series that show when valve release is initiated in addition to the two pressure data series. Table appendix 5 gives an overview over the connections that are used. This information is also visible in IFD-01-01.

Table appendix 5: Used channels on the DAQ module in this project.

Port type	Port number	Signal	Purpose
Digital Output	0	Binary 0-5 V	Trigger piezoelectric
	1	Binary 0-5 V	Trigger release valve
	2	Binary 0-5 V	Release valve trigger record
	7	Binary 0-5 V	Trigger camera
Analogue Input	0	Analogue 0-5 V	Record release valve trigger
	1	Analogue -10 - +10 V	Amplified pressure signal – explosion chamber
	2	Analogue -10 - +10 V	Amplified pressure signal – HP reservoir

### A.3.5 Computer program (HMI)

#### Test logger

The test logger program was purpose built for this project by PhD fellow Matthijs van Wingerden. It both controls the timing of the different actions throughout an experiment as well as receive logged values from the DAQ module. As mentioned in A.3.3 above, the amplifier gives out a voltage signal within the range -10 - +10 V. This signal is converted to its corresponding pressure difference value by the *Test logger* program, based on the selected magnitude of the output signal from the amplifier.

The *test info* pane has text fields where meta data and miscellaneous information about the experiment could be added. A print screen of the pane is shown in Figure appendix 12. The target folder for the generated data file is also selected from this page. In addition to that, an automatically updated “experiment number” is also presented here. This number could be changed manually if necessary.

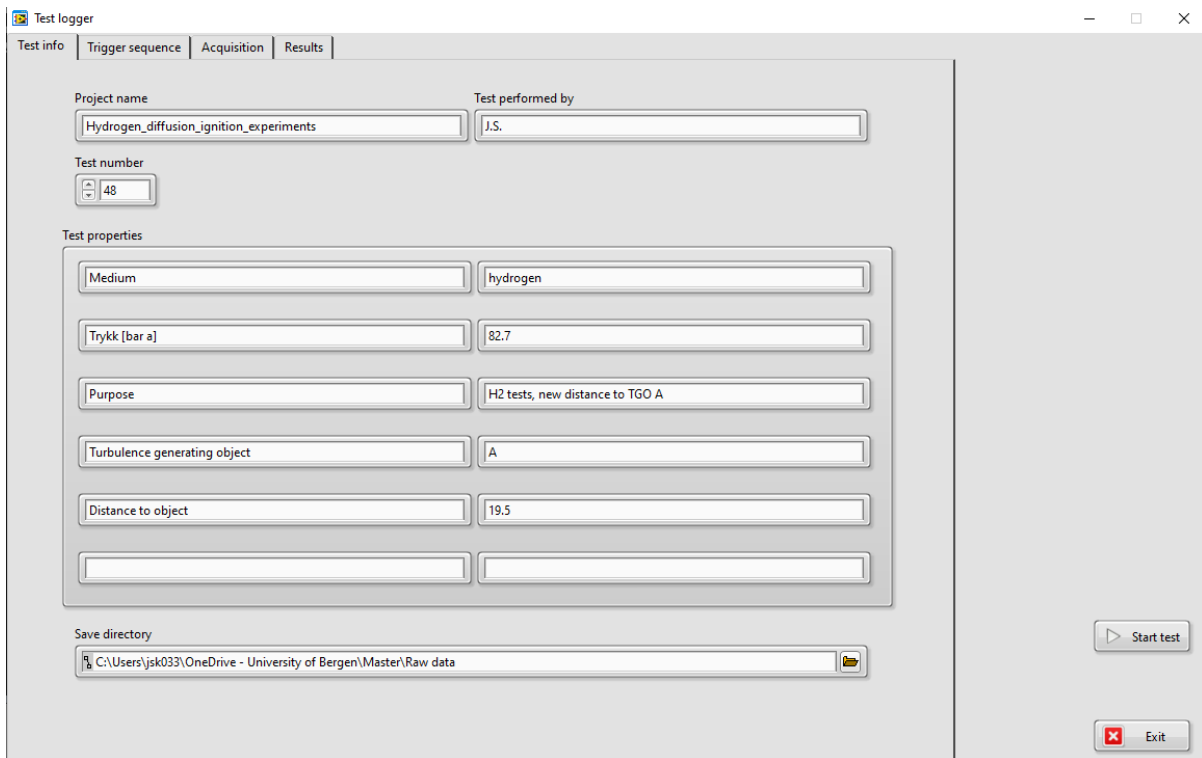


Figure appendix 12 “Test info” pane in the Test logger program

Details about the experimental events and their timing are changed in the *trigger sequence* pane. This pane displays a graphical “trend-like” overview of the selected timing settings. The total length of the sequence is changeable, and this changes the length of the “plot”. By selecting each individual output signal on the graphical overview, properties such the number of cycles it should perform during the sequence start and stop times for each cycle could be changed. This pane in addition to the dialogue box that is used to edit an individual output signal is shown in Figure appendix 13.

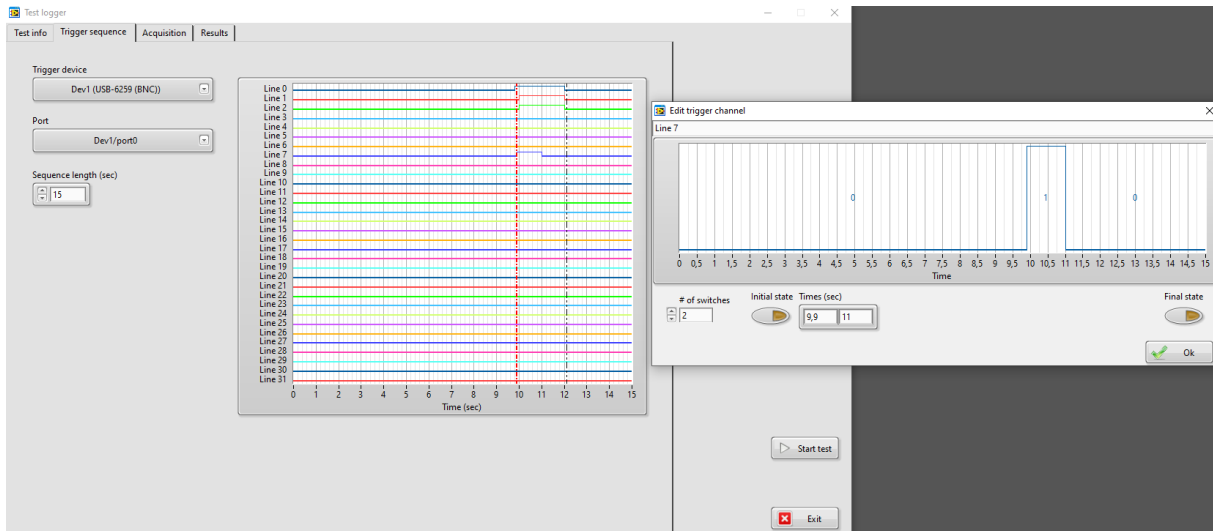


Figure appendix 13 "Trigger sequence" pane and dialogue box for adjustment of an output signal

In the *acquisition* pane, which is shown in Figure appendix 14, the available input channels are showed. The channels that should be used/logged must be selected, and this must be done each time the program is started. The start time and duration of the recording is also set in this pane.

The trigger signal does not necessarily match the time frame where the returned pressure values are recorded in the program. However, it is not a problem if the trigger signal is sent earlier than the recording is started, as the trigger only reset/initiate the amplified signal. The amplified signal might in worst case have drifted off a but during this time frame from the triggering to the start of the recording.

In this program, the amplifier is triggered 100 ms before the recording is started, but the recorded values were still close to zero at the beginning of the record. Further information about the timing values used in this project is given in 4.8.1.



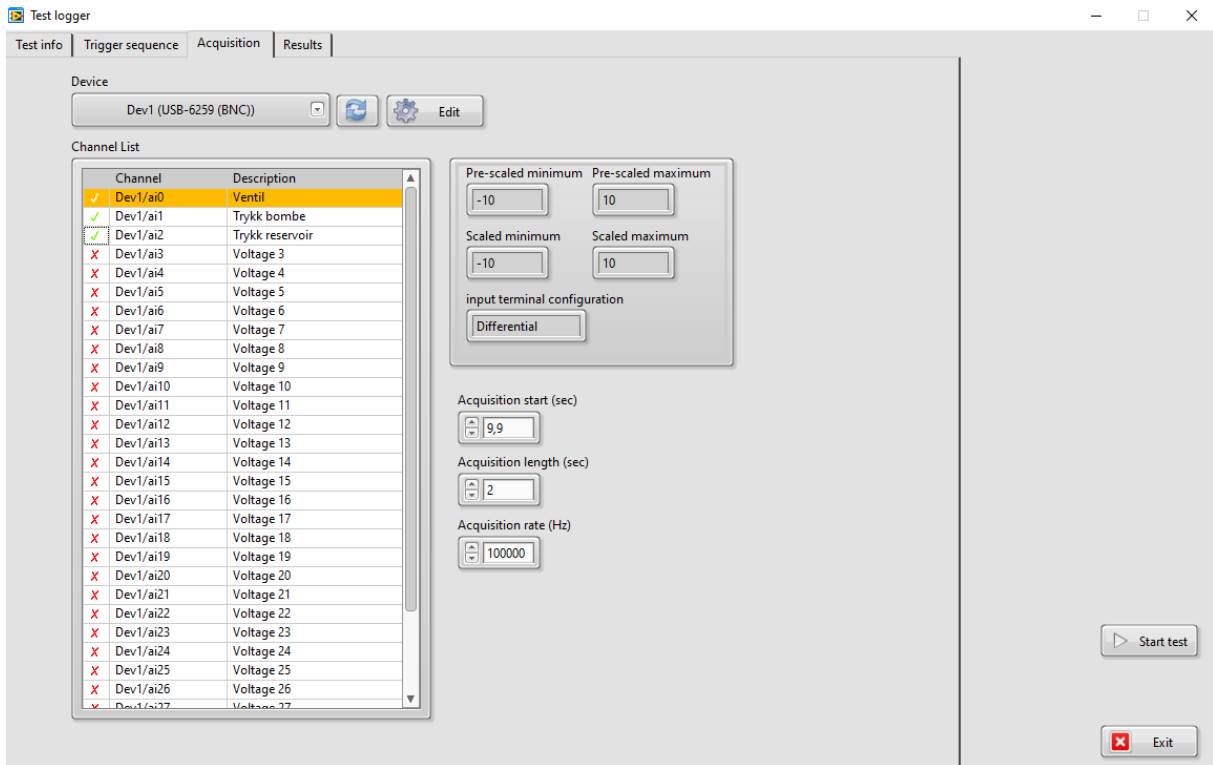


Figure appendix 14 "Acquisition" pane in Test logger

The *result* pane provides a generic plot tool which could be used for simple visualisation of the recorded values for all recorded parameters. The pane is shown in Figure appendix 15.

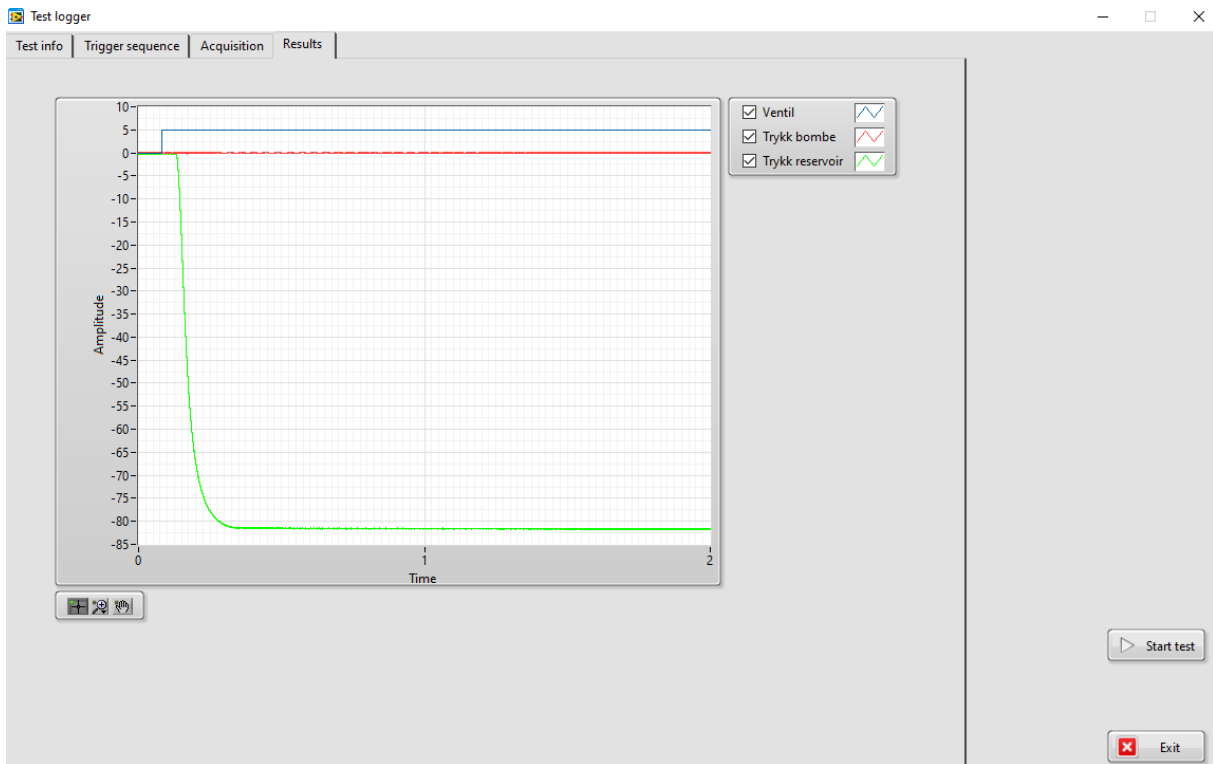


Figure appendix 15 "Results" pane in Test logger

## PFV 4 camera software

The Photron Fastcam Viewer 4 software is developed by Photron to be used together with their high-speed cameras. It is used for all phases of the recording process

- Adjustment of camera settings before recording, for instance:
  - Resolution
  - Frame speed
  - Shutter speed
  - Trigger mode
- “Arm” the camera for recording
  - Start recording if external trigger signal is not used.
  - This is done through the software even when the camera is triggered with external trigger signal.
- Basic video processing afterwards
  - Application of measuring tools
  - Stabilisation of viewing frame relative to one or two axes
  - Adjustment of colours, brightness, dynamic range, etc
  - It is possible to apply some of these tools pre-recording as well.

Further information about the software is available elsewhere [121].

## A.4 Structural supports

A combination of components specifically made for this project and existing components with small modifications have been used to serve all needs related to support.

### A.4.1 Mechanical support structure

The 20-litre explosion chamber is mounted on an aluminium plate, placed on top of the foundation for a 3.6-m flame acceleration tube {[122], [123]}, Four elevated support fundamentals measuring 145×105 mm is located adjacent to each corner of explosion chamber. A new support structure measuring 570×820×1500 mm (L×W×H) is mounted onto these supports. The structure is made of 60×60 mm square shaped steel profiles, perforated with numerous holes for mounting different equipment, both in the current application and potential future projects. In the current setup, this structure fulfils two purposes; it holds a support clamp for the blowdown pipe, as mentioned in A.1.4 as well as serving as fundament for the Shadowgraph system. The structure is primed and painted black with a two-component spray paint system.

The aluminium plate beneath the explosion chamber was initially used for another purpose but has been equipped with two “guiding” beams on the underside to avoid any horizontal movement relative to the red support structure it is located on. The plate has some predrilled and threaded holes which are used to attach the support structure for the high-pressure hydrogen system and instrument air system, as described in A.4.3.

### A.4.2 Support stand for camera and lenses

The shadowgraph system, which consist of a high-speed camera and a light source connected to one lens each, must be properly aligned along a common axis to function properly. This sets certain requirements to the support system. As the exact position of the obstruction objects as well as the point of interest during the experiment related to this object may vary, it is necessary with an adjustable system. The viewing frame in this camera setup is also quite small, only 36x24 mm. It is thus even more important with a fast and reliable adjustment mechanism. The main components in the system are:

- Bracket for the aluminium beam – fixed to the mechanical support structure (2x)
- Aluminium profile beam
- Lens and camera supports made from milled aluminium plates (2x)

### **Brackets**

One bracket on each of the two legs of the support structure located at the backside of the explosion chamber hold the aluminium profile beam. The brackets are made of 80 mm wide and 12 mm thick steel bars together to form a rectangular “hole”. As the structure is made from conventional carbon steel, it is primed and painted in the same way as the mechanical support structure.

The hole has internal measures of 188x200 mm, and the steel bars are oriented so that their widest side forms the inner surface of this hole. The steel bars oriented towards the support structure has a length of 360 mm, with a 17 mm hole in each end. The brackets are mounted to the support structure with one M16 bolt in each of these holes. As neither the holes in the brackets nor the structure is threaded, conventional bolts with discs and nuts are used. A reinforcement plate is welded on in the 90<sup>o</sup> angle between the vertical plate oriented towards the vessel and the lower parallel piece of steel. This will strengthen the construction and avoid the clamp from becoming “parallelogram shaped” when exposed to extensive forces in the downward direction.

Each clamp has four set screws to adjust and secure the beam to the clamp. A plastic liner is located in the bottom of the clamp to provide a softer and smoother surface for the aluminium beam to move on. The height of this liner is adjusted with two set screws, located near each “short end” of the liner. One of the remaining set screws are located at the top of the structure, while the last is located on the back side of the bracket (pushing the beam towards the explosion chamber). Cylindrical shaped liners are used for these two last set screws, will secure the beam in the desired position and angle. All set screws in the clamps have M12 threads. To provide satisfying guidance of these liners, each set screw rest in a hole in the liners, and a section of the threads with a length of a few millimetres longer than the depth of these holes, is removed from the set screws.

### **Aluminium profile beam**

The aluminium beam was procured for an earlier project. It is designed for securing camera and lens equipment, as it has been used to in this project. However, the beam was designed to be oriented with the profile pointing upwards, in other words, the beam is intended to be directly below the camera equipment. In this project, it must be oriented “sideways” as the space beneath the explosion chamber is allocated to the high-pressure system. The long horizontal distance from the camera to the beam, together with heavy weight on the equipment applies a large rotational force on the beam. The profile on the front of the beam is well suited for holding small weights without any additional forces applied through torque but is not intended to withstand such forces as they are subject to in this setup. To avoid any damage to the relatively soft aluminium surface, the full profile of the beam is not used. Instead, clamps that surround the beam with a set screw on the back side is used. The connection plates push on some of the larger surfaces on the front of the beam.

The aluminium profile beam, as well as the connection plates, clamps and stabilisation plates connected to it, are shown on MECH-03-01 and MECH-03-02.

The beam is 182 mm wide and 143 mm high in the orientation used in this setup. This maximum height is behind the profile that is not used, and the height of this profile is approximately 108.6 mm. A vertical surface goes straight from the point with the maximum height and down the height of the profile. As the profile is centred on the total height, this vertical surface is approximately 17 mm on each side of the profile, which is sufficient to provide a proper fundament for the connection plates. From the front of the profile and back to this surface used as fundament, it is 27.5 mm. The total length of the beam is

approximately 2.5 metres, however only a section of just above 1.5 metres is used in this setup. As the remaining length is not blocking or obstructing anything, it was not necessary to cut the beam.

### **Lens and camera holders**

The lens holders are made from several aluminium plates and other parts, assembled with screws. Each of the two lenses has its own separate holder. As the light source is lightweight and small, the bayonet connection to the lens can hold its weight without any additional support. The camera on the other hand, is both heavy and long, thus cannot be supported only on the bayonet connection to the lens. The support plate for the lens attached to the camera is therefore longer than the plate for the other lens, and an additional plate is attached orthogonally to it, working as a shelf for the camera to rest on. The camera itself is attached to another plate, which rests on four adjustment screws in the “shelf plate”, as described in Adjustment principles

All components related to this section, are drawn with measures in MECH-04-01, MECH-04-02, MECH-04-03 and MECH-04-04.

As mentioned in the section about the Aluminium profile beam

above, the plates that connect the camera holders is not fixed to the profile shape of the beam, but instead rest against wide surfaces on each side of the profile. To reach these surfaces without applying any load on the profile, the middle section of the connection plates is milled down 30 mm compared to the outer ends. To ensure that the lenses are perfectly aligned along a common axis, all five connection plates were milled as one common block and installed in the same direction relative to each other.

A clamp is fixed to each of the plates. It consists of one 25 x 6 mm steel bar on each side (“support stays”) of the connection plate and a 50 x 20 mm bar (“back plate”) between the support stays at their end. The back plate has a 25 mm wide and 10 mm deep groove on each side where the narrow bars are welded in place. This ensures a stiff and stable construction. The narrow bars are attached to the connection plate with two M10 screws on each side. The length of the support stays corresponds to the width of the beam, plus the overlap into the connection plates and a few centimetres of air gap between the back plate and the beam. The length of the back plate corresponds to the width of the connection plate plus an additional 20 mm to allow the support stays to be integrated in the plate, as described above.

A fastening screw and its corresponding cylindrical plastic liner is mounted in the centre of the 50 x 20 mm “back plate”, it ensures that the connection plate rests properly against the intended surfaces on the beam. The set screw and plastic liners are almost identical as those in the support bracket and are thus thoroughly described in the section about the Brackets. The only difference is that the set screw on the clamp is larger with its M16 threads.

The lenses are fastened in a holder that is purpose built for these lenses. Each holder has two clamps that holds the circular lens with three contact points. One clamp holds directly onto the lens body, while the other holds on a collar on the lens body. In this way, the two clamps can have the same internal diameter, despite the tapered shape of the lens. These purpose-built holders are fastened to their corresponding fundament plate with six M6 screws. The connection plates are fastened to the back of these fundament plates with two M10 bolts in each plate. The support for the light and lens has two connection plates, while the longer and significantly heavier support for the camera and its lens, has three connection plates.

To ensure that all plates and components are aligned with each other, the plates are milled to the right dimensions. The outer surfaces of the plates were milled to ensure that all corners are exactly 90° and that the opposite sides are aligned to each other. Correct angles and measures on the outer edges is a prerequisite to get correct measurements, which again is a prerequisite for making a system that is aligned. 3 mm deep groove was milled on all surfaces where one plate is attached orthogonally to

another. This means all the connection plates as well as the “shelf plate” for the camera. In addition to the plates actually used for mounting equipment, a number of bracing plates were also used to strengthen the construction. For instance, the gap between the two support plates on the light lens support is covered by an aluminium plate with a length that exactly matched the gap. This ensures that the connection plates remain orthogonal to the fundament plate, regardless of what forces the parts are exposed to.

### **Adjustment principles**

The system is adjusted along the z-axis (vertical direction) by adjusting the support plates below the aluminium beam within the brackets. As the set screws in each bracket are adjusted independently, it is also possible to adjust the camera axis (axis with direction along the axis from the light to the camera through the lenses and the chamber) to deviate from the horizontal plane, if necessary. Adjustment in the horizontal axial direction is done by sliding the lens supports on the aluminium beam. Separate holders for each lens allow individual adjustment of the distance between the visualization window on the explosion chamber and the lens on each side

If adjustments along the axis perpendicular to the camera axis is necessary, spacers must be inserted either between the support structure and the brackets or between the aluminium beam and the inside of the clamps. However, as adjustment along this axis is not supposed to be necessary, this is an acceptable solution.

If it by some reason becomes necessary to rotate the lens and camera along the axis running from the light to the camera, this could be done by combined adjustment of all set screws in the brackets. Each bracket has two set screws below the beam (however, both set screws is connected to a common nylon plate) as well as one screw in the top and one on the “back side”, pushing the beam towards the chamber.

The position of the camera relative to its lens is also adjustable. The shelf plate has, as mentioned earlier, one upward pointing adjustment screw in each corner. The camera is mounted to another plate, which rests at the end of these four screws. This mechanism allows adjustment in all direction and angles to avoid any tension on the bayonet connection between the lens and camera. A slot in the “shelf plate” along the camera axis together with two threaded M10 holes in the plate mounted directly on the camera, allows the camera to be secured to the shelf plate when it has been adjusted. No further adjustments should be necessary after the camera has been adjusted during installation unless the camera is replaced.

### **A.4.3 Support system for high pressure hydrogen system and instrument air**

The high-pressure hydrogen system and its functionality is described A.2. As this system is intended to release high hydrogen pressure very fast, it will be subject to substantial reactive forces according to Newton’s 3<sup>rd</sup> law. Especially as the gas changes direction 90° on its way through the fast-acting valve. It is therefore important to secure these components properly, despite their small dimensions and volumes. The fastening system is made from a combination of aluminium, plastic and plywood. The components are shown on MECH-01-01 and MECH-01-02.

The actuator on the fast-acting valve is secured in a two-piece clamp made from aluminium. The aluminium clamp is lined with a layer of rubber to spread the load on a wider section of the clamp in addition to protect the actuator from scratches. However, as the principle of the high-pressure tubing and fittings systems means that the valve must be inserted from below, the support clamp must be installed after the valve. The support system is therefore designed so that the clamp for the actuator could be slide in place along with the rest of the high-pressure system after the release valve has been installed. The fitting on the upstream side of the high-pressure valve will then be connected simultaneously as the actuator clamp is installed below the release valve actuator. The purpose of the design is otherwise to enable the system to remain in one piece even though it is detached from the explosion chamber and release valve.

The actuator clamp is mounted on a 12.3 mm aluminium plate, which is 150 mm wide and 300 mm long. This plate is attached with 3 M8 bolts to an aluminium beam of 350 mm length and 47 mm height. It is free holes in the aluminium beam and threaded holes in the plate. The support plate for the actuator clamp rests on a 12 mm thick bottom plate in the “stool” between the explosion chamber and the supporting aluminium plate, while the 350 mm beam lies directly on the supporting plate. The horizontal free holes in the beam are therefore elevated an extra 12 mm to account for this. A plywood plate is placed on the top of this aluminium beam. The other end of the plywood plate rests on a beam of 400 mm length and the same height of 47 mm.

Because the actuator for the fast-acting valve has a much larger OD than any other component in the system, it is necessary to elevate the supports to ensure all components reach the same elevation for their centre. It is most convenient to elevate the common support plate for all components instead of building individual supports for each component all the way from the lowest level. Therefore, the aluminium beams that support the plywood plate are as tall as they are. Both aluminium beams are secured to the underlying plate with two bolts each. The bolts pass through the plywood plate and the beam and is attached to threaded holes in the aluminium plate below. M12 is used in the front beam (the one with 350 mm width) while M10 is used at the back beam.

The “system centreline” is approximately 53 mm above the top of the plywood plate, which means that all components must be elevated 20-30 mm above it. Two plastic clamps secure the pressure vessel, which has a cigar shape with OD 48 mm. The clamps have an ID of 52 mm and is lined with a rubber band. One M8 bolt on each side goes through both parts of the clamp and the plywood plate, thus pushing the clamp together and locking the pressure cylinder to the plate when tightened. It was necessary to put a 3 mm spacer under the clamp to get the correct height. Three different cylinder sizes were procured for this project, namely 150, 300 and 500 ml. They all have the same OD but different length. Change of cylinder size is therefore easy to facilitate by simply moving the two plastic clamps and move the other components accordingly.

The “connection hub” with one M10x1 and 6 NPT ports in one piece of stainless steel, is lifted from the plywood plate with two spacers made from plywood. Two M8 bolts are perforating all layers of plywood and is attached to threaded holes in the hub.

Plywood spacers are also used to elevate the instrument valves to the right centre height; however, they are not attached to the plate with bolts as the main components are. Instead, holes are drilled through all layers of plywood on each side of all valves to allow a flexible fastening with plastic strips. As the distance from the hub to the valves is small, this strips solution is strong enough.

It is important to allow sufficient flexibility in the longitudinal direction until all fittings are tightened to ensure that all sealing surfaces are properly connected. The pressure vessel could easily be moved in this direction by simply moving it within the plastic clamps before they are tightened. The holes in the plywood plate below the connection hub are in fact small slots, with a length of approximately two times the width which is also quite oversized compared to the M8 bolts used with its 11-12 mm. The plastic strips solution used for alle the valves is also flexible enough to accommodate for minor changes in position due to this flexibility.

The air system is located on back side of the explosion chamber, as close as possible to the actuated valve. In order to have as short air hoses as possible, the 3/2 solenoid valve is elevated so that its outlet port is in the centreline height. The air connection on the actuator is in the centre of the actuator, thus in centreline height. The inlet port on the solenoid valve is a bit lower than the outlet, and the air reservoir is elevated so that its outlet port is on the same elevation as this inlet. Both the solenoid and the air reservoir are also oriented in the same direction. When the hose connections have the same height and direction, it is possible to locate the components very close, with only a few centimetres of hose in between.

An issue with this layout, is that the components need much space in the direction perpendicular to the explosion chamber to be able to keep the hoses as short and straight as possible. The components are therefore mounted on a 20 mm thick wooden plate with sufficient length for both components along one axis. The plate is held in place by two M10 bolts which is fastened to threaded holes in the aluminium plate under the chamber. The wooden plate is 350 mm wide in the end closest to the explosion chamber, which is sufficient to provide necessary strength around the holes with a centre distance of 310 mm. However, as the components are oriented along the centre of the plate, the plate has a trapezoidal shape where it narrows down to approximately 15 cm of width in the outer end. The plate is 350 mm long. Most of the wooden plate hangs unsupported in the air, and the centre of the two bolts are located only 65 mm from the edge of the aluminium plate. In addition to the large force applied to the bolts due to the torque arm, this configuration also entails a certain risk of breaking the wooden plate above the edge of the aluminium plate, which will act as a pivot point.

## A.5 Material selection

As much as possible of this system is made of 316L stainless steel. At least the parts that are in contact with hydrogen or outdoor climate. This material is selected mainly for two reasons: hydrogen has a propensity to cause embrittlement to certain materials. This will deteriorate the strength of the material over time, and especially if the material is exposed in cyclic pattern to high pressures, as will be the case in this system. 316L is very resistant against thin embrittlement mechanism. The second reason is that stainless steel is resistant against corrosion.

As the exhaust pipe will be partly open towards the ambient atmosphere, the inner side of the pipe will be exposed to air with varying temperature and high relative humidity in addition to rain drops (typical Bergen weather). Humid air and varying temperatures will also cause condensation. Painting, coating, or other means of surface treatment of the inside of the pipe is not feasible, so low alloy materials will corrode under these circumstances. On the other hand, the open-ended exhaust pipe will not see large, sustained pressures, only short pressure impulses of moderate magnitude. The hydrogen concentration will also be diluted relatively quickly after an experiment, so the blowdown pipe will only be exposed to hydrogen for short periods of time. However, when both weather and hydrogen exposal is considered, it seems most reasonable to use 316L stainless steel.

The high-pressure hydrogen system will not be exposed to humid, outside air. On the other hand, this part of the system must withstand higher pressures of hydrogen for the duration it takes to perform an experiment. This duration will be in the range from a few minutes to maybe an hour, depending on how much preparatory work it is necessary to carry out between pressurisation and release.

There are some exceptions from the selection of 316L stainless steel. The most significant is the 20L constant volume vessel, that is made from carbon steel. This vessel was initially constructed for a slightly different purpose, namely constant volume explosions of dust or gas mixed with air. Neither hydrogen embrittlement nor corrosion due to moist outdoor air was an issue in the initial usage. The outer surface is painted, while the interior of the vessel is untreated. As the interior will be exposed to humid air and possibly changing temperatures, surface corrosion should be expected to a limited extent. However, as this vessel is designed to withstand enclosed dust and gas explosions (constant volume) and subsequent pressure build-up, the vessel should be able to handle the pressure impulses it will be exposed to in this application with an open exhaust pipe, even with a slight degree of corrosion and hydrogen embrittlement. A new vessel with appropriate material selection is planned in the future, as described in B.3.2.

The support components are also made from other materials: The frame that envelops the constant volume vessel was made during this project. It is made of carbon steel with two layers of surface coating (spray primer and spray painting). The brackets that connect the camera mounting system to this structure is also made of carbon steel, painted with the same paint. The system that holds the high-speed camera and corresponding lenses are made of aluminium. All these components will only be subject to static mechanical loads in indoor air. For this purpose, both aluminium alloys and painted carbon steel are well suited.

## B Other aspects related to the design and construction work

As this kind of experiments have not been performed at the institute for physics and technology, a lot of infrastructure and equipment needed to come in place. The initial strategy was to use existing equipment as much as possible, as this would be the most cost and time efficient approach. The design and functionality of the equipment that was designed during this project is thoroughly described in Appendix A. The following sections provide some relevant additional information concerning the background and timeline for the design and constructional work, as well as elements that can be added or improved in the future.

### B.1 Background and early work

Due to both safety and practical concerns, the Department of Physics and Technology (IFT) decided to move the *Gas explosion laboratory* from Room 271 on the second floor in the southern wing to Room 604 on the roof (sixth floor) of the northern wing of the IFT building at Allégaten 55. The upgraded laboratory will be part of the new *Hydrogen Safety Laboratory* (HySALA). With the buoyant properties of hydrogen, the potential for accumulating hazardous volumes of explosive atmospheres is significantly lower in the top floor of the building, compared to the old location at the second floor. The walls in the new location must only support its own roof, and not overlying structures or floors. These aspects reduce the consequence of potential accidental explosions significantly.

Only a small part of the building's base floor area is used on the sixth floor. The rest of the area is a flat fenced-in rooftop with easy access from the laboratory through a door. This makes it easy to work on the outer wall of the laboratory, as it can be accessed without scaffolding. And as described further down, changes on the outside were necessary to get a safe and durable blowdown pipe from the experimental equipment.

Another positive aspect with the relocation was that the new room is adjacent to the *Dust explosion laboratory*. As both laboratories are used by the same research group, using the same instrumentation, tools and inventory of hazardous materials, there are significant synergy effects from the co-location.

Since both laboratories were in use by students, the moving operation was done at the start of the autumn semester, in August 2020. A mid-semester moving at an earlier time would have been more convenient for the present master project, but this would have come in conflict with other ongoing projects in the laboratories.

Most of the equipment and inventory from rooms 271 and 604 were moved in two sessions with voluntary contribution from students and employees after normal working hours in August 2020. Some work remained after these sessions, and this was completed over the following weeks and months. One of the remaining tasks after the sessions in August was to transport two new flame proof cabinets for



storage of gas cylinders into the new lab. These cabinets were too large to fit in the elevator of the building, and too heavy to be transported by hand up the stairs. Each cabinet weighed almost 500 kg. The cabinets were therefore lifted by a mobile crane on the outside of the building and into the lab through the door from the rooftop. Internal skidding in the room was done by rolling the cabinets on steel axles on the floor. In addition to the two cabinets, a large frame intended to be used as support for experimental setups was moved up this day in December 2020. The frame probably weighed some 200 kg and was about 4 meters long.

## B.2 Leakage testing

Leakage tests were performed as described in 4.4.1. The results for the final test on the full system, including hydrogen supply line, are shown in Table appendix 6. The final nitrogen test evaluated the full volume from the nitrogen bottle valve to the hydrogen bottle valve, as described in 4.4.1. The final hydrogen test, however, was performed with both the valves from the nitrogen and hydrogen supply lines closed (HA-103 and HA-122 on P&ID-01-01).

*Table appendix 6: Results from leakage tests performed with nitrogen on the full experimental setup.*

Test description	Time [minutes]	Pressure [bar]	Leakage rate [bar/min]
Tests before the last corrections	0	81.70	0.037
	10	81.33	
Final test with nitrogen	0	97.04	0.029
	30	96.15	
Final test with hydrogen	0	61.81	0.014
	10	61.67	

As Table appendix 6 shows, there are slight pressure decays on the last leakage tests as well. Since no external leakages could be observed with bubbling soap film during these tests, the pressure decays could be caused by reasoned by other things than external leakages. Small internal leakages through the valves leading to atmospheric pressure, as for instance the release valve could cause such leakages. Another plausible issue for this pressure change, is temperature effects. E.g., changes in pressure due to changes in the temperature of the gas when it is introduced to the high-pressure system. It is also possible that the system has external diffusions of such small magnitude that they either don't produce bubbles at all, or bubbles that are too small to be detected visually.

Generally, it is also a possibility that external leakages or internal leakages out of the tested volume are camouflaged by internal leakages of equal magnitude from a pressure source into the system. In these tests, the hydrogen and nitrogen bottles were not disconnected during the tests, as this would trigger the need for a new assembly and leakage test. Thus, it is in theory a possibility that some leakage is camouflaged this way. However, as the bottles has been stored for long time without any notable pressure loss, it is demonstrated that the bottle valves don't have any leakage of importance.

Considering the small volume of the system, such small pressure drops that are observed here, are neglectable.

## B.3 Further improvements on the experimental setup

The experimental setup that could be put in place for this project has some several limitations. Economical, practical or time related considerations have in some cases limited the design compared to the ideal. Other aspects have turned out to not function as well as intended and should therefore be improved at a later occasion. Further research purposes might also require modifications to the setup.

### B.3.1 Pressure booster and equipment with higher pressure rating

The maximum working pressure is limited to the pressure delivered from the gas bottle in the current setup. Investigation of spontaneous ignition behaviour at releases from high pressure will probably be of interest for future work. Procurement of a pressure booster will enable investigation at much higher pressures. Many vendors deliver boosters that can produce more than 1000 bars. Pressure rating on the equipment in the present setup varies, but the equipment with the lowest rating is designed to 5000 psi (344 bars). The pressure cylinders/vessels are among the components with 5k psi rating, thus must be replaced for a future setup with pressure booster.

Some of the equipment in the current setup was purchased with a potential future setup including pressure booster, thus have pressure rating of 1000 bars or more. The fast-acting release valves are among this equipment.

Procurement of a pressure booster in addition to all necessary components downstream of the booster with sufficient pressure rating will be very costly. The equipment alone will probably cost several hundred thousand NOK. Introduction of moving parts in contact with high pressures are also likely to increase maintenance costs.

Increased pressure along with moving parts will also increase the risk. The released energy if a leakage at such high pressure should occur is significantly larger than at pressures investigated in the current setup. Maximum pressure delivered from a pressure booster is a function of the available instrument air pressure and the ratio of area at the air side compared to the gas side of the compressor piston(s):

$$p_{final,hydrogen} = p_{air} * \frac{A_{air}}{A_{hydrogen}} \quad (i)$$

Usage of such pressure devices entails a certain risk of overpressuring the system, if for instance air supply with higher pressure than usual is used by mistake or the system is operated without sufficient level of caution. This risk together with the complexity of a system containing a pressure booster mean that it requires more competence to operate this system than the current system.

### B.3.2 New explosion vessel

As earlier mentioned, the vessel used in this project was initially built for another purpose. It is also made of carbon steel, which is not the desired material quality for the system, as described in section A.5. In its initial purpose, the vessel was used standalone and had a hinged lid at the top. Even though the lid is secured with 16 M20 bolts, the unconstrained space around it together with the hinge, made opening of the vessel easy.

This hinged lid is replaced with a flange without hinges in the current setup. As the lid is also connected to, and partially supports, the exhaust tube with a bolted flange, it is rather time consuming to get access to the interior of the vessel. A faster way of getting access is to remove the axial compensator located above the concentric reducer at the lid. However, it is necessary to split two flanges to remove this

component, and the approximately 150 minimum ID at the top of the reducer does not provide full access to the vessel.

The layout and number of viewing windows, connection ports and mount for other instrumentation also have room for improvement.

Based on these observations, a future vessel should be made from 316L stainless steel and have an easily accessible hatch at one of the sides for access to interior of the vessel. The hatch must be big enough to make it practical to change obstruction objects, maintain or change position of instrumentation, etc. This is especially important if the experiments require changes to equipment within the vessel between each run.

### **B.3.3 Branched blowdown pipe for simultaneous use of different experiments**

The current design has only one inlet to the blowdown pipe, thus only one experimental facility could be connected to the exhaust at a time. Modification of a setup to match a new set of experiments tend to be time consuming. With the current layout with only one system, projects cannot be run in parallel, and the change of projects will require some downtime.

However, with a branched blowdown system, it could be possible to have multiple “experiment stations” connected at the same time. With valves or other measures for easy isolation of systems when experiments are not conducted, this should be a feasible solution. Simultaneous explosion experiment would cause unacceptable interference between the systems but performing the actual explosion experiments is only occupying a small amount of the total project time. Preparation and after work and not at least all analytical work where the experimental facility is idle but cannot be modified occupies most of the time. For most preparation and after work, the blowdown pipe can be shut off without affecting the progress.

It will raise some issues. For instance, the introduction of a possibility to close off a blowdown pipe leg would also introduce a risk of unintentional gas filling with subsequent ignition in a closed system. The isolation valve must be able to withstand the pressure waves generated by explosions in the other branches of the system, thus it will also withstand the same magnitude of statical pressure if the system is unintentionally gas filled while isolated. If ignition occurs within this compressed mixture, it could cause extensive overpressure and a possibility of violent deformation of the system.

The use of interlocks, pressure release devices and a robust procedure will help mitigate this risk. The isolation valve should also be designed to collapse at a pressure as low as possible.

### **B.3.4 System for easy replacement of sealing plastic films at the vessel top**

The current system was designed with compression springs below the lid of the vessel to make it easy to put plastic film between the vessel and the lid. Experiments with modified atmosphere require this possibility of isolation from the ambient to allow addition of correct amount of desired gas and subsequent mixing to create a homogenous atmosphere.

It quickly turned out that the “steel beam” mounted at the underside of the vessel lid to hold obstruction objects would come in conflict with a plastic sheet, thus make this approach to plastic sealing very impractical. Insertion of the sheet in one of the flanges further downstream in the blowdown pipe became the backup plan. It should be possible to insert this plastic sheet into one of the flanges, but an extra gasket might be required to ensure sealing between each flange face and the plastic sheet. Modified atmospheric concentrations were not investigated in this thesis work, and this sectioning principle was therefore not needed.

For potential future purposes, it is desirable to keep this premixed volume as low as possible. Therefore, the design should allow insertion of plastic film between vessel and lid.

### B.3.5 Flame arrestor on the blowdown pipe outlet

In case of ignition within the explosion vessel or in the blowdown pipe, the system should have a flame arrestor to avoid the combustion to propagate out of the system and into the ambient atmosphere. A flame arrestor is a device that will let gas flow through a mesh, but as the openings in the mesh are smaller than the maximum experimental safe gap, a combustion/explosion cannot propagate through it. To compensate for the flow restriction caused by the fine mesh, the diameter and cross-sectional area is increased.

The location of the lab at the roof will reduce the consequences if an explosion propagates from the experimental facility to the outside by two reasons: It is not much building mass in the vicinity of the outlet of the blowdown pipe, and the buoyant properties of hydrogen will cause it to flow upwards thus preventing the accumulation of a large cloud of air-gas mixture near the outlet.

# C Checklists and procedures

## C.1 Daily safety check list

1. Perform a visual check of all components.
2. Verify that the blowdown pipe and its outlet are free from any congestions.
3. Put up barrier bands around blowdown outlet.
4. Ensure proper ventilation.
  - a. Mechanical fan in bottle cabinet
  - b. Natural ventilation in lab
5. If setup has been partly disassembled since last experiment, or the system has not been used for a while:
  - a. Perform simplified leak test (holding test) with nitrogen.
6. Proceed to checklist C.2.

## C.2 Procedures before first experiment each day

1. Power up instruments and logging equipment
  - a. High speed camera
  - b. External power supply for release valve relay. 12 V,
  - c. External power supply for light source. 12V, 350 mA
  - d. National instruments logging card.
  - e. Kistler signal amplifier.
  - f. Remove lens covers on both lenses.
2. Open air supply.
  - a. Valve on wall outlet
  - b. Combined shutoff/blowdown valve on air regulator 02-PCV-103.
  - c. Verify sufficient air pressure at manometer on air reservoir B-102.
3. Start camera and logging programs on lab PC.
  - a. Verify that camera is functional with a working picture on “live view”.
  - b. Verify that parameters and activation times and intervals are correct.
4. “Tick off” boxes for all analogue input channels that should be logged. Must be done every time the program is started:
  - a. Piezo transducer in pressure reservoir.
  - b. Piezo transducer in explosion chamber.
  - c. Signal for triggered valve
5. Verify line up according to Figure appendix 16
6. Proceed to checklist C.3.

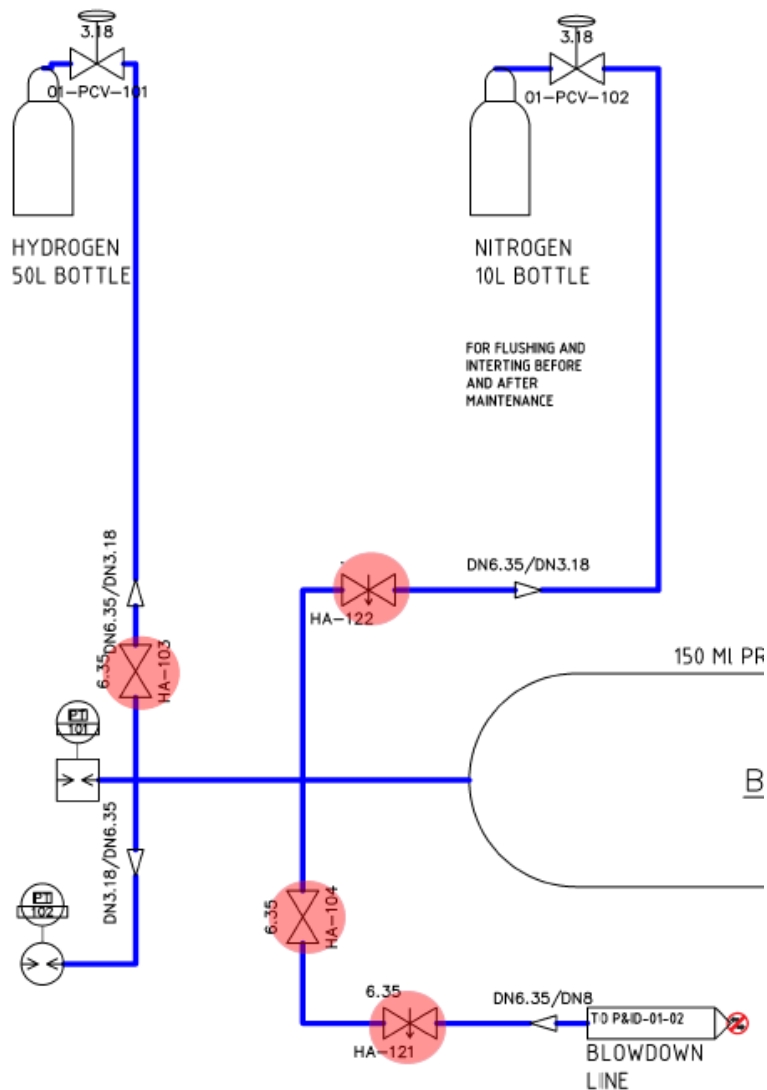


Figure appendix 16 Line up prior to filling of desired gas. All valves closed

### C.3 Procedure for each experiment

1. Flush explosion vessel with plant air to displace gas or combustion product from last experiment and ensure stable humidity.
2. Prepare camera for recording.
  - a. Verify that the “live view” shows “ready” in a green box.
3. Power up portable digital manometer on high-pressure hydrogen system.
4. Open filling valve for desired gas.
  - a. HA-103 for hydrogen.
  - b. HA-122 for nitrogen.
5. Open bottle valve and pressurise to desired pressure with regulator.
  - a. 01-PCV-101 for hydrogen.
  - b. 01-PCV-102 for nitrogen.
6. Close isolation valve from gas supply (HA-103 or HA-122).
7. Add meta data about experiment.
  - a. Verify that the automatically updated experiment number is correct

- b. Add information about gas and initial pressure read at portable manometer.
8. Initiate experiment sequence.
9. See through camera recording from the experiment and save relevant section.
  - a. Save into folder with description of which experiment number it belongs to.
10. Verify that a .txt file with the pressure recordings has been saved.
11. Take notes!
12. Repeat this check list for the next experiment or proceed to C.4 if finished.

## C.4 Checklist after last experiment each day

1. Close gas bottle valve on all bottles.
2. Verify that the high-pressure hydrogen system is depressurised.
  - a. Including segment from bottle valve via regulator to inlet valve on HP system
3. Purge explosion chamber and blowdown pipe with air if necessary
4. Close air supply at wall outlet.
5. Shut off all instruments and logging equipment.
  - a. High speed camera.
  - b. External power supply for release valve relay. 12 V, ? mA.
  - c. External power supply for light source. 12V, 350 mA.
  - d. National instruments logging card.
  - e. Kistler signal amplifier.
  - f. Add lens covers on both lenses.

## D Documents and drawings

This chapter contains both mechanical drawings of components in the experimental system, as well as P&ID's. Each document is sorted under its own heading to make it easier to cross-refer to the documents from the places where they are mentioned in the text.

*MECH-drawings:* The drawings with drawing name "MECH" are mechanical drawings of various mechanical components that are used in the experimental setup. Except from the "Explosion chamber flange" on MECH-02-03 and the "Alignment beam" on MECH-03-01, all components shown on these mechanical drawings have been manufactured as a part of this thesis work.

*P&ID-drawings:* The two Piping and Instrumentation Diagrams (P&ID) show the enclosed part of the experimental setup from a process functionality point of view.

*IFD-drawing:* A Instrumentation and Functionality Diagram (IFD) shows the instrumentation in relation to the mechanical parts of the setup. The diagrams shows how the instrumentation is interconnected, and thus describe its function.

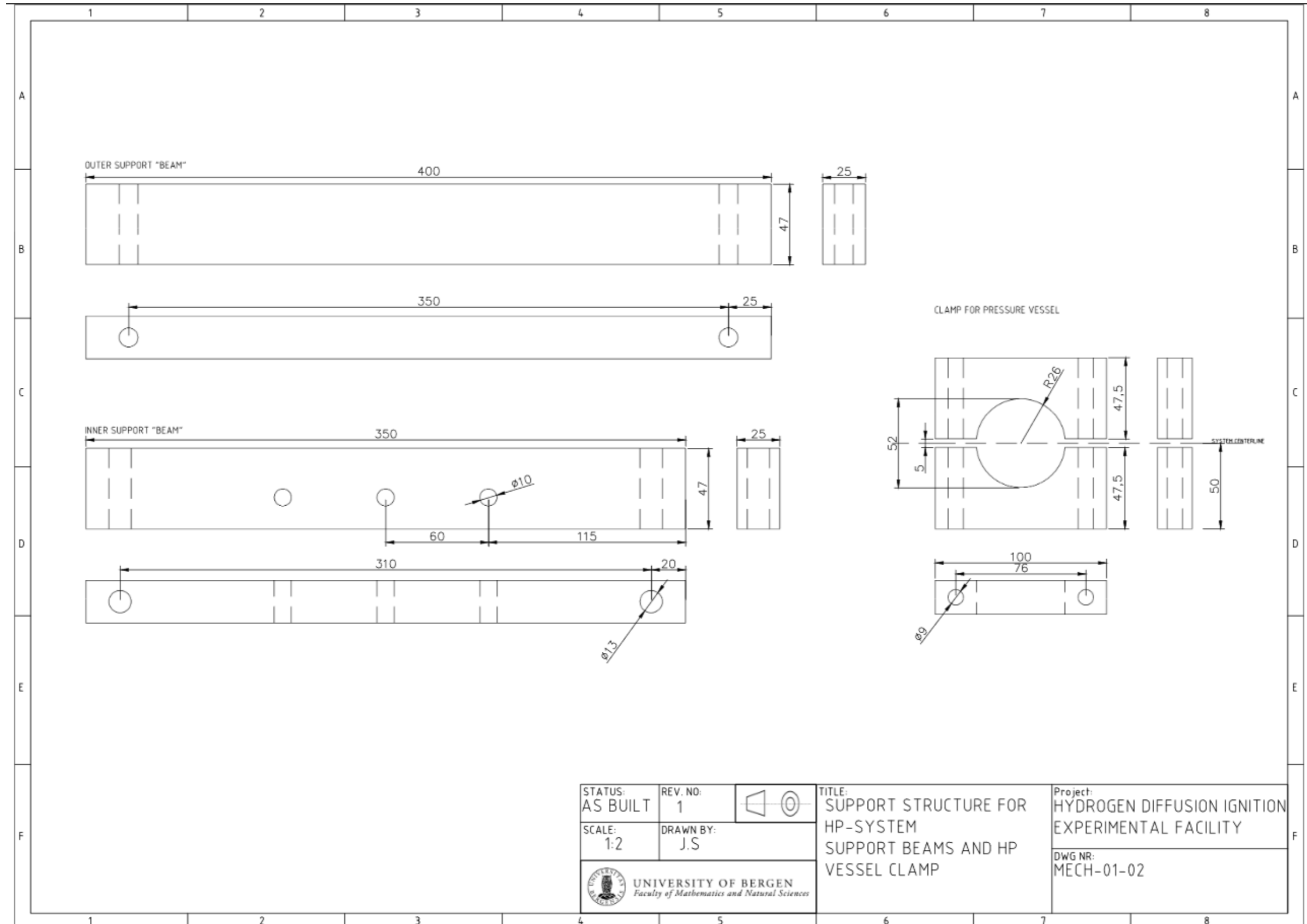








## D.2 MECH-01-02

### Support structure for HP system – Support beam and HP vessel clamp



STATUS: AS BUILT	REV. NO: 1	
SCALE: 1:2	DRAWN BY: J.S	
 <b>UNIVERSITY OF BERGEN</b> <i>Faculty of Mathematics and Natural Sciences</i>		

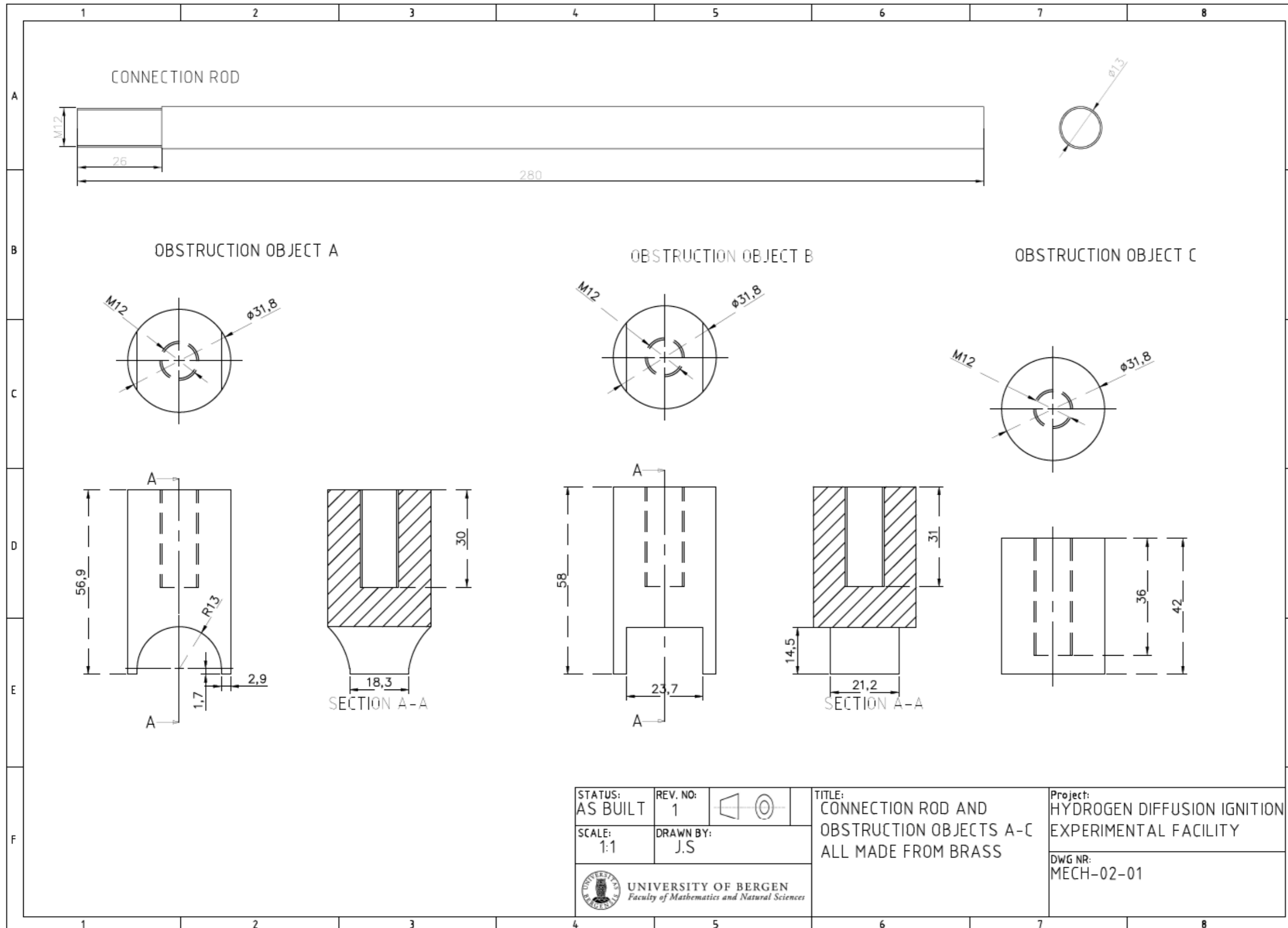
TITLE:  
SUPPORT STRUCTURE FOR  
HP-SYSTEM  
SUPPORT BEAMS AND HP  
VESSEL CLAMP

Project:  
HYDROGEN DIFFUSION IGNITION  
EXPERIMENTAL FACILITY

DWG NR:  
MECH-01-02

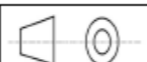
# D.3 MECH-02-01

## Obstruction objects A-B-C and connection rod



STATUS: AS BUILT

REV. NO: 1



TITLE: CONNECTION ROD AND OBSTRUCTION OBJECTS A-C ALL MADE FROM BRASS

Project: HYDROGEN DIFFUSION IGNITION EXPERIMENTAL FACILITY

SCALE: 1:1

DRAWN BY: J.S

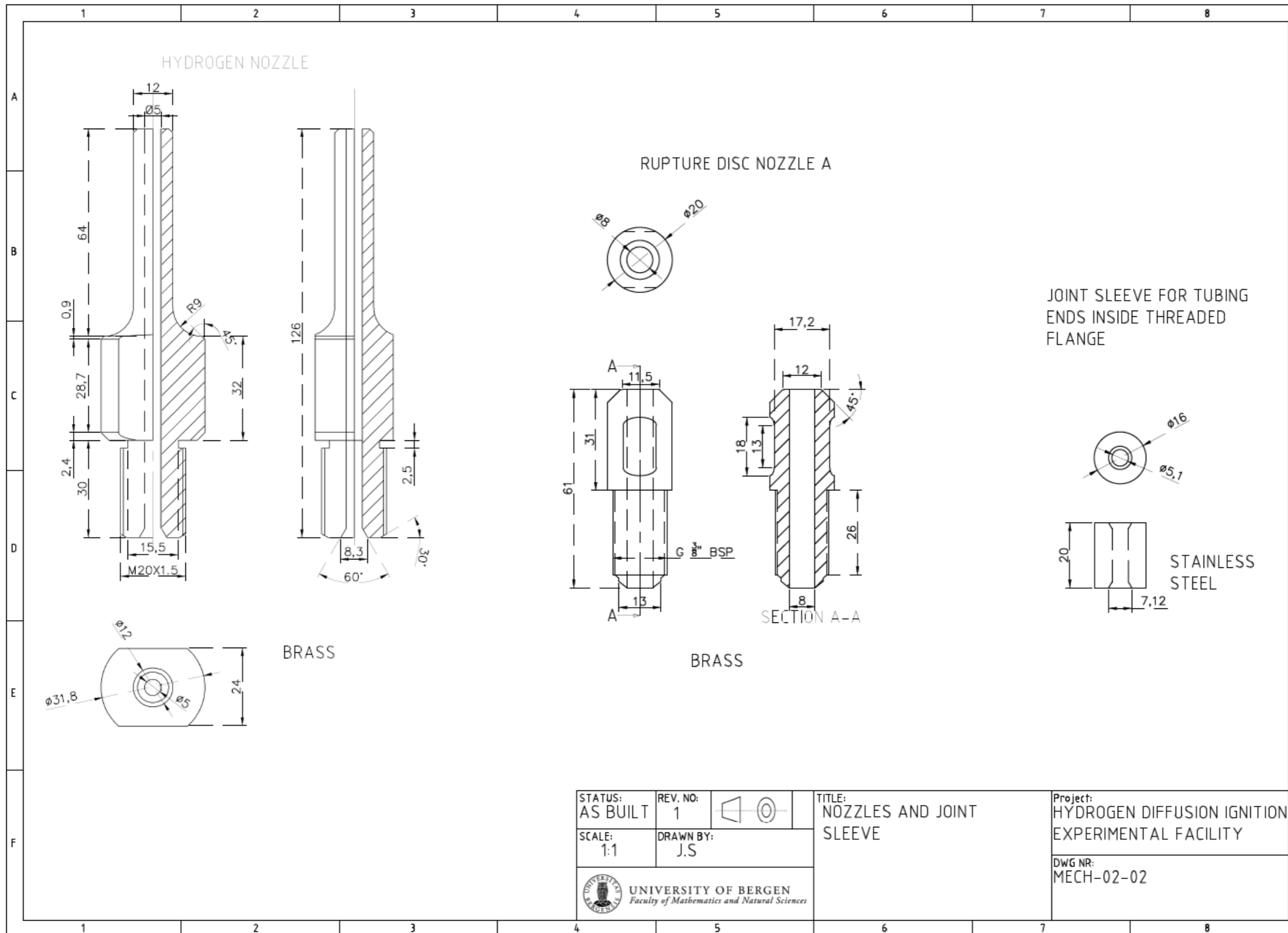
DWG NR: MECH-02-01



UNIVERSITY OF BERGEN  
Faculty of Mathematics and Natural Sciences

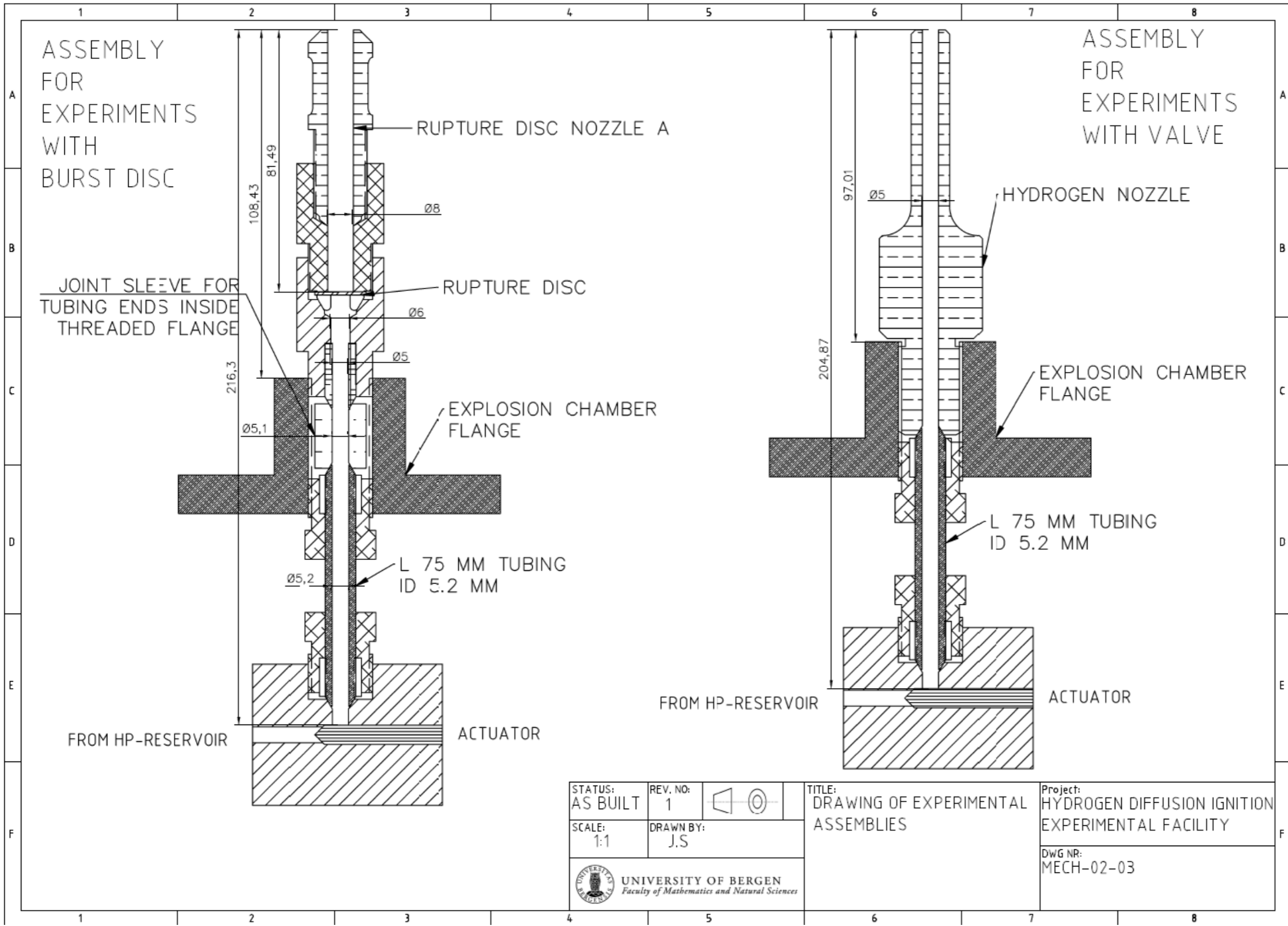
## D.4 MECH-02-02

Nozzles and joint sleeve



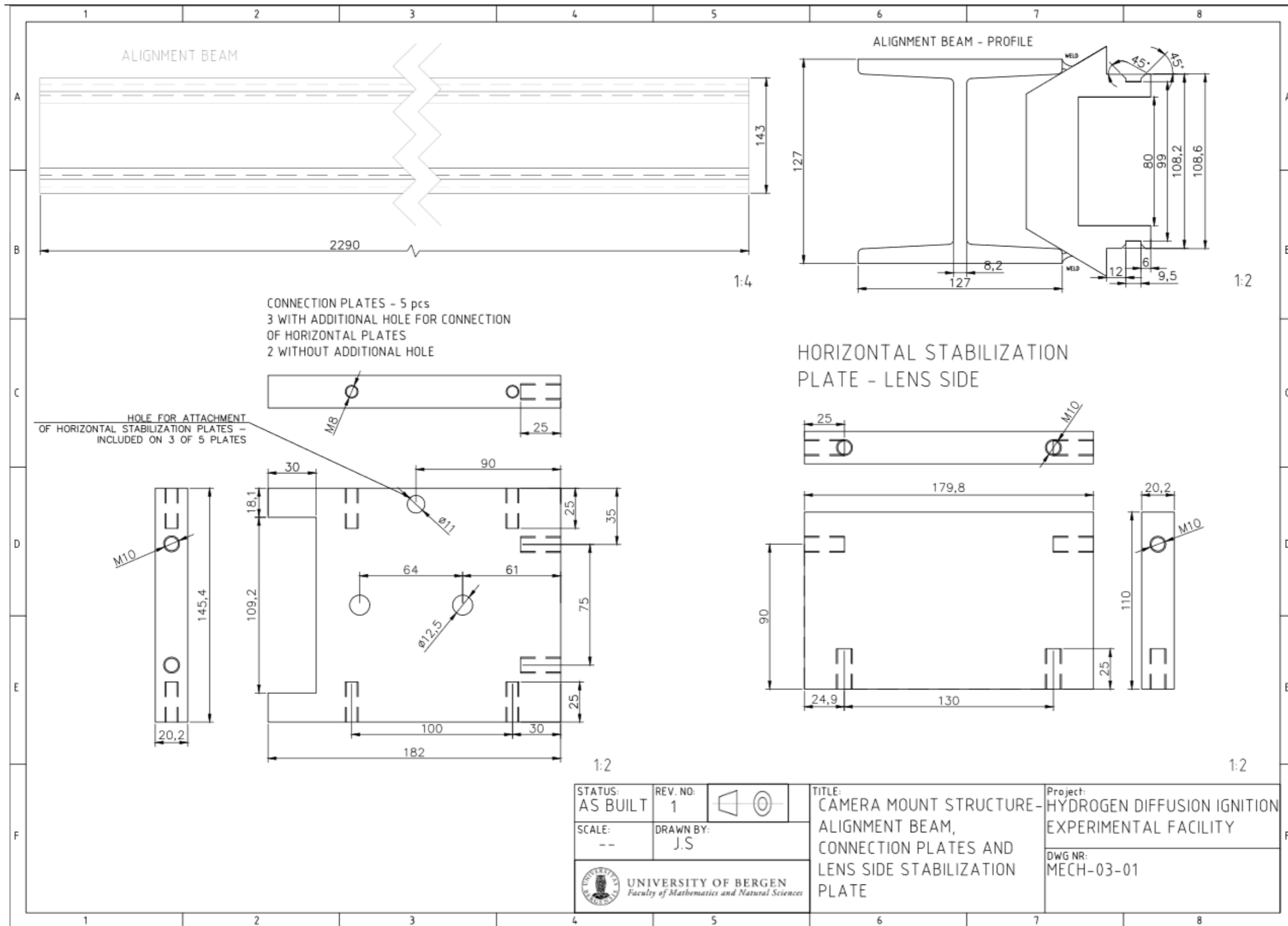
## D.5 MECH-02-03

Drawing of experimental assemblies



# D.6 MECH-03-01

## Camera mount structure – alignment beam, connection plates and lens side stabilisation plate



STATUS: AS BUILT	REV. NO: 1	
SCALE: --	DRAWN BY: J.S	
<b>UNIVERSITY OF BERGEN</b> <i>Faculty of Mathematics and Natural Sciences</i>		

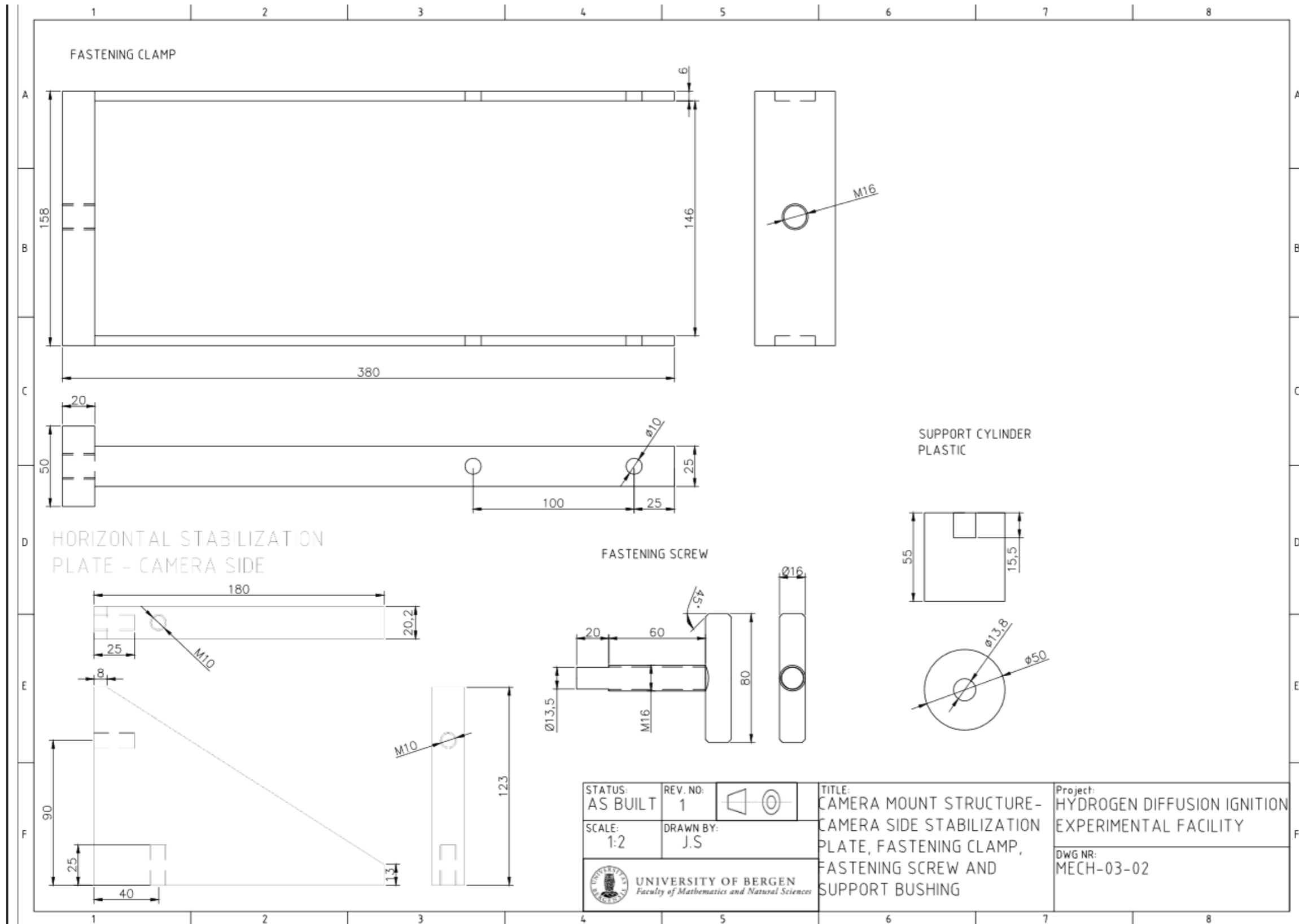
TITLE:  
CAMERA MOUNT STRUCTURE -  
ALIGNMENT BEAM,  
CONNECTION PLATES AND  
LENS SIDE STABILIZATION  
PLATE

Project:  
HYDROGEN DIFFUSION IGNITION  
EXPERIMENTAL FACILITY  
DWG NR:  
MECH-03-01



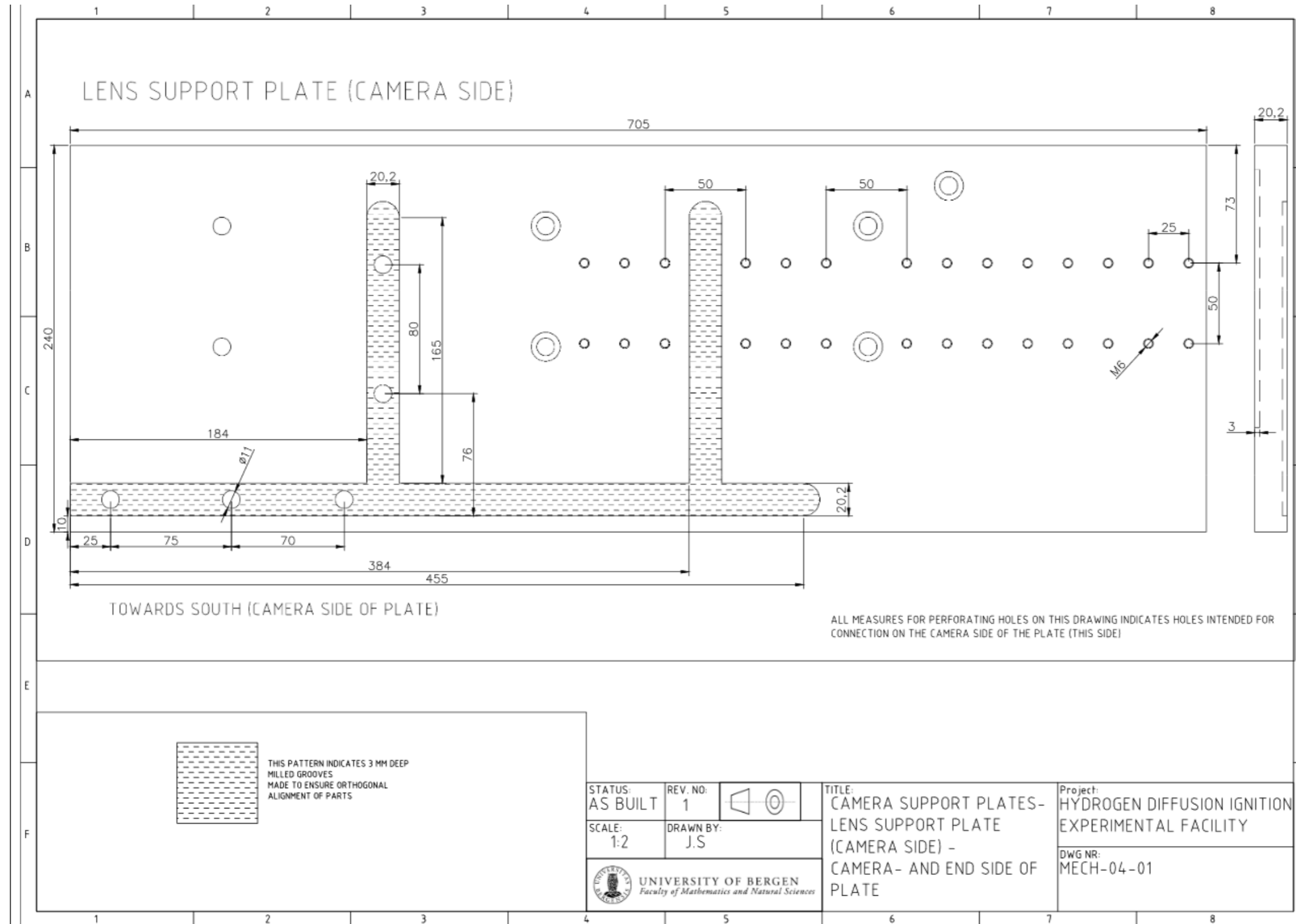
# D.7 MECH-03-02

Camera mount structure – camera side stabilisation plate, fastening clamp, fastening screw and support bushing



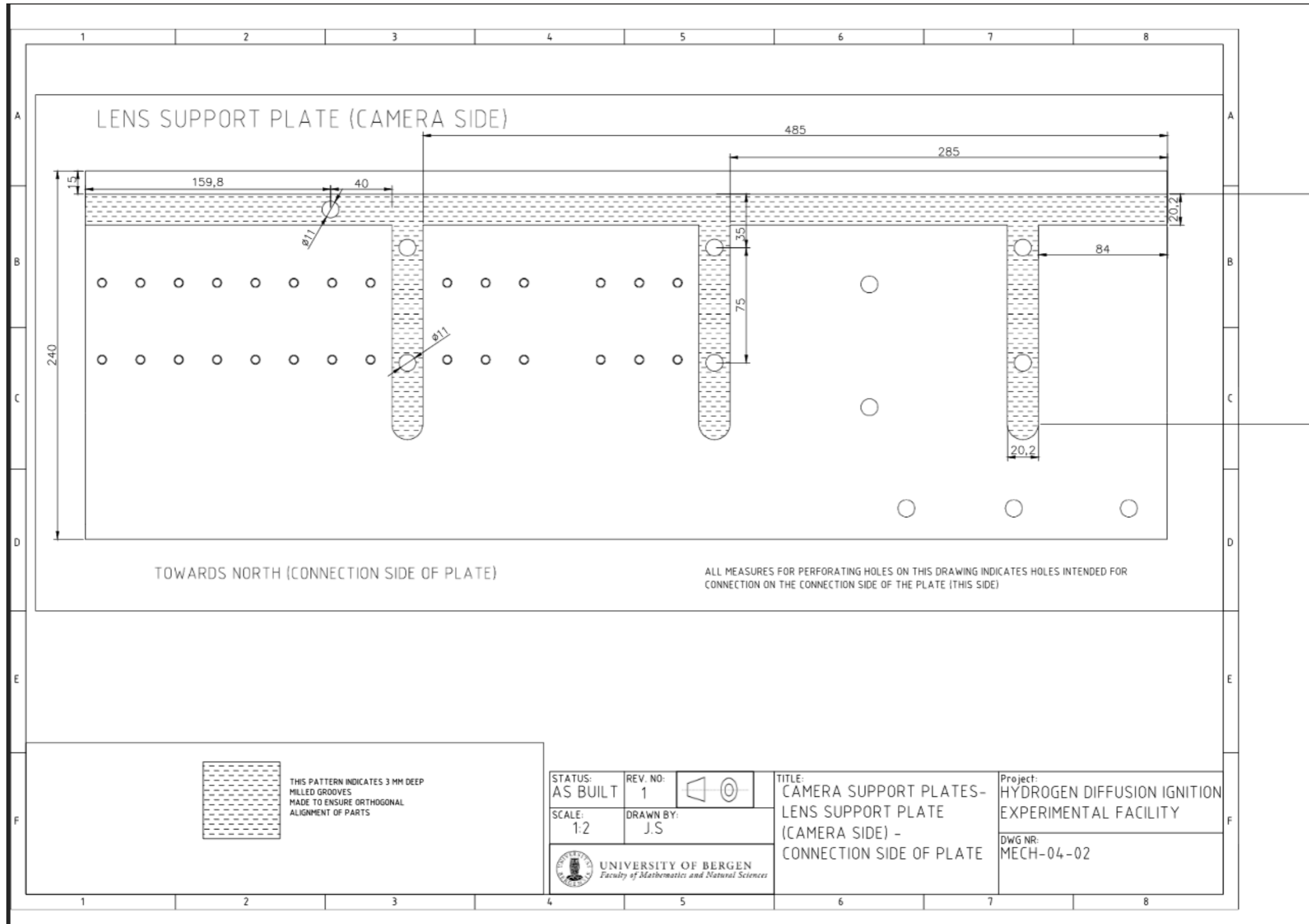
# D.8 MECH-04-01

## Camera support plates – lens support plate (camera side) – camera and end-side of plate



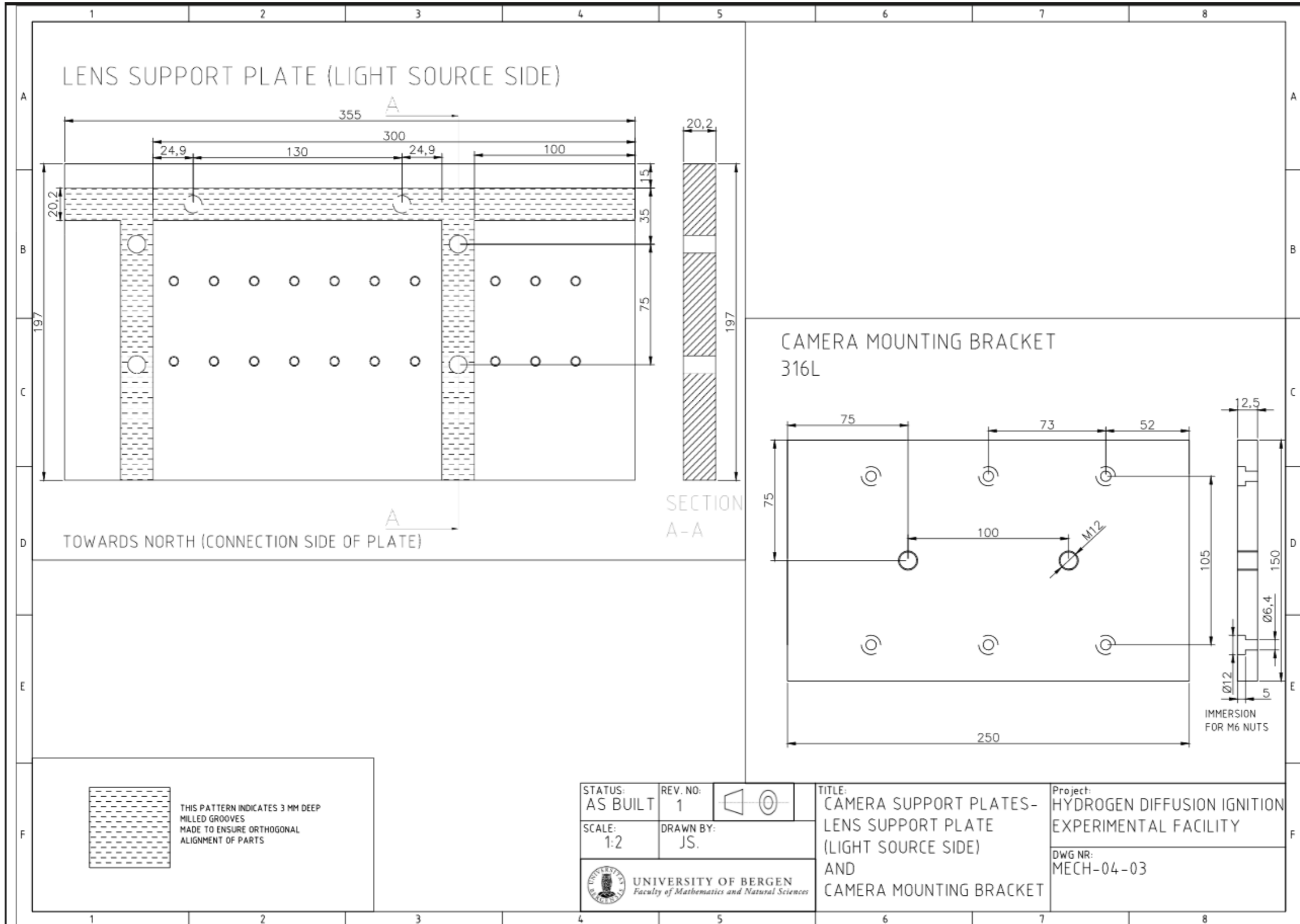
# D.9 MECH-04-02

## Camera support plates – lens support plate (camera side) – connection side of plate



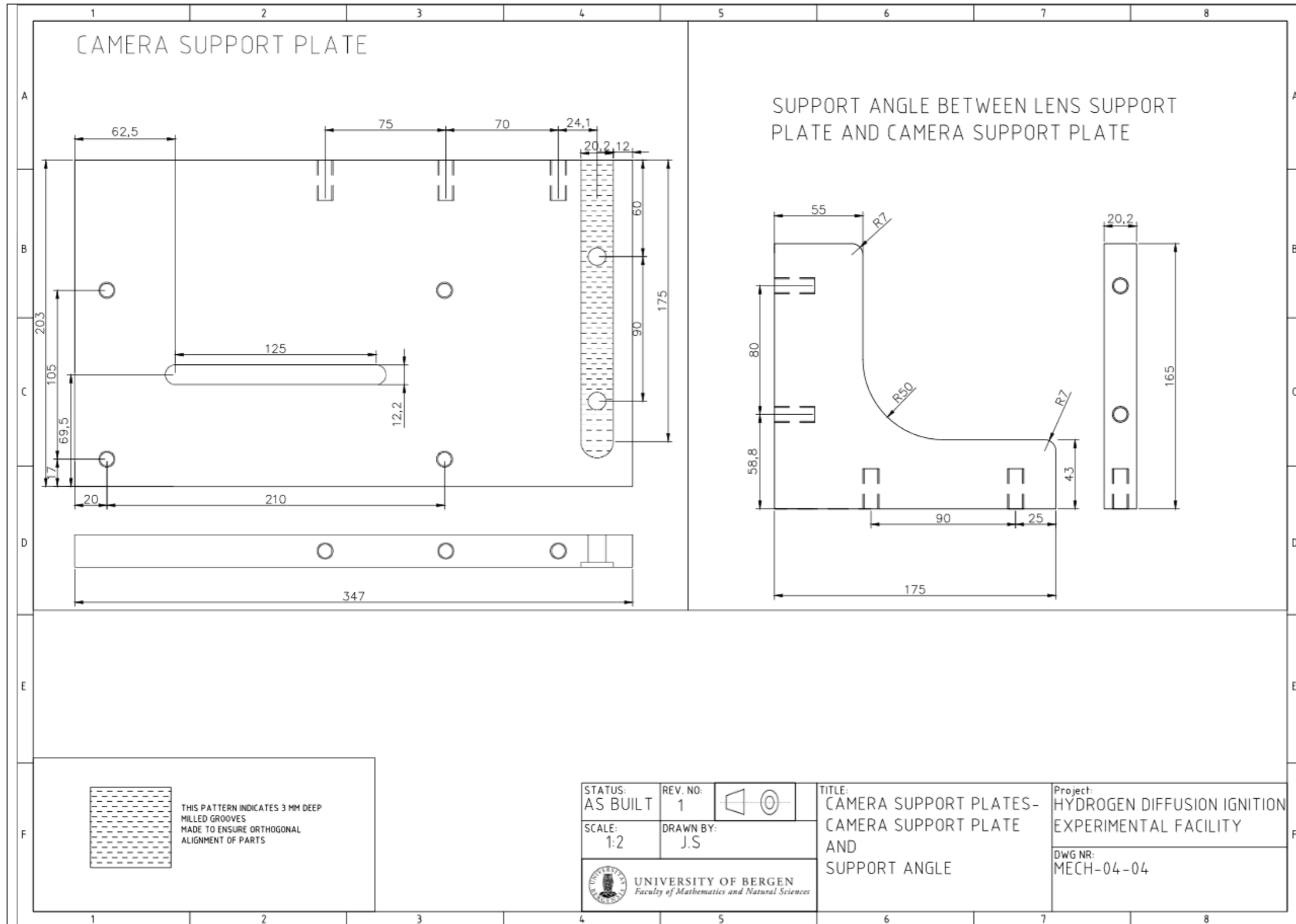
# D.10 MECH-04-03

Camera support plates – lens support plate (light source side) and camera mounting bracket



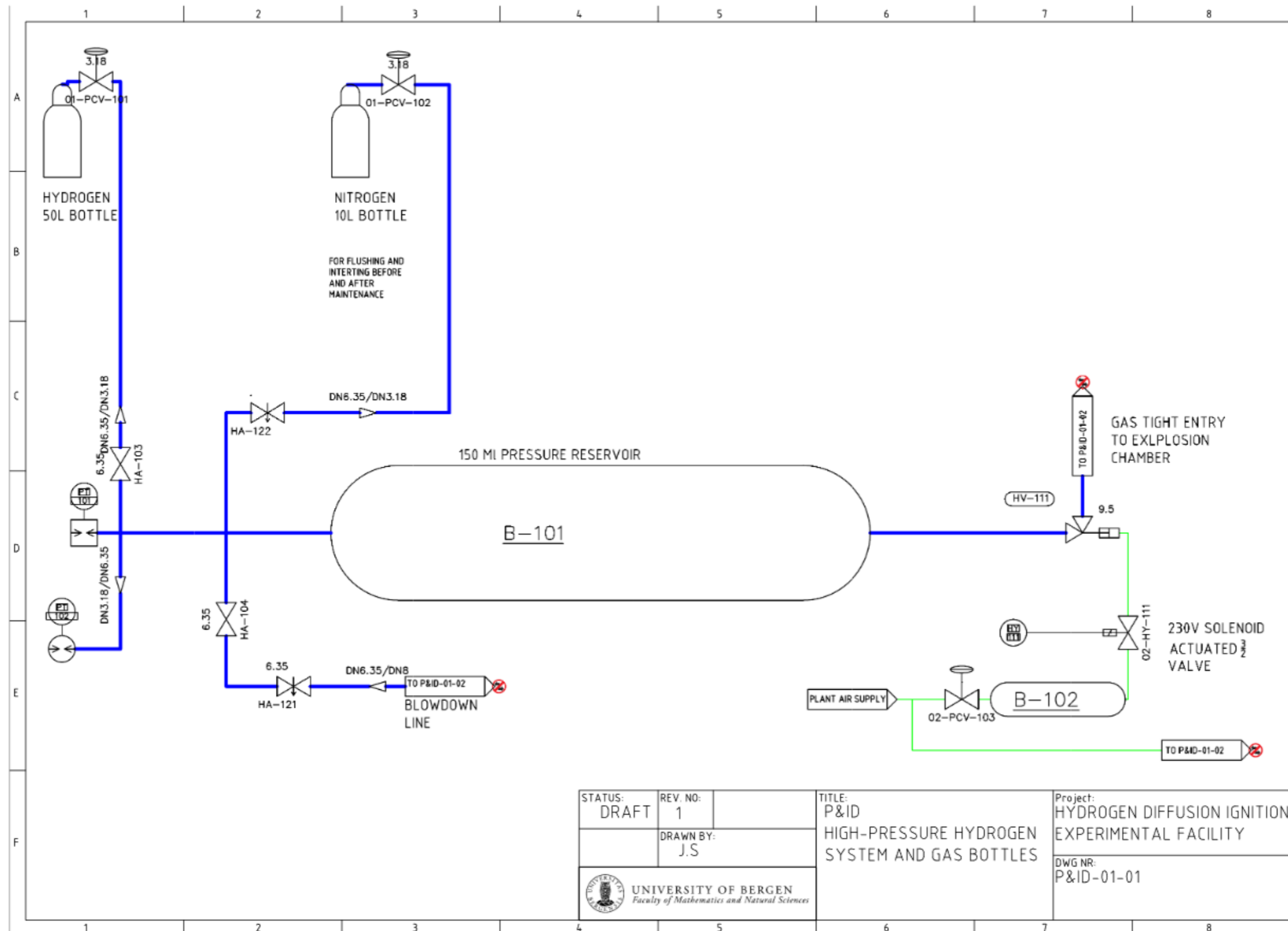
# D.11 MECH-04-04

## Camera support plates – camera support plate and support angle



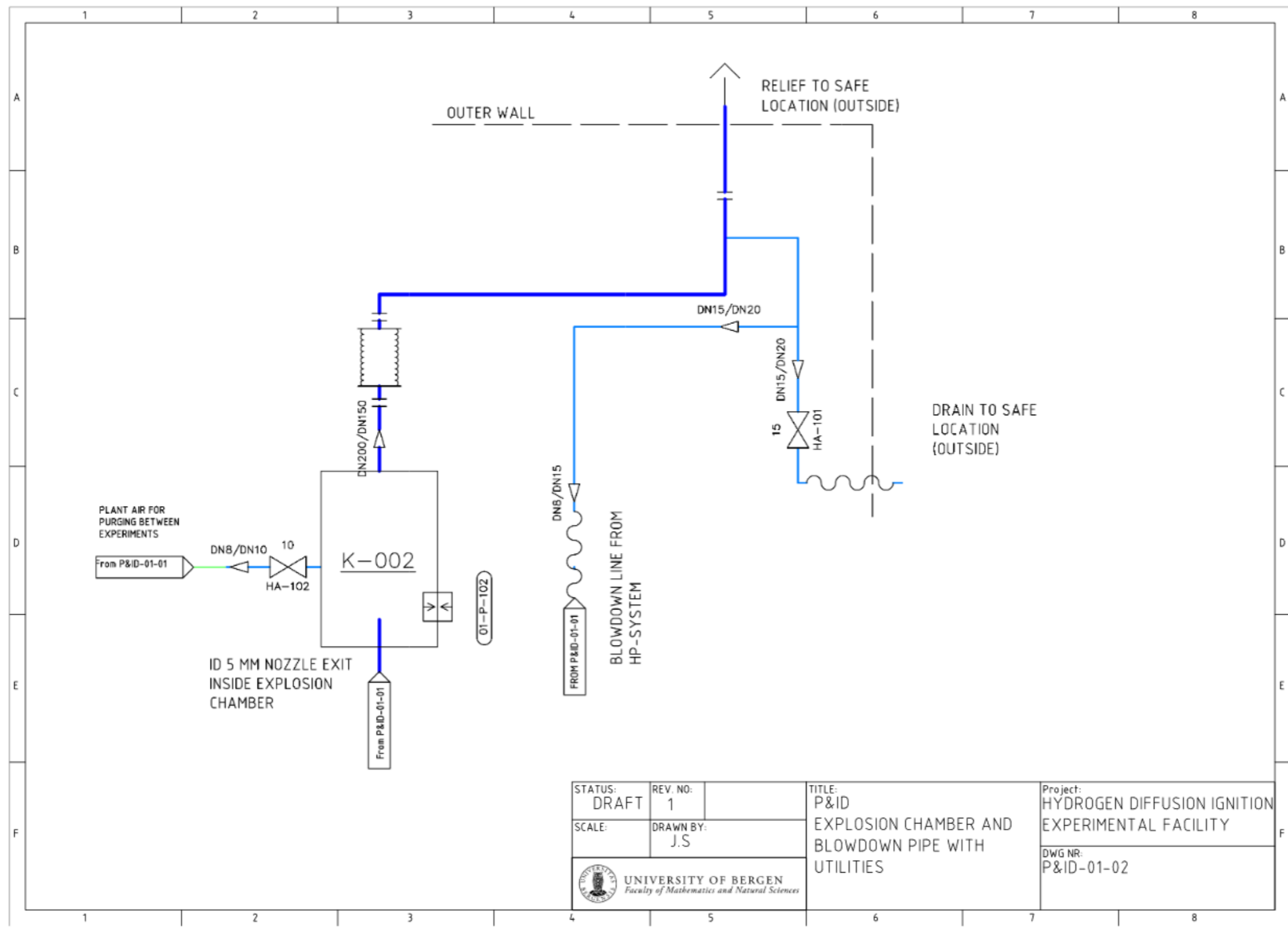
# D.12 P&ID-01-01

## High-pressure hydrogen system and gas bottles



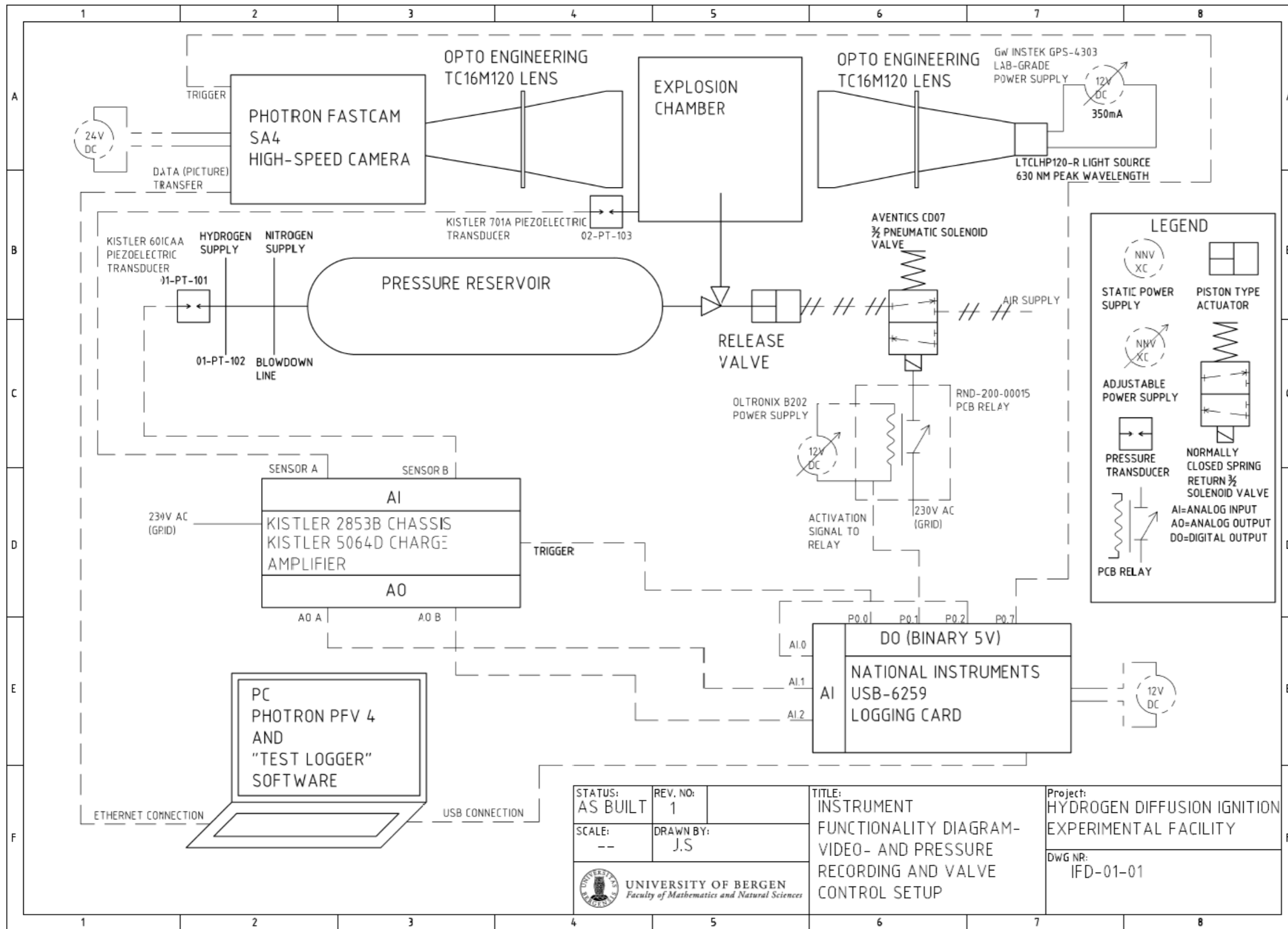
# D.13 P&ID-01-02


## Explosion chamber and blowdown pipe with utilities



# D.14 IFD-01-01

Instrument functionality diagram for video and pressure recording and valve control system



STATUS: AS BUILT	REV. NO: 1
SCALE: --	DRAWN BY: J.S
 <b>UNIVERSITY OF BERGEN</b> <i>Faculty of Mathematics and Natural Sciences</i>	

TITLE:  
INSTRUMENT  
FUNCTIONALITY DIAGRAM-  
VIDEO- AND PRESSURE  
RECORDING AND VALVE  
CONTROL SETUP

Project:  
HYDROGEN DIFFUSION IGNITION  
EXPERIMENTAL FACILITY

Dwg NR:  
IFD-01-01



# E Complete list of experiments

The table on the following pages summarises all experiments conducted as a part of the thesis, including the initial tests of the equipment. Some essential meta data about the experiments is also included in the table.

**Test no.:** A number assigned to each experiment based on the chronological order they were conducted. The index values with yellow background colour indicate experiments where ignition occurred.

**Gas:** Specifies the gas released in each experiment.

**Initial pressure:** The initial pressure in the HP reservoir before the release. This value was manually read from the digital manometer.

**Obstruction object:** Specifies the obstruction object:

OO A = Obstruction object A

OO B = Obstruction object B

OO C = Obstruction object C

Rod only = The connection rod that holds the OO, used as an obstruction object itself

None = No objects installed

**Distance from nozzle exit to impact point on object:** Specifies the distance from the nozzle exit to the central, most distant impact point on the obstruction object.

**Video?:** This column specifies if a video recording from the experiment has been saved.

**Rupture disc?:** Specifies if a rupture disc was used in the experiment, and if yes, which rated rupture it had.

**Ignition?:** Specifies if ignition was observed in the experiment.

**Release?:** Used to segregate the few attempts with rupture discs where the disc did not rupture.

**Max pressure difference, 1 ms intervals:** Specifies the maximum detected pressure difference in reservoir pressure during a 1 ms interval.

**Time of occurrence for max slope:** Specifies the time stamp for the middle of the 1 ms interval when the largest pressure difference was detected.

**Pressure decline at occurrence of max slope:** Specifies the

**Volumetric flow:** Shows the calculated volumetric flow rate from the maximum pressure difference, based on Eq. (11)

**Valve initiated:** Specifies the time stamp for when the valve release was initiated

~~Strikethrough~~-values indicate that the returned max slope value corresponds to an erroneous time. This only occurs on the experiments with low pressures, as the instrument oscillations produced steeper slopes than the actual release for some of these.

~~Double-strikethrough~~ is used to indicate the rupture disc experiments where the disc did not rupture.

Test no.:	Gas	Initial pressure [bara]	Obstruction object	Distance from nozzle exit to impact point [mm]	Video?	Rupture disc pressure [bar]	Ignition?	Release?	Max pressure difference, 1 ms intervals [bar ms <sup>-1</sup> ]	Time of occurrence for max slope [ms]	Pressure decline at occurrence of max slope [bar]	Pressure at max slope [barg]	Volumetric flow rate [Sm <sup>3</sup> s <sup>-1</sup> ]	Valve initiated [ms]
1	-		None	-		-								
2	-		None	-		-								
3	-		None	-		-								
4	-		None	-		-								
5	-		None	-		-								
6	-		None	-	Yes	-								
7	-		None	-		-								
8	-		None	-		-								
9	Air	6	None	-		-								
10	-		None	-		-								
11	Air	3.8	None	-	Yes	-								
12	Air	6	None	-	Yes	-								
13	Nitrogen	11.6	OO A	13.6	Yes	-			0.51	89.7	0	40.6	0.086775	84.8
14	Nitrogen	11.6	OO A	13.6	No	-						10.6	0	
15	Nitrogen	11.6	OO A	13.6	Yes	-						10.6	0	
16	Nitrogen	21.55	OO A	13.6	Yes	-			0.28	157.21	2.57	17.98	0.047641	82.9
17	Nitrogen	31.17	OO A	13.6	Yes	-			0.386	171.5	6.4	23.77	0.065677	84
18	Nitrogen	41.25	OO A	13.6	No	-						40.25	0	83.72
19	Nitrogen	41.05	OO A	13.6	Yes	-			0.43	199.54	16.64	23.41	0.073163	83.72
20	Nitrogen	51.25	OO A	13.6	Yes	-			0.535	151.47	4.725	45.525	0.091029	84.81
21	Nitrogen	61.62	OO A	13.6	Yes	-			0.992	150.45	5.567	55.053	0.168786	83.18
22	Nitrogen	71.12	OO A	13.6	Yes	-			0.7	168.78	15.01	55.11	0.119103	83.45
23	Nitrogen	81.25	OO A	13.6	Yes	-			0.83	155.76	11.14	69.11	0.141222	84
24	Nitrogen	92.5	OO A	13.6	Yes	-			0.89	155.34	11.33	80.17	0.151431	82.9
25	Nitrogen	101.1	OO A	13.6	Yes	-			1.06	159.3	14.01	86.09	0.180356	83.4
26	Hydrogen	11.3	OO A	13.6	Yes	-						40.3	0	81.54
27	Hydrogen	24.92	OO A	13.6	Yes	-			0.9402	87.35	0.1538	23.7662	0.159973	83.72
28	Hydrogen	54.9	OO A	13.6	Yes	-			1.34	148.91	11.32	42.58	0.227998	82.09
29	Hydrogen	41.5	OO A	13.6	Yes	-			1.017	147.98	8.82	31.68	0.17304	83.72
30	Hydrogen	31.75	OO A	13.6	Yes	-			1.198	87.76	0.12	30.63	0.203837	82.9
31	Hydrogen	21.15	OO A	13.6	Yes	-			0.553	152.03	3.103	17.047	0.094092	83.72
32	Hydrogen	54.3	OO A	13.6	Yes	-			1.21	154.92	18.54	34.76	0.205878	84.27
33	Hydrogen	54.3	OO A	13.6	Yes	-			1.28	155.72	15.74	37.56	0.217789	87
34	Hydrogen	54.1	OO A	13.6	No	-			1.233	145.46	9.87	43.23	0.209792	83.18
35	Nitrogen	29.7	OO A	13.6	Yes	-			0.367	165.36	5.62	23.08	0.062444	80.18
36	Hydrogen	61.67	OO A	13.6	Yes	-			1.31	159.54	24.42	36.25	0.222893	81
37	Hydrogen	71.75	OO A	13.6	Yes	-			1.52	151.61	17.33	53.42	0.258624	84
38	Hydrogen	81.48	OO A	13.6	Yes	-			1.67	158.92	25.23	55.25	0.284146	82.9
39	Hydrogen	92.6	OO A	13.6	Yes	-			1.86	163.33	25.47	66.13	0.316474	84.81
40	Hydrogen	104	OO A	13.6	Yes	-			2.28	154	33.35	69.65	0.387936	84
41	Hydrogen	104	OO A	13.6	Yes	-			2.25	158.28	35.3	67.7	0.382832	83.72
42	Hydrogen	104	OO A	13.6	Yes	-			2.18	161.7		68	0.370921	85.6
43	Hydrogen	103.5	OO A	19.5	Yes	-			2.09	155.2		77.1	0.355608	80.45
44	Hydrogen	112.75	OO A	19.5	Yes	-			2.29	154.2	31.65	80.1	0.389638	84.01
45	Hydrogen	92.3	OO A	19.5	Yes	-			1.86	152.9	23.44	67.86	0.316474	82.9
46	Hydrogen	82.7	OO A	19.5	Yes	-			1.77	154.06	28.2	53.5	0.301161	81.27
47	Hydrogen	82.7	OO A	19.5	Yes	-			1.75	158.54	30.1	51.6	0.297758	82.36
48	Hydrogen	82.8	OO A	7.9	Yes	-			1.67	154.38	25.11	56.69	0.284146	81.27

Test no.:	Gas	Initial pressure [bara]	Obstruction object	Distance from nozzle exit to impact point [mm]	Video?	Rupture disc pressure [bar]	Ignition?	Release?	Max pressure difference, 1 ms intervals [bar ms <sup>-1</sup> ]	Time of occurrence for max slope [ms]	Pressure decline at occurrence of max slope [bar]	Pressure at max slope [barg]	Volumetric flow rate [Sm <sup>3</sup> s <sup>-1</sup> ]	Valve initiated [ms]
49	Hydrogen	82.8	OO A	7.9	Yes	–			1.67	158.23	23.72	58.08	0.284146	84
50	Hydrogen	92.6	OO A	7.9	Yes	–			1.95	153.43	24.34	67.26	0.331787	84.81
51	Hydrogen	103.8	OO A	7.9	Yes	–			2.17	160.5	33.55	69.25	0.36922	83.72
52	Hydrogen	103.8	OO A	7.9	Yes	–			2.11	153.47	24.35	78.45	0.359011	83.72
53	Hydrogen	108.9	OO A	7.9	Yes	–			2.33	153.45	27.68	80.22	0.396443	83.18
54	Hydrogen	108.3	OO A	7.9	No	–			2.39	153.82	29.21	78.09	0.406652	82.63
55	Hydrogen	71.6	Rod only	7.2	Yes	–			1.41	159.54	21.62	48.98	0.239908	83.45
56	Hydrogen	82.6	Rod only	7.2	Yes	–			1.71	155.96	22.23	59.37	0.290952	82.9
57	Hydrogen	92.6	Rod only	7.2	Yes	–			1.98	151.51	27.89	63.71	0.336892	82.36
58	Hydrogen	103.6	Rod only	7.2	Yes	–			2.17	161.09	33.09	69.51	0.36922	84
59	Hydrogen	103.6	Rod only	7.2	Yes	–			2.12	156.13	32.57	70.03	0.360713	82.9
60	Hydrogen	61.7	None	-	Yes	–			1.25	149.97	10.67	50.03	0.212684	84.27
61	Hydrogen	71.6	None	-	Yes	–			1.35	155.32	16.78	53.82	0.229699	83.72
62	Hydrogen	81.7	None	-	Yes	–			1.77	155.81	24.6	56.1	0.301161	85.9
63	Hydrogen	92.7	None	-	Yes	–			1.88	162.4	26.35	65.35	0.319877	83.72
64	Hydrogen	107.1	None	-	Yes	–			2.15	154.6	28.02	78.08	0.365817	84
65	Hydrogen	107.1	None	-	Yes	–			2.17	152.5	26.96	79.14	0.36922	83.18
66	Hydrogen	105.1	None	-	Yes	50	No		2.15	153.23	33.7	70.4	0.365817	79.36
67	Hydrogen	106.8	OO A	15.25	Yes	80	Yes		2.25	152.71	28.05	77.75	0.382832	80.45
68	<del>Hydrogen</del>	<del>106</del>	<del>OO A</del>	<del>14.5</del>	<del>No</del>	<del>100</del>	<del>No</del>	<del>No</del>				<del>105</del>	<del>0</del>	
69	<del>Hydrogen</del>	<del>105.6</del>	<del>OO A</del>	<del>14.5</del>	<del>No</del>	<del>100</del>	<del>No</del>	<del>No</del>				<del>104.6</del>	<del>0</del>	
70	Hydrogen	103.1	OO A	14.4	Yes	50	No		2.4	153.56	30.01	72.09	0.408354	84.81
71	<del>Hydrogen</del>	<del>124.8</del>	<del>OO A</del>	<del>14.4</del>	<del>No</del>	<del>100</del>	<del>No</del>	<del>No</del>				<del>123.8</del>	<del>0</del>	
72	<del>Hydrogen</del>	<del>164.7</del>	<del>OO A</del>	<del>14.4</del>	<del>No</del>	<del>100</del>	<del>No</del>	<del>No</del>				<del>163.7</del>	<del>0</del>	
73	Hydrogen	179.7	OO A	14.4	Yes	100	Yes		9.475	157	9.535	169.165	1.612147	83.18
74	Hydrogen	177.5	OO C	13.8	Yes	100	Yes		4.2	149.35	44.78	131.72	0.714619	83.72
75	Hydrogen	176.6	OO C	30.2	Yes	100	Yes		4.12	147.23	47.74	127.86	0.701007	81.27
76	Hydrogen	176.1	None	-	Yes	100	No		3.77	154.77	48.92	126.18	0.641456	86.72
77	Hydrogen	176.3	Rod only	14.4	Yes	100	No		3.99	157.12	53.47	121.83	0.678888	84.54
78	Hydrogen	106.3	OO C	14.4	Yes	80	Yes		2.3	142.06	28.11	77.19	0.391339	73.91
79	Hydrogen	107	OO C	30.0	Yes	80	No		2.17	156.32	28.2	77.8	0.36922	84.54
80	Hydrogen	104	Rod only	14.4	Yes	80	No		2.24	153.87	34.9	68.1	0.38113	82.09
81	Hydrogen	104.4	OO A	14.6	Yes	80	Yes		2.23	151.46	28.43	74.97	0.379429	83.45
82	Hydrogen	103.5	OO A	10.2	Yes	50	No		2.25	148.25	25.28	77.22	0.382832	81.54
83	Hydrogen	103	OO B	10.1	Yes	50	No		2.06	154.14	30.1	71.9	0.350504	82.63
84	Hydrogen	165	OO A	13.6	Yes	–			3.61	142.28	45.36	118.64	0.614232	74.45
85	Hydrogen	166.4	OO A	13.6	Yes	–			3.84	148.46	46.01	119.39	0.653366	82.9
86	Hydrogen	161.6	OO A	13.6	Yes	–			3.7	149.9	43.17	117.43	0.629545	84.27
87	Hydrogen	129	OO A	13.6	Yes	–			2.82	150.59	34.92	93.08	0.479816	82.63